UNIVERSITY OF Southampton

University of Southampton Research Repository

Copyright © and Moral Rights for this thesis and, where applicable, any accompanying data are retained by the author and/or other copyright owners. A copy can be downloaded for personal non-commercial research or study, without prior permission or charge. This thesis and the accompanying data cannot be reproduced or quoted extensively from without first obtaining permission in writing from the copyright holder/s. The content of the thesis and accompanying research data (where applicable) must not be changed in any way or sold commercially in any format or medium without the formal permission of the copyright holder/s.

When referring to this thesis and any accompanying data, full bibliographic details must be given, e.g.

Thesis: Author (Year of Submission) "Full thesis title", University of Southampton, name of the University Faculty or School or Department, PhD Thesis, pagination.

Data: Author (Year) Title. URI [dataset]

UNIVERSITY OF SOUTHAMPTON

FACULTY OF ENGINEERING AND PHYSICAL SCIENCES

Engineering Sciences – Mechatronics Group

Applying Control Algorithms to Acoustofluidic Particle Manipulation

by

Zaid Shaglwf

Thesis for the degree of Doctor of Philosophy

January 2019

UNIVERSITY OF SOUTHAMPTON

ABSTRACT

FACULTY OF ENGINEERING AND PHYSICAL SCIENCES

Engineering Sciences – Mechatronics Group

Doctor of Philosophy

Applying Control Algorithms to Acoustofluidic Particle Manipulation

By Zaid Shaglwf

In recent years, manipulating micro particles and cells using acoustic waves has experienced significant growth in association with the latest developments of Lap-on-Chip devices. As a result, many scientific fields such as analytical chemistry have relevant applications for particle manipulation. There are many possible areas where particle manipulation can be used, for example, bringing cells to a specific position for observation and analysis. Traditionally, several techniques and methods have been employed for positioning micro particles using ultrasonic waves. However, none of these methods have demonstrated a precise positioning of particles using an automatic feedback control system using a sensor, actuator and controller.

The achievement of shifting and positioning particles automatically using lateral acoustic radiation forces is the specific objective of this project where two different control algorithms (navigation and steering) have been explored. Two main acoustofluidic devices have been employed as examples. Both algorithms are based on a feedback loop which considers the direction and distance to the target at each step and then applying a chosen acoustic force. The methods rely on using two resonant frequencies: the first one is the acoustic half-wave resonance frequency that functions to levitate the particles at the half-height of the device using the axial radiation force; the second resonance frequency is chosen from a set of possible resonances, and functions to shift levitated particles in the required direction.

List of Contents

List of Tables

List of Figures

Accompanying Materials

Thesis supplementary Data has been uploaded to the university repository web (http://dx.doi.org/xxxxx) as accompanying materials. These data include all relevant (Matlab and Arduino) files used to produce the results of both suggested manipulation algorithms (Navigation and Steering). They also contain three video examples of the steering algorithm (one for each steering method in a single trajectory and another one for a square shape).

Acknowledgment

First of all in regards to every single event in my whole life, I foremost thank Allah who made me successful, in particular, in my PhD research.

I am grateful to my parent Ibrahim and Fahima for their unlimited and unstoppable supplications and support since my birth.

I would like also to thank my wonderful wife Nouria for her huge sense of responsibility towards our small family and being patient and strive to make me fully dedicated to my PhD research.

My full appreciation and big thank goes to my enthusiastic supervisors Dr Peter Glynne-Jones and Dr Dina Shona Laila for their intensive academic supervision , guidance and support they gave me throughout my PhD program.

The USW group headed by Martyn Hill are appreciated too for their effective contributions and advises towards inspiration my PhD research.

Finally, I would like to gratefully acknowledge the support of the Ministry of Higher Education and Scientific Research, Libya, for the PhD scholarship.

Declaration of Authorship

Print name:	ZAID SHAGLWF
Title of thesis:	Applying Control Algorithms to Acoustofluidic Particle Manipulation

I declare that this thesis and the work presented in it are my own and has been generated by me as the result of my own original research.

I confirm that:

- This work was done wholly or mainly while in candidature for a research degree at this University;
- Where any part of this thesis has previously been submitted for a degree or any other qualification at this University or any other institution, this has been clearly stated;
- Where I have consulted the published work of others, this is always clearly attributed;
- Where I have quoted from the work of others, the source is always given. With the exception of such quotations, this thesis is entirely my own work;
- I have acknowledged all main sources of help;
- Where the thesis is based on work done by myself jointly with others, I have made clear exactly what was done by others and what I have contributed myself;
- Parts of this work have been accepted as:

1- Zaid Shaglwf, Bjorn Hammarström, Dina Shona Laila, Martyn Hill, Peter Glynne-Jones ,'' Acoustofluidic particle steering '', The Journal of the Acoustical Society of America.

Signature:		Date:	

Abbreviations

Abbreviation	Description
1D	One-dimensional
2D	Two-dimensional
3D	Three-dimensional
VVFMs	Velocity Vectors Force Maps
FM	Frequency Mode
SAWs	Surface Acoustic Waves
IDTs	Interdigital Transducers
PZT	Piezoelectric Transducer
MEMS	Micro Electro-Mechanical System
µPIV	Micro Particles Image Velocimetry
DM	Direct Method
CFM	Combined Forces Method

Chapter 1. Introduction

Recently, manipulating micro particles and cells using acoustic radiation forces – acoustofluidics - has found numerous applications in lab-on-chip devices[1]. Potentially useful manipulation operations include bringing cells to specific positions, bringing cells or cells and microbeads together and the control of motile organisms for observation. The acoustic radiation force, described in more detail below, is a time average force that results from non-linear acoustic terms and can be considered relating to the momentum carried away by waves scattered by the levitated particles. The trapping locations and force distribution are determined by the gradients of the distribution of acoustic energy. Typically standing waves are used as they create larger gradient forces. In its simplest form, acoustic manipulation is limited to moving particles to fixed positions within a device. The standing wave patterns that can be created are largely determined by the device geometry and the associated boundary conditions.

In this work, a control system is presented that uses radiation forces (and potentially acoustic streaming) to manipulate particles levitated in a half-wave resonator. A microscope/camera arrangement takes images of the position of particles, and applies a control algorithm programmed on a PC to actuate a PZT transducer that can excite a number of different acoustic modes within the resonant manipulation chamber. The frequencies of the modes are determined in advance but the forces that result from them are assessed using two different methods that suggest novel control strategies (''*navigation*'' and ''*steering*'' control algorithm) for the particle manipulation.

Particle manipulation is the principal aim of this work and automatic particle shifting and positioning using the lateral acoustic radiation forces are the specific objectives of this work. The types of acoustofluidic devices used in this research are both planar resonators.

The two algorithms explored in these thesis can be briefly described as:

a) The *navigation* algorithm, which is based on a microscope system observes the position of the target particles, and (during the "*manipulation*" phase) chooses a suitable acoustic resonance to direct the particle along its intended track at each temporal step. In order for the navigation algorithm to know what forces are created by each resonant frequency the available forces are measured in the possible device modes, and choose those modes which look promising – later called the "*registration*" phase.

b) A *steering* algorithm that does not require prior knowledge of available forces. Instead, a feedback arrangement using a microscope imaging system allows measurement of forces during manipulation. The steering algorithm consists of two processes: the ‘’*testing*’’ and ‘’*shifting*’’ stage. Two variations of steering method (the “*Direct Method*”, DM, and the “*Combined Forces Method*”, CFM) are established for this algorithm.

1.1 Acoustic Radiation Forces

Micro particles exposed to an ultrasonic standing wave field are affected by acoustic radiation forces that typically (for dense, compressible particles) move them to acoustic pressure nodes and acoustic velocity antinodes which are created by the acoustofluidic device geometry[2-4]. These acoustic radiation forces are determined based on the fluid and particle properties as well as the shape and amplitude of the acoustic field [5-7]. In the case of acoustofluidic devices which have a piezoelectric transducer that drives the propagated acoustic waves normal to the major device surfaces, the primary acoustic radiation forces typically consist of two main components: axial and lateral forces. The axial force is the component of the force in the direction of the acoustic field propagation. It is typically stronger, and drives particles (general assumption of a dense, compressible particle here for the sake of clarity) to the pressure node (*Figure 1.1(a)*), often levitating particles against the gravitational force. Due to lateral variations in the acoustic field, there are also gradients laterally, creating the lateral force (*Figure 1.1(b)*) which produces transverse particle displacements. At the pressure node, this term is entirely composed of gradients from the acoustic velocity field[8].

Gor’kov [6] derived the acoustic radiation force expression resulting from gradients in energy density terms. The force on a small (compared to the wavelength) particle is given (in a non-viscous approximation) by the following gradient[6],

$$F = \nabla\left(\left(\frac{3(\rho_p - \rho_f)}{(2\rho_p + \rho_f)}\langle E_{kin}\rangle - \left(1 - \frac{\beta_p}{\beta_f}\right)\langle E_{pot}\rangle\right)\right)V \qquad (1.1)$$

with

$$E_{pot} = \frac{\beta_f}{2}\,p^2 \qquad (1.2)$$

$$E_{kin} = \frac{\rho_f}{2}\,u^2 \qquad (1.3)$$

where *F* is the time averaged force on a particle of volume *V*, and E_{kin} and E_{pot} are the kinetic and potential energy densities respectively. These are functions of acoustic velocity magnitude *u* and acoustic pressure field *p*, and the brackets $\langle \dots \rangle$ denote the time averaging. The particle and fluid densities are ρ_p and ρ_f, while β_p and β_f are the particle and fluid compressibility respectively.

It can be seen that there are two terms that contribute to the force, based on gradients of the kinetic and potential energy densities which (for particles less compressible and denser than the surrounding fluid) direct the particles towards acoustic velocity antinodes and pressure nodes respectively. The axial force, which is aligned with the standing wave direction, has contributions from both terms of Equation (1.1), and in a half-wave system tends to levitate particles at the pressure node (which is also coincident with the velocity antinode) at the chamber centre. In the plane of the pressure node, which may undulate [2], there are no gradients in the potential energy term, and it is only gradients in the kinetic energy which give rise to the lateral component [9]. In this work the levitation position of particles may vary depending on the precise mode that is excited, thus forces from gradients in both terms are likely to act. Additionally, acoustic streaming is typically also present and could also be used for manipulation (this is found to be a factor in chapter 5).

If the levitated particles move close to each other, with a separation distance, *d*, (*Figure 1.1(c)*), the particles (spherical particles with identical radius) are subject to a particle-to-particle interaction force called a secondary radiation force F_s or Bjerknes force [10]. This force is expressed in Equation (1.4). The force is caused by the interaction of acoustic energy scattered from particles reaching other particles, and scales with the sixth power of the particle radius: [11]

$$F_s = 4\pi r^6 \left(\left(\frac{(3\cos^2\theta - 1)\,(\rho_p - \rho_f)^2}{(6\rho_f\, d^4)}\, u^2(\mathrm{x}) - \frac{\rho_p\ \omega^2 (\beta_p - \beta_f)^2}{(9d^2)}\, p^2(\mathrm{x}) \right) \right) \qquad (1.4)$$

Where ω is the angular frequency, r is the particle radius and θ is the angle between the x-axis of the propagation acoustic wave and the perpendicular axis to x-axis (particles centre-to-centre line) [11].

Figure 1.1 illustrates 1D axial and 2D lateral manipulation. Particles in all locations are driven towards the pressure nodal plane where the pressure gradient is zero (zero potential zone) as shown in Figure 1.1*(a)*. Then, the 2D manipulation (the lateral manipulation) initiates when the kinetic energy $E_{kin}(\mathrm{x})$ has a maximum contribution to the total force at the zero potential zone (particles are already trapped at the pressure node) and particles are pushed towards the acoustic velocity antinodes. *Figure*

1.1(b) shows the lateral manipulation where the particles tend to aggregate at the acoustic velocity antinodes [7, 9]. The secondary radiation forces cause the nearby levitated particles to aggregate together as shown in *Figure 1.1(c)* at the maximum magnitude of the acoustic velocity field. *Figure 1.2* shows the graphical illustration of the opposite relation between acoustic pressure (*P)* field and velocity (*V)* field.

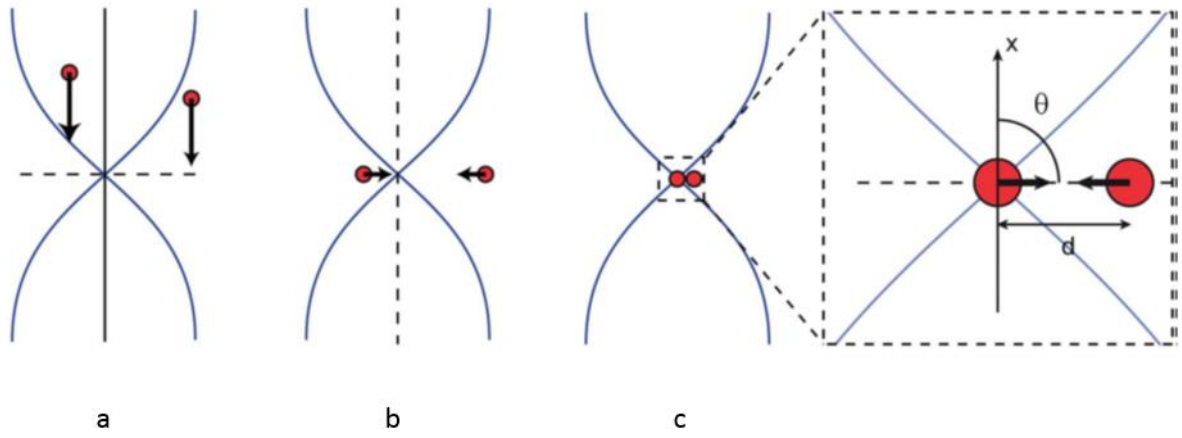

Figure 1.1: Illustration of particle manipulation in a half wave resonator. The acoustic pressure field (crossing blue lines) is applied and two example particles are shown (red circles). (a) The particles are driven to the pressure zero node by the axial component of the primary radiation force. (b) The levitated particles are then driven to the nearest velocity antinodes by the lateral component of the primary radiation force. (c) The effect of the secondary radiation force starts when the particle to particle separation distance, d becomes significantly small and angle ϑ must be 90 degrees [8].

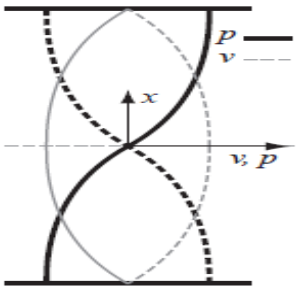

Figure 1.2: Schematic diagram of pressure, P, and velocity, v, fields in a one-dimensional standing wave. Fields represent the gradient of potential energy density and kinetic energy density respectively[12].

1.2 Acoustic Streaming

Acoustic streaming, which is a bulk movement of the fluid carrying the acoustic wave, occurs when energy is absorbed, either in bulk or in boundary layers [13]. Different types of acoustic streaming have been discussed in previous literature [14] based on the motion of the micro particles and the

geometry of the acoustofluidic device. The three main types of acoustic streaming are Eckart, Schlichting and Rayleigh streaming [15-17].

Rayleigh streaming is a motion in the bulk of a chamber driven by Schlichting streaming. These vortices have scale one quarter wavelength in the resonance direction, and typically extend towards the centre of the chamber [12, 18, 19]. Schlichting streaming has vortices of width comparable with the acoustic boundary layer, but also one quarter wavelength long in the resonance direction. It is driven by dissipation in the boundary layer [17]. Additionally, acoustic energy absorption in the bulk fluid causes Eckart streaming [16] and this results in typically large scale streaming vortices, but is less important in smaller devices where dissipation in the bulk is not significant.

1.3 Motivations and Objectives

The measurement of the velocity and displacement of the micro objects has become easier following the latest developments in micro-imaging cameras and acoustofluidic devices. However, to date, no fully automated control systems have employed a robust algorithm for accurate acoustic 2D positioning of the cells and particles within a microfluidic device.

This work mainly explores the possibility for automated manipulation of the levitated particles using the lateral acoustic radiation forces generated within suitable acoustofluidic devices. The lateral component of the acoustic radiation force is much harder to measure or predict than the axial component, and thus requires measurement either before or during manipulation and active control.

The research uses an approach that combines two frequencies, one for levitation of the particles at the half height of the fluid chamber using the axial forces and the second frequency is then used to move the particles laterally. This approach is motivated by the desire to be able to work with devices that are poorly characterised or have unpredictable force distributions, making manipulation with a much wider range of devices possible.

The main objective identified for this work is to establish an entire closed loop feedback system that links between acoustic resonators, cameras and controllers to provide real acoustofluidic particle navigation and steering. Such a feedback system will be capable of exploring various possibilities for other applications such as tissue engineering and cell analysis and observations.

1.4 Thesis Structure

The structure of this thesis is divided into the following chapters:

- The topic of particle manipulation is introduced and reviewed in Chapter 2 where various forms of particle manipulation using ultrasonic waves are discussed.
- Chapter 3 describes the design of devices that are used in manipulations in subsequent chapters for both control algorithms.
- The characterization of the forces in devices and generation of VVFMs (Velocity Vectors Force Maps) which are used by the navigation algorithm is established in Chapter 4.
- Chapter 5 describes and evaluates the first control algorithm (navigation) that uses the VVFMs measured before manipulation for particle manipulation as a "map". This chapter also presents a simulation of this algorithm.
- Chapter 6 describes the second control algorithm (steering algorithm) that measures the forces at steps during manipulation runs. Hardware is developed and two alternative steering methods are evaluated (the "Direct Method", DM, and the "Combined Forces Method", CFM). Also included in this chapter are statistical results to compare the performance of each algorithm in terms of their manipulation speed, and magnitude/direction errors.
- Chapter 7 states the main conclusions and the recommendations for further work to be carried out in future.

Chapter 2. Literature and Background

2.1 Acoustofluidic Manipulation

An early example of acoustofluidic manipulation [20] was shifted suspended particles using ultrasonic standing waves generated between one transducer and a reflector in water. Small variation in frequency could be used to adjust the trapping position, and create a limited degree of manipulation. However, greater control over the acoustic field is required in order to achieve more flexible manipulation.

The standing wave pattern that also determines trapping locations can be considered a superposition of two counter propagating waves, which in the case of a fixed reflector comes from the reflected wave. However, by aligning transducers at an oblique angle [21, 22], using transducers that minimise reflections [23], or by relying on absorption [24], systems can be created that allow each of these components to be independently created with arbitrary phase differences. Thus, by modulating the phase difference, arbitrary trapping positions can be attained. An alternative to controlling the pressure node position is to exploit the kinetic energy gradient contribution to the radiation force, which tends to move particles levitated in a 2D pressure node to regions of maximum acoustic velocity. This movement can be effected by arrays of transducers [25, 26].

With respect to other particle manipulation systems, particle separations, fractionation, focusing and sorting of particles based on their sizes have been established using separation [11, 27-33], or by switching between different modes to create time averaging effects [34-36]. Moreover, pattern generation has been described as a type of particle manipulation [14, 37]. Trapping and positioning the cells for instance by Courtney et al. [23, 38] and transport of cells and particles by the use of frequency-modulated acoustic actuation of a microfluidic device have also been reported [39].

In addition to the above, manipulation of micro particles using acoustic waves can be classified in according to different parameters. Following Drinkwater et al. [40], manipulation devices are classified based on the type of acoustic field, where the standing wave devices are able to produce dynamic fields [41] and static fields [2, 42-44]. Temperature issues can become significant in many of these devices [45] particularly in opposed travelling wave devices where energy needs to be absorbed after passing through the manipulation region. Moreover, manipulation can be assessed by type of wave form; bulk wave (BW) [46-48] and surface acoustic wave (SAW) [49-51] where the control method and the number of transducers are varied in each type. Despite the recorded studies with different

approaches for controlling the position of particles, new manipulation capabilities need to show more accurate positioning of particles using new control strategies.

In terms of navigating and steering single particles, to date, several techniques and methods have been used for positioning micro particles using lateral acoustic radiation forces [9, 37, 52]. However, none of these methods has demonstrated a precise positioning and steering of a single particle using an automated closed loop-feedback control system. Regarding the type of actuating force, the attempts to steer and position particles have been performed by using different types of manipulation forces, electrical, optical and mechanical forces for instance [53]. Few of these efforts have been employed for steering individual or multiple particles with the feedback control systems [38, 54-61]. As the actuation force has two components (axial and lateral) most of these steering studies have used the axial component of the propagation wave as the actuating force. Hence this allows a more predictable manipulation trajectory (force magnitude and direction are known) as well as achieving higher control precision.

Magnetic [61] and optical tweezers [57] have shown significant development of particle steering in the field of MEMS. Although acoustic tweeers are not so well developed, they are an attractive technology considering the low material and component costs.

Through the use of acoustic fields carrying angular momentum such as Bessel beams, acoustic tweezers have the ability to generate rotational motion through acoustic vortices that rotate the trapped particles around the fluid chamber centre. The 2D manipulations resulting from the acoustic tweezers, use the axial component of the primary acoustic force [38]. A type of manipulation using lateral acoustic forces to shift groups of particles using tweezers has also been introduced in the field of MEMS by Glynne-Jones et al. [9]. The technology employed a 1D planar multilayer resonator array that levitates the particles at the pressure node of the half wavelength plane and moves them along the device based on the location of the maximum velocity antinode above the centre of the activated array.

2.2 Particle Positioning

Many different techniques can be employed to manipulate cells using acoustic waves. Haake et al. [52] presents one of these techniques which is capable of displacing and positioning cells without causing damage to the cells. In their study the displacement ranges from 50 µm to 1.5 mm. It is based on exciting the flexural vibrations in the layer formed at the base of the device. In order to achieve different results in positioning the cells, the device is demonstrated using two types of cells, MCF60A

and HL60, where the first type was difficult to control after 2 hours because they coalesced with each other rapidly making one group of cells. The second type of cell can be successfully suspended. These results are achieved within an acoustofluidic device which has a 300 µm fluid layer vibrating at a range of frequencies (0.4-2.2 MHz). The acoustic positioning of the cells has been attained in two separate forms (see *Figure 2.1*). These are lines and individual points that were obtained by using 2D and 3D sound fields respectively. Controlling the position of group of particles has also been demonstrated in *Figure 2.2* where group of cells are shifted over a 180 µm total distance.

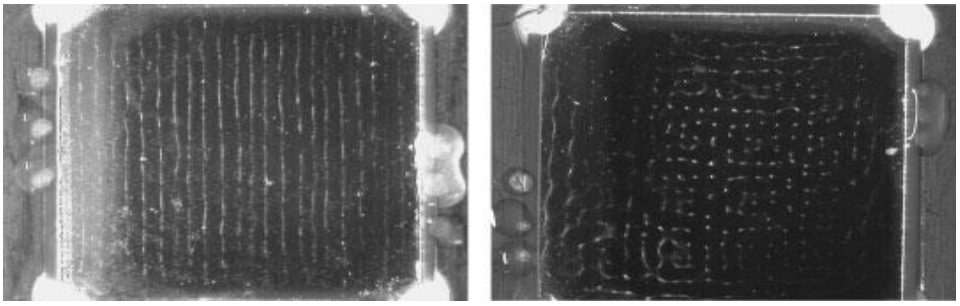

Figure 2.1: Positioning the HL60 cells in line (left) and point (right) patterns at spacing of 0.55 mm [52].

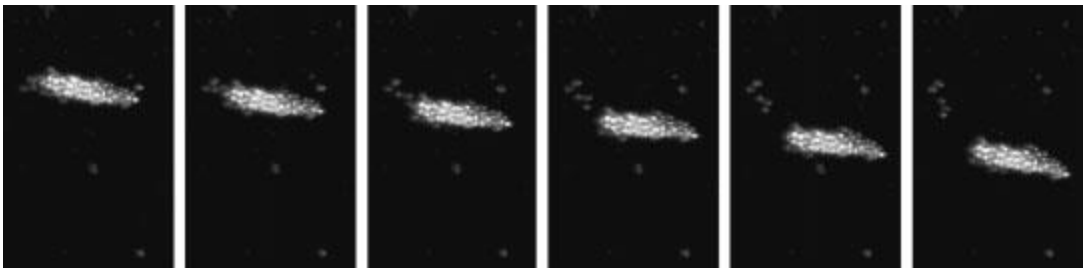

Figure 2.2: Shifting a group of HL60 cells by varying the amplitude of two drive signals generated by two opposite transducers [52].

2.3 Pattern Generation

In addition, the possibility of forming different patterns has been investigated by Oberti et al. [37]. They used separate 2D arrays to excite different operating modes by using a square piezoceramic plate (piezoelectric transducer) attached to the bottom of the fluid chamber on the acoustofluidic device. Four divisions were made on the transducer (see *Figure 2.3*). The transducer divisions are perpendicular to each other and are connected to four electrodes to generate one or two dimensional pressure fields. In the case of activating two orthogonal transducers, two operating modes were generated: one uses two signals which are identical in frequency and amplitude to trap particles in an elliptical shaped group (see the right side image in *Figure 2.3*). The other operating mode uses two signals but slightly different in frequency and amplitude to trap particles in a circular shaped group. In

the case of activating only one transducer (see the left side and centre image in *Figure 2.3*), the particles are trapped in parallel lines of kinetic energy density maxima corresponding to the activated transducer. In general, particles are focused in one or two directions depending on which way the electrodes are activated where a maximum of two electrodes can be activated at the same time. However, the approach of activating different transducer's divisions leading to varying the position of kinetic energy densities can be utilized for precise positioning of a single particle or a group of particles using a closed loop feedback system.

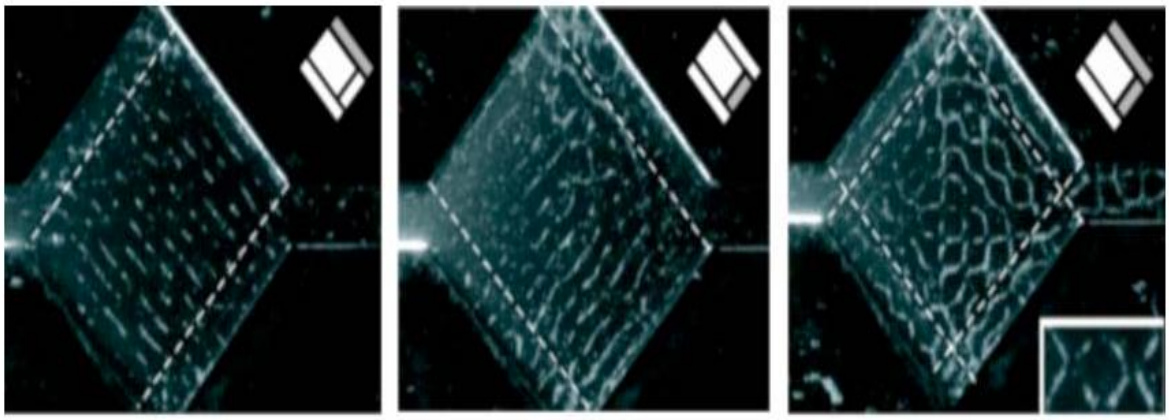

Figure 2.3: Generation of different particle patterns (9.6µm copolymer particles are used). When one electrode (left and middle image) is activated resulting in lines parallel (maximum kinetic energy densities) to the activated electrode. Two orthogonal electrodes (right image) are activated by the same voltage at the same time. This results in creating potential minima causing particles to gathering in oval shapes [37].

2.4 Particle Fractionation and Separation

Particle separation can be achieved by using different methods, one of these methods has been described by Harris et al. [34]. They introduced a technique to differentiate between large and small particles. The described technique uses an efficient multilayer device that produces three operating modes of frequency generated by two transducers, as shown on Figure 2.4 and *Figure 2.5*. After all particles enter the chamber, the process starts by applying the first mode (half wave mode with 660 kHz) to centralize all particles into one known point which is the zero pressure node. This is done by activating the first transducer. The second (quarter wave mode) and the third (third wave mode) modes are subsequently applied by activating the second transducer. The second mode (with 1.31 MHz resonance frequency) is used to separate and shift the larger particles from the first centralized point (half wave pressure node) into two acoustic pressure nodes. At this stage the smaller particles have not reached the outer nodes due to their velocity being slower than the larger particles. Then, the third mode with a resonance frequency of 1.926 MHz is applied to regulate the small and large

particles into three pressure nodes. However, the separation method presented only uses the pressure field which is applied in one dimension in the same direction as the propagating wave. Therefore, the velocity fields with their traps (velocity antinodes) can also be utilised for 2D particle separation using multi frequency modes, irrespective of number of transducers to be used.

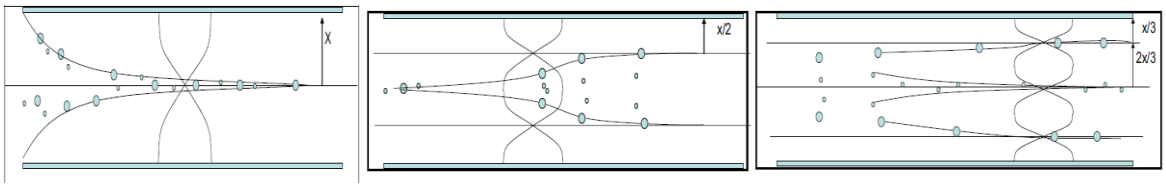

Figure 2.4: Separation sequence demonstration based on the resulting pressure fields. (Left) First mode applied to centralize all particles in the half wave height of the device, second and third application mode to separate particles into 2 and 3 nodal lines (zero pressure nodes) respectively based on their sizes [34].

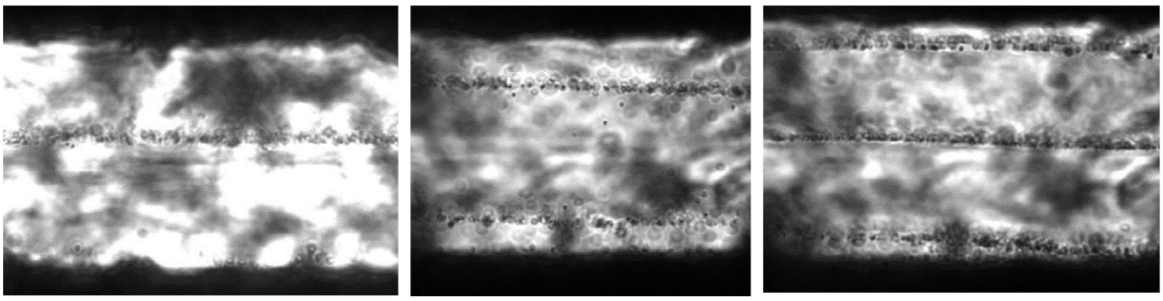

Figure 2.5: The experiment images which show the separation method for two different sizes of particle using three different pressure fields. Each pressure field has its zero pressure nodes: (Left) 660 kHz provides one pressure node, (middle) 1.31 MHz provides two pressure nodes and (right) 1.926 MHz provides three pressure node respectively [34].

Liu et al. [35] carried out a study on the use of resonance frequencies to displace and fractionate spheres to a desired position within the chamber height. This separation result has been achieved in a stationary fluid and by switching between two modes (half and third wave modes) with the duty cycles T_1, T_2 (2 seconds for each). The first f_1 and third f_3 resonance modes of the fluid channel are 1.88MHz and 5.59 MHz respectively. These generate one and three acoustic pressure nodes respectively so that particles tend to move towards these nodes using each mode. As shown in *Figure 2.6*, the separation process begins by applying the first mode, and the spheres are injected into the chamber after the offset time t_o. The separation method depends on the particle size, where larger particles experiencing a larger acoustic force which moves them faster towards the centre node C. The smaller particles move more slowly. When the third mode is switched on, the node A will be closer to the large particles and the small particles will begin gathering at a suitable starting location. By repetitive switching between the standing acoustic waves for number of cycles, the large and small spheres are separated and placed at the C and A nodes as required.

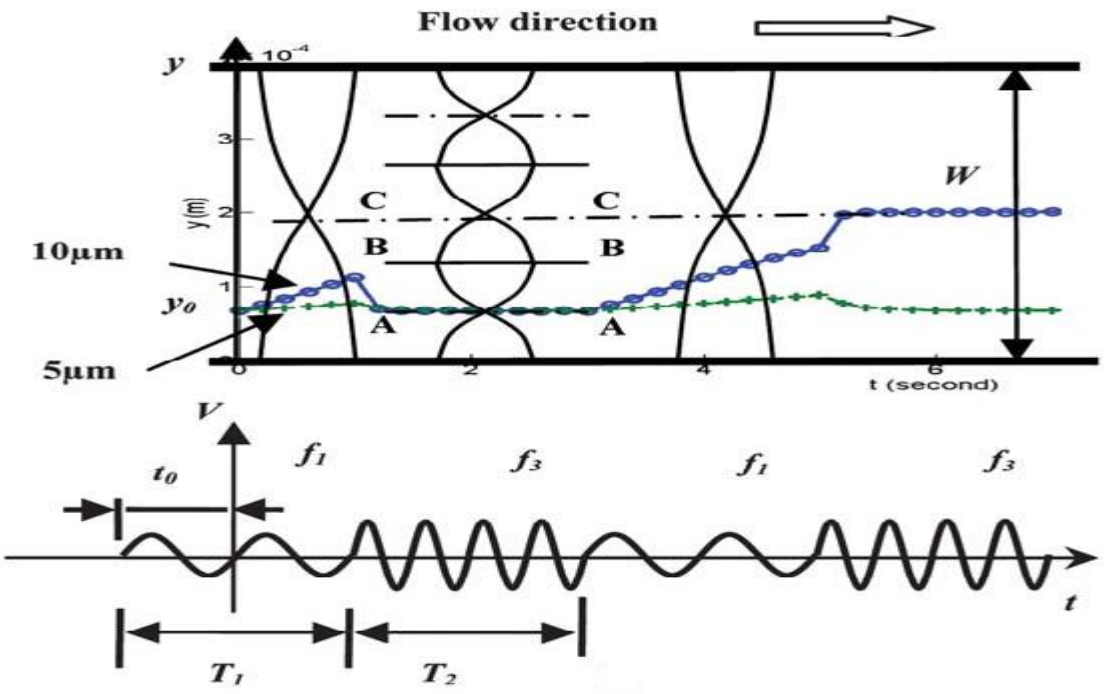

Figure 2.6: Duty cycles between two modes f_1 and f_3 . The results show the manipulated 5 (green dots) and 10 (blue circles) µm particles separated at the A and C nodes respectively [35].

2.4 Acoustofluidic Devices

2.4.1 Opposed Travelling Wave Tweezers

A device consisting of 64 transducer element in a circular array was demonstrated by Courtney et al. [38] to electronically produce and control arbitrary pressure fields within the circular chamber. This device has the ability to generate acoustic vortices in order to rotate the trapped particles around the centre of the fluidic chamber as well as shifting them in 2D directions. The approach used a superposition of fields from the array of transducers to create a higher order Bessel beam (or several such) that had a pressure node at its centre. *Figure 2.7* demonstrates the shifting of 2 trapped 90 µm particles in opposing y directions. The first three images (a, b and c) demonstrate the experiment manipulation steps using variations of opposite arrays while the last image (d) shows the magnified manipulation area including both the model and actual particle paths as well as the desired path. The total displacement is 800 µm (which is less than 10x particle diameter), and the deviated distance

between the desired (direct) and actual path is 130µm. *Figure 2.8* (a, b and c) shows the rotation of three trapped 90 µm particles at 400 µm distance from the chamber centre.

However, this kind of tweezers is expensive, complicated to build, and has high power consumption due to the usage of a high number of element arrays.

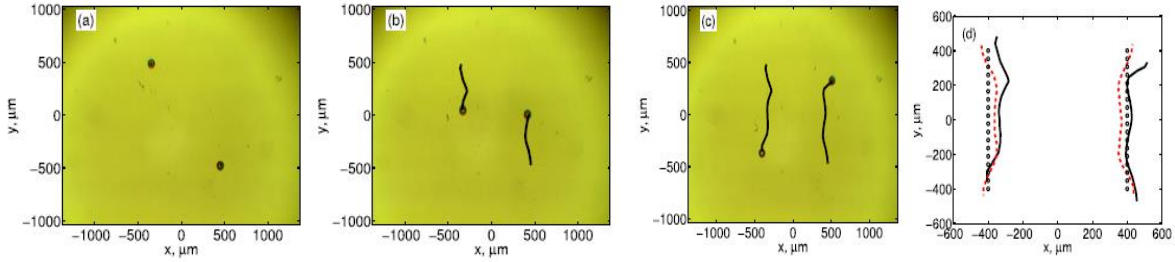

Figure 2.7: The first three images (a, b and c) demonstrate steps of 800 µm displacement for two 90µm particles moving in opposite directions. The last image (d) is the comparison between model (red circles) and actual (black line) paths while the black dots indicate the desired paths [38].

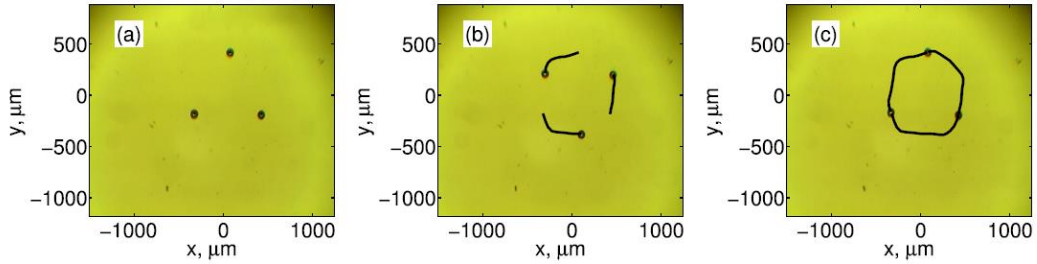

Figure 2.8: The anticlockwise rotation of three 90µm particles (all three particles are brought to the centre of the chamber later) [38].

2.4.2 Surface Acoustic Waves (SAWs) Devices

Another method to trap and manipulate micro particles using a new type of acoustic wave that employs acoustofluidic devices has been introduced in the field of MEMS. These types of acoustic waves are called Surface Acoustic Waves (SAWs). The SAWs have been integrated into to a single layer microfluidic chip [49, 62]. Guo et al. [62] used this kind of acoustic wave, where the application was to manipulate and control micro particles such as polystyrene beads, cells and organisms within a channel substrate. The type of transducer used to produce these SAWs relies on two pairs of chirped interdigital transducers (IDTs) (Figure 2.9(A)) which generate a radio frequency to suspend the particles at the pressure nodes of the standing acoustic waves. These IDTs are situated opposite to each other in order to generate two pressure fields (one for the x axis and one for the y axis) such that particles are manipulated in 2D within the SAWs navigation plane.

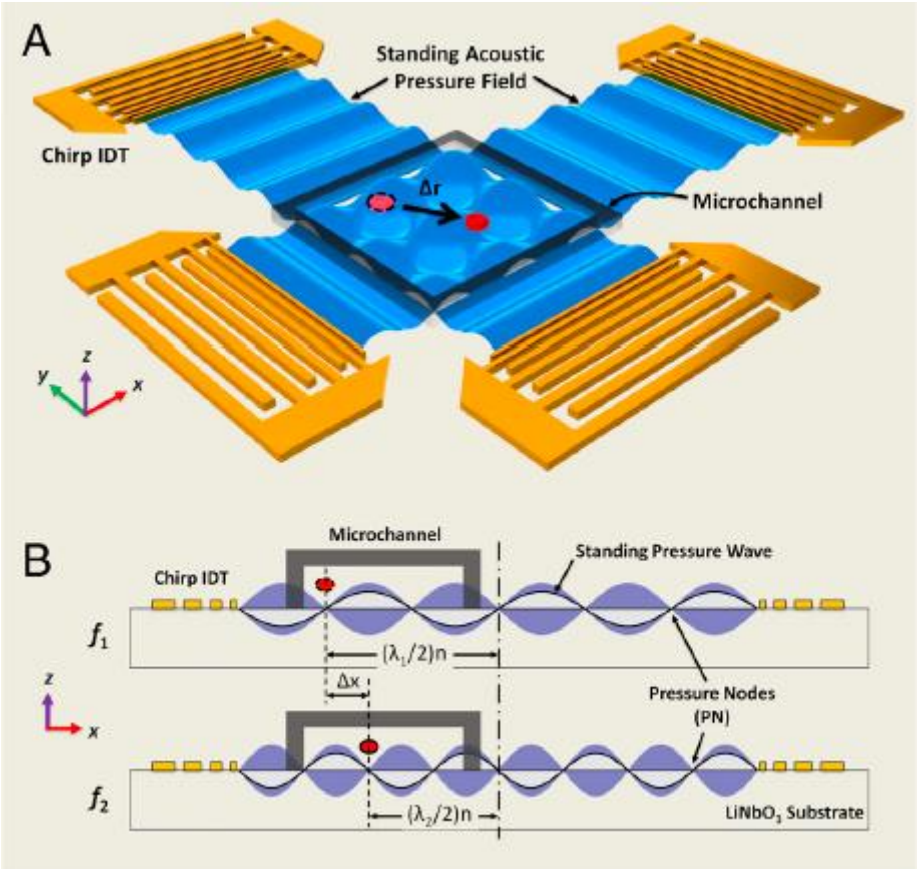

Figure 2.9: Illustrations demonstrating manipulation of a micro particle using technology consisting of an orthogonal pair of chirped interdigital transducers (IDTs) that generate a SAW. (A) A schematic of the microfluidic device with orthogonal pairs of chirped IDTs for generating perpendicular standing SAWs. (B) Standing SAWs generated by driving chirp IDTs at two frequencies f_1 , f_2 to shift a particle (red dot) a distance Δx (Δx is the distance between the f_1 and f_2 pressure nodes) [62].

The basic method to move a single particle in the x direction from one pressure node position to another is shown in *Figure 2.9(B).* The position is shifted from one location to another by switching between two standing wave frequencies f_1 and f_2 generated by one transducer. However, in comparison to other planar resonators, this technology of IDTs seems to be expensive and it is complicated to build integrated transducers within the microfluidic chips.

2.4.3 Wedge Transducer

Typical acoustofluidic manipulation devices are designed to generate an acoustic standing wave produced by either two opposing transducers, or one by transducer with a reflector layer. These devices typically provide pressure nodes located parallel with the transducers. However, in some cases, the pressure nodes are not generated in the same direction of the propagation acoustic waves. For example in situations where there is a requirement for minimizing heat transferred from transducers[63], the pressure nodes can be generated by a Wedge Transducer that allows for long

term manipulation. In addition, Manneberg et al. [64] have employed a Wedge transducer to investigate the result of combining two different resonance frequencies in order to achieve better 2D particle manipulations. The approach involved using an optimal design of asymmetric transducer alignments, where two wedge transducers are perpendicular to each other which generates a combined standing wave field. They found that this wedge transducer design can achieve 1D and 2D manipulations either with one transducer that makes the switching between different modes; or with two transducers that drive different resonance frequencies at the same time.

2.4.4 Transducer Arrays

The advantage of using the lateral radiation forces to shift the levitated particles, has been introduced in the field of MEMS by Demore et al. [65]. The device was constructed by connecting a glass capillary to a transducer array that consists of a number of elements. The manipulation method uses the advantage of the axial and lateral components of the primary radiation force, where the agglomerated particles are levitated by the axial force at the half wave pressure node of the capillary channel. Then, the trapped particles move laterally along the channel length by shifting (activating) the adjacent active elements as a result of varying the position of the maximum kinetic energies. This is shown in *Figure 2.10*. A small lateral velocity compared to axial velocity was recorded (1.9 and 61 pN respectively), The shifted distance is about 3mm with a lateral velocity 0.02 mm/s. Similar work has been performed using the same 1D planar array [9]. This device is only capable of moving levitated particles in 1D due to the transducer design. However, it can be refabricated to manipulate particles in 2D where this matter was addressed using 2D array [66]. Nevertheless, there are concerns about these transducer technologies which focus on their expense and the complication in building them.

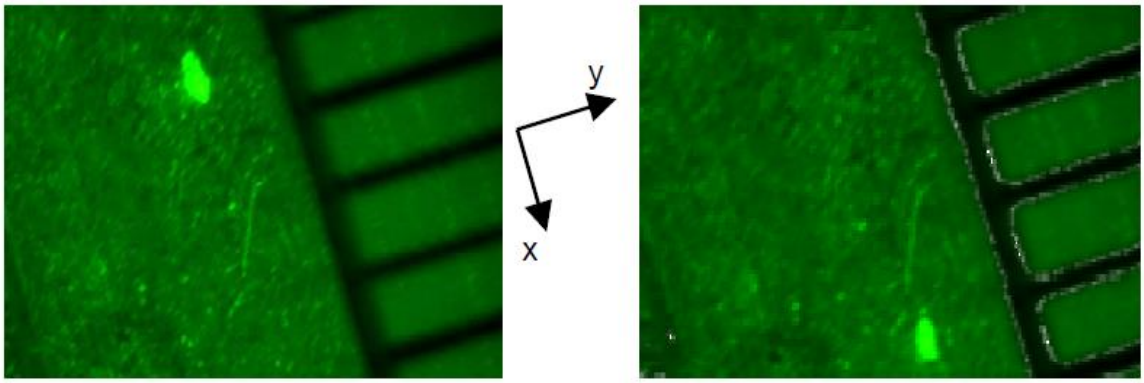

Figure 2.10: A 3 mm lateral shifting of a group of 10µm polystyrene beads along the microfluidic device using the advantage of varying the kinetic energy densities over the activated array [65].

2.5 Shifting Particles using Mode Switching

A rapid switching between resonance frequencies can be used to establish modal trapping positions between the fixed positions of the two contributing modes. Glynne-Jones et al. [67] demonstrated this approach by gradually changing the duty cycle of two resonance modes to move the particles trapping position to any arbitrary positions between the half and quarter wave pressure nodes. As the mode switched rapidly back and forth between the half and quarter wavelength frequencies, particles flipped between two nodal pressure positions (stable of forces equilibrium) within the fluid chamber. *Figure 2.11* shows one cycle of the particles being shifted gradually from the central position (half wave pressure node) of the flow-through chamber, to the upper height of the chamber (quarter wave pressure node). According to this result, a combination of two modes has been implemented to shift the particles to an arbitrary position between the pressure nodes. However, this demonstration of particle manipulation has only shown 1D shifting and positioning of particles using the axial component of the primary acoustic radiation force within the device pressure field of the frequency modes. More sophisticated methods are required for 2D shifting using both pressure and velocity fields.

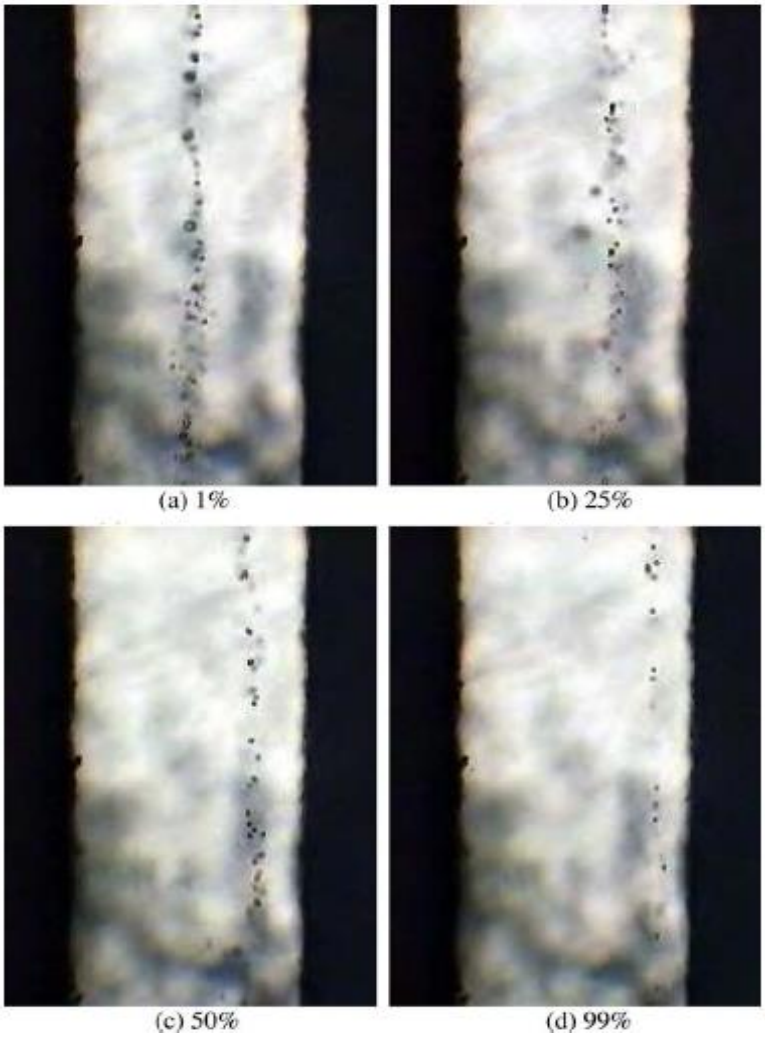

Figure 2.11: The manipulation of beads being shifted gradually between half and quarter wave pressure nodes. The annotations of each image demonstrates the percentage proportion of the quarter wave. As the percentage of the quarter wavelength mode increased over the time with exciting of the half wave mode, the beads are being mobilized gradually towards the quarter wave pressure node [67].

Chapter 3. Acoustofluidic Devices

This chapter presents the design of devices that are used in subsequent chapters to test the control algorithms. The method of construction for each device is shown, in addition to the initial characterisation by electrical impedance. A 1D transfer-impedance model is also used as a design tool to show the expected distribution of acoustic pressure amplitude through the devices.

3.1 Capillary with Bulk PZT

The manipulation device described in this section is constructed from a glass capillary (ID 0.3 x 6 x 50 mm; Vitrocom, NJ, USA) glued to the PZT (1 x 6.6 x 25 mm, PZ26, Ferroperm) where the assembled device is shown in *Figure 3.1*. This device has a half-wave resonance for levitating particles in a vertical plane (z-axis) at the half-height of the fluid chamber at the zero pressure node (minimum acoustic potential energy) where particles at this cavity vertical position tend to agglomerate to locations of maximum velocity antinodes.

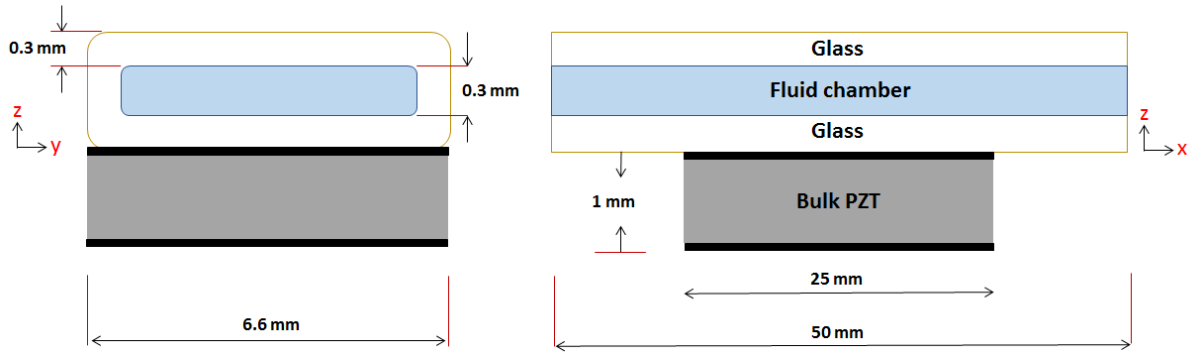

Figure 3.1: The dimensions of glass capillary device. Cross-section (left) and length section (right).

In order to manipulate particles laterally at the levitation plane (moving them in x, y axis), other resonances are introduced to induce forces that could be used to move particles around within the chamber. The approach here is to combine these resonances with the half-wave resonance so that particles are manipulated in 2 dimensions within the levitation plane.

The main acoustic resonance frequency was evaluated by generating the acoustic electrical impedance of the device in two states, filled with water and air respectively where the resonances are conductive in water unlike air medium. *Figure 3.2* shows the impedance of the acoustic device at a wide range of frequencies.

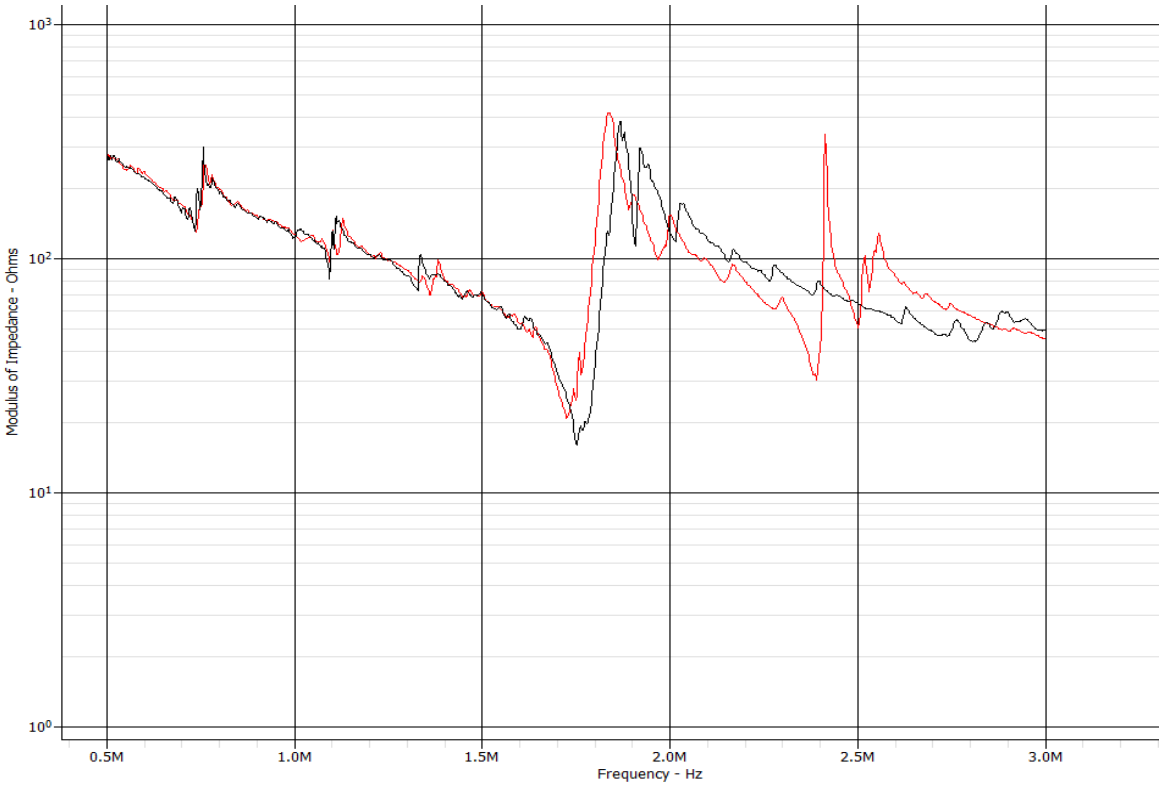

Figure 3.2: Characteristic impedance measurement of the glass capillary with two media (water is red curve and air is black curve). The half wave resonance frequency is indicated by peaks at around 2.4 MHz, this is only manifested in the water curve. As the main device resonance occurred in water only at the minimum electrical impedance while the PZT resonance peaks in both mediums. .

Figure 3.2 shows features/peaks at various resonance frequencies. The majority of peaks are found in both the air and water filled plots, and represent resonances in the device that do not have significant energy in the fluid layer. The precise nature of these resonances is not easily deducible from the plot. The sharp peak that is found only in the water filled device is the half wave resonance, this being confirmed by experimental observation of particle manipulation.

The half wave resonance of the device which is responsible for particles levitating is found at (experimentally by performing the frequency sweeps) 2.4 MHz. This is the minimum impedance which occurs with water only. Other minimum peaks can have some lateral resonance that help for moving the particles sidewise. The investigation of these lateral frequencies is presented in Chapter 4.

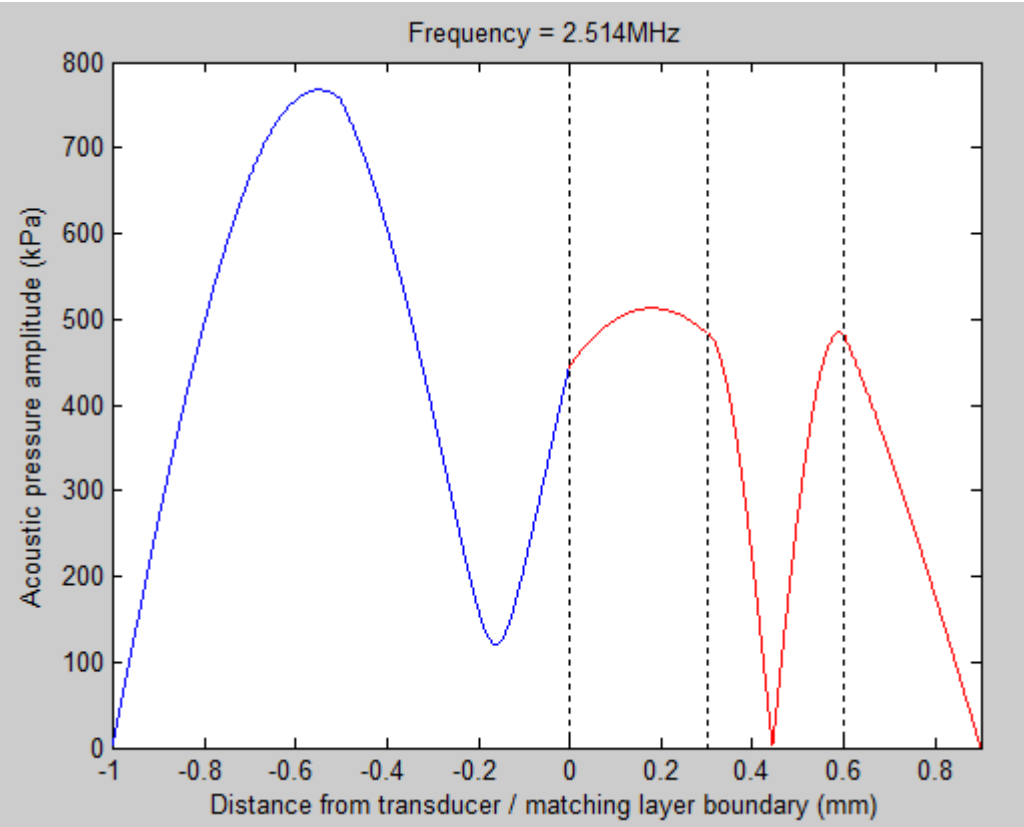

Figure 3.3: Predicted zero pressure node position for glass capillary device at resonant frequency 2.514 MHz where the minimum pressure (zero pressure node is the zero acoustic pressure amplitude within the fluid chamber) occurred at the half distance of the vertical axes in the acoustofluidic device's fluid chamber.

The predicted position of the zero pressure node is plotted using the KLM model for this device and is shown in *Figure 3.3*. The cavity half wave resonance frequency in which particles in all axial locations to be driven to the zero acoustic pressure node (minimum acoustic potential energy) is modelled at 2.514 MHz. This value is slightly different than the characterized value presented in *Figure 3.2*. The above figure is generated using 10 volts where 484.6 and 484.9 kPa are the maximum acoustic pressures at the contact of the fluid layer with carrier layer and reflector layer respectively, while acoustic pressure decreases towards the half height of the cavity layer.

3.2 Planar Resonator

A new acoustofluidic device has been fabricated with a cavity layer of 0.3 mm of double sided tape shown in *Figure 3.4*. The device dimensions are shown in *Figure 3.5* and *Figure 3.6*. The design criteria is based on the need for strong lateral acoustic radiation and streaming forces. A rectangular device is deliberately designed which is shown in the channel plan view, to introduce more horizontal streaming patterns to the acoustic field within x, y plane where the interested manipulation area is shown in *Figure 3.4*. According to Lei [68] , the aspect ratio of this device, 0.03, (the ratio between the

height (h) and the width (w) of the cavity) is considered to be a low aspect ratio ($h/w \leq 1/20$). This ratio determines that there is transducer plane streaming stems from the transducer in form of x, y horizontal streaming. Therefore, the acoustic streaming forces are likely to be a significant factor in this device that contribute to a better 2D manipulation process.

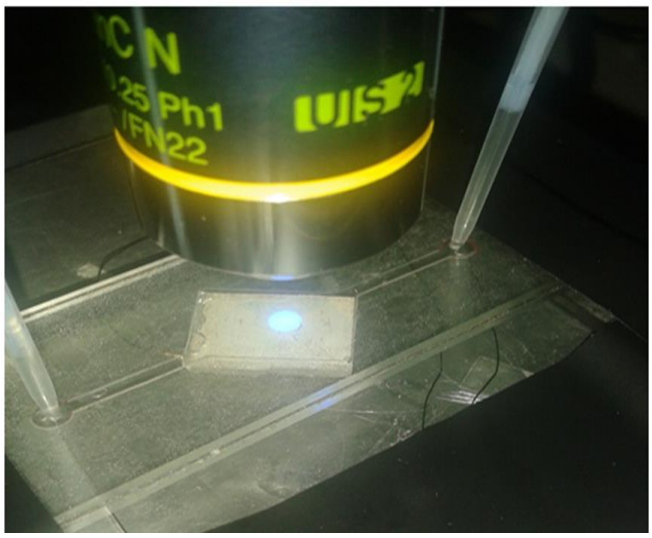

Figure 3.4: The acoustofluidic device which is made from double sided tape as a fluid layer . The 10x objective is focussing on the area of interest where both stages are going to use it.

The fabrication of the device started by drawing the plan dimensions on SolidWorks as shown in *Figure 3.5*. Then, a laser cutting operation was performed on a stack of three 100 µm double sided tape strips in order to make a 300 µm cavity layer of the same dimensions. The resultant cavity sheet was finally sandwiched between two identical glass slides (25x75x1.25mm) to complete the device assemblage. One inlet and one outlet was machined using a 1 mm drilling bit. *Figure 3.6* shows the device from the front and side views The PZT x, y dimensions is exactly equal to the (rectangular dimension) cavity x, y plane dimensions. The PZT is glued to the carrier layer using Epoxy super glue (Epoxy 301 Epotek Billerica, MA, USA).

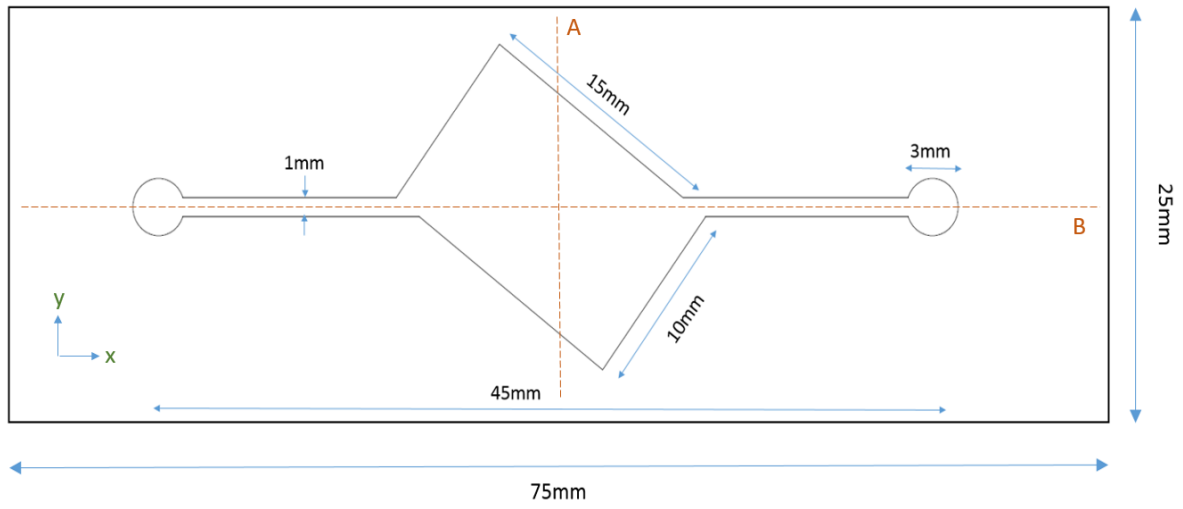

Figure 3.5: Device dimensions (plan view)

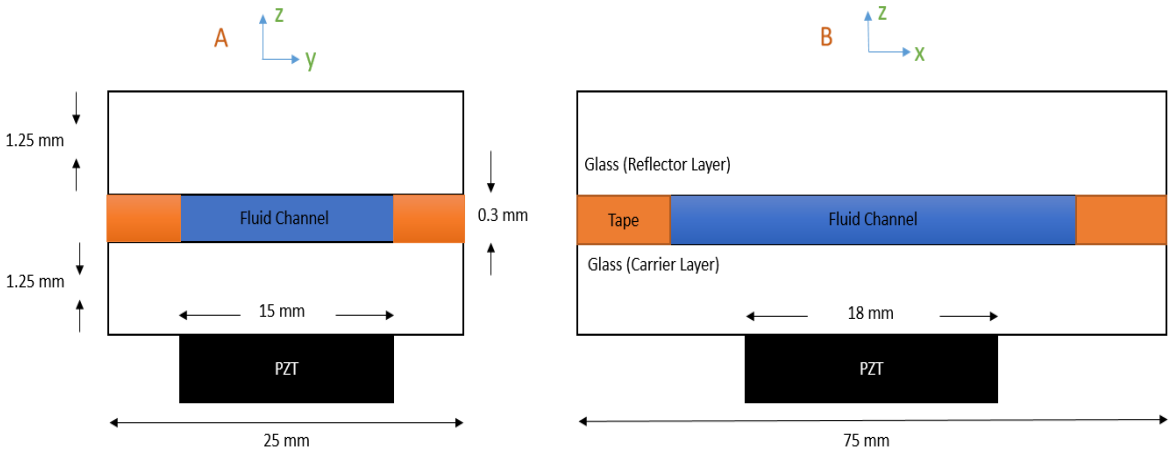

Figure 3.6: Front and side view of the device (corresponding to A and B dashed lines in Figure 3.5), the plan view area of the PZT (black) is identical to the area of the fluid rectangular chamber in Figure 3.5.

With this cavity layer thickness, the device has a theoretic half wavelength resonance frequency at 2.5 MHz. This wavelength resonance is slightly different than the experimental result found using Cyphergragh analyzer plots as shown in *Figure 3.7* and *Figure 3.8*.

The main acoustic resonance frequency was evaluated by generating the acoustic electrical impedance of the device in two states, filled with water and air. *Figure 3.7* shows the characteristic impedance of the acoustofluidic device at a wide range of frequencies. The impedance measurement has been performed with two medium (water and air) to characterise the half wave resonance.

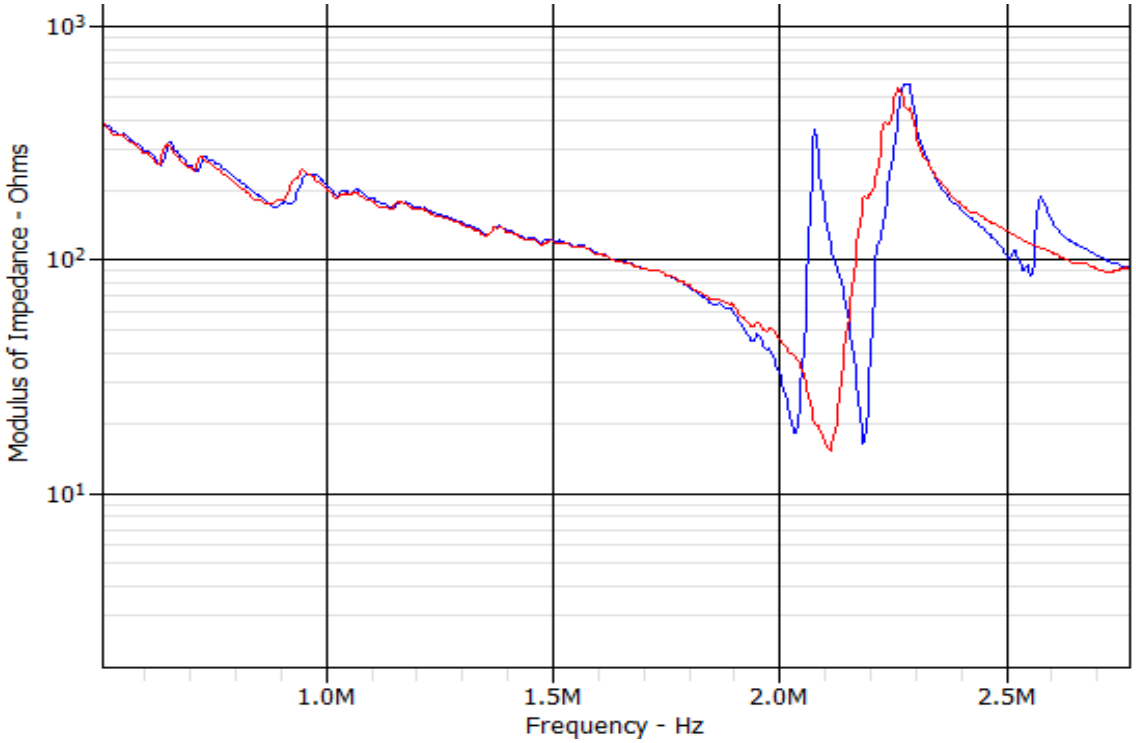

Figure 3.7: The whole view of the measured characteristic impedance of the planar resonator device with two media (water is represented by the blue line and air shown by the red line). The minimum peak of interest is found at around 2.55 MHz which is the half wave resonance frequency.

The frequency characterization was determined over the entire span of the system frequencies to find the lowest electrical impedance with water medium versus the air medium. The half wave resonance of the device which is responsible for particles levitating is found at around 2.55 MHz. This is close to the minimum impedance occurring with water only while other nearby minimum peaks can have some lateral resonance that contribute to moving the particles sidewise. The sweep process to search for lateral frequencies has been experimentally performed around the half wave resonance frequency. *Figure 3.8* shows that four other resonance frequencies were found at 2.52, 2.53, 2.54 and 2.56 MHz (labelled as F_1 , F_2 , F_3 , F_4 respectively and $F_{\frac{1}{2}\lambda}$ is the half wave resonance) which are nearby the main resonance frequency which makes them sensitive to temperature variations (see Section 5.7.3).

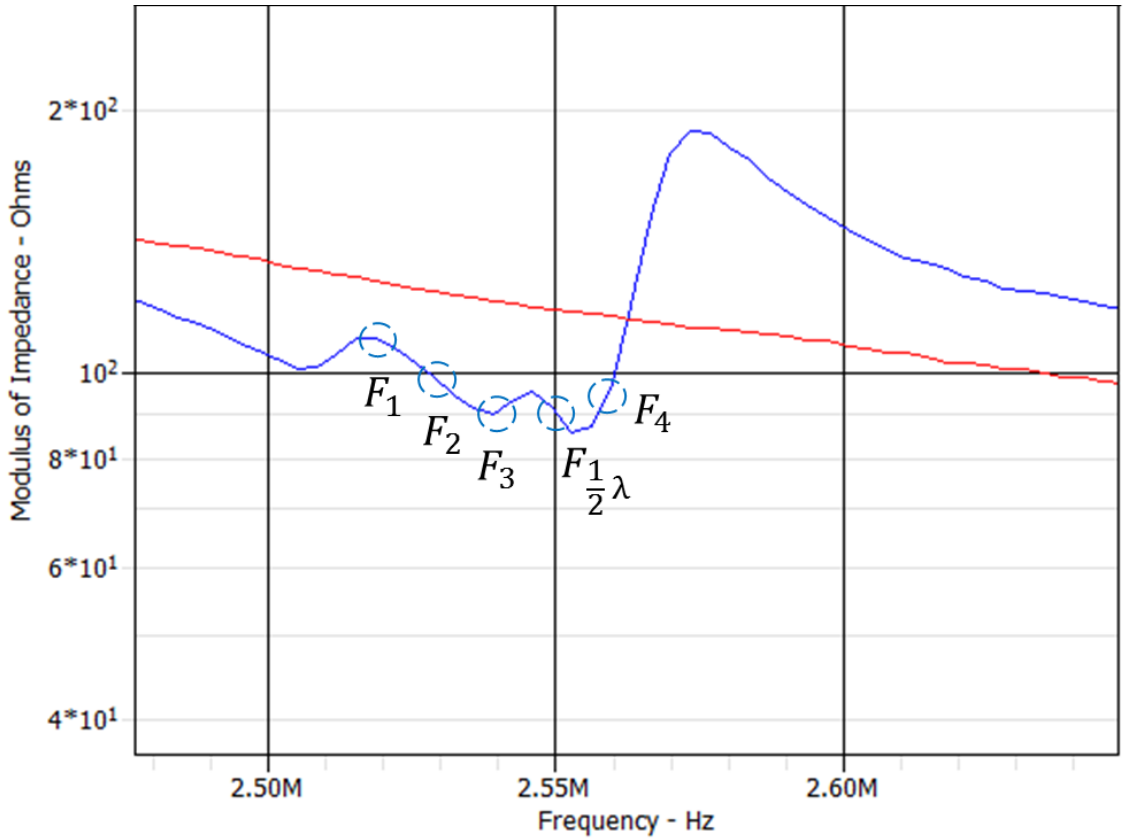

Figure 3.8: Zoomed in view of the additional interesting resonance frequencies. Four other resonance frequencies were found at 2.52, 2.53, 2.54 and 2.56 MHz corresponding to F_1, F_2, F_3, F_4 respectively. $F_{\frac{1}{2}\lambda}$ is the half wave resonance.

The precise nature of these clustered nodes is not easy to determine, but is likely to be a complex set of modes which closely resemble an ideal half-wave mode. Each one will have a slightly different distribution of energy in the various structures of the device including thickness and flexural modes.

The estimation of the zero pressure node was performed using an acoustic transfer impedance model (KLM model) of the transducer implemented in MATLAB (code supplied by Hill et al.) [69]. *Figure 3.9* shows the pressure profile through 1 dimensional distance of the device structure.

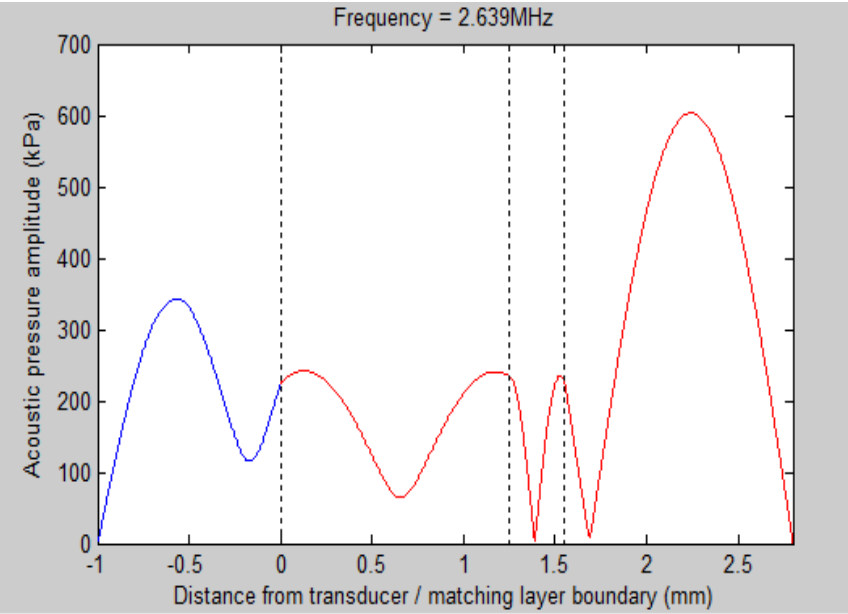

Figure 3.9: Predicted zero pressure node position for planar resonator device at resonant frequency 2.63 MHz. The minimum pressure occurred at the half distance along the vertical axes of the device.

The KLM model is used to show the expected distribution of acoustic pressure amplitude through the device as well as prediction of the main resonance frequency. The main resonance frequency is found at 2.63 MHz, which is slightly different from the measured value show in *Figure 3.7*. The device is modelled with 10 volts, the maximum amplitude pressure is 235 kPa at both contacts of the fluid layer with carrier and reflector layer while acoustic pressure decreases towards the half height of the cavity layer.

3.3 Capillary with Two Transducers

The final acoustofluidic device to be presented in this research is designed to overcome the limitations of the previous devices which suffered from not having a sufficiently diverse range of forces to enable effective manipulation, and also tended to suffer from heating issues. This design returns to a capillary chamber as the previous, tape based device, lacked longer term stability due to the tape construction. Therefore, the features of the microfluidic devices are designed for long-term stable manipulation, and created weaker lateral resonances.

The device features transducer made from a single piece of PZT whose electrodes are divided on one side into two areas, in order to create diversity of available forces by actuating either or both areas selectively.

The device dimensions with the modified bulk PZT is illustrated in *Figure 3.10*. The bulk PZT is divided into two equal parts along the x-axes direction in order to create a force in x direction. The operating principle behind this concept is similar to the array-controlled device explained by Jones et al[9], where controlling the position of maximum kinetic energy density through activating different PZT regions is the mechanism for shifting levitated particles along the fluid chamber in the x-axis direction.

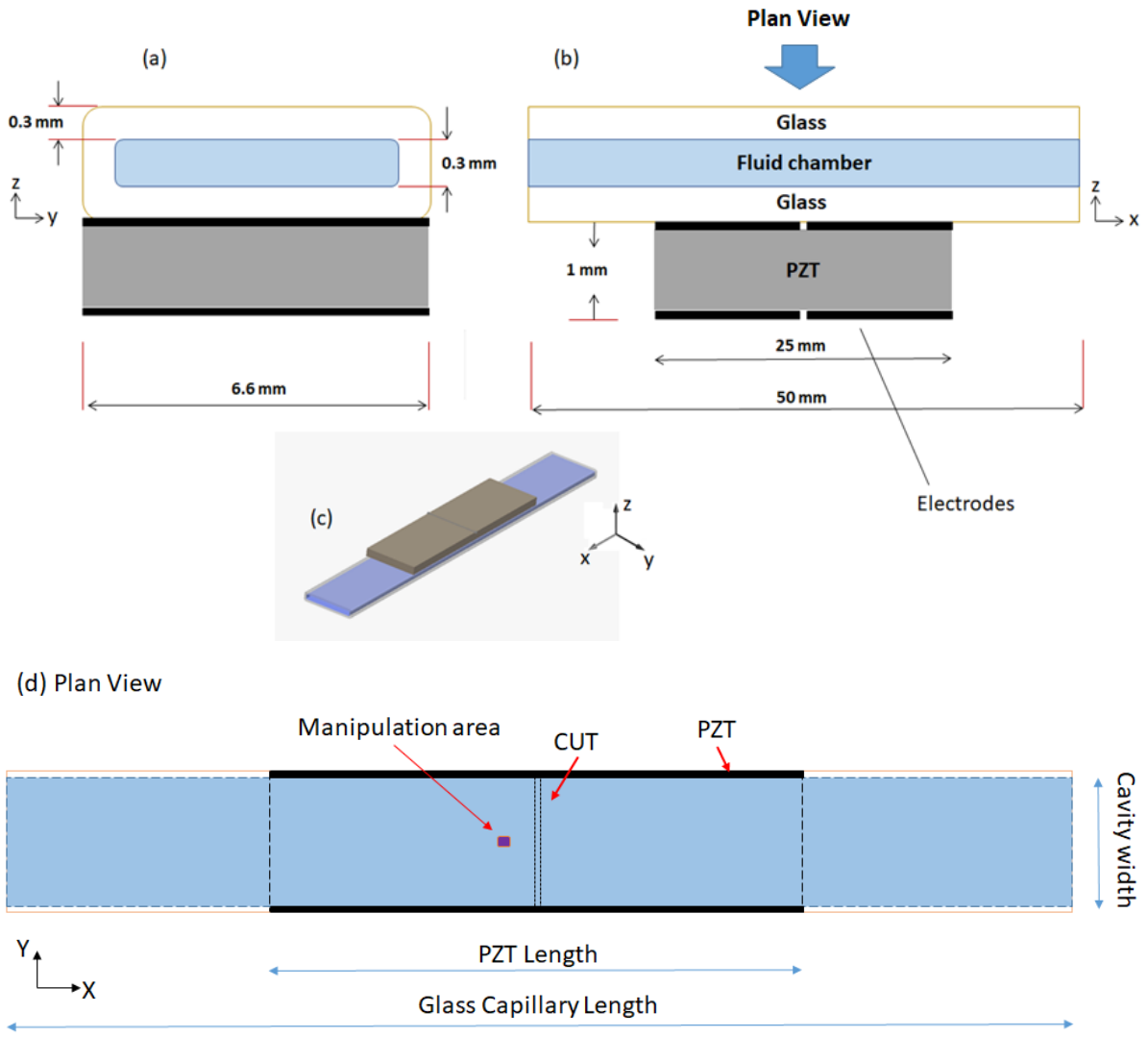

Figure 3.10: The microfluidic device dimensions. Length section (b) and cross-section (a). The cut (Length section) has been made at the middle of the conductive substrate (black layers) in both PZT sides (upper and lower sides) in order to make separate left and right PZT activation regions. (d) The plan view showing the manipulation area position relative to the PZT.

According to the measured electrical impedance in both media (water and air) for this device, the half wave resonance as well as other resonances can be characterised as shown in *Figure 3.11*. The half-wavelength resonance frequency was experimentally found at 2.382 MHz which is slightly different (132 KHz different between them) from the modelled one with the 300 µm fluid chamber thick in

Figure 3.3 (the first used device in Section 3.1 has similar layer thicknesses and dimensions except the PZT is cut).

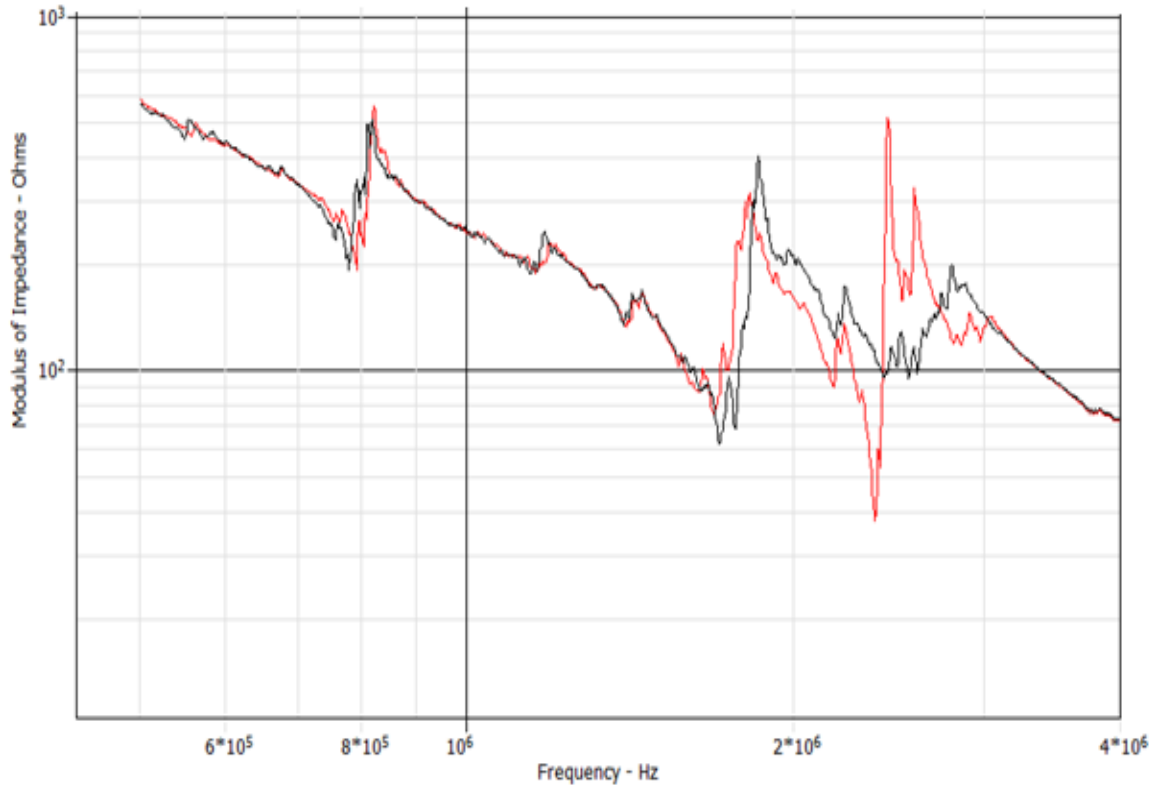

Figure 3.11: Impedance measurement of the glass capillary with two media (water is represented by the red line and air is shown by the black line). The half wave resonance frequency is indicated by peaks at around 2.382 MHz. This only occurs in the water curve.

The figure above shows the electrical impedance of the device of the left part, which is associated with a transducer whose area selected to be the main manipulation area. The other transducer's electrical impedance is giving a similar half wave resonance with negligible difference of lateral frequency modes.

After performing the frequency sweeps on this device (the process of looking for the lateral resonances), the predetermined five lateral frequency modes were chosen based on their force strengths and variations which were not significantly close to each other (2.480, 2.536, 2.568, 2.814 and 2.382 MHz). This ensures less sensitivity to temperature variation compared to the previous device (these selected frequencies values are far away from each other, hence less affected by temperature causes frequencies shifting). These lateral frequencies are shown in *Figure 3.12*.

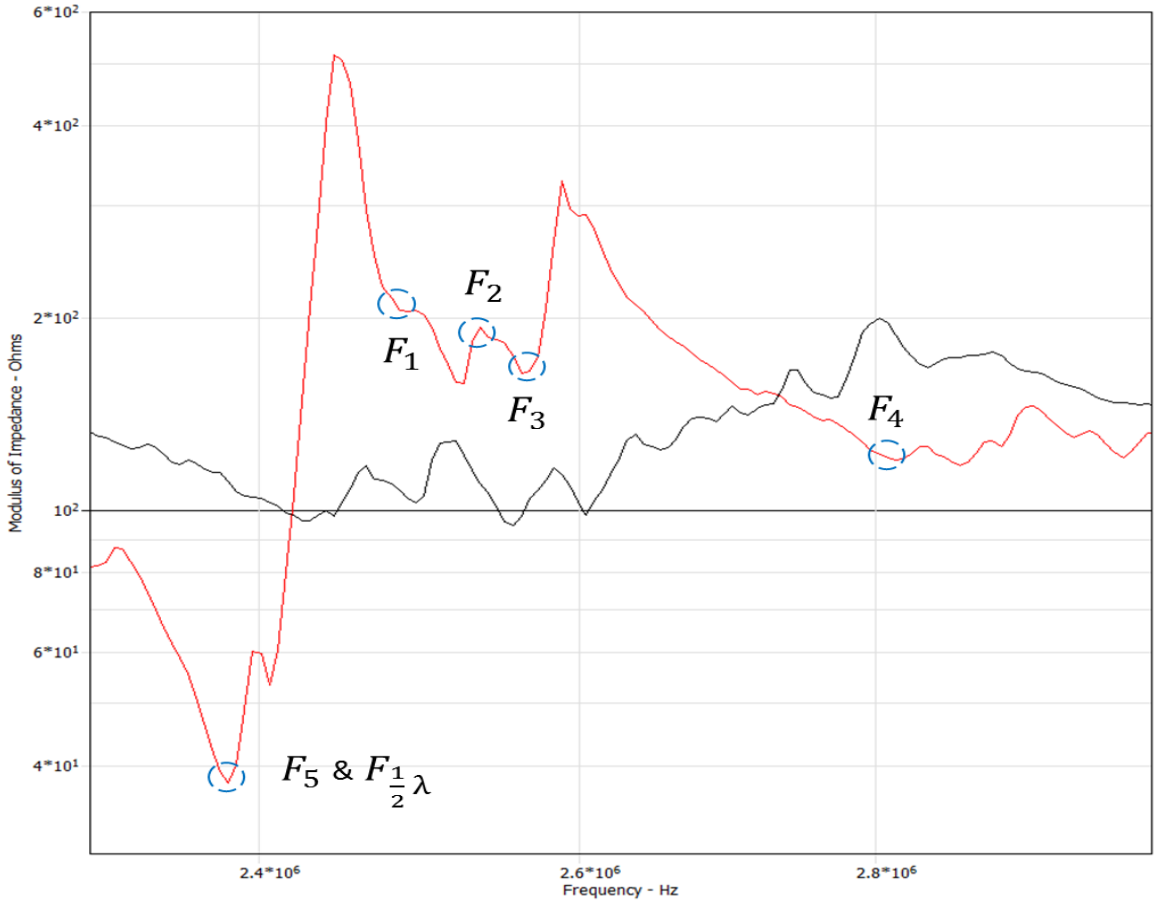

Figure 3.12: Zoomed in view of the interesting resonance frequencies with the half wave resonance. Four other resonance frequencies were found at 2.480, 2.536, 2.568 and 2.814 where 2.382 MHz is selected to be the fifth resonance frequency as well as the half wave resonance frequency.

It was found that by activating just one of the transducer regions, there were more significant forces in the length direction of the capillary chamber. Typically, when observing in a region between the transducer centres, the forces tended to be towards the activated region, although forces directly above the electrode cut were low. *Figure 3.13* breaks down the available directions that the algorithms in chapter 6 could request, and shows which transducer(s) were activated for a given required direction. Although there is still some uncertainty over the direction of actual forces that will be created for a given actuation, this increases the chance of there being suitable forces available, and the measurement phases described in chapter 6 are able to determine what is actually available at each step.

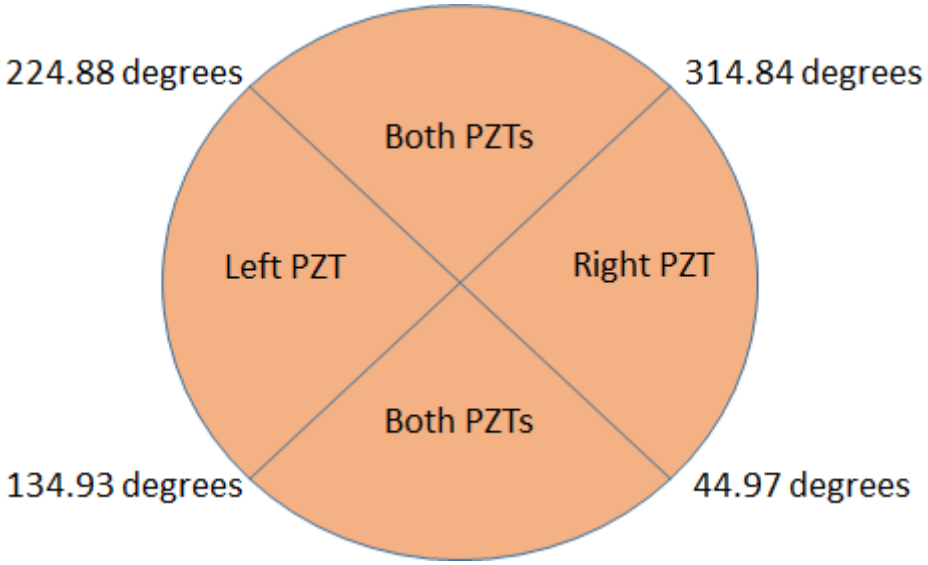

Figure 3.13: The circle of the required direction that determines the PZT configuration.

The manipulation area was selected above the left PZT (PZT2), 1 mm away from the cut and 2.7 mm away from the capillary sidewalls (see Figure 3.10 (d)).

Chapter 4. Creating Force Maps for Subsequent Particle Navigation and Steering

Chapters 4 and 5 focus on the principle of measuring the acoustic forces available within a device before using those forces to manipulate a particle (for the navigation algorithm). This chapter describes work to measure force maps (the 2D velocity vector force field) generated from devices using µPIV. In addition to the fields that are required, it is found that there are some unwanted background velocity field resulting from flow. The force maps measured in this section are also used in the simulated steering described in chapter 6.

4.1 Force Measurement and Choice of Modes ("Registration")

Prior to manipulation, the forces available in the various modes identified in the previous chapter are measured and a smaller set of "useful" modes selected for subsequent manipulation. The maps of forces across the field of view for a given frequency are here called VVFMs (Velocity Vectors Force Maps). Each VVFM maps the forces for a combination of both the chosen levitation frequency plus summed with the frequency intended to create lateral forces. This registration phase is demonstrated in *Figure 4.1*.

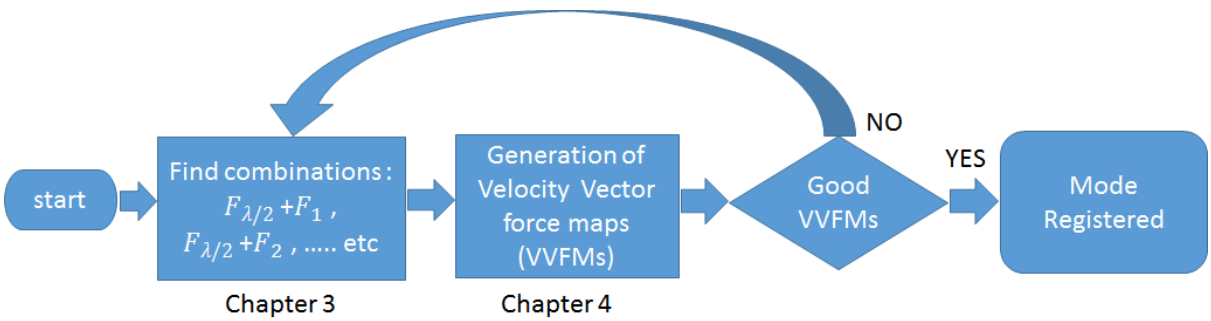

Figure 4.1: The flow chart of the registration phase.

A number of VVFMs are generated by the µPIV (see section 4.3 for µPIV) that show the lateral force maps of the displaced particles. Following this, the optimum modes are then registered. There can be any combinations of $F_{\lambda/2}$ +F_1 , $F_{\lambda/2}$ +F_2 ... etc. where the primary frequency ($F_{\lambda/2}$) is the half wave resonance frequency which is constant for any specific half wave resonator. The decision to register the mode is an operator decision based on observing whether the measurement was reliable (related to the distribution of tracer particles) as well as the strength and directions of the particle velocity vectors.

4.2 Experimental Setup

A schematic diagram of the hardware system is shown in *Figure 4.2* . The experimental setup consists of the following hardware: A USB microscope camera (Thorlabs DCC1645C) which uses a 10x objective connected to a Windows PC. The PC uses MATLAB software to embody the control algorithm. A standard infuse/withdraw USB syringe pump (11 Elite Programmable Syringe Pumps, Harvard Apparatus, USA) is controlled by a MATLAB code (running original control algorithms and pump control code written by myself). The junction box shown on *Figure 4.2* consists of three main parts: one DDS module (Analogue devices, AD9850) connected to a microcontroller (Arduino UNO) which is programmed by an uploaded Arduino code (authored by Peter Glynne-Jones, and modified by myself) to operate the DDS module, and a summing amplifier (based on Analogue devices, LT1210). The DDS module is used to create the half wave frequency ($F_{\lambda/2}$) while the function generator (TTi TG2000 20MHz DDS Function Generator) is used to generate different lateral resonances to control the 2D manipulation of the levitated beads. The two signals are combined by the summing amplifier. The output amplitudes of the DDS board and the function generator are kept fixed at 3 and 10 Volt for the levitation and manipulation frequencies respectively.

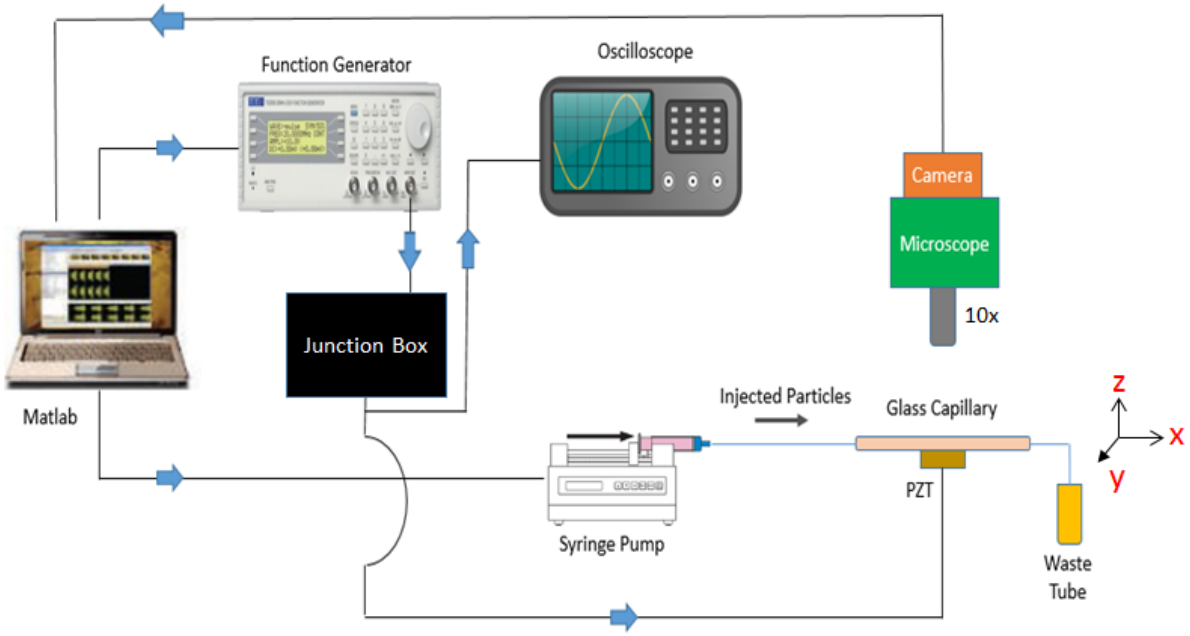

Figure 4.2: Experimental hardware diagram represents the main parts of the particle control system. This hardware is utilized in both stages (registration and manipulation). The blue arrows are the direction of the electrical signals between the devices.

Before the generation of the VVFMs, the MATLAB code (in this phase only) synchronises the pumping of new particles with the switching on and off the PZT throughout the hardware components and imaging of the suspended particles within the dedicated manipulation area. This sequential process ends after a number of consecutive images are recorded and saved into the system to be recalled for the VVFMs generation later on. The main priority is to avoid a sedimentary deposition problem with the particles and to keep a higher number of particles in the levitation plane. However, these timings have to be accurately controlled in order to guarantee imaging of the new group of pumped particles. Another challenge for this experiment is to guarantee that the acoustic lateral forces are only present without any interventions from other forces such as background velocity or secondary acoustic forces between nearby particles. The following sections discuss these phenomena associated with force map generation using µPIV.

4.3 µPIV Measurement

µPIV (micro particle image velocimetry) is a Matlab toolbox used to obtain the velocity measurements of particles within a microfluidic system [70-73]. µPIV measures the 2D velocity field by taking two consecutive images of shifted particles and using correlation to measure the displacements between the two frames and hence deduce the velocities.

In order to understand how µPIV produces its outputs, the techniques of µPIV pre-processing and post-processing is outlined below. The basic operation of the µPIV method cross correlates two consecutive images to determine how far the particles have moved and an algorithm generates velocity vector force fields. However, in order to accurately probe the forces in a device, the seed particle density must not be too high, otherwise inter-particle forces will distort the observed movements. The strategy employed here is to take multiple pairs of images, and combine them into a single combined image to create the required particle density for accurate PIV. *Figure 4.3* shows the sequential steps of the adopted technique and the code execution flow to produce the VVFMs using µPIV.

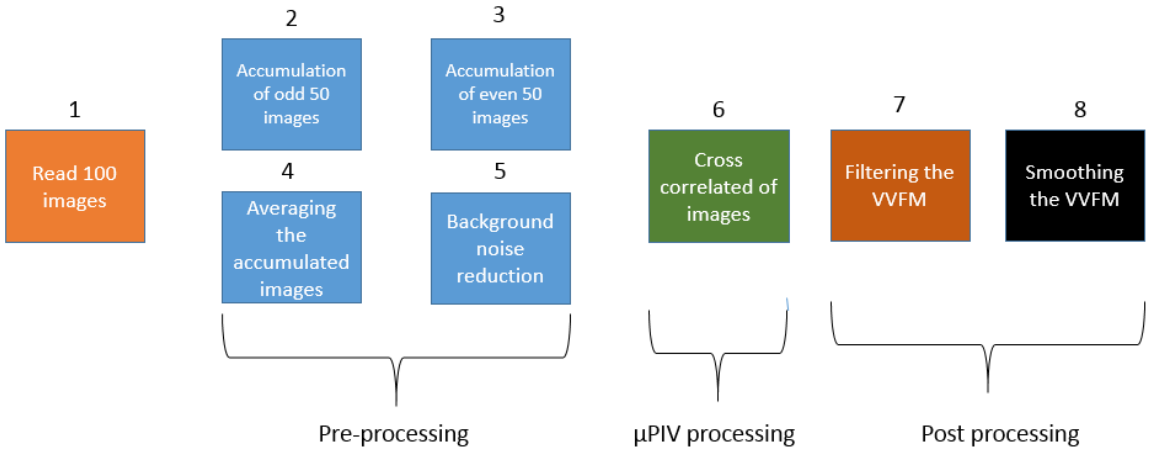

Figure 4.3: The VVFMs generation is explained with steps of the µPIV pre and post-processing. There are 100 source images in total for better concentration of particles. The source images will be divided into two (even and odd) groups. The background noise is then removed by an averaging technique. The resultant source pair is cross correlated by the µPIV.

The number of source images has to be sufficient during the pre-processing to ensure background noise reduction and uniformity of particle distribution. For example with 100 source images, there are 50 consecutive image pairs, with a fresh distribution of beads for each pair.

The sub-group *A* and *B* represent the odd and even 50 images respectively. Each sub-group is accumulated by itself and added to its counterpart (*A* and *B*) and averaged by the total number of images; which in this case is 100. The following Equations 4.1, 4.2 and 4.3 show the steps that are performed in the pre-processing stage:

A is the accumulated odd images while *B* is the accumulated even images. Then addition both of them (*A+B*) is required to calculate the average of all images *AV*.

$$AV = \frac{accumelation\ of\ all\ images\ (A+B)}{100} \quad (4.1)$$

Background noise reduction aimed to remove any static particles that can make false µPIV detection. By using the averaged accumulated images as outlined previously, the noise subtraction can be calculated as follows:

$$A' = A - 50 * AV \quad (4.2)$$

$$B' = B - 50 * AV \quad (4.3)$$

Where A', B' are the new sub-groups after applying the pre-processing technique. By cross correlating the resultant two pair (A', B') of the accumulated pre-processed images, the µPIV output represents the VVFM. The filtering function of the µPIV output aims to remove false velocity vectors that have been generated during the µPIV measurements and missing vectors which occur from interpolation. Smoothing the filtered VVFM reduces measurement noise and error, based on the assumption that the underlying acoustic force field varies only slowly (e.g. with order of one quarter wavelength) in space.

The above diagram presents an example of the steps that are used in the registration stage as well as the stage to determine the repeatability of the force map for the same measurements. These steps may vary from one case to another and may also depend on the imaging conditions. Additionally, particle concentrations and random distribution of particles are not necessary, thus there is no requirement for the pre-processing of a high number of particles and only two or three consecutive images are required. The result for the mentioned method for VVFMs generation is discussed in detail in Section 4.4.3.

4.4 VVFMs Generation using the Glass Capillary Tube with Bulk PZT

On examining the initial measurements, there was found to be a significant background flow in the device. This was thought to be a result of unbalanced hydrostatic pressure at both ends of the device. This is addressed next, followed by experiments to select parameters for the VVFM measurement process.

4.4.1 Net Flow Measurements

The measurement of the lateral acoustic radiation forces requires a particular static condition of the levitated particles. This means that no other type of forces are permitted to cause the levitated particles to move. In other words, after pumping a new group of particles into the device and setting the levitation resonance frequency to the lowest possible levitation voltage (Section 4.4.3), particles in all axial locations should be driven to the zero pressure node and remain stationary. For this to be achieved, a number of experiments have been conducted to investigate the net flow behaviour that was observed after stopping the pump flow inside the chamber. This net flow can be explained as a remaining bulk velocity v resulting from a dynamic fluid drag force on the levitated particles in the direction of the lower hydrostatic pressure. This drag force F_d is given by Equation 4.4 from Stoke's law.

$$F_d = 6\pi\mu r v \qquad (4.4)$$

Where μ is the fluid viscosity and r is the particle radius. Stoke's Law is limited to slow particle velocity (low Reynolds number) as well as steady flow condition and constant viscosity. The net flow velocity was measured by repeating the experiment 5 times for different time delays varying from 1 to 8 seconds after shutting off the pumps. The experiment is initiated by starting and stopping the pump flow and capturing two consecutive images and measuring the mean velocity after a time delay. The mean velocity was calculated as 22 pixel/s. The experiments were developed using conventional 2-way In-line valves connected before and after the fluidic device (at both ends of the device). In the experiment, the manual valves were closed immediately after stopping the flow and then two consecutive images were captured which yielded a 0.04 pixel/s mean velocity. However, manual valves cannot be used for long automated run experiments as they need a high number of loops with precise timing of events. As a result, micro solenoid electronic valves are introduced (D351, SIRAI, BUSSERO (MI), Italy) at both sides of the fluidic chamber as shown in *Figure 4.4*.

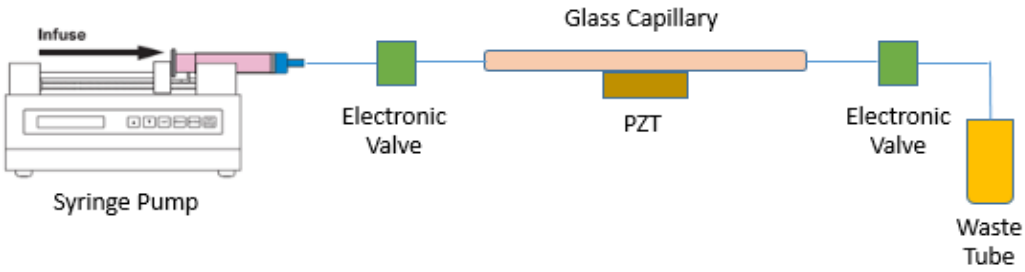

Figure 4.4: The acoustofluidic device with two electronic solenoid valves for the net flow investigation measurement.

The net flow measurements need to be performed in the absence of the ultrasound radiation force. Other forces are considered; these include the gravitational force and fluid dynamic drag forces. The experiment starts by opening the valves to pump a new group of particles inside the chamber for 1 second and then closing the valves. Two consecutive images are taken with a time interval of 0.2 seconds to measure the moving velocity from which the remaining velocity can be obtained. *Figure 4.5* describes the sequence steps to perform the net flow measurements using 1 and 10 µm fluorescent beads, where the TD is the time delay between closing the valves and capturing the first image. The suggested TD for this net flow investigation varies from 1 to 8 seconds.

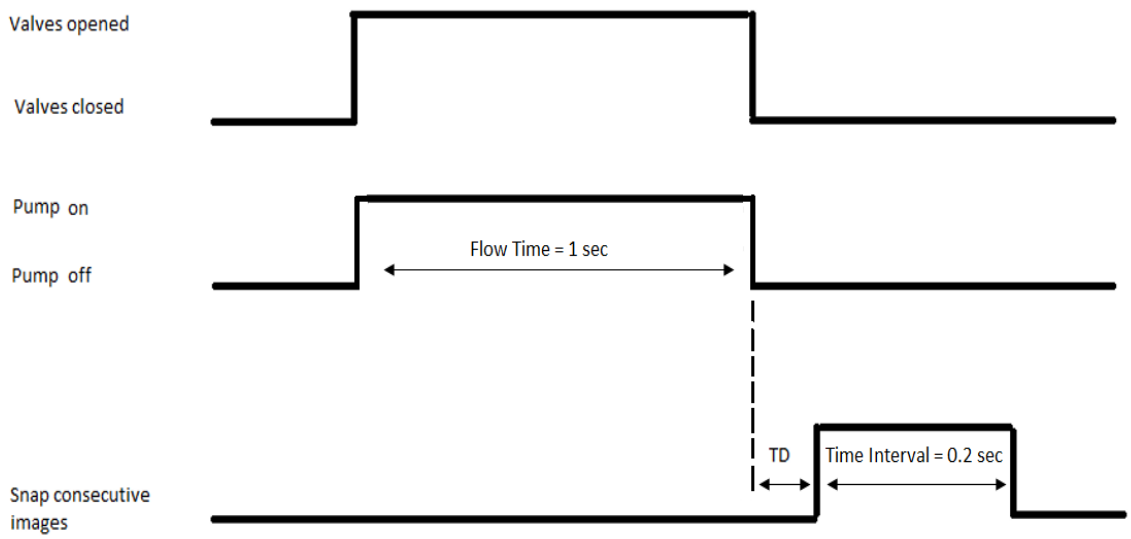

Figure 4.5: The experimental time schedule for net flow measurement. The valves and the pump are synchronised at the same time. After time delay, two Images are captured consecutively with 0.2 s time interval.

The initial experiments were conducted using 10 µm beads. These experiments showed mean velocity of 0.9 pixel/s after a *TD* of 10 seconds. The decreased velocity is considered to be due to gravitational force effects. In addition to the sedimentation concerns for the 10 µm beads, parabolic flow phenomena associated with capillary devices especially at the inlet side cause variance in particles speed with different cavity depths. This can result in uncertainty in the velocity measurements. Therefore, 1 µm beads were used (they have much lower sedimentation rate than 10 µm beads) and these have shown promising performance towards visualising and measuring the net flow. *Figure 4.6* shows the difference in the mean velocity of 1 µm particles when using one or two valves. The configuration with one valve which is placed at the inlet side of the fluidic device stops the flow direction. This causes a variation in the velocities at repeated time delays and the drag velocity is present due to unequal pressures at both sides. *Figure 4.6* shows that the mean of the net flow

velocity is seen to increase after 5 seconds towards the open outlet which is connected to the waste tube.

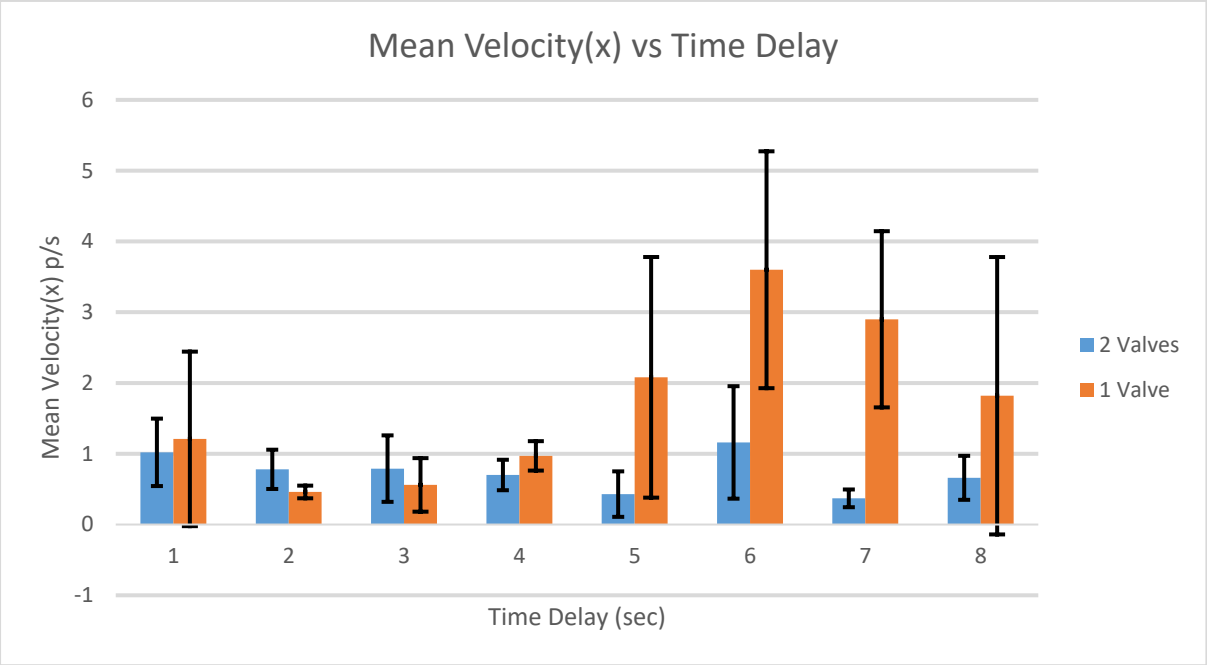

Figure 4.6: Comparison of the net flow (the mean of the remaining velocity) resulting from using 1 and 2 valves. The net flow velocity was measured by repeating the experiment 5 times for different time delay (TD) varying from 1 to 8 seconds after shutting off the pumps. The error bars are the standard deviations.

The two valve configuration has indicated a lower net flow velocity than the one valve configuration. This is as a result of lower differential pressure (more stable pressure) at both sides of the chamber thus creating less variation of velocities at the repeated time delay inside the device. This is supported by the smaller standard deviation error bars shown on each time delay associated with two valves. This phenomenon can be explained by the significance of the differential pressure after closing one valve thereby generating higher velocities with a longer time delay which is observed to be about 3.6 pixel/s. On the other hand, with the two valve configuration velocity of 0.3 pixel/s (the fluid reacts back and forth in the direction of the main flow) the velocity reduced after five seconds of time delay and the optimal equilibrium hydrostatic pressure at both device ends is observed, thus reflecting the aim of this part of investigation. Finally, a range of mean net flow velocities from 0.3 – 1.16 pixel/s has been recorded with the two valves configuration.

4.4.2 Parameter Selections

The experiments for the VVFMs generation are automated using a MATLAB script to capture the groups of source images (see *Figure 4.13*). The parameter of this process need to be optimized in order to measure the lateral acoustic radiation forces accurately. The next two sections describe two important parameters. First, the pump flow rate and time for refilling the device with fresh beads are investigated. These are important in order to provide the required number of sufficiently distributed beads per window. These are to be added at the stage of image pair accumulation. Secondly, the required focus time for all flowing particles to be driven to the zero pressure node of the device cavity after applying the levitation voltage is discussed. These two parameters have a significant impact to the quality of µPIV calculation for the distance and velocity of the shifted levitated particles resulting from only the lateral acoustic radiation forces being applied.

4.4.2.1 Flow Rate and Flow Time Measurement

In order to obtain the correct pump flow rate with the correct pump flow time to provide a sufficient number of beads and avoid the sedimentation issue associated with the 10 µm beads, two fixed flow rates (10 and 20 ml/min) have been chosen while varying the flow time. Equation 4.5 defines the flow rate Q which depends on the capillary section area A (1.8 mm²) and the fluid velocity V mm/min:

$$Q = A * V \tag{4.5}$$

The 50 mm length of the capillary tube can be used as a 100% displacement (this is the absolute distance that beads travel) of the flowing 10 µm beads moving from the inlet to the outlet. If the flow rate is 10 ml/min then the required flow time can be calculated from Equation 4.5 and is approximately 0.54 seconds. Likewise, a 20 ml/min flow rate requires 0.27 seconds for this 100% displacement. However, if the flow time selection is based on the imaging zone, at the centre of the chamber for instance, this dictates 25 mm is the displacement distance (that is 50% displacement for half capillary length). In this situation there will be a chance that other problems may obstruct the flow, for example, small bubbles moving within the flow. In addition, some conditions require that the flow time is doubled (for instance these conditions may be when an experiment contains long time delays) to avoid losing beads at the bottom of the system tubes and pump syringe. *Figure 4.8* and *Figure 4.8* show the results of two different flow rate experiments (10 and 20 ml/min) that contain a different number of

beads for varying flow times. The experiments have been performed based on the time sequence shown in *Figure 4.7*.

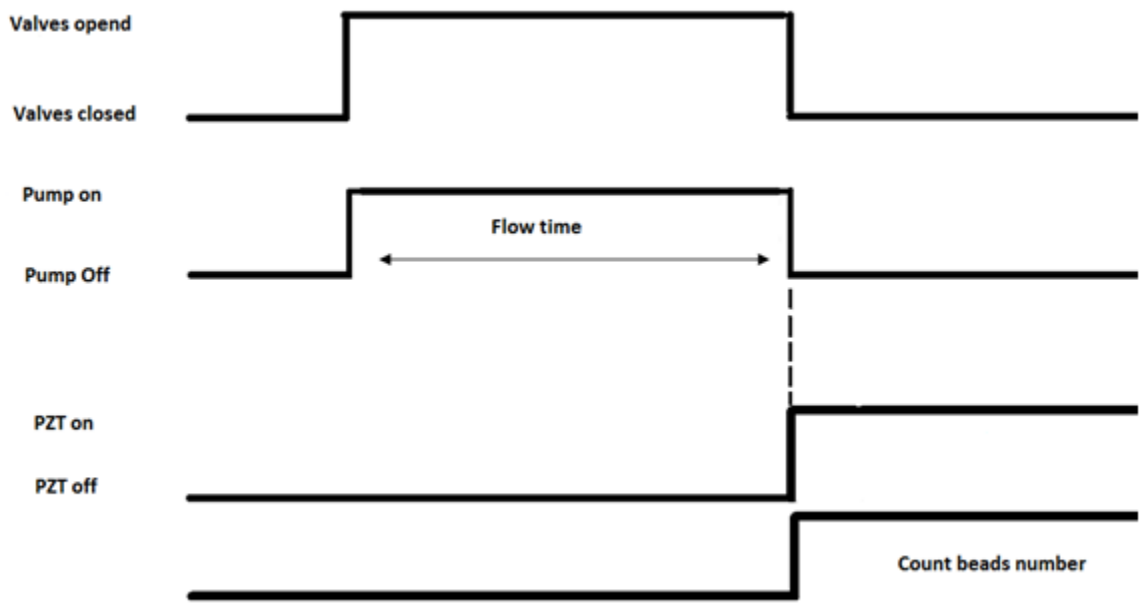

Figure 4.7: The experiment time sequence to count the beads. The valves and the pump are synchronised at the same time. Then the process of counting the beads starts with the activation of the ultrasonic wave.

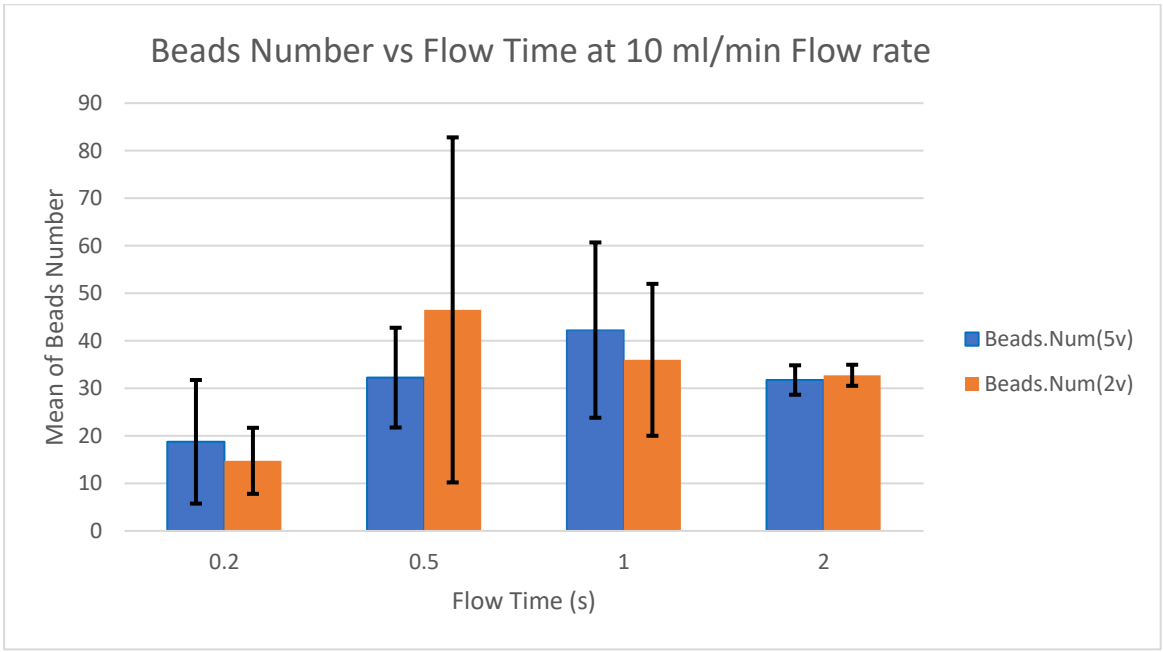

Figure 4.8: The effect of 10 ml/min flow rate with different flow times on the number of beads brought into the imaging area. Measurements are conducted with two different ultrasound voltages of 5 and 2 volts. Maximum error bars (SD) associated with 5v group is ± 18 beads while ±36 beads for 2v group.

As seen in the figure above, there are 4 different pump flow times (0.2, 0.5, 1 and 2 seconds). These pump flow times are selected based on the bead's displacement percentages (50, 100, 200 and 300% for 10 ml/min flow rate) which guarantees a new generation of beads is introduced within the device. The process of counting the beads has been done manually regardless of the focus time as long as beads can be seen. The number of beads with higher variations which effects this measurement makes the flow time selection more difficult. The flow time of 0.2 second has a low number of beads with high variations, however there is a significant increase in the number of beads flowing with 0.5 seconds flow time but also with higher variation. Based on the lowest variations associated with the flow times and similar numbers of beads between 2v and 5v groups, the number of beads can still give a rough inference of the flow rate which reflects the ability to push the beads. This is especially visible with the 1 second flow time which have some variations and the 2 second flow time with the lowest variations. Finally, neglecting the condition (related to the lower flow time) that limits the whole fluid system which was discussed earlier, it is recommended to set the flow rate to 1 or 2 seconds flow time whilst focussing the syringe volume experiment for a high number of loops. This can also limit the higher flow time (the syringe volume has to be considered to be enough for the whole experiment loops).

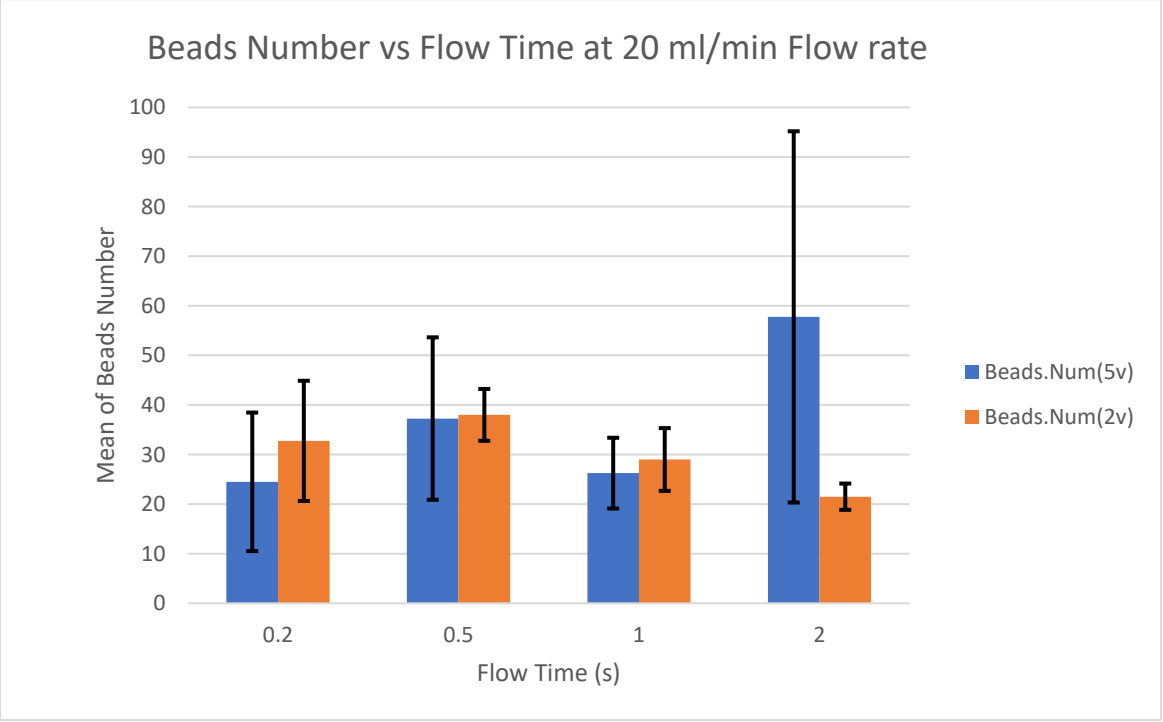

Figure 4.8: The effect of 20 ml/min flow rate with different flow times on the number of beads brought into the imaging area. Measurements are conducted with two different ultrasound voltages 5v and 2 volt. Maximum error bars (SD) associated with 5v group is ± 37 beads while ±12 beads for 2v group.

The figure above shows a wide variation associated with the 5 volt group with 2 seconds flow time despite the higher number of beads. In contrast, the 2 volt group with the same flow time has the lowest number of beads. The stability of the number of beads can be seen with the 1 second flow time exhibiting an acceptable variation margin of bead number (SD around ±8) as well as with the 0.5 seconds flow time that has a higher variation margin. In comparing the two flow rates, the 20 ml/min, 0.5 and 1 seconds flow time give around 30 and 40 beads per window respectively, therefore, they give sufficient bead displacement for 200% and 300% respectively (regardless the syringe volume, sufficient beads number with 200% displacement can be selected) . Likewise, with 10 ml/min, 1 and 2 seconds flow time give around 30 and 40 beads per window respectively. Therefore; 10 ml/min and 1 seconds for flow rate and time respectively will be used later for the generation of the VVFMs (Section 4.4.4).

4.4.2.2 Focus Time for Levitation Voltage Measurement

After applying the acoustic standing wave field to the particles at different depths of the fluid cavity, the required time for particles at all locations to be driven towards zero pressure gradient (the nodal plane of the fluidic device) is called the “focus time”. As one of the important experiment parameters, there is a need to measure this focus time (all particles in the zero pressure node are visually clear with no blurs) for the particles to be ready for imaging after the lateral mode was applied. Two different methods was selected to measure the focus time using the levitated particle which is driven towards the pressure node. This focus time is dependent on the particle axial position and three different forces that the particles experiences; the acoustic radiation force (axial component), the buoyancy force and the gravitational force. The drag force is neglected because of the small net flow which results from using valves that stop the main flow. As expected, the amplitude of the acoustic radiation force is proportional to the levitation voltage. After the first method was conducted, *Figure 4.9* shows the decrease in the measured focus times as the levitation voltage increased. *Figure 4.10* shows the time sequences for the first method employed to measure the focus time using 10 µm fluorescent beads.

The levitation voltage amplitudes applied to the focus time measurement is suggested based on the voltage drop value of 0.7 volt which holds the levitated particles in the equilibrium position. The gravitational force balances with the axial component of the acoustic radiation force and buoyancy force. This position is located at one eighth of the wavelength below the pressure node[74]. The

measurement of the voltage drop was carried out by following the method described by Spengler et al[75]. The acoustic radiation force F_{ac} acting on particle with radius r can be rewritten in terms of the gravitational force as Equation 4.6 [74].

$$F_{ac} = \frac{4\pi r^3}{3} \left(\rho_p - \rho_f\right)\mathrm{g} \qquad (4.6)$$

Where g is the gravitational constant, ρ_p and ρ_f are the particle and fluid densities respectively.

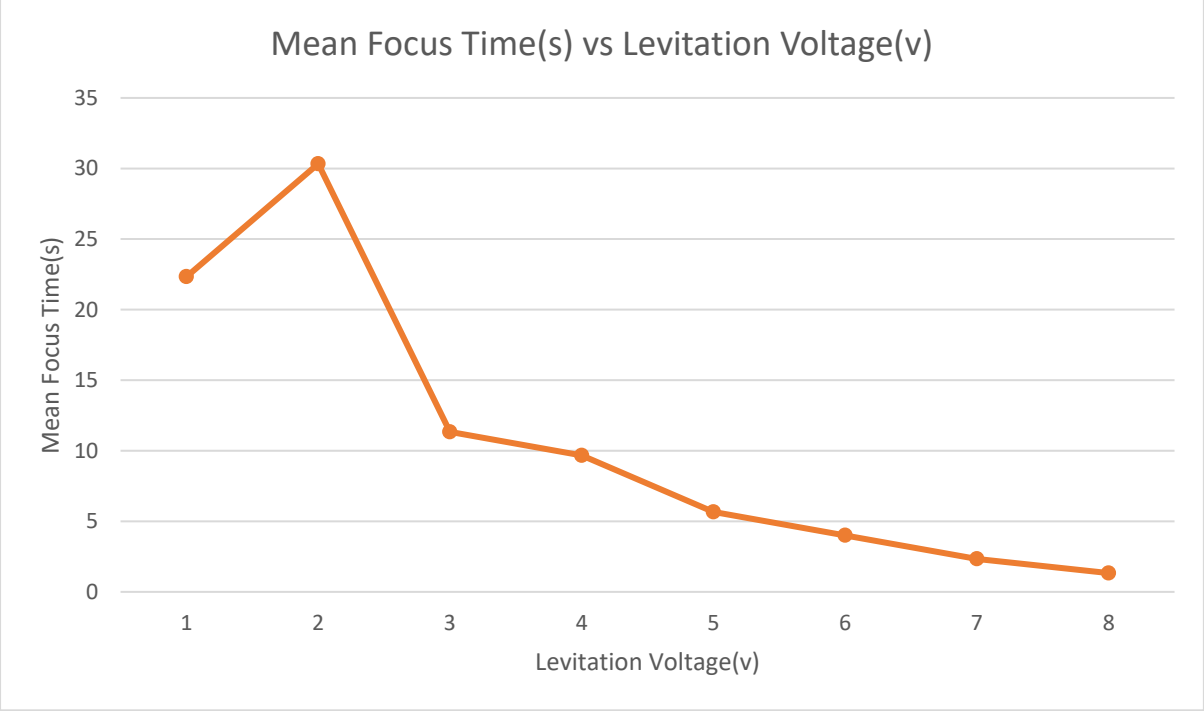

Figure 4.9: Graph of measured focus time at different levitation voltage amplitudes using the method described above. Each data point represent the mean of three focus time readings.

After applying the acoustic wave field, random particles in different vertical positions with regard to the pressure node experience forces in different forms. In the upper half of the device cavity, the gravitational and acoustic radiation forces are pulling particles downwards, while the acoustic radiation force is pushing the particles upwards against the gravitational force in the lower half of the device. This implies that particles in the upper half are driven towards the pressure node faster. As shown in *Figure 4.9* when 1 volt is applied and the focus time is recorded, some particles are noticed at a deeper depth which could not be levitated. However, increasing to 2 volt levitation voltage they can be levitated but a time delay for levitation is introduced. These particles are subject to a constant

net gravitational force and a varying acoustic radiation force. If the acoustic radiation force is less than the net gravitational force, those particles at deeper positions cannot be levitated and vice versa.

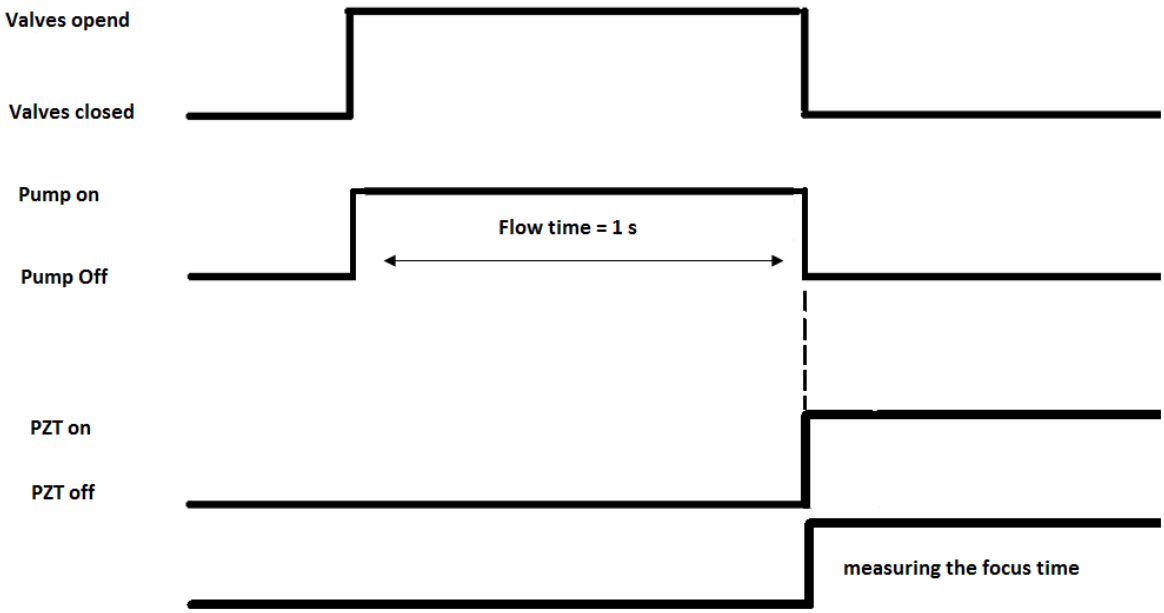

Figure 4.10: The sequence steps for measuring the focus time using the first method. The valves and the pump are synchronised at the same time. Then the process of measuring the focus time starts with the activation of the ultrasonic wave.

The focus time is measured immediately after the levitation voltage starts and is stopped immediately after all particles settle (particles are visually clear with no blurred) at the device pressure node. The applied acoustic radiation force is able to levitate particles at deeper positions in the lower half of the device as the levitation voltage amplitude increases.

A second method for measuring the focus time has also been employed. This method is based on sedimented particles that are subject to the positive acoustic radiation force in the lower half of the device cavity. The same group of sedimented particles have been examined using varying acoustic radiation forces. *Figure 4.11* shows the time required for those sedimented particles at the base of the fluidic chamber to be levitated to the pressure node. The sequence of steps for measuring the focus time in the second method is different. Both pump and valves were switched off during this experiment to exclude the effect of the net flow, while only the PZT is turned on and off based on the experiment sequence.

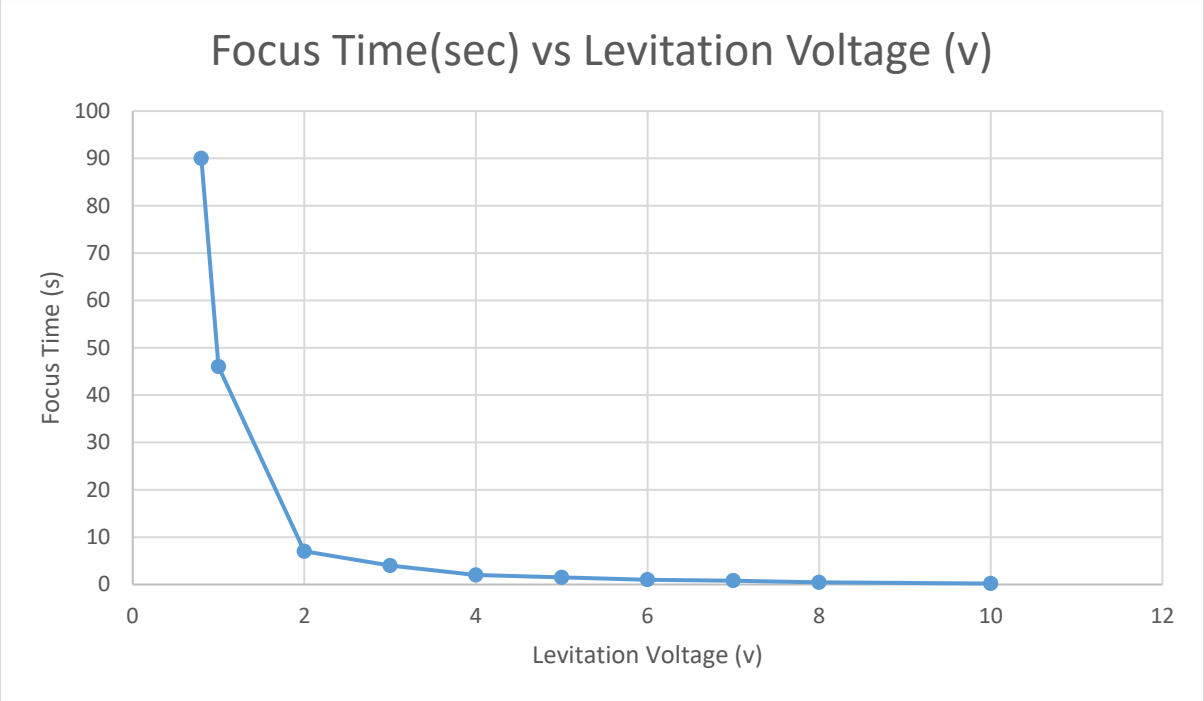

Figure 4.11: Graph of measured focus time resulting from different levitation voltages generated using the second method as described above.

The experiment starts by allowing all particles to be fully stationary at the bottom of the device cavity chamber. This is done by turn off the PZT. Then the time recording starts immediately after applying the ultrasound wave (by turning on the PZT) and stops when all particles are observed to be situated and focused at the device's zero pressure node. The driving levitation voltage amplitudes selected in this experiment were based on the voltage drop which is 0.7 volt where the first recorded time was at 0.8 volt. From the above *Figure 4.12*, the focus time dramatically decreased as voltage amplitude increased. Above an amplitude of 8 volt the focus time is 1 second.

In summation, the recorded focus time in the second method is more accurate as a result of using only those forces acting on particles in the lower half of the device. However, particle distribution throughout the cavity depth is expected during the experiment of VVFMs generation, hence it is more realistic. *Figure 4.11* shows the trend of the inverse relationship between the voltage amplitudes and the focus time, hence a relationship trend can be derived.

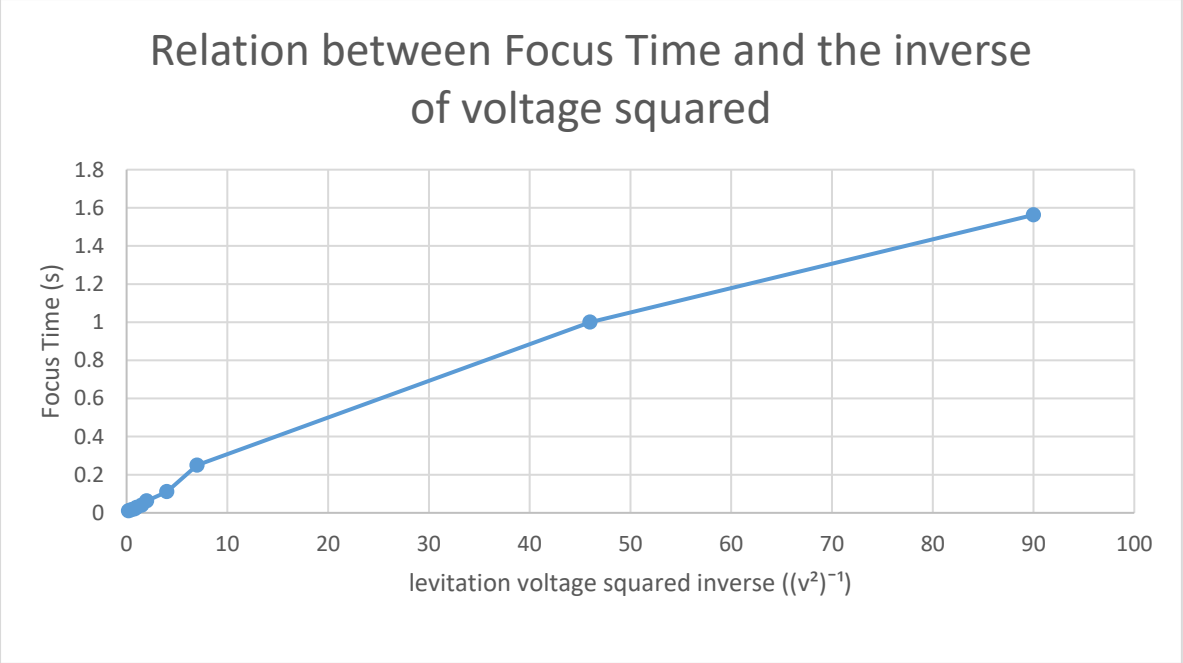

Figure 4.12: Shows the linear relationship between focus time and the inverse of voltage squared.

This proves the inverse relationship between the focus time and the driving voltage amplitude is proportional to both acoustic pressure and acoustic radiation force (Equation (1.1)). Figure 4.12 shows the relationship that is expected to be linear between the focus time and the inverse of the voltage squared.

4.4.3 Investigation of Lateral Movement with Only Levitation Voltage

The purpose of the levitation frequency is to provide sufficient levitation and a stationary condition for the particles at the device zero pressure node. Ideally it would produce no lateral motion, however even at low voltages a small amount of movement is present, and this is characterised here. There are three possible sources of these lateral movements. First, the acoustic radiation force of the levitation frequency may have a small lateral component. Second, there could be some remaining net flow as a result of electronic valves malfunctioning (see the alternative valve in *Figure 4.18*). Third, noise and vibration from the surrounding measurement environment can cause a random lateral movement of the levitated particles leading to a position uncertainty (see section 4.6.3). This section discusses the first possible reason (while other reasons are discussed too later) regarding the lateral component of the primary radiation force which can cause some drifting and changing in position.

The next experiment which is described has been performed to investigate whether there is lateral movement of the particles under the levitation frequency (2.4 MHz) only, with a voltage amplitude 3 volt. The set of parameters have been selected based on the previous investigation sections to correctly measure the levitated particle lateral movement. The adopted flow rate and flow time were chosen to be 10 ml/min and 1 sec respectively (as a result of repeatable bead number per window shown in figure 4.8).

In order to measure the lateral movement everywhere within the imaging window a large number of particles were required as well as a uniform distribution of particles. A number of consecutive frames have been imaged and added together to get a range from 1000-1500 total particles per window based on the selected flow rate. The accumulated odd and even image pairs are shown in *Figure 4.14*.

Before generating the velocity vector force maps VVFMs, the histogram contrast for the light intensity of the accumulated pairs was adjusted to eradicate the background noise from the sedimented particles and for better µPIV detection. The µPIV was performed to obtain the final lateral forces corresponding to the selected levitation voltage and the calculated maximum and mean velocities are based on the 0.2 s time interval between two consecutive images. *Figure 4.13* shows the sequential steps to get one pair of consecutive images. This process was repeated 50 times.

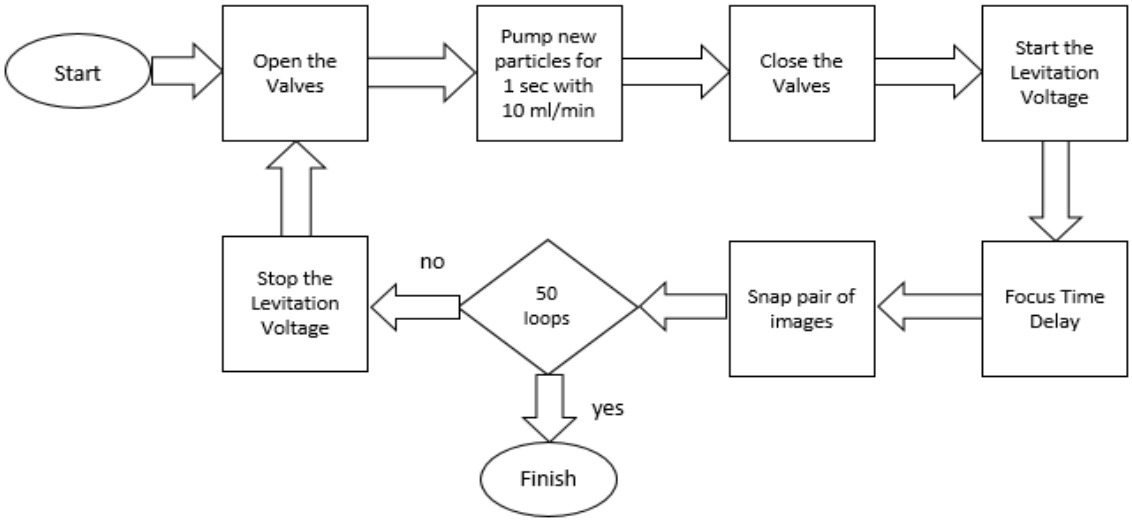

Figure 4.13: The experiment sequential steps to capture 50 image pairs for the levitation mode only.

The above sequence was repeated to capture 50 image pairs (50 odd and 50 even images) with a levitation voltage of 3 volts and a focus time delay of 11.3 seconds. Twelve pairs were removed from the calculation process (38 pair were left) as a result of the low quality imaging during the experiment.

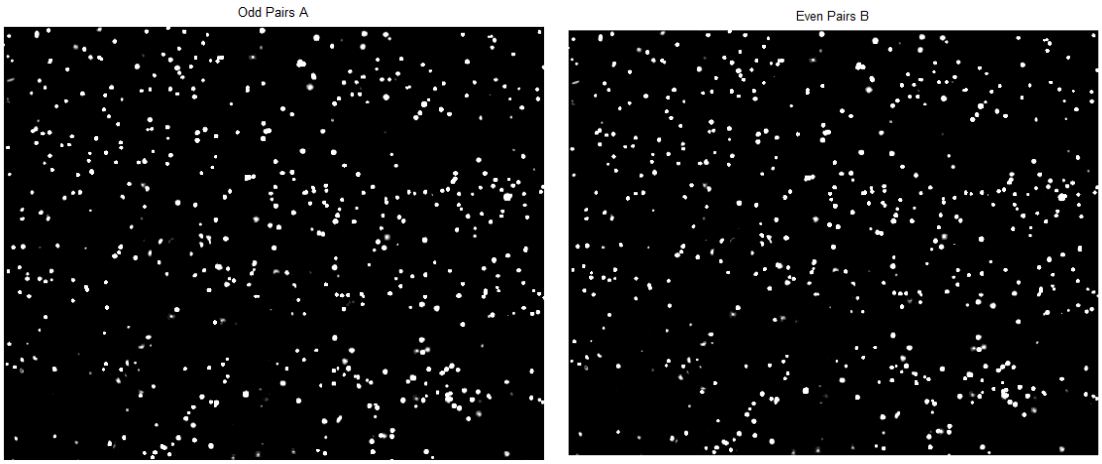

Figure 4.14: The accumulated (odd and even) images from the 38 pairs of source images for the levitation voltage 3 volt. The left image is the accumulated odd images while the right image is the accumulated even images. The time interval between every single image pair (odd and even) is 0.2 s. The images are captured using a 10X objective.

Figure 4.14 shows the accumulated source image pairs. The calculated particle number is 1140 particles per window for 38 image pairs based on the selected flow rate while the real number of particles is 495 per window. That generates about 56% error in particle number. *Figure 4.15* and *Figure 4.16* show the µPIV cross correlation result for levitation voltage of 3 volts. These figures are the

displacement vector field and filtered, interpolated and smoothed velocity field, respectively. The applied µPIV window size is 128 with 50% overlapping, this creates 18x14 vectors.

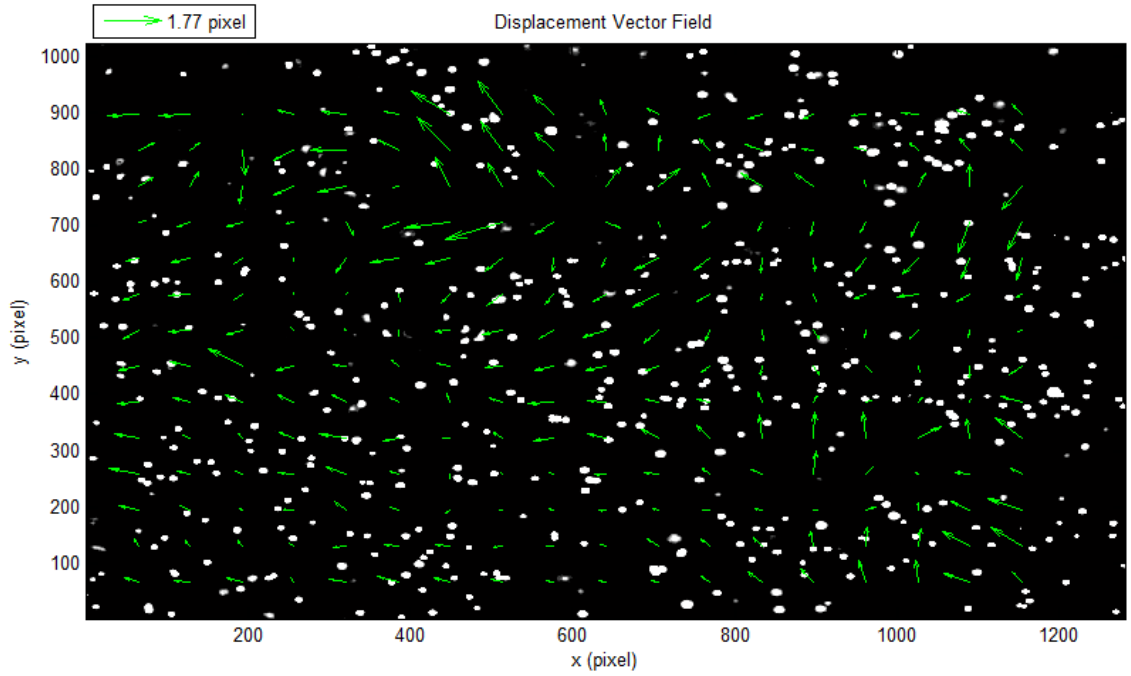

Figure 4.15: The µPIV result of displacement vector force map for a levitation voltage 3 volts. The green vectors show the displacement of particles between two consecutive frames (the pair shown in figure 4.15). The legend indicates the maximum measured displacement by the µPIV calculation.

.

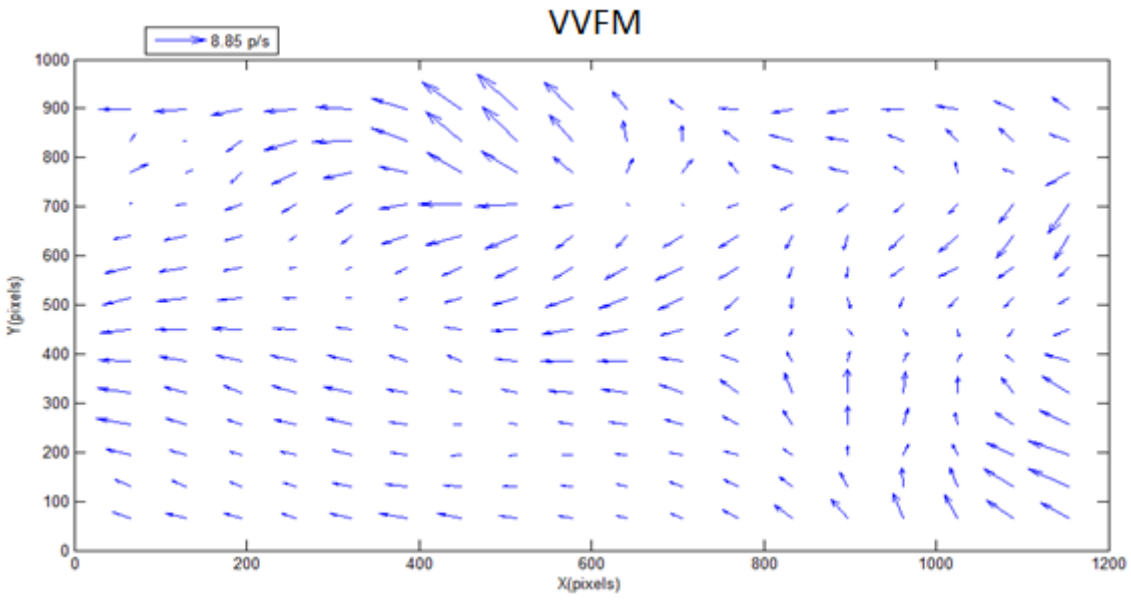

Figure 4.16: The velocity vectors force map (VVFM) for a levitation voltage 3 volts. The blue vectors are the filtered, interpolated and smoothed velocity vectors. The legend shows the maximum measured velocity by the µPIV calculation.

Figure 4.15 and *Figure 4.16* show the µPIV output (VVFM) with a significant maximum displacement and velocity vectors as a result of using high levitation voltage. The maximum and mean velocities are 8.85 pixel/s and 1.95 pixel/s respectively. The contribution of the net flow velocity can be also taken into the account if using a lower levitation voltage, However, there is still doubt regarding some net flow effects, where it is not considered that all of these lateral movements are attributed to the lateral acoustic radiation force, especially the trend of the velocity vectors at the left side, which are directed to the same bulk stream (net flow) direction which is in the left direction.

The above experiment sequential steps and µPIV generation have been repeated for various levitation voltages (1 and 2 volts) with the focus time assigned for each one. A number of low quality pairs were not included in the generation of µPIV which contributed to a lack of concentration of particles at some window regions. In order to have a reliable comparison between the three different voltages and to reduce the false and outlier vectors that µPIV creates during the interpolation process, different µPIV window sizes have been tested and a range of velocities have been recorded (see *Figure 4.17*).

The next figure gives an indication of velocity variations over the three voltages and can also be valuable for estimating the initial lateral forces produced by the levitation mode with respect to net flow velocity.

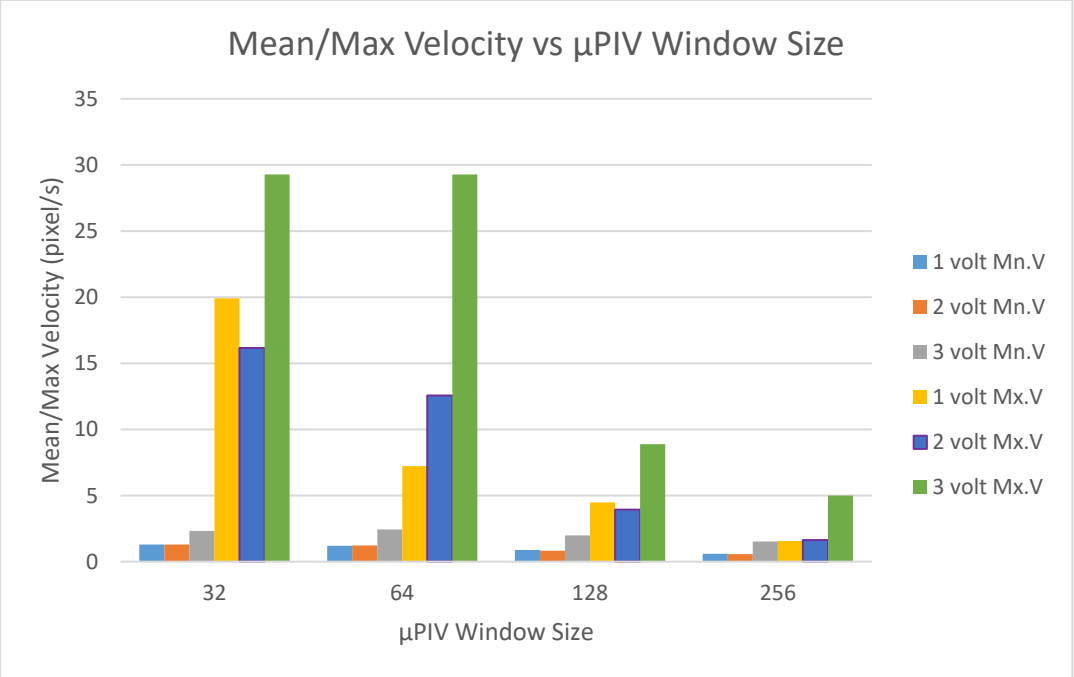

Figure 4.17: Mean and max velocities for different µPIV window sizes for three different levitation voltages. Note the decreasing maximum velocities as window sizes increases at 3 volts in particular. Steady mean velocities for all voltages with low values creates more sensitivity for the net flow velocity.

The figure shows the effect of window size selections on the mean and maximum velocities for the three levitation voltages. Maximum velocities were observed at 32 and 64 window size. These are considered as outliers, in particular with 3 volts (29 pixel/s) the velocities dramatically decreased as window size increased. The mean velocity for all voltages and at all window sizes were observed to be consistent (considerably low occurrence of outliers and false vectors). At 1 and 2 volts, the lateral movement (mean velocities of 0.59 and 0.56 pixel/s respectively at 256 window size) is still affected by net-flow which suggest precaution when using these voltages. Overall, the maximum velocities cannot be used for selection decision of the µPIV window size because they are affected by outliers. Mean velocities are more reliable if the effect of net flow velocity is disregarded. The 3 volt results show the expected scaling with voltage squared, and also demonstrate similar patterns. This gives confidence in this experimental method. However, it is obvious that the extra velocities resulting from these levitation voltages can cause inaccurate lateral radiation force measurements which belong only to the lateral resonance frequency. In addition, the source of these lateral movements have not been determined to be caused by the lateral component of the levitation resonance frequency if the electronic valves used are not functioning as required (it was noticed that there was some malfunctioning for long term automated experiments). The next sections describe a new kind of valve that provide better hydrostatic pressure stability for the force measurement system.

Recent literature [45] has shown the potential of valves to help in extinguishing the lateral acoustic forces. As a result, an important step has been introduced to create static flow conditions and a suitable environment for the control approach after shutting off the pump. A 2-mode 6-points Gilson valve (819 Injection valve actuator, Middleton, USA) which is shown in *Figure 4.18* is used for this purpose. For a more robust function to stop the residual velocity, the Gilson valve has replaced the electronic valve which was used in the previous measurements. This process is explained in this chapter.

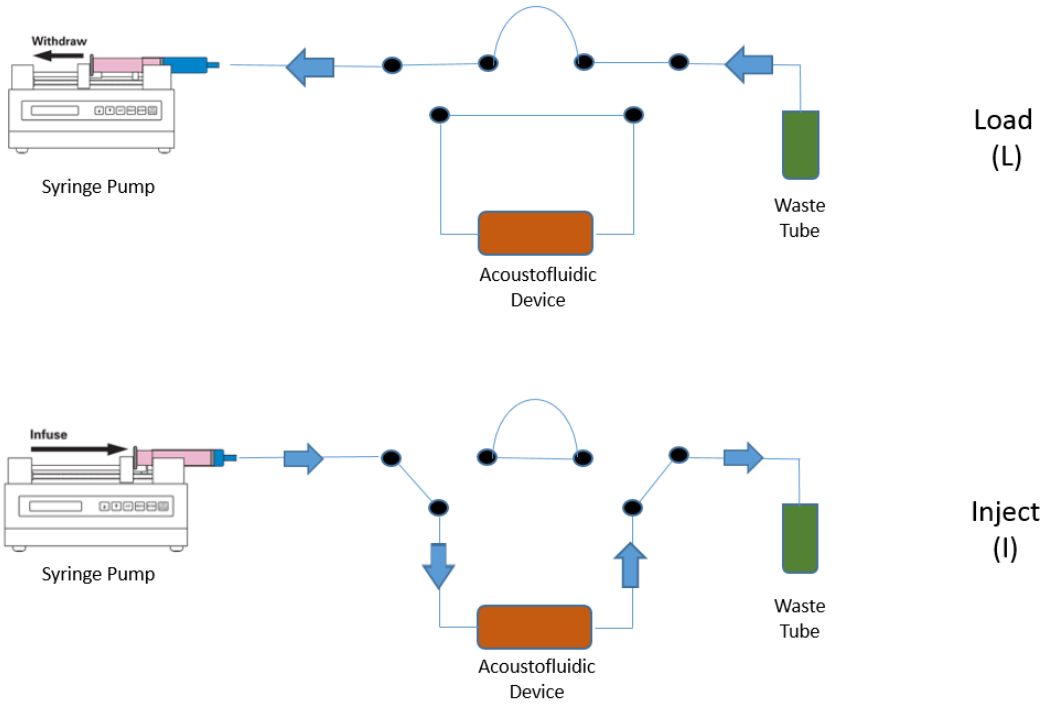

Figure 4.18: Demonstration of two mode flow direction using the Gilson valve. The six black dots represent the valve connection points. Both measurements of forces and control phase work on load mode (L).

The above figure demonstrates the two modes for this valve which are injecting micro particles from the syringe to the acoustofluidic device and also loading the used ones from the waste tube. The process is controlled by an Arduino code that synchronizes the motor shield and the Arduino Uno boards to switch between two modes automatically. During the particle manipulation and forces measurements (VVFMs generations) process the valve must be in load mode (the load LED is on in *Figure 4.19*). This is indicated by the closed loop state which provides equilibrium hydrostatic pressure at both ends of the device leading to stable measurement conditions and static particle positions.

Figure 4.19: Gilson valve with its six connection points and two mode LEDs.

4.4.4 Production of VVFMs

The generation of the velocity vector fields is a significant part in this project. The reliability of the lateral forces is important as they are employed later at the manipulation stage. One of the main requirements to make reliable VVFMs is to have a convenient acoustofluidic device which meets the requirements of the 2D acoustic field conditions. Also a stable 2D sound wave reflection is necessary. The current acoustofluidic device was used to investigate whether 2D manipulation can be achieved by having sufficient 2D lateral forces in all directions. The experiment steps to capture 25 pairs of images was performed (see the flow chart in *Figure 4.20*) using Gilson valve to provide the required lateral force measurements in static fluid conditions within the device. The two combined signals (levitation and lateral) are excited at 3 and 2 volts respectively. The focus time used is 11 seconds for the 3 volt levitation signal.

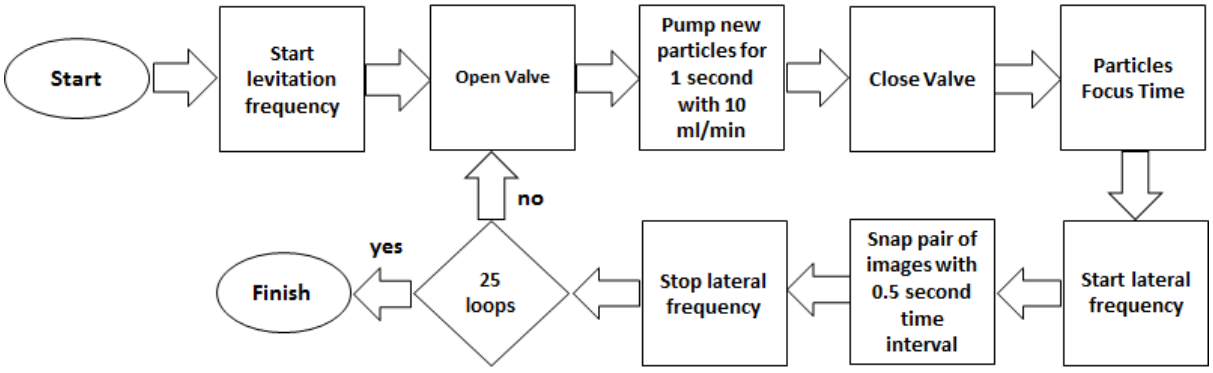

Figure 4.20: The experiment steps to capture 25 pairs of images for VVFMs generation. The time interval between two consecutive images is 0.5 seconds after applying the lateral frequency. The image pairs are saved in the system memory to be recalled later for VVFMs production. Note: the levitation frequency is always turned on.

Unlike the previous µPIV outputs that represent lateral force fields (*Figure 4.15*) for only the levitation frequency, a first attempt to produce the lateral forces generated by combinations of resonance frequencies (one to provide levitation and one for lateral movement) was conducted. The above sequence was employed to test some of the frequencies shown in *Figure 3.2*. In this case there are often a number of closely spaced resonances around the half-wave resonance of the device [2, 76]. The investigation of the lateral frequency was focused around the main resonance frequency and a number of experiments were conducted, following which their µPIV outputs were examined. The outcome indicated that none of the frequencies provide sufficient evidence to be used as lateral modes. *Figure 4.21* shows one of these µPIV outputs for a lateral frequency of 2.52 MHz. In this case the significant mean velocity was only in the direction of the sidewalls of the device (y direction only).

The maximum kinetic energy gradients are clearly evident with this voltage level, producing a 31.3 pixel/s mean velocity.

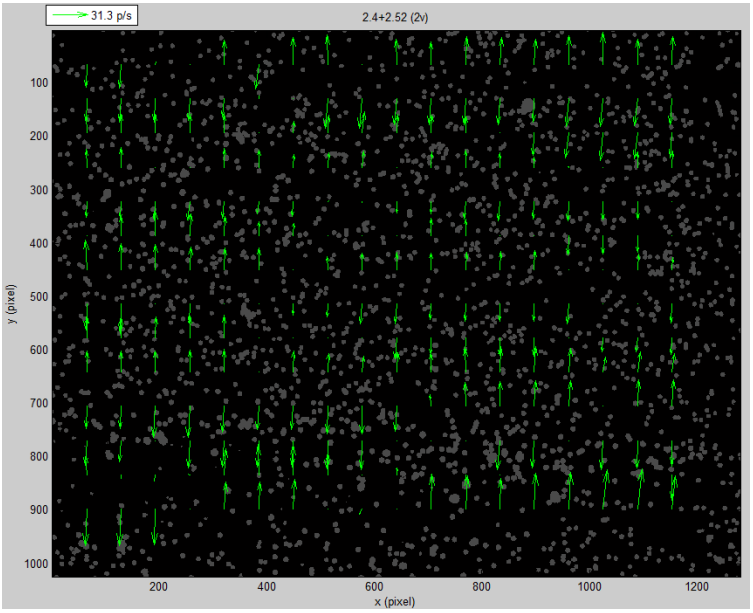

Figure 4.21: µPIV result of velocity vector field for 2.4MHz (3v) and 2.52MHz (2v) primary and secondary frequencies respectively. The legend represents the mean velocity (31.3 pixel/s) in the direction of y-axis only.

To conclude the above measurement outcomes, the velocity force maps for combined frequencies show no possibility for 2D manipulation in this current glass capillary device because of the strong dominance of the y component of the velocity over the x component. The main reason for that is due solely to the sound field reflections which seem to occur towards the glass wall boundary in y direction, while the open ends in the x directions cause no reflections. A decision was taken to try an alternative acoustofluidic device to replace the current device for a more convenient 2D manipulation.

4.5 VVFMs Generation using the Planar Resonator

The velocity vector fields shown in this section are generated using the system hardware depicted in *Figure 4.2* and employing an alternative acoustofluidic device. The selected device is a planar resonator as described in Section 3.2. For this control approach, the manipulation area must be fixed for the same field of view. This ensures the usage of the same forces in both stages (registration and manipulation). This is achieved by using reference images that include clear signs and scratched marks

on the attached PZT or other alternative methods to eradicate any device movement during the operation of these two stages.

The generation of the VVFMs was initiated by capturing 25 pairs of source images using the same sequence as demonstrated in *Figure 4.20*. The levitation voltage was set at 3 volts (this voltage is always turned on) which is above the voltage drop of this device (1.9 volts). To guarantee effective particle suspension at the device zero pressure node, a measured focus time of 27 seconds was applied for this levitation voltage immediately after closing the valves. This experiment was performed four times for each selected lateral frequency from *Figure 3.8*. The lateral frequency is applied, the camera captures image pairs with a time interval of 0.5 seconds. These images are then saved and pre-processed for VVFMs production. The µPIV cross correlation technique of image pairs is performed using a MATLAB script which was written as described in Section 4.3. The interrogation window size was set to 128 with 50% overlap so that each force map contains 252 vectors. A similar procedure of µPIV post processing as described earlier in this project is also employed for this analysis. This is used to generate the final filtered, interpolated and smoothed velocity vectors VVFMs (*Figure 4.22, Figure 4.23, Figure 4.24* and *Figure 4.25*) which will be employed at the manipulation stage. These force maps are stored in system memory in the form of direction and magnitude as matrix files and the control code to recall them at simulation time and during experiment manipulation is described in Chapter 5.

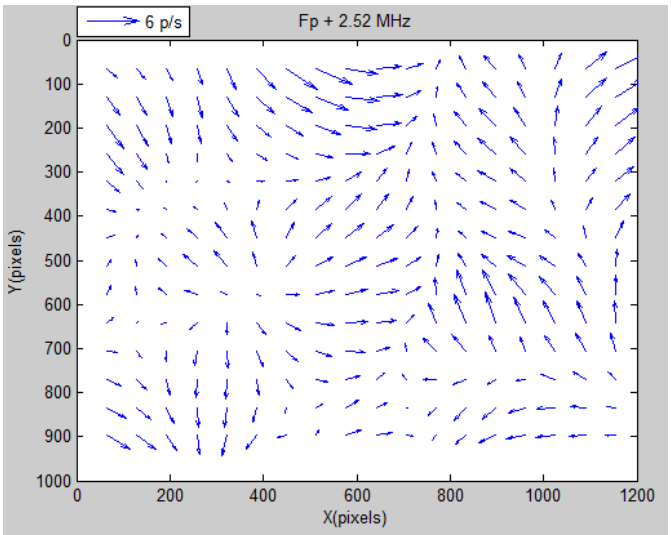

Figure 4.22: The first velocity vector field at the lateral combination mode 1 (primary frequency+2.52 MHz). 6 pixel/second mean velocity is considered as the lowest among the VVFMs collections.

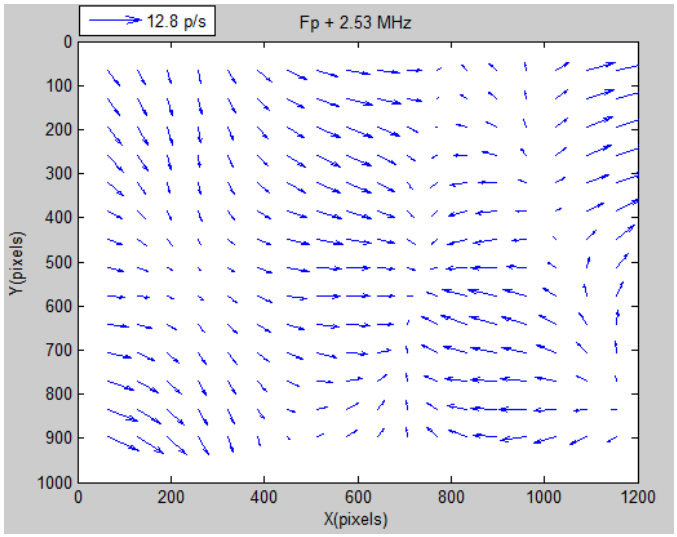

Figure 4.23: The second velocity vector field at the lateral combination mode 2 (primary frequency+2.53 MHz) with mean velocity of 12.8 pixel/second.

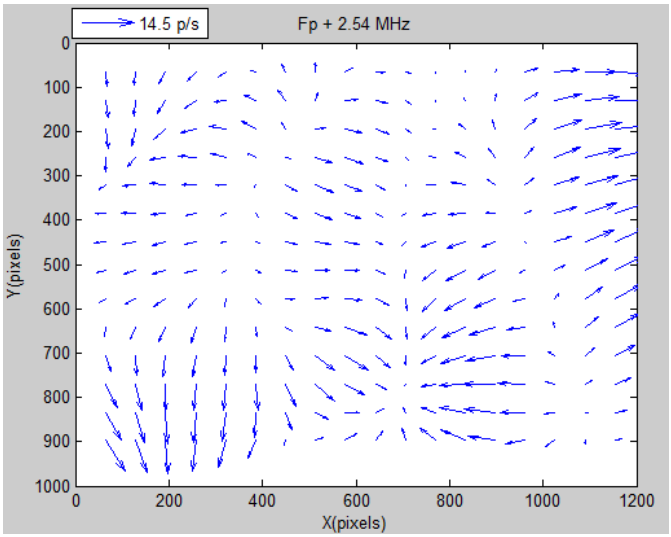

Figure 4.24: The third velocity vector field at the lateral combination mode 3 (primary frequency+2.54 MHz) with mean velocity of 14.5 pixel/second.

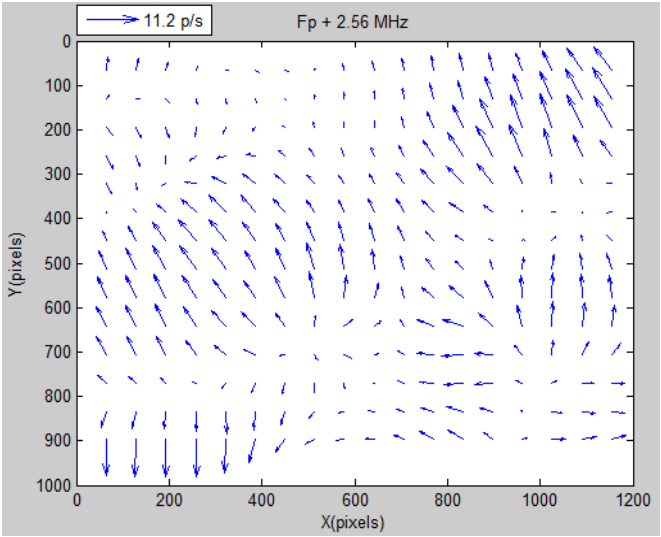

Figure 4.25: The fourth velocity vector field at the lateral combination mode 4 (primary frequency+2.56 MHz) with mean velocity of 11.2 pixel/second.

These figures show the interpolated, filtered and smoothed velocity vectors after applying µPIV post processing. Although a sufficient number of well distributed particles for the image pairs are used in this VVFMs production, the reliability of these maps have not been well examined (the manipulation phase using these maps will be the real examination of their reliability). The false vectors in the areas which lack particle movement are eliminated and interpolated early during the µPIV processing. This decreases the reliability of the data regarding the direction and the magnitude of the shown lateral acoustic forces. Reproduction of these maps might yield a degree of similarity which will be an indication of the VVFMs reliability towards performing successful manipulation later on.

4.5.1 VVFMs Repeatability Test

The aim of this test is to check how repeatable these lateral forces are. Two measures area obtained. The first is to calculate the mean magnitude error percentage, which is the mean value of the difference between the magnitudes of subsequent measurements of these forces (see Section 4.5.2). The second is to generate a colour map that helps to identify the spatial distribution of these errors. It should be noted that both methods of investigating the differences are fully dependent on the steps of pre-processing and µPIV post processing.

The VVFMs for two repeated measurements are shown in *Figure 4.26*. Despite using identical parameters, the only uncontrollable difference between the two experiments is the accumulated particle number within the image pairs. These are 1883 and 2252 particles respectively. Visually, the VVFMs display a high degree of similarity in term of direction. However; as result of automatic fitting of the vector length based on window size, the direction is more likely to be accurate rather than the

magnitude. The mean velocity difference in the two fields is considerably low (11.2 and 12.6 pixels/second for the first and second experiment respectively).

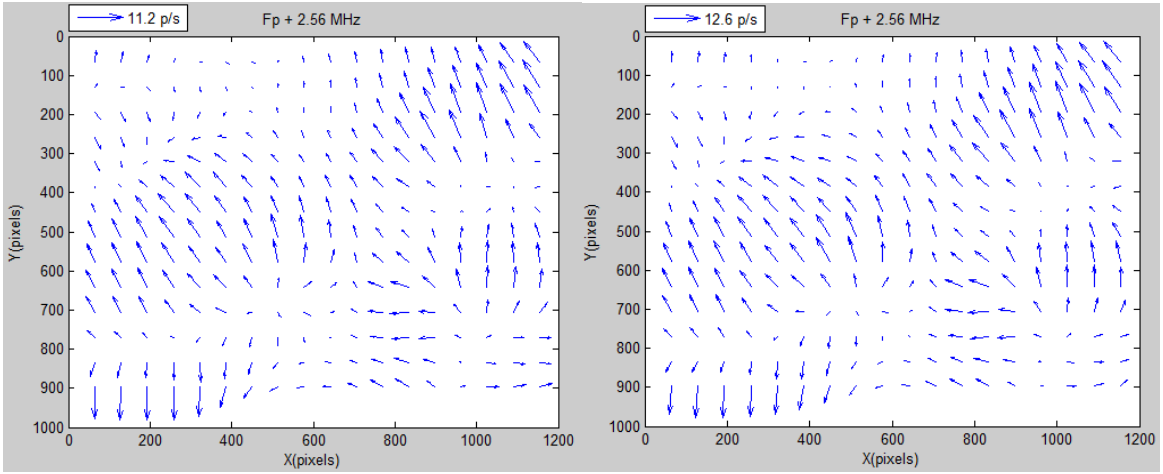

Figure 4.26: The final VVFMs for two measurements of frequency mode Fp+2.56 MHz. (left force map is the µPIV result for the first experiment while right force map for the second experiment). The mean velocity for these lateral acoustic radiation forces is slightly different in the compared maps.

4.5.2 Proportional Magnitude Error Calculation

The error difference between the two separate experiments can be obtained by calculating the proportional magnitude error percentage. Alternatively the error difference can be obtained by producing the colour maps that display the visible maximum and minimum errors. To calculate the error percentage that yields a real indication of the µPIV repeatability, a number of steps have been performed.

The µPIV code creates matrices giving the x and y components of the calculated velocity vectors. denoting the combination of these as the matrix of vectors, V.

To calculate the error between successive measurements of the force map, V_1 and V_2, calculating the mean value (at different spatial locations) of the magnitude of the vector error between these two measurements. Equation 4.7 defines the mean error as

$$\overline{|E|} = \overline{|V_1 - V_2|} \tag{4.7}$$

The average error can be expressed (4.8) as a percentage,$AE\%$ where

$$AE\% = \frac{|\overline{E}|}{|V_1|} * 100\% \quad (4.8)$$

After applying the above Equations which calculate the final averaged error percentage $\%$, the result is found to be 18 % **.**

The colour map is generated to validate the final error percentage and give some approximation of similarity percentage. The final command in the series of code is used to generate the colour map. To observe the full view field in the difference between the two VVFMs, the colour map is used as a visual tool that can help to determine where the areas of maximum and minimum difference occur. *Figure 4.27* shows that the maximum error is about 63% and it occurs only once at approximately the centre while the averaged error percentage is 18%. The colour bar shows the maximum error that is measured and it can be recognised by the dark red colour with a value of 63% occurring at (500,550) pixels. Finally, from the calculation of the proportional error percentage, the VVFMs are 82 % repeatable.

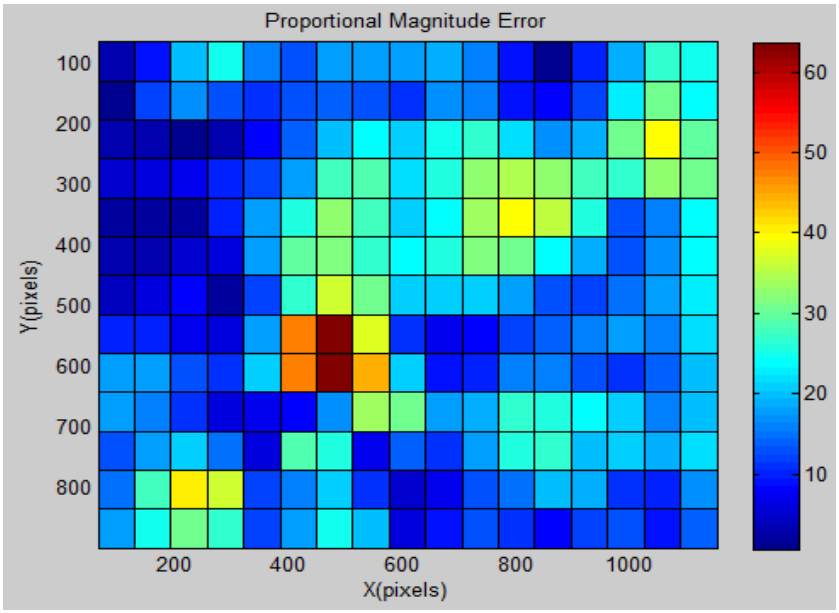

Figure 4.27: The distribution of the proportional error percentage throughout the colour map which covers the whole manipulation area. As shown, the maximum error is about 63% occurring around the centre while the averaged error percentage is 18%.

After completing the error calculation and generation of colour map, the µPIV repeatability and reproducibility can be determined based on the 18% error percentage as confirmed by the colour map which will lead to reliable µPIV outputs. Nevertheless, this averaged error can be minimised by utilising with reasonable number that directly affect the VVFMs. believing that the most essential

consideration for this kind of experiment is the random number and distribution of flowing particles entering the microfluidic device. This issue cannot be controlled accurately unless the number of images is greater than 200 images.

4.6 VVFMs Generation using the Glass Capillary with Two PZT

As the second algorithm does not require VVFMs to steer the levitated particle and it uses instantaneous forces measurements instead, the VVFMs in this section was generated for two purposes. Namely to simulate the proposed steering algorithm and also to investigate the lateral movement for this suggested algorithm.

The simulation section also used these force maps in order to investigate the device's efficiency to produce convenient lateral forces in the case where the decrease of the lateral mode strengths have been noticed. This happens with the first device as a result of epoxy material fatiguing after extended periods of transducer heat exposure. Thus, another similar device has been fabricated (identical device) to be used for the steering algorithm.

4.6.1 Steering Hardware

The hardware for the steering control system was designed based on two main requirements. Firstly, the need for rapid particle steering; and secondly, the geometry of the acoustofluidic device which is in the form of a rectangular glass capillary with 300 µm thick fluid chamber (the device dimensions are shown on *Figure 3.10*). The idea to use this device was based on the results shown in *Figure 4.21* which prove the dominance of the y-axis lateral radiation forces over the x-axis forces. The device is coupled to one bulk transducer which is divided into two parts (PZT_1 and PZT_2) in order to move the particles in the longitudinal direction of the capillary (x-axis).

Figure 4.28 shows the layout of the system hardware. A USB microscope camera (Thorlabs DCC1645C) uses a 10× objective and a FITC emission fluorescence filter (Thorlabs MF530-43) to visualise fluorescent microspheres (Fluoresbrite YG 10 µm, polysciences) that are illuminated by a royal blue 1W LED (Lumileds, Luxeon Rebel Star, 440-450 nm). The camera is connected to a Windows PC that uses MATLAB to execute the control algorithm. The output from the program is routed via a USB digital IO board (NI, USB-6002). This board controls two devices: a) analogue switches (VO14642AT, Vishay Semiconductors) that control which of the transducer regions are activated; and (b) a microcontroller

(Arduino UNO) which in turn communicates with two DDS (direct digital synthesis) modules (Analogue devices, AD9850). The Arduinos are preloaded with the required frequencies (*Figure 3.12*), and are able to rapidly change the outputs of the DDS modules depending on control signals from the IO board.

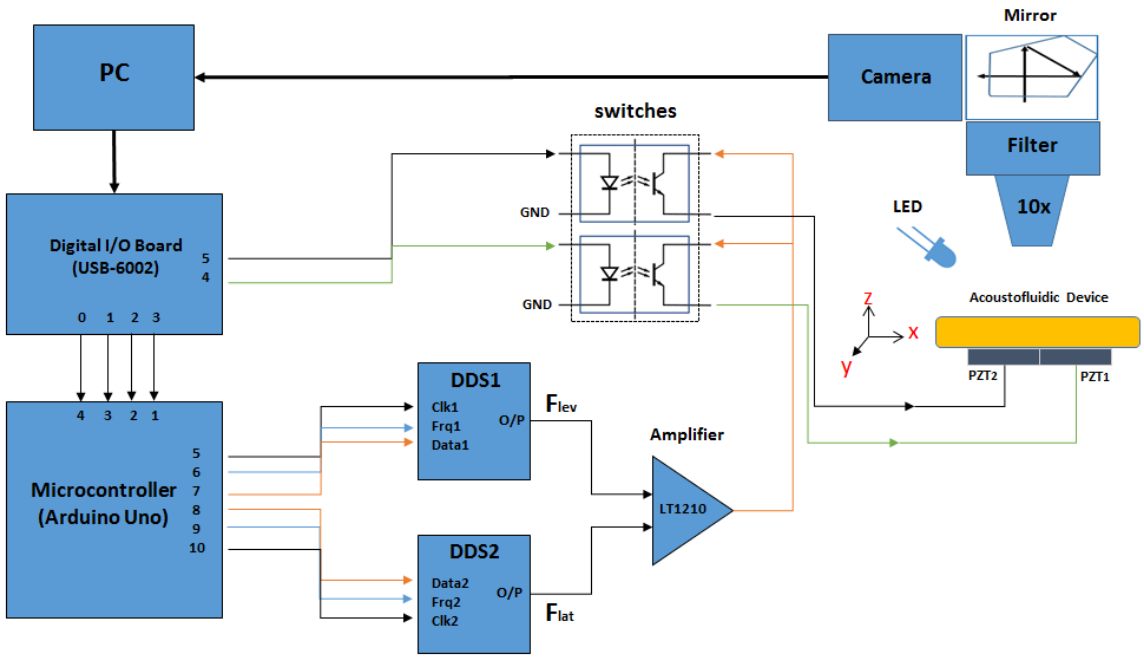

Figure 4.28: The steering system hardware used in steering algorithm and in generating the VVFMs.

The system hardware shown above uses a group of components arranged such that a 10× objective is coupled to a camera via a fluorescence filter and pentaprism mirror cube. The hardware images the acoustofluidic chamber in the region where ultrasonic resonances are actuated by a PZT transducer with two electrodes. The control algorithm programmed on the PC takes input from the camera and uses an interface board and microcontroller to communicate with DDS boards to synthesise MHz waveforms to excite the resonances. The signals are summed and amplified, then applied to the electrodes which is under the control of an analogue switch.

Figure 4.29 demonstrate the signal flow diagram from the steering algorithm code programmed in MATLAB to activating the desired PZTs configuration throughout digital IO board, the Arduino UNO board, two DDS boards, the summing amplifier and finally the relay switch. The reason for using two DDS boards is to synchronise the lateral frequency with the levitation frequency and then combine them using the summing operation amplifier. This amplifies the 1 volt input signal to the dedicated output voltage (1.5 volts for levitation and one and 20 volts for lateral voltage).

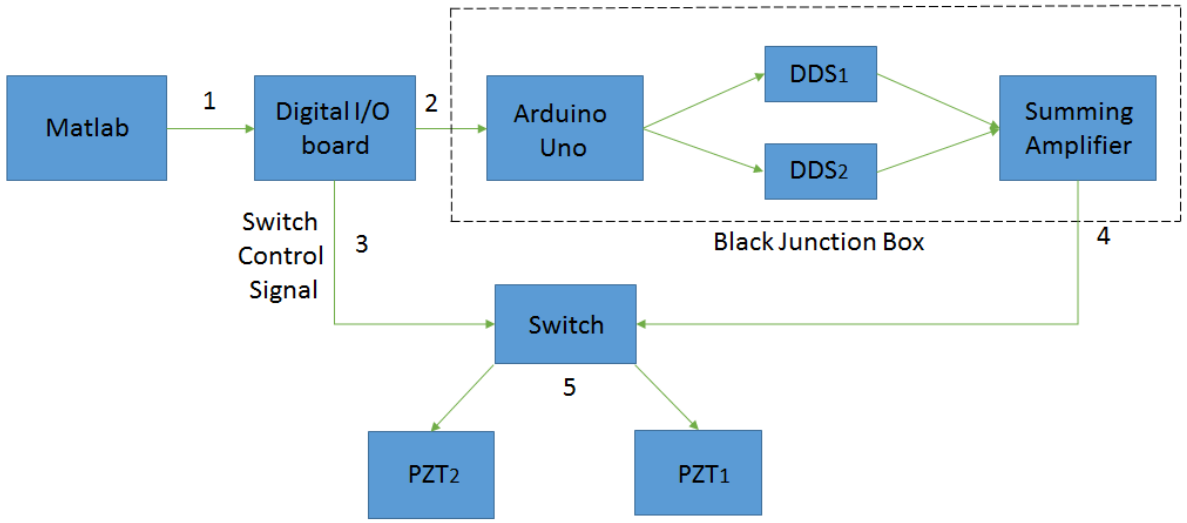

Figure 4.29: The general hardware block diagram for the developed steering control system.

According to the above figure, MATLAB sends the commands to configure the Arduino output through the I/O board. The MATLAB commands are coded in output vectors which control the activation of the two DDSs and PZTs. *Table 4.1* presents the assignment of this output configuration vector $\boldsymbol{V}$ that enables both Arduino and I/O board to achieve a specific configuration with the frequency modes.

Table 4.1: Hardware configuration pins for the steering system where the 5th and 6th I/O pins are connected directly to the relay switch.

I/O pins	Arduino pins	Configuration	Action
P_0	4	S	$\mathrm{F_{Lev}}$
P_1	3	L_1	$\mathrm{F_{Lat}}$
P_2	2	L_2	$\mathrm{F_{Lat}}$
P_3	1	L_3	$\mathrm{F_{Lat}}$
P_4	-	PZT_1	Right Direction
P_5	-	PZT_2	Left Direction

When activating both levitation and lateral resonance frequencies for a time period, T, MATLAB sends data signals to I/O ports in a binary manner with status,S. If the status is equal to one levitation is

activated and status zero means no levitation is applied. In this experiment the status is set to 1 and then data signals are removed from the port lines (with status zero) after a time period, T. The I/O board receives a vector with 6 bits from MATLAB (Equation 4.9 and Equation 4.10). The first bit controls the activation of the levitation frequency and the 2nd, 3rd and 4th bits are assigned to the lateral frequency while the 5th and 6th bits are assigned to the PZTs configuration. The MATLAB variable Fm can only be equal to a single value ranging from 1 to 5 which corresponds to the order of the lateral frequency number on the corresponding MATLAB frequency selection table, $\boldsymbol{Fm_{table}}$(Equation 4.11). If assuming that the output configuration vector $\boldsymbol{V}$ is assigned in the following manner to the I/O board:

$$\boldsymbol{V = [P_0\ P_1 P_2 P_3 P_4 P_5]} \tag{4.9}$$

The corresponding vector for the Arduino will be,

$$\boldsymbol{V = [F_{Lev}\ \ L_1 L_2 L_3 PZT_1 PZT_2]} \tag{4.10}$$

And the frequency selection table $\boldsymbol{Fm_{table}}$ represents five frequency modes.

$$\boldsymbol{Fm_{table}} = \begin{bmatrix} 0 & 0 & 1 \\ 0 & 1 & 0 \\ 0 & 1 & 1 \\ 1 & 0 & 0 \\ 1 & 0 & 1 \end{bmatrix} \tag{4.11}$$

Where the first row controls the first lateral frequency mode and so on. The bits $L_1, L_2\ and\ L_3$ represent the digital numbers for the selected frequency. If these digits are equal to 010, it means the selected frequency is three volts. Consequently, the $\boldsymbol{PZT_{table}}$ in Equation 4.12 is designed in the same manner as the frequency table.

$$\boldsymbol{PZT_{table}} = \begin{bmatrix} 1 & 0 \\ 0 & 1 \\ 1 & 1 \end{bmatrix} \tag{4.12}$$

Where the right hand side PZT configuration for the bits PZT_1, PZT_2 in Equation 4.10 represents the first row for the PZT_1 (right direction) and so on.

The advantage of this configuration is that it allows for the levitation frequency to be activated separately from the lateral frequency. This is in order to keep the tracked particle levitated; for example, during the calculation time, the optimal direction in which the system spends the shortest time where the levitated particle must be static.

4.6.2 VVFMs of the Steering Acoustofluidic Device

The advantage of the current configuration between the hardware (*Figure 4.28*) and the acoustofluidic device (*Figure 3.10*), is that it provides more direction patterns (different kinetic energy densities) for a limited number of characterised frequency modes and PZT configurations. There are (*FMn* x *PZTn*) possible force maps which can be generated for convenient manipulation, where *FMn* is the number of frequency modes and *PZTn* is the number of PZT configurations.

Before these force maps were generated, there was a need to investigate an unexpected lateral movement which was noticed during the steering runs (using another identical device to the one in *Figure 3.10* which was used early in the study before a noticed decrease in its performance. Its predetermined frequencies are presented in *Figure 4.30*). The steering of the levitated particles to the required targets was quite difficult. Therefore, production of VVFMs can help to investigate these steering difficulties. Simulations of the steering algorithm using these VVFMs gives an estimation for unsuccessful steering runs (see Section 6.7). The visual inspection of the lateral movement in these steering runs produced VVFMs which also help for interpretation if these lateral movements are not mostly matched with activated PZT configuration (at least 2 out of 5 of these force maps show the expected movement trend, in case of the right or left configuration in particular).

The investigation for the noticed decreasing of the lateral movements for that device was carried out by production of VVFMs, where, fifteen VVFMs have been generated using a similar experimental sequence as shown in *Figure 4.20* and with the parameters described earlier (time interval equal to 50 ms, 38 pairs of number, 1.5 and 20 volts applied for levitation and lateral frequency respectively). Visual inspections of these VVFMs have been performed. Noticeable unexpected lateral forces were observed especially for those positions above the left PZT when activating only the right PZT in order to visualize the anticipated right direction. Therefore, only 10 out of 15 force maps (five force maps belong to the right PZT configuration were removed) can be used for the simulation. *Figure 4.30* shows the one of the selected force maps generated from the equipment. This is used to simulate the steering algorithm as well as verifying the lateral forces for each mode. This gives an indication of the efficiency of the kinetic energy. These VVFMs (only 5 out of 10) were selected based on their dominant directions corresponding to the PZT configurations (first 3 configurations for left and last 2 one for both PZT configuration).

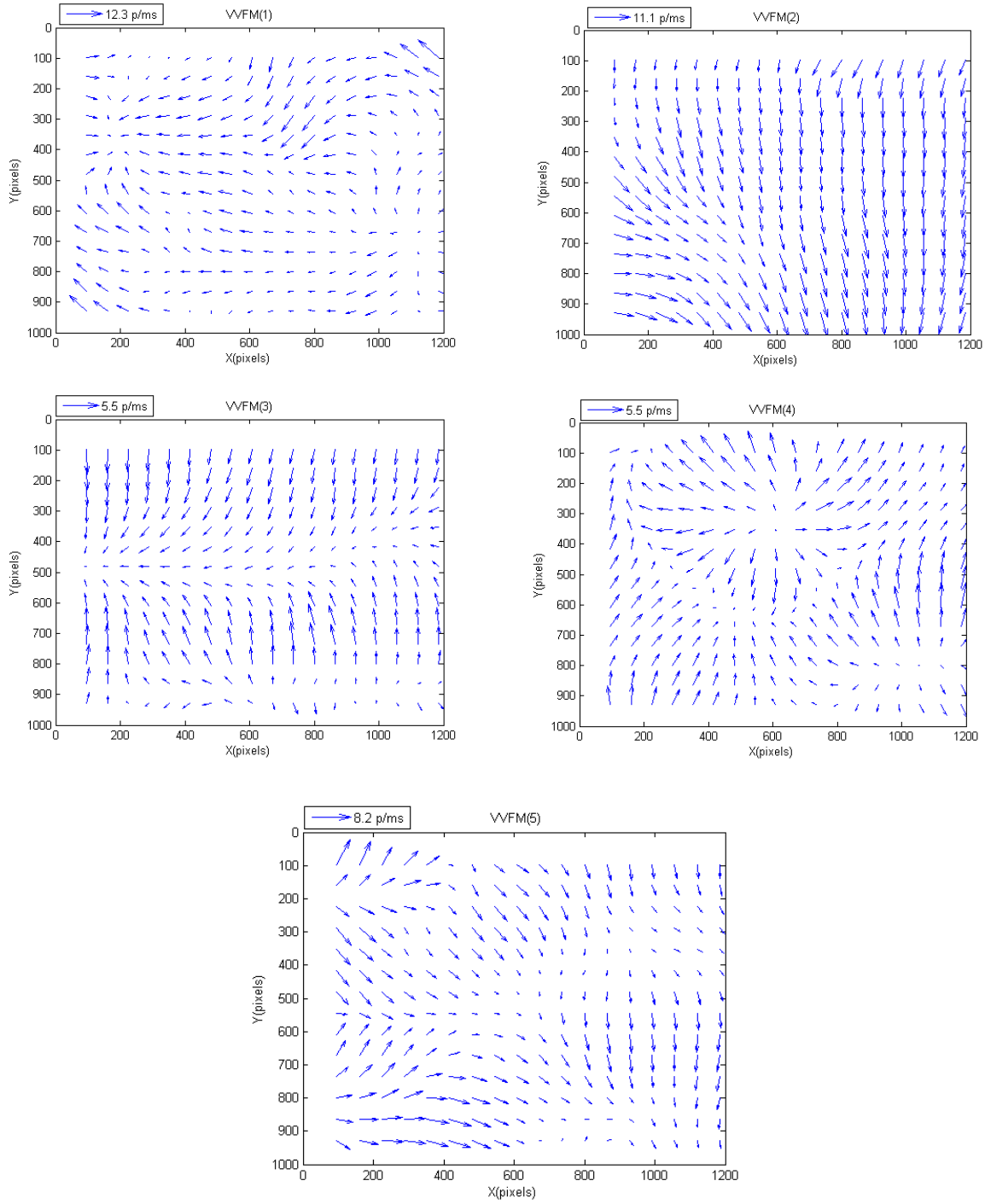

Figure 4.30: The five selected force maps from the 15 force obtained using the first glass capillary device with the two PZT configuration. The legend shows the mean velocity in pixel/ms. The first three maps are for the left PZT configuration while the last two maps are for two PZT configuration. The lateral frequency for each force map from the first to fifth are: 2.42, 2.44, 2.47, 2.50 and 4.55 MHz respectively. The levitation frequency is 2.37 MHz.

4.6.3 Vibrational Noise (Position Uncertainty)

Mechanical vibrations in the experimental rig cause the observed position of levitated particles to also vary with time. This vibrational position noise is important as it places limits on how accurately small displacements can be measured, which is key for the control algorithms presented in the rest of this thesis. Measuring these vibrations occurs once at the beginning of the steering run. It is necessary to separate the effect of residual background flow from the vibrational noise, which is handled as follows.

The measurement process for the particle position has been developed by producing a compensated function that measures any undesired shifting at the beginning of each manipulation run. This function is called position error and the output of this function is a value which represent the degree of position uncertainty. This value has to be taken into the account every time the system measures the particle position. This value is considered to be a vibrational noise value for the particle position.

Figure 4.31 shows an example of the measurement technique that produces the vibration value and Table 4.2 shows the resulting vibration values after applying the technique's Equations. The total measurement time 2.8 seconds and the vibration value is 1.5 pixels (0.75 μm).

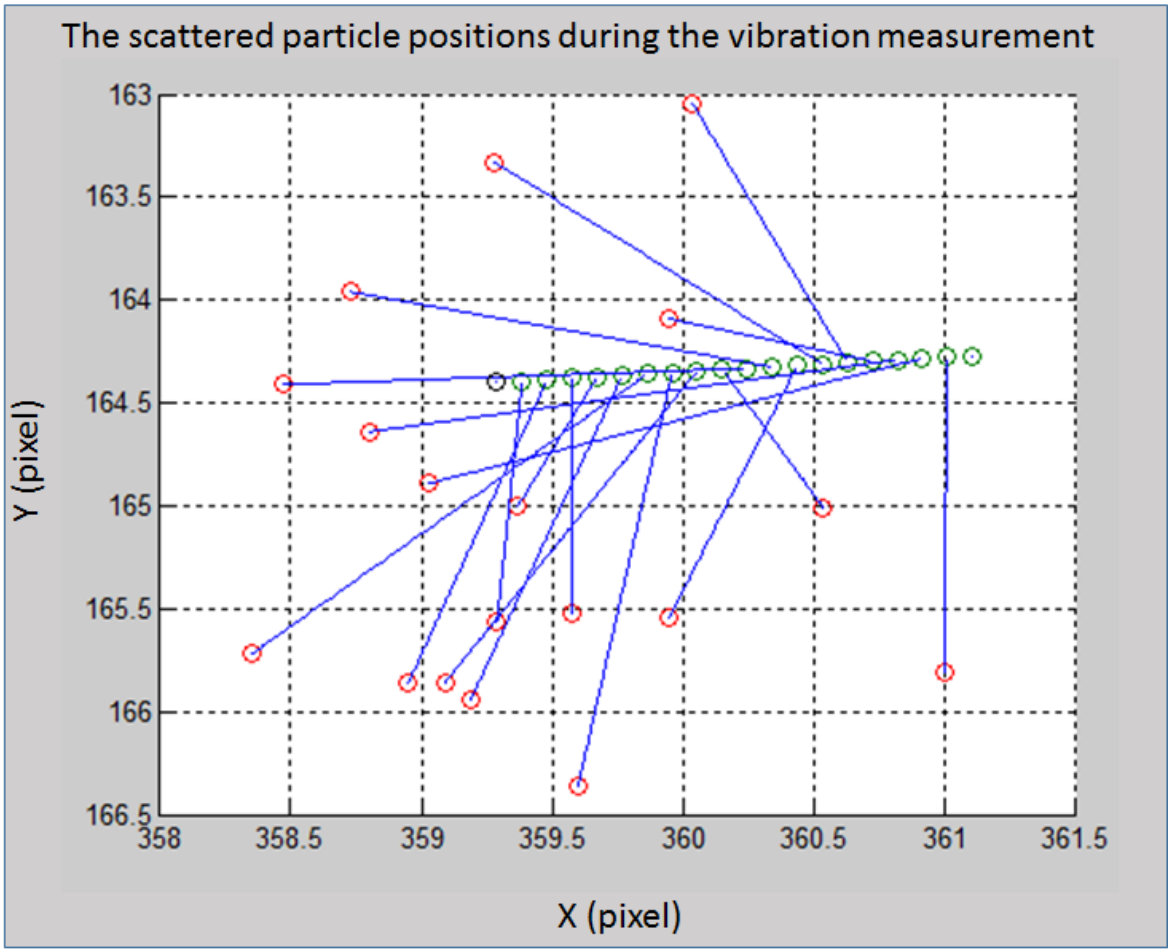

Figure 4.31 : An example of the measurement technique that produces the vibration value (position error). The red circles represent the real measured particle scattered positions while green circles are the projected matched positions. The projected drift line terminates at the black circle and starts at the green circle (real last and first particle position respectively). The resulting vibrational value is 1.5 pixel (0.75 µm).

Table 4.2: The vibration measurement details resulting from the above example.

Measurement Time (seconds)	Increment rate (pixel/Frame)	Frame Time (seconds)	Vibration (pixel)
2.8	0.09	0.140	1.5

The process starts by capturing 20 consecutive images of the levitated particle and recording the particle scattered position (red circles in *Figure 4.31*) each time. Then these positions are saved into a coordinate matrix system. Following this stage 20 projected positions (green circles in *Figure 4.31*) are generated on the straight path between the first and the last particle positions. These projected positions (generated and plotted by a MATLAB fixed scatter function), are equally separated by a drift distance incremental rate $\boldsymbol{l}$, which is set to 0.09 pixel/frame in the above example. This incremental

rate is calculated by dividing the Cartesian distance between the first and last position by the number of positions n.

In order to obtain the vibration value, the Cartesian distance Δx , Δy between the real positions and the projected positions are calculated. Then the distance R (blue lines in *Figure 4.31*) can be computed from Equation 4.13,

$$R = \sqrt{\Delta x^{\,2} + \Delta y^{\,2}} \qquad (4.13)$$

Finally, Equation 4.14 defines the vibration value pos_err as follows:

$$pos\_err = \sqrt{\frac{\sum_{i=0}^{n} R_i^2}{n}} \qquad (4.14)$$

At the end of each vibration measurement, the vibration value (pos_err) is an important indication of the acoustofluidic conditions before starting the particle manipulation step. Using this method the acceptable range is less than two pixels (1 µm).

4.6.4 Availability of Forces

The successful manipulation depends on the available forces that produce a number of different directions. Therefore more options to manipulate the tracked particle or to shift it close to the intended direction will yield a greater accuracy. However, in some cases the selected manipulation area does not provide options for convenient forces to move the particle towards the intended direction. The next example (the steering algorithm was applied in this example using the general flow chart steps shown in *Figure 6.1*) shown in *Figure 4.32* and *Figure 4.33* demonstrates the impact of the forces available in one particular area of manipulation which makes a significantly large manipulation for a required target distance only 400 pixels. This example was terminated by the user in order to assist the selected manipulation area to determine the available forces with the configuration of both PZTs.

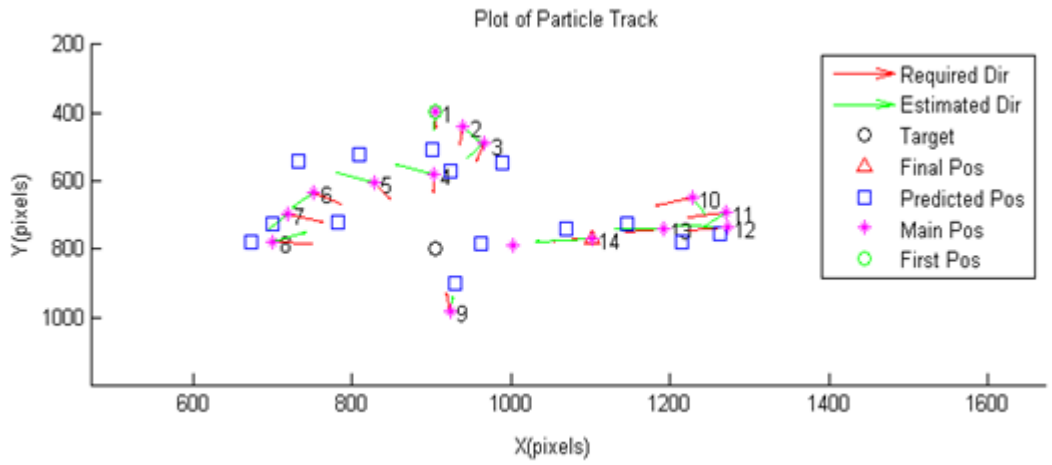

Figure 4.32: Plot of particle positions for a manipulation track from top to bottom; the direct distance between the first particle position and the target is 400 pixels. At each manipulation step the required direction and closest available force direction ("estimated") are plotted.

Figure 4.32 shows the real track of the manipulated particle from its first position to its final position which is close to the target (less than 100 pixels distance). It is possible to evaluate the availability of forces at each step by visual inspection. The different angles between the estimated direction (the selected direction among the other available directions) and the required target direction is taken to be a measuring tool for the force's efficiency at that region of the manipulation area. In this case the smaller the angle, the better the manipulation area.

In order to evaluate the above manipulation area in term of forces availability the above plot is magnified to determine what causes the particle trajectory to be significantly altered from the required direction (regardless of the direction error between the estimated and real direction which is not shown here). *Figure 4.33* shows the enlarged image of all forces available in the fourth manipulation step. It should be noted that all forces are pointing away from the target. The significant deviation of the manipulation trajectory happened after the manipulation step number three. This is due to the lack of forces in the downward direction. The fourth manipulation step occurs at the start of the absence of any significant forces and consequently the fifth and sixth steps where the different angle is significant as shown in the plot of *Figure 4.32*.

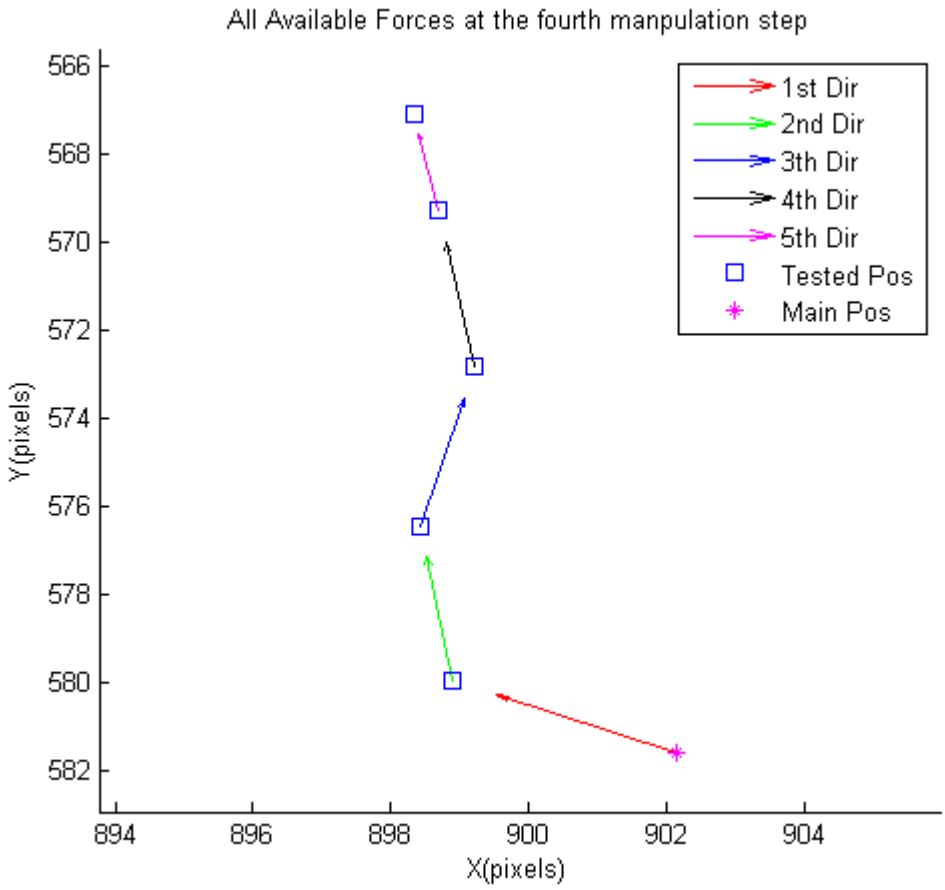

Figure 4.33: Magnified image of all forces measured at the fourth manipulation step. None of these forces are pointing towards the downward target position.

In the above plot, the zoomed in image of the available forces at the fourth manipulation step shows that four forces are pointing upwards (in the opposite direction to the target direction). The first force (indicated by the red arrow) has the closest direction to the target (best direction). The first force was then applied in the experiment to shift the particle at that manipulation step which is indicated in *Figure 4.32*. In this case, the designed steering control system has no influence to steer the particle towards the target and the only purpose it has is to choose the closest force to the required direction.

Finally, the importance of varying the different directions is considered as the best manipulation option. Therefore, higher probability of angle variations between the measured forces yields a higher percentage of fewer particles with travel distances and times towards the target. Considering the above selected manipulation area, the decision was taken to look for another area within the device which provides better force availability.

4.7 Conclusion

Progress has been achieved towards solving the issue of the bulk flow (which causes drift) using a 6 port valve . This valve has helped to ensure that the particle lateral motion is attributable only to the lateral acoustic forces. Hence it has assisted in better selection of acoustofluidic devices.

A number of additional acoustofluidic devices have been designed, built, tested and characterised. Finally, two acoustofluidic devices have been selected for the two different control algorithms (navigation and steering).

For the navigation algorithm that uses the VVFMs (Chapter 5), the planar resonator apparatus has been chosen to be the acoustofluidic device for the automatic manipulation. This is due to its multiple acoustic streaming patterns and requisite conditions of levitation. Furthermore it has more than three lateral resonance frequencies that can yield more direction options. Four resonance frequencies have been selected to achieve the 2D manipulation in combination with the main resonance frequency, where one of the VVFMs shows about 82 % repeatability of same measurements.

For the steering algorithm which uses real time forces measurements, the glass capillary with divided PZT has been chosen for its ability to steer the levitated particle in all available directions even in the direction of the glass capillary length. Five resonance modes have been selected to be excited for steering the particles laterally. This algorithm is comprehensively explained in Chapter 6 .

Chapter 5. Navigation Algorithm with Force Maps

This chapter uses the force maps measured in the previous chapter, and integrate them with a navigation algorithm to manipulate particles. Modelling results from simulated particle trajectories are initially presented. Then, experimental results for the real particle manipulation is demonstrated in four examples. Discussion of the errors associated with magnitude and direction of the manipulation is included as a possible reasons behind the significant errors. In the light of the poor performance obtained with this method – primarily due to the variation (or drift) in forces between the measurement phase and the later manipulation, alternative methods based on measuring available forces at each step are explored in Chapter 6.

5.1 Control Method and Approach (Manipulation Phase)

The measurement of VVFMs is integrated with the algorithm that follows. Each time a manipulation is required the "registration phase" that measures the VVFMs is performed prior to the manipulation.

The control algorithm for the manipulation phase is built using a simple feedback loop concept that is written in MATLAB code. The MATLAB code aims to move one particle along a path between the assigned first and target positions. *Figure 5.1* shows the flow chart of the automatic control algorithm that targets a precise 2D shifting and positioning of the particles within the levitation plane at the zero pressure node of the acoustofluidic device.

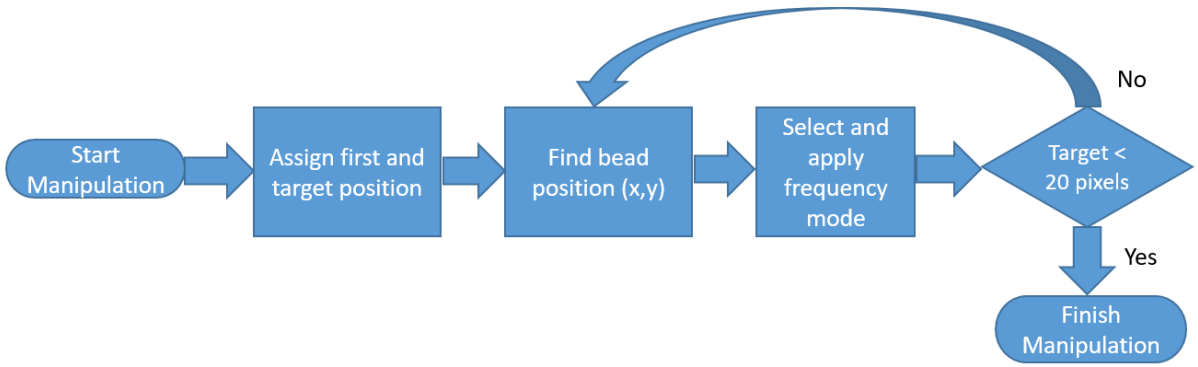

Figure 5.1: The flow chart for the manipulation phase for the first suggested control method. The selection of the frequency mode is based on the measured force directions of VVFMs at the bead position. The application time for the selected frequency mode to shift the bead through a required displacement is calculated from the selected force time and displacement at that

bead position. The iteration loop continues these steps until bead is positioned within the target region (1 pixel is equal to 0.95 µm).

The process of manipulating the bead position starts by take real time images using the microscopic camera to find the desired particle that needs to be manipulated towards a certain target (both the start and target position have to be selected by the system user). The control algorithm finds the closest available direction to the target by recalling all registered forces from the VVFMs at that particle's position. The levitated particle is then laterally shifted using the selected lateral frequency for a specific time to achieve the required distance. The control algorithm continues using the registered forces for shifting the particle until the particle is within the locality of the target. The target distance to finish the manipulation (the distance at which the manipulation is considered successful), was chosen to be 20 pixels (19µm), based on the bead size and the tendency of the algorithm to overshoot if this was set much smaller. This control process is explained with more details in the next section.

5.2 Control Model Design

The proposed control model for the first suggested algorithm is explained in detail in this chapter with the use of simulated results. The design of the control model was based on the empirical result of the VVFMs shown in Section 4.5, where the forces (direction and magnitude) are varying from one position to another. This leads to a stochastic field (not a deterministic field). This stochastic field represents the relation between the lateral acoustic waves and their displacement (manipulated variable and controlled variable respectively, as shown in *Figure 5.2*). However, it is still possible to build a software model that can deal with this stochastic input and output at every manipulation step [77-79]. In this research, a simple feedback control system is proposed for ultrasonic particle position manipulation using a linear extrapolation for the actuation time of the frequency mode (Equation 5.4) based on known forces (measured time and displacement from VVFMs). Hence the prediction of the next particle position can be determined. *Figure 5.2* demonstrates the automatic process for the ultrasonic particle manipulation where blocks of the actuator, acoustofluidic device and sensor represent the physical components of the control system. The updated resulting particle position is likely to be different from the predicted particle position due to the linear extrapolated method for the shifted time. This calculation method is only valid within a uniform acoustic field for the lateral forces over a distance of (λ/4), as the acoustic field varies over length scales of this order.

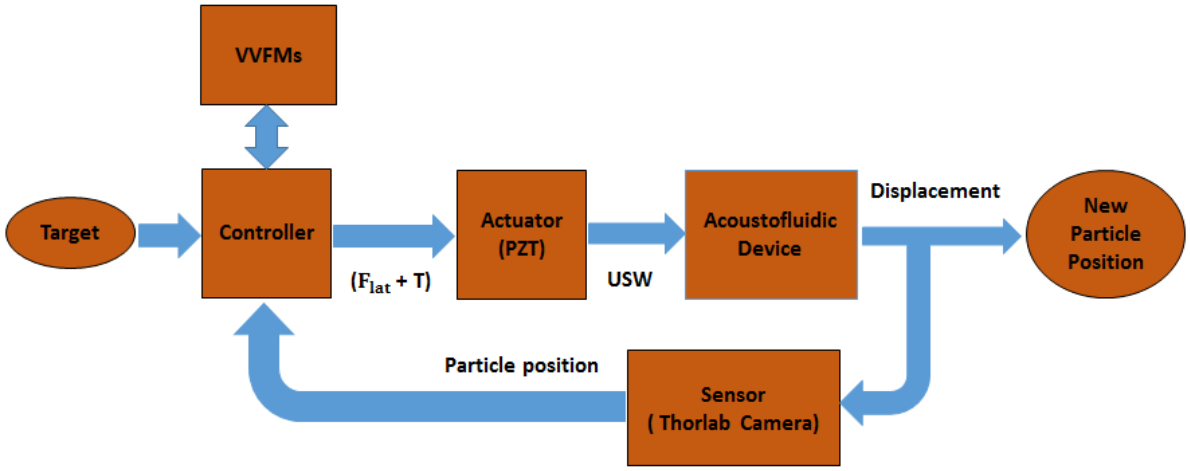

*Figure 5.2: The function block diagram for the automatic control system that is used in this project for ultrasonic particle manipulation. The presented control elements are a camera as a sensor, PZT as an actuator and a MATLAB code as a controller. The process occurs in the acoustofluidic device. The controller selects and calculates the frequency mode and actuation time respectively. The manipulated variable is the activated ultrasonic wave **USW** while the controlled variable is the resulted particle displacement. The controller determines the error signal between the target (set point) and the new particle position logically and then (if the error signal is not equal to zero) calculates the required manipulated variable parameters (actuation time **T** and lateral frequency F_{lat}) of the USW. The first suggested control algorithm assumes that no disturbance signal interferes in the process.*

The above diagram demonstrates the control elements that is employed to achieve the particle manipulation. The input and output of each element's box (the main elements in particular) explain the manipulation process in terms of variables. The controlled variable (the ultrasonic waves USW, with its parameters (F_{lat} +T)) is applied to shift the tracked particle (suspended at the levitation plane of the acoustofluidic device) for a given displacement (manipulated variable). During the real manipulation experiment, the resulting new particle position (the measured variable) is observed by the camera and returned to be compared with the target position by the controller. However, some experiments have to be terminated by the user if the particle movements are out of control. This is discussed in this chapter.

The main model assumption in both suggested (navigation and steering) algorithms is that the ratio between measured/tested displacement and time is equal to the ratio between shifted displacement and time for distances less than λ/4, where forces only vary over distances of order λ/4 so this model assumes the force will stay the same in less than this distance.

The next series of equations represent the control model that is used in both cases of manipulation (simulation and experiment).

Assuming that the first (current position) and the target (final position) position are specified. The algorithm calculates the required direction, REQ_D. Also denoting the current and the final position as ($X_{current}, Y_{current}$) and (X_{final}, Y_{final}) in pixels.

To calculate the required direction, the distance (*Δ*) between the two points must be first calculated. Equations 5.1 and 5.2 show the difference between X, Y values of the two positions respectively.

$$\Delta X = X_{final} - X_{current} \quad (5.1)$$

$$\Delta Y = Y_{final} - Y_{current} \quad (5.2)$$

Then the required direction can be calculated from Equation 5.3,

$$REQ_D = tan^{-1}\left(\frac{\Delta Y}{\Delta X}\right) \quad (5.3)$$

After calculating the required direction, the system begins to find the closest available direction from the measured directions in the VVFMs at that particular position. If the current particle position is located between the measured forces positions in VVFMs (forces are stored in form of direction and two velocity components), then the algorithm linearly interpolates the direction. All interpolated directions are then stored in a temporary matrix which called *D.* For example, see Table 5.1 which has four interpolated directions at each manipulation step computed from the four reference VVFMs. The algorithm chooses the closest direction (the selected direction Sel_D) from the matrix *D* with its internal matrix index. The index value corresponds to the frequency mode *FM* which is to be applied. The algorithm applies this frequency mode for a predetermined time (actuation time *T* in seconds) to shift the particle through a proposed distance *dx* (dx is the displacement in pixels; in this study 20 pixels in all simulations and experiment examples). Before calculating the actuation time *T*, the algorithm uses 2D linear interpolation to attain the interpolated velocity components (U_{int}, V_{int}) based on the selected direction Sel_D and the current position ($X_{current}, Y_{current}$). The actuation time (T) is then calculated using Equation 5.4 where V_{mag} is velocity magnitude which is defined in Equation 5.5.

$$T = \frac{dx}{V_{mag}} \quad (5.4)$$

$$V_{mag} = \sqrt{{U_{int}}^2 + {V_{int}}^2} \quad (5.5)$$

The actuation time calculation in this model is also important in order to predict the later particle position. Where the later position can be predicted from the following Equations,

$$X_p = T * U_{int} + X_{current} \qquad (5.6)$$

$$Y_p = T * V_{int} + Y_{current} \qquad (5.7)$$

X_P , Y_P are the predicted next position coordinates. The tables which show the experimental manipulation examples have different columns for the real position coordinates X_R , Y_R (that are returned from the real images) and the predicted positions for each step. However, only the simulated particle positions are shown on the tables which to model manipulation examples.

Section 5.4 demonstrates both cases of successful and unsuccessful manipulation experimentally and discusses the reasons of deviations in both cases. The next section presents the ability of the model to manipulate a single simulated particle on a trajectory which is based on a specified start point and target points in four different directions. It uses VVFMs to do this.

5.3 Model Manipulation Examples

The aim of these examples is to demonstrate the model robustness and its reliability for creating the expected trajectory of the dynamic particle based on the available forces taken from VVFMs. Four examples were selected to show the model output in different four directions (*Figure 5.3*). Furthermore, these four examples show the model response and reactions to the changing of direction every time the particle moves to new position. These examples are shown in the figure below which gives a better view of their manipulation areas.

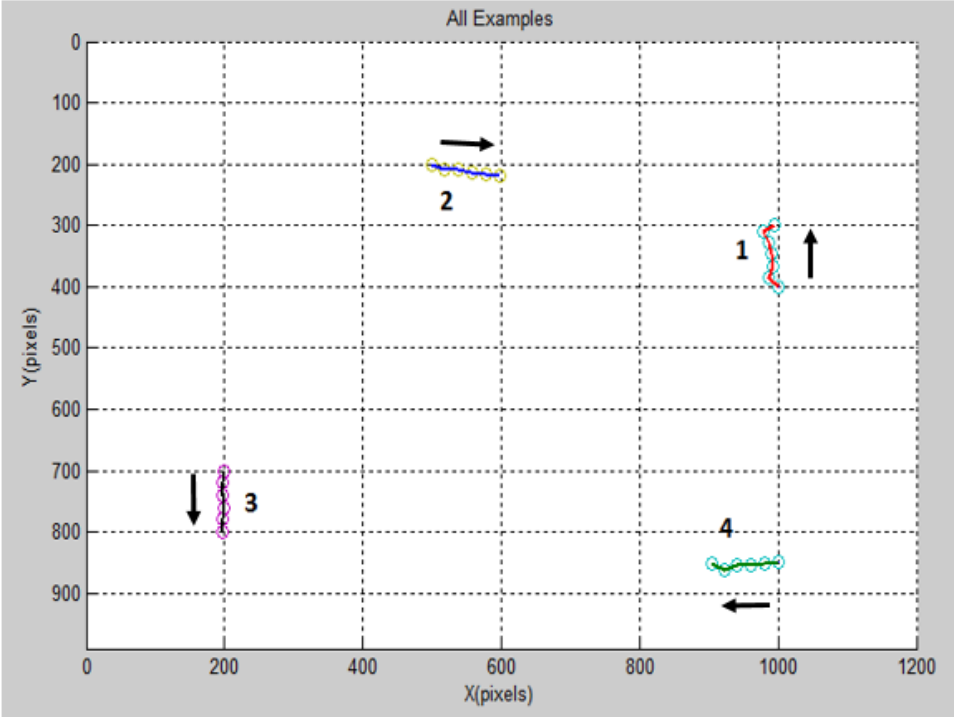

Figure 5.3: Four model examples in different directions (1 pixel is equal to 0.95 µm).

The above figure demonstrates the four model examples with the whole field of view where the trajectories are in the course of 100 pixels. The possibilities to achieve certain manipulation trajectories (for known start and target point regardless the trajectory shape) can be determined by visual inspection on available VVFMs (The method of connected arrows can be applied to develop a trajectory). The simulation examples have been designed using possible directions that avoid the hanging areas. These are regions where the nearby forces are not harmonic and there is no specific tendency for the particle to move in defined directions. In addition, there are some areas that should be avoided with the VVFMs as these areas have weak velocity magnitudes. These weaknesses affect the manipulation process so that more time will be needed to achieve the required displacement. Therefore the thermo-effect increases and produces a reduced precision with regards to direction and magnitude of displacement.

5.3.1 Upwards Direction Model Example

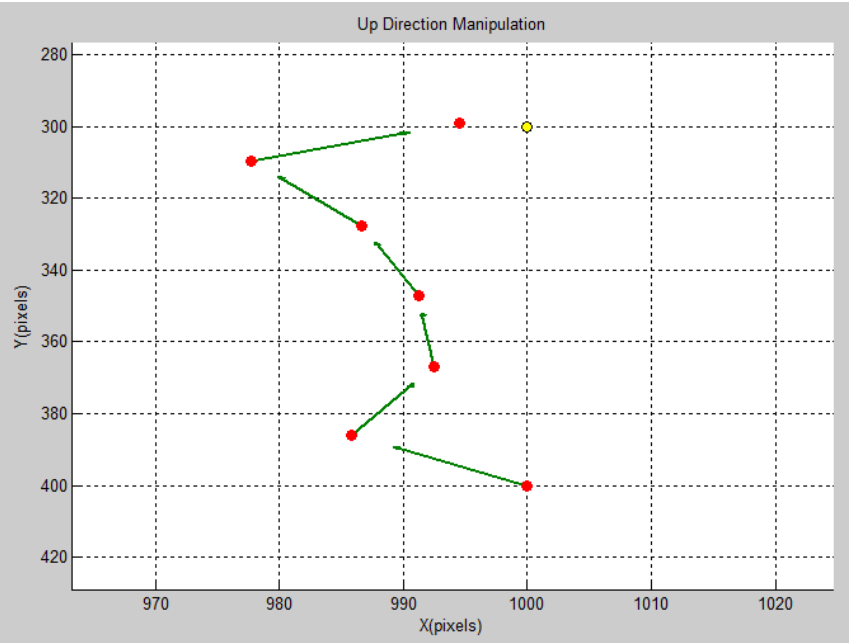

Figure 5.4: Vertical upwards direction from (1000, 400) to (1000, 300). The red dots are the simulated particle positions while the green arrows represent the selected directions (only 80% of the vector length is shown in order to make the direction clear). The yellow circle is the desired target. The final particle position is 5.4 pixels away from target (1 pixel is equal to 0.95 μm).

Table 5.1: Direction decisions at every step of model Example 1. A critical decision at step 1 is to take FM 1 as the closest required direction by 0.01 rad closer than FM 4. Directions unit is radian.

Step	REQ_D		Interpolated Directions Matrix (*D*)					Sel_D	*FM*
1	4.7124		3.987	0.61165	6.0015	5.4424		3.987	1
2	4.8764		3.94	1.6744	5.8972	5.0658		5.0658	4
3	4.8245		4.0673	0.42306	5.863	4.998		4.998	4
4	4.8972		4.1238	5.7806	5.8126	4.7439		4.7439	4
5	5.1621		4.1408	4.7262	5.743	4.4893		4.7262	2
6	5.8705		4.0798	4.1458	5.6523	4.3806		5.6523	3

Table 5.2: Velocity components and simulation time at each step of model Example 1. Velocity units are in pixel/seconds, positions are in pixels while the time unit is seconds.

Step	U_{int}	V_{int}	$X_{current}$	$Y_{current}$	*Dx*	*T*
1	-1.7269	-1.7073	1000	400	19.997	8.236
2	0.31771	-0.8985	985.78	385.94	20.001	20.986
3	-0.13264	-2.1139	992.44	367.08	19.999	9.4427
4	-0.82913	-3.56	991.19	347.12	20	5.4716

5	-0.80082	-1.5924	986.66	327.64	19.995	11.22
6	5.5578	-3.5424	977.67	309.78	20.004	3.0346
			994.54	299.03		

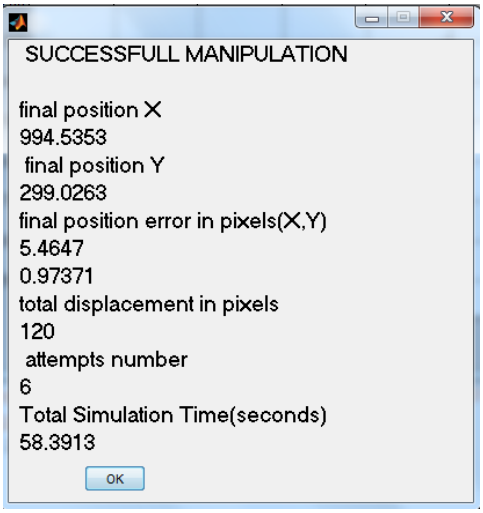

Figure 5.5: The successful manipulation confirmation window for the first model example. The final position error indicates the Cartesian distance from the target to the final particle position. The total indicated simulation time is the accumulated time in the previous table after 6 manipulation steps.

5.3.2 Right Direction Model Example

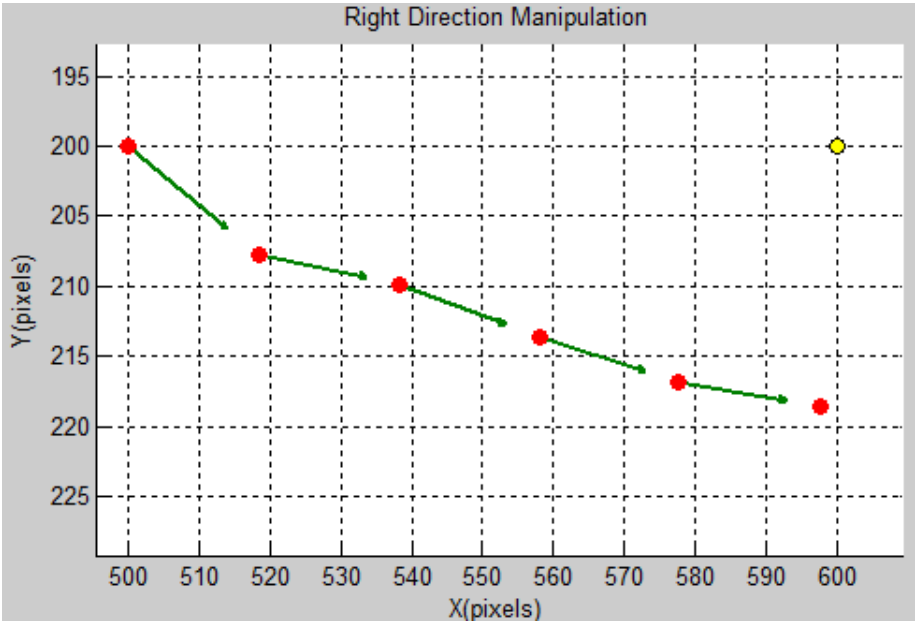

Figure 5.6: Right direction model from (500, 200) to (600, 200). The red dots are the simulated particle positions while the green arrows represent the selected directions. The yellow circle is the desired target. The final particle position is 18.6 pixels away from target (1 pixel is equal to 0.95 µm).

Table 5.3: Direction decisions at each step of model Example 2. Directions unit is radian.

Step	REQ_D		Interpolated Directions Matrix (*D*)					Sel_D	*FM*
1	0		0.3997	0.50558	5.8705	4.1872		0.3997	1
2	6.1892		0.32329	0.47175	0.048627	4.3179		0.048627	3
3	6.1252		0.24382	0.45397	0.1348	4.3906		0.1348	3
4	5.9695		0.16164	0.43788	0.21896	4.4532		0.16164	1
5	5.6372		0.079505	0.42206	0.28955	4.5162		0.079505	1

Table 5.4: Velocity components and simulation time at each step of model Example 2. Velocity units are in pixel/seconds, positions in pixels while the time unit is seconds.

Step	U_{int}	V_{int}	$X_{current}$	$Y_{current}$	*dx*	*T*
1	3.8328	1.5963	500	200	20	4.8171
2	5.065	0.54366	518.46	207.69	20	3.9261
3	5.9766	1.159	538.35	209.82	20	3.2852
4	4.6443	0.74242	557.98	213.63	20	4.2524
5	4.9377	0.43413	577.73	216.79	20	4.0349
			597.65	218.54		

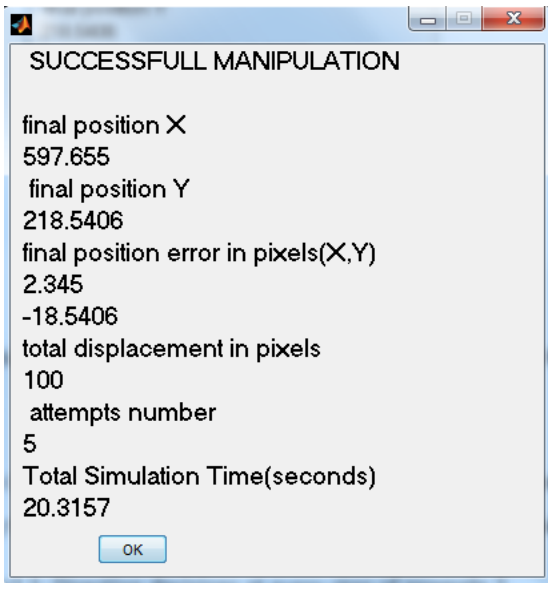

Figure 5.7: The successful manipulation confirmation window for the second model example. The final position error indicates the Cartesian distance from the target to the final particle position. The total indicated simulation time is the accumulated time in the previous Table after 5 manipulation steps.

5.3.3 Downwards Direction Model Example

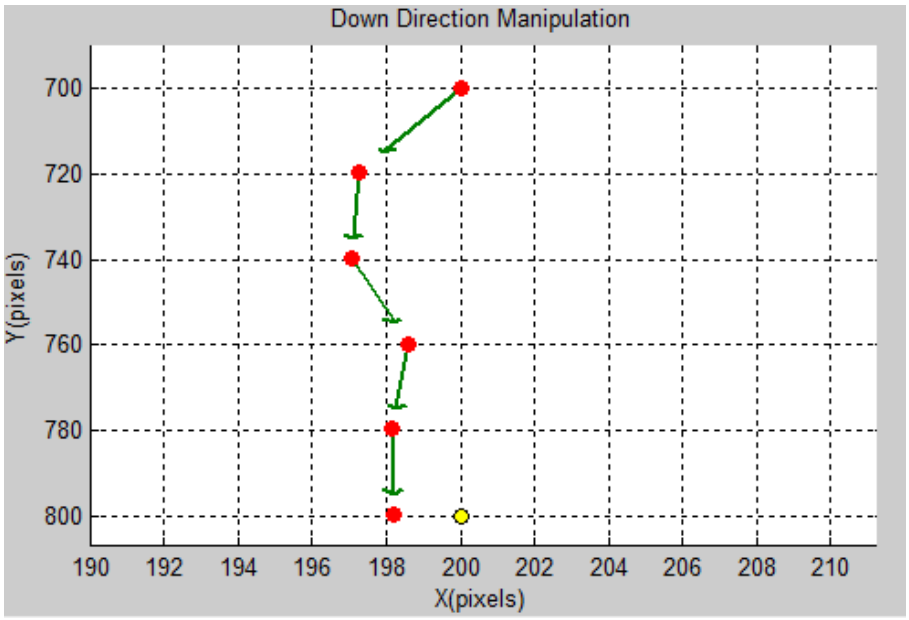

Figure 5.8: Downwards direction from (200, 700) to (200, 800). The red dots are the simulated particle positions while the green arrows represent the selected directions. The yellow circle is the desired target. The final particle position is 1.8 pixels away from target (1 pixel is equal to 0.95 µm).

Table 5.5: Direction decisions at each step of model Example 3. Directions unit is radian.

Step	REQ_D		Interpolated Directions Matrix (*D*)					Sel_D	*FM*
1	1.5708		1.7475	0.80285	1.7155	4.2311		1.7155	3
2	1.5366		1.5944	0.8126	1.664	4.1578		1.5944	1
3	1.5221		1.514	0.82064	1.6287	4.0502		1.514	1
4	1.5358		1.4387	0.83427	1.5954	3.928		1.5954	3
5	1.4804		1.3684	0.83639	1.5709	4.5302		1.5709	3

Table 5.6: Velocity components and simulation time at each step of model Example 3. Velocity units are in pixel/seconds, positions are in pixels and the time unit is seconds.

Step	U_{int}	V_{int}	$X_{current}$	$Y_{current}$	*dx*	*T*
1	-1.3576	9.7916	200	700	20	2.0232
2	-0.02104	2.2703	197.25	719.81	20	8.8092
3	0.1923	2.5202	197.07	739.81	20	7.9129
4	-0.26564	12.467	198.59	759.75	20	1.6038
5	0.011993	13.192	198.16	779.75	20	1.516
			198.18	799.75		

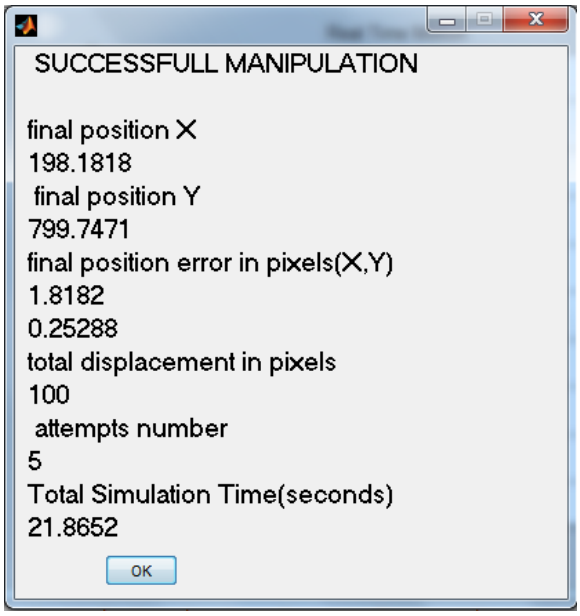

Figure 5.9: The successful manipulation confirmation window for the third model example. The final position error indicates the Cartesian distance from the target to the final particle position. The total indicated simulation time is the accumulated time in the previous table after 5 manipulation steps.

5.3.4 Left Direction Model Example

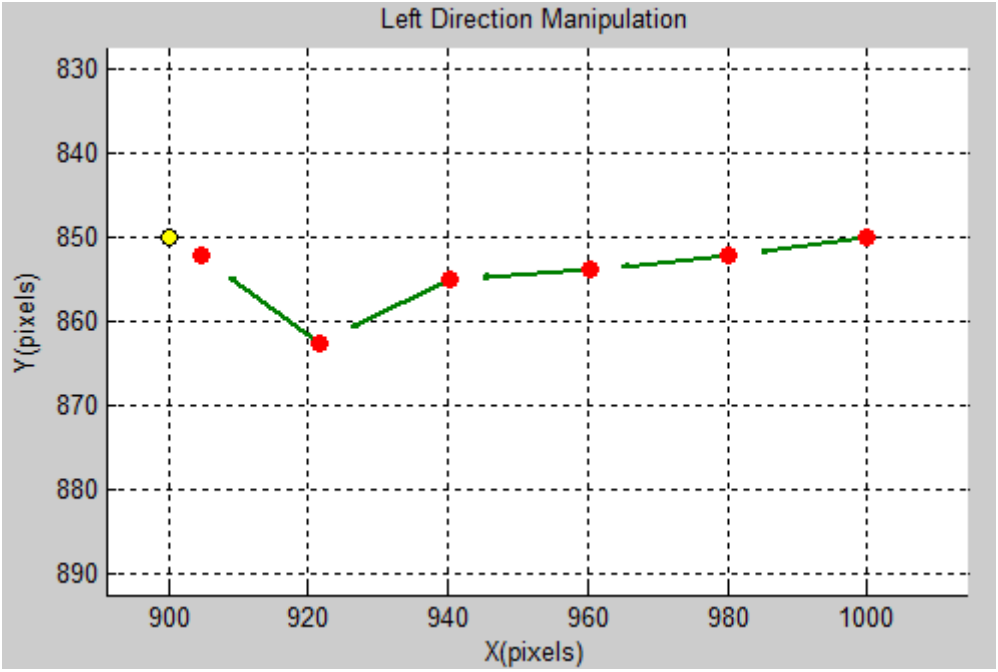

Figure 5.10: Left direction from (1000, 850) to (900, 850). The red dots are the simulated particle positions while the green arrows represent the selected directions. The yellow circle is the desired target. The final particle position is 5.0 pixels away from the target (1 pixel is equal to 0.95 µm).

Table 5.7: Direction decisions at each step of model Example 4. Directions unit is radian.

Step	REQ_D		Interpolated Directions Matrix (*D*)					Sel_D	*FM*
1	3.1416		2.9814	3.0305	2.9153	5.5797		3.0305	2
2	3.1685		2.919	3.0534	2.9955	4.9816		3.0534	2
3	3.2056		2.8553	2.9502	2.9513	4.4357		2.9513	3
4	3.2635		2.7444	1.0224	1.0515	4.1778		2.7444	1
5	3.6649		2.6696	5.5194	5.5747	4.0296		4.0296	4

Table 5.8: Velocity components and simulation time at each step of model Example 4. Velocity units are in pixel/seconds, positions are in pixels while time is in seconds.

Step	U_{int}	V_{int}	$X_{current}$	$Y_{current}$	*dx*	*T*
1	-9.348	1.0139	1000	850	20	2.127
2	-9.8215	0.83808	980.12	852.16	20	2.029
3	-10.261	0.5508	960.19	853.86	20	1.9464
4	-2.9092	1.1956	940.22	854.93	20	6.3587
5	-2.2447	-1.3613	921.72	862.53	20	7.6184
			904.62	852.16		

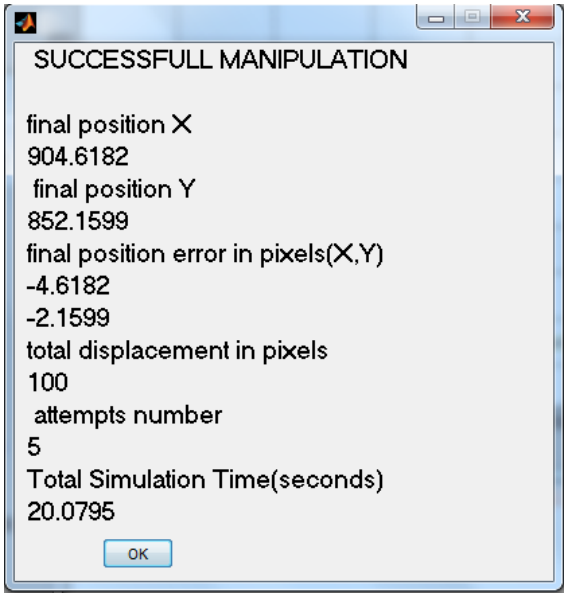

Figure 5.11: The successful manipulation confirmation window for the fourth model example. The final position error indicates the Cartesian distance from the target to the final particle position. The total indicated simulation time is the accumulated time in the previous table after 5 manipulation steps.

The above model examples have demonstrated the feasibility of the first suggested control algorithm for an automatic particle manipulation based on the four available VVFMs. The first objective of this control model is to find the best direction option each time the particle moves to a new location. The second objective is to shift the particle to another position by a fixed step size until it reaches the target location. This will be addressed in the next section where the focus will be on achieving the required step size and direction in real manipulation experiments.

5.4 Model Results Compared with Experiment Results

This section compares experimental manipulation examples to the simulated results. 25 manipulation experiments were performed (5 were successful and 20 were not successful) and three of them are shown here as successful manipulations. Other (only one is shown) experiments deviated from the expected pattern and were recorded as non-successful manipulations due to a number of reasons. It will also be necessity to carry out an investigation into these failed experiments. Section 5.5 is dedicated to discussing the possible causes of this deviation between the model and experiment results.

All of the physical manipulation examples are based on the same method of calculating the desired particle velocity (see Equation 5.4) which is according to the interpolated one used in the VVFMs. An unsuccessful manipulation example is shown in this section in order to help investigate the divergence

between the model and the experiment results. Whilst focussing on the deviating manipulation experiment results this comparison investigation also includes some successful manipulation examples. This is due to the occurrence of a significant error between the expected (selected) and observed (real) directions and magnitudes of the applied frequency modes, especially at the beginning of manipulation run; after which corrections led to the target point being attained at the end.

The demonstration of all examples are in the same sequence. First, a MATLAB output shows both model and experimental trajectories. Then, a series of real images illustrating the dynamic steps of the selected particle from start point to final position. Finally, tables of values and comparisons between the experiment and the model results are shown.

The sequential steps of the experimental manipulation examples start by injecting 10 µm beads into the acoustofluidic device where the levitation frequency only is activated. The valves are shut off and all particles are focused at the nodal plane, this takes approximately 27 seconds. One image is captured and an evaluation is performed as to what are all the possible trajectories (following the velocity vectors in VVFMs) which can be achieved based on the availability of the distributed levitated particle positions. Then, the start and target coordinates are assigned and finally the experimental manipulation code is run.

Despite the highly viscous fluid system which damps the particle lateral movements after switching off the lateral frequency, there is still a small initial velocity from the 3 volt levitation frequency. For this reason there is no time delay between the lateral frequency switching, notwithstanding the time spent for capturing the image and the computational time which is about 5.2 seconds.

The accuracy of landing on the target position has a limitation of around 20 pixels (1 pixel is equal to 0.95 µm). This is approximately twice the bead diameter. The control system algorithm is designed to stop the manipulation once the distance become less than target accuracy limit. After completing the experimental path, the system stores all the raw data in form of displacement, velocity and travel time to be recalled for later analysis and for comparison with the model results.

The next sections present the results from the physical experimental examples. The associated figures and tables are displayed and discussed. The abbreviated variables used in the tables are described in Section 5.3. However, some variables were not presented earlier, these are V_R and $Disp_R$, which are the real velocity and displacement respectively.

5.4.1 First Successful Manipulation

The first manipulation attempt focussed on moving one particle from the start position (766, 661 pixels) to a target position (782, 500 pixels), thus the main trend is in the upwards direction. Figure 5.12 shows the real attempt to move the tracked levitated particle (red trajectory) while the blue trajectory is the modelled one. The maximum deviation between model and experiment at the middle way of the manipulation process is about 90 pixels.

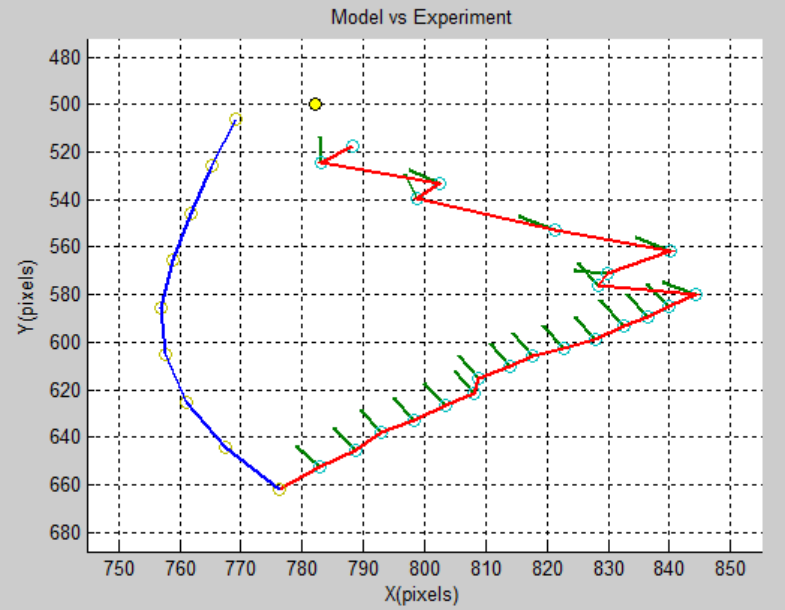

Figure 5.12: Zoomed in view of both the model and experiment results for manipulating the 10 µm particle (1 pixel is equal to 0.95 µm) in the first example. The blue path is the model result while the red path is the experimental result and the green arrows are the selected directions at each step. (The yellow circle is the target point).

From the above figure, the distance between the experiment final position and the target position is greater than the particle diameter and within the accuracy limit. *Figure 5.15* shows the final details of the comparison between the real and model results in terms of precision. By enlarging the view in the manipulation area, *Figure 5.12* shows a significant difference between the selected and the real direction (green arrow and red line respectively). The accumulation of real images is presented in *Figure 5.13* while the travelling steps of the manipulated particle are shown in *Figure 5.14*.

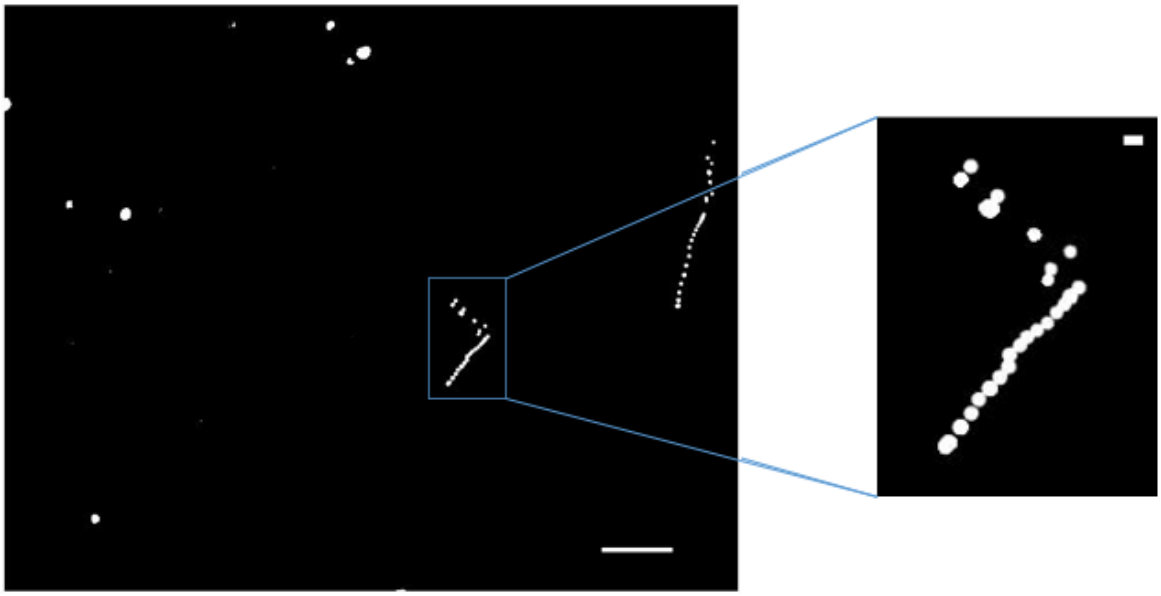

Figure 5.13: (left) Accumulation sequence for 24 images with scale bar of 100 pixels (1 pixel is equal to 0.95 µm). (Right) Zoomed in view of the real experiment accumulated images for manipulating one 10 µm particle. The scale bar at the upper right location is 10 pixels.

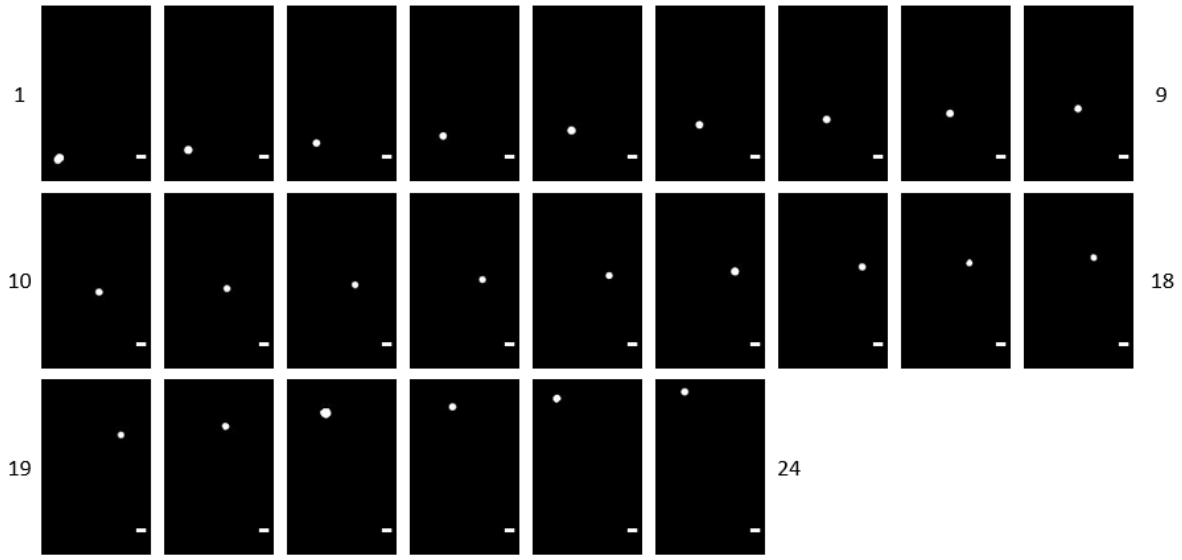

Figure 5.14: Demonstration of 24 steps of the lateral displacement for the 10 µm bead by using the automatic control system. The resultant displacement is 228 pixels (216 µm). The field of view size is 112x180 pixels. Each image has a scale bar at the lower right location which is 10 pixels (9.54 µm).

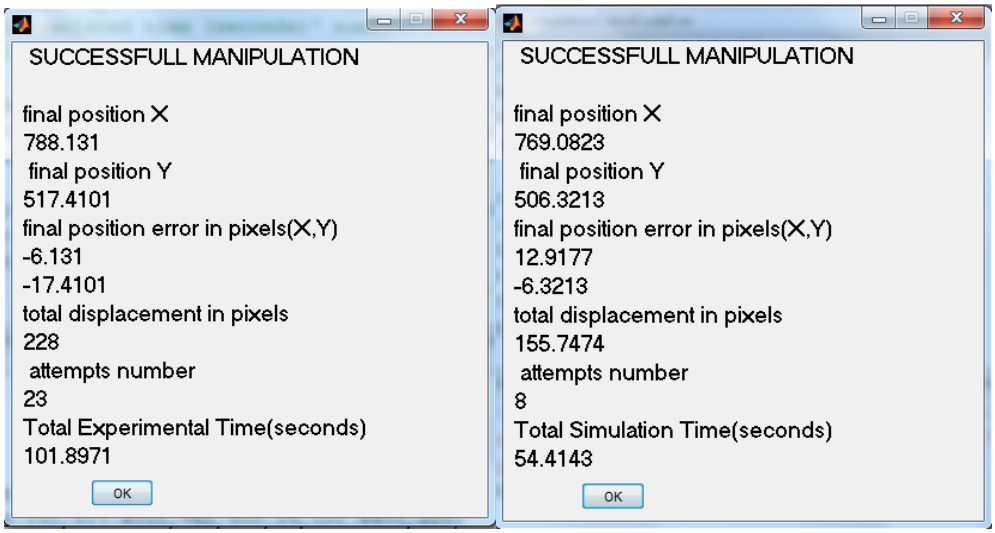

Figure 5.15: Comparison between final details of both the experiment and model results. The left window is the final details for the experiment result while the right window for the model one. The experiment final position is 18.45 pixels away from the target while the model result is 14.38 away. The model achieved the target position in less manipulation time (about 47 seconds difference), it was more accurate (about 73 pixels difference) and also required less manipulation steps (15 steps difference).

Table 5.9: Direction decisions at every step of the experiment manipulation for Example 1. Directions unit is radians.

Step	REQ_D		Interpolated Directions Matrix (*D*)					Sel_D	$Real_D$	*FM*
1	4.7474		4.2414	3.5918	2.499	3.6276		4.2414	5.3299	1
2	4.7063		4.3012	3.5838	2.501	3.6796		4.3012	5.3808	1
3	4.6663		4.3449	3.5777	2.5063	3.5938		4.3449	5.2394	1
4	4.6334		4.3759	3.5658	2.5098	3.5191		4.3759	5.4987	1
5	4.5903		4.3851	3.5452	2.5255	3.5474		4.3851	5.4271	1
6	4.5458		4.3922	3.5249	2.5391	3.5794		4.3922	5.4146	1
7	4.5007		4.3956	3.5062	2.5515	3.6109		4.3956	4.8316	1
8	4.4836		4.4067	3.494	2.5454	3.6486		4.4067	5.5478	1
9	4.4298		4.4017	3.477	2.5614	3.6756		4.4017	5.3849	1
10	4.3885		4.3984	3.4638	2.5702	3.7018		4.3984	5.7124	1
11	4.3349		4.3863	3.4503	2.5879	3.7208		4.3863	5.6274	1
12	4.2758		4.3721	3.4358	2.605	3.7449		4.3721	5.4174	1
13	4.2146		4.3583	3.4208	2.617	3.7786		4.3583	5.489	1
14	4.1632		4.3526	3.4119	2.6205	3.8237		4.3526	5.3827	1
15	4.1148		4.3489	3.404	2.6202	3.8713		4.3489	5.4322	1
16	4.0519		4.3423	3.3946	2.6206	3.9308		3.9308	3.3875	4
17	4.1654		4.3852	3.5378	2.5744	3.8826		4.3852	5.0183	1
18	4.118		4.3684	4.0144	2.5829	3.8923		4.0144	5.5482	2
19	3.9565		4.3123	4.8743	2.6099	3.9496		3.9496	3.5782	4
20	4.0736		4.3987	5.6885	2.5556	3.9339		3.9339	3.681	4
21	4.3116		4.5701	0.61278	2.487	3.9911		4.5701	5.2507	1
22	4.1579		4.5434	1.1955	2.5062	4.0039		4.0039	3.5509	4
23	4.6702		4.7312	1.8972	2.4581	4.0597		4.7312	5.3284	1

Table 5.10: Velocity components and manipulation time at every step of the experiment for Example 1. Velocity units are in pixel/seconds, positions are in pixels while time is in seconds.

Step	U_{int}	V_{int}	X_R	Y_R	X_P	Y_P	V_R	$Disp_R$	V_{mag}	T
1	-1.6	-3.3	776.3	661.9			2.1	11.4	3.7	5.5
2	-1.5	-3.6	782.0	652.6	767.5	643.9	1.8	9.3	3.9	5.1
3	-1.5	-4.0	788.7	645.3	775.1	634.2	1.8	8.4	4.2	4.7
4	-1.5	-4.1	792.9	638.0	781.5	626.6	1.7	7.6	4.4	4.6
5	-1.5	-4.2	798.3	632.7	786.2	619.2	1.7	7.7	4.5	4.5
6	-1.5	-4.3	803.3	626.9	791.6	613.8	1.7	7.3	4.6	4.4
7	-1.5	-4.4	808.1	621.3	796.7	608.0	1.4	6.2	4.6	4.3
8	-1.5	-4.3	808.8	615.1	801.5	602.4	1.6	7.1	4.6	4.4
9	-1.5	-4.4	814.0	610.4	802.4	596.2	1.3	5.7	4.7	4.3
10	-1.5	-4.4	817.6	605.9	807.6	591.4	1.4	6.1	4.7	4.3
11	-1.6	-4.5	822.7	602.6	811.1	587.0	1.6	6.7	4.8	4.2
12	-1.7	-4.6	828.0	598.6	816.0	583.8	1.7	7.1	4.9	4.1
13	-1.7	-4.6	832.6	593.1	821.2	579.8	1.4	5.6	4.9	4.0
14	-1.7	-4.6	836.6	589.1	825.6	574.4	1.3	5.3	4.9	4.1
15	-1.7	-4.6	839.8	585.0	829.5	570.4	1.6	6.6	4.9	4.1
16	-4.6	-4.7	844.2	580.0	832.7	566.3	5.4	16.4	6.6	3.0
17	-1.5	-4.3	828.3	576.1	830.1	565.8	1.2	5.4	4.5	4.4
18	-8.9	-2.1	829.9	570.9	821.7	557.2	6.3	13.8	9.1	2.2
19	-4.1	-4.3	840.2	561.7	810.5	566.3	6.2	20.8	5.9	3.4
20	-3.9	-3.9	821.3	552.9	826.2	547.4	7.3	26.4	5.5	3.6
21	-0.5	-2.9	798.7	539.4	807.1	538.8	1.1	7.4	3.0	6.8
22	-3.2	-3.6	802.5	533.0	795.1	519.7	5.1	21.2	4.8	4.2
23	-0.0	-2.5	783.0	524.6	789.3	518.0	1.1	8.8	2.5	8.0
			788.1	517.4	782.9	504.6				

Table 5.11: Direction decisions at every step of the model for Example 1. Direction unit is radians.

Step	REQ_D		Interpolated Directions Matrix (*D*)					Sel_D	*FM*
1	4.7474		4.2414	3.5918	2.499	3.6275		4.2414	1
2	4.8125		4.4	3.6638	2.3889	3.5268		4.4	1
3	4.878		4.6033	3.8213	2.2647	3.6989		4.6033	1
4	4.9407		4.7551	3.9494	2.1873	3.8447		4.7551	1
5	4.9986		4.8581	4.0022	2.1524	3.9611		4.8581	1
6	5.0531		4.8937	4.8296	2.194	4.0234		4.8937	1
7	5.1287		4.9016	0.010141	2.2755	4.0619		4.9016	1
8	5.2867		4.9123	1.6318	2.3603	4.105		4.9123	1

Table 5.12: Velocity components and simulation time at every step for the model Example 1. Velocity units are in pixel/seconds, positions are in pixels while the time unit is seconds.

Step	U_{int}	V_{int}	$X_{current}$	$Y_{current}$	T
1	-1.6047	-3.2788	776.33	661.9	5.4788
2	-1.1571	-3.4037	767.54	643.94	5.5633

3	-0.57291	-3.153	761.1	625	6.2411
4	-0.09365	-2.9402	757.53	605.32	6.7989
5	0.27072	-2.8173	756.89	585.33	7.0665
6	0.41176	-2.7038	758.8	565.42	7.3128
7	0.44106	-2.5556	761.81	545.65	7.712
8	0.46937	-2.3811	765.21	525.94	8.241
			769.08	506.32	

First 15 steps of the experiment path, the trajectory of the particle drifts significantly away from the desired direction. Table 5.9 and Table 5.10 show that FM1 and FM2 have a maximum direction error of 1.3 rad (74 degrees) between the real and selected direction while FM4 has an error range between 0.3 to 0.5 rad (17 to 28 degrees). In addition to the error associated with the direction, the required displacement magnitude (the desired displacement of 20 pixels) was not achieved by either FM1 or FM2. FM4 has one displacement step equal to desired step size and two slightly higher (2 pixels maximum). From the results presented in the figures and tables, the performance of the control system is acceptable. The correction to shift the micro particle a distance of 216 µm can be made after 221s of completion time in a controlled manner (102 s of the manipulation time and 119 s of the computational time for 23 steps). The expected performance is to be determined later. This will be analysed in the investigation section at the end of this chapter.

5.4.2 Second Successful Manipulation

Another attempt to move one particle from the start position (586, 386 pixels) to a target position (700, 383 pixels) which is to the right direction is presented in this section. Figure 5.16 shows the real attempt to move the tracked particle. The maximum deviation between model and experiment path at the final point was about 40 pixels. This was before the control algorithm made the correction to get the tracked particle close to the target (last manipulation step).

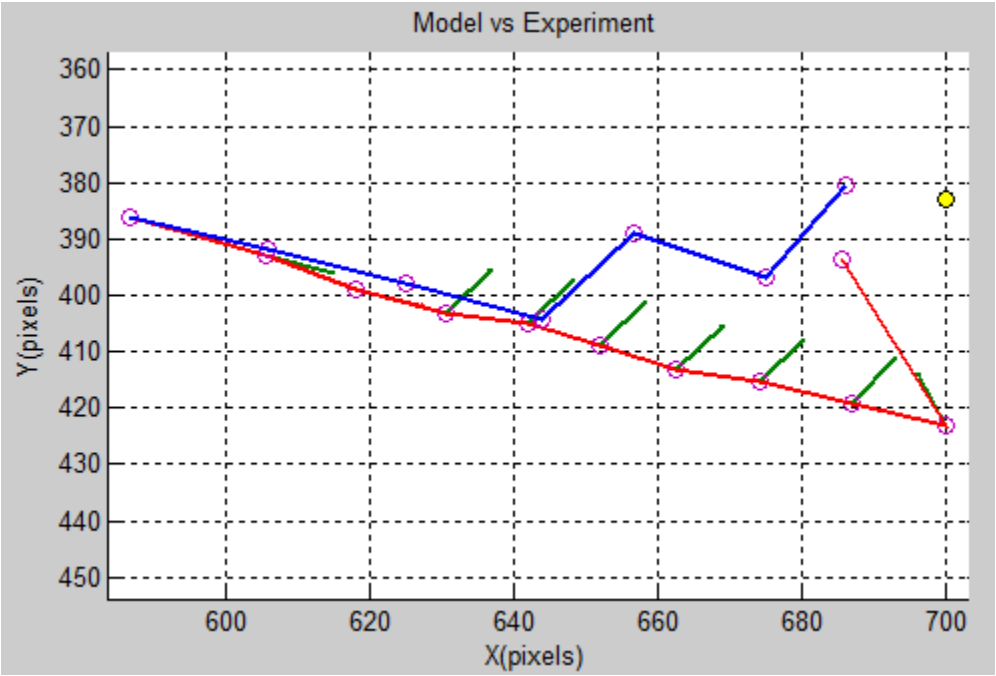

Figure 5.16: Zoomed in view of both the model and experiment results for manipulating the 10 µm particle (1 pixel is equal to 0.95 µm) in the second example. The blue path is the model result while the red path is the experiment result. The green arrows are the selected directions at each step. (The yellow circle is the target point).

The above figure shows that the first and third real steps (red line) have no green vectors. This indicates a small direction error (between selected and real directions) which is in the range of 0.03 to 0.05 rad (1.7 to 2.8 degrees) for the FM2. The second and final steps have a 0.1 rad direction error for FM2 and FM4 respectively (see Table 5.13 and Table 5.14). A critical cross over from FM2 to FM1 occurs due to the 0.01 rad difference at manipulation step 4. Then the rest of the steps are classified as FM1; the significance of this is discussed later (see *Figure 5.29*). A low directional mode quality exists where the maximum direction error is still about 1.3 rad (74 degrees) between the real and selected directions. Regarding the step size (required displacement), FM2 exhibits the optimal displacement compared to the others where 19.9 pixels was achieved at the first step.

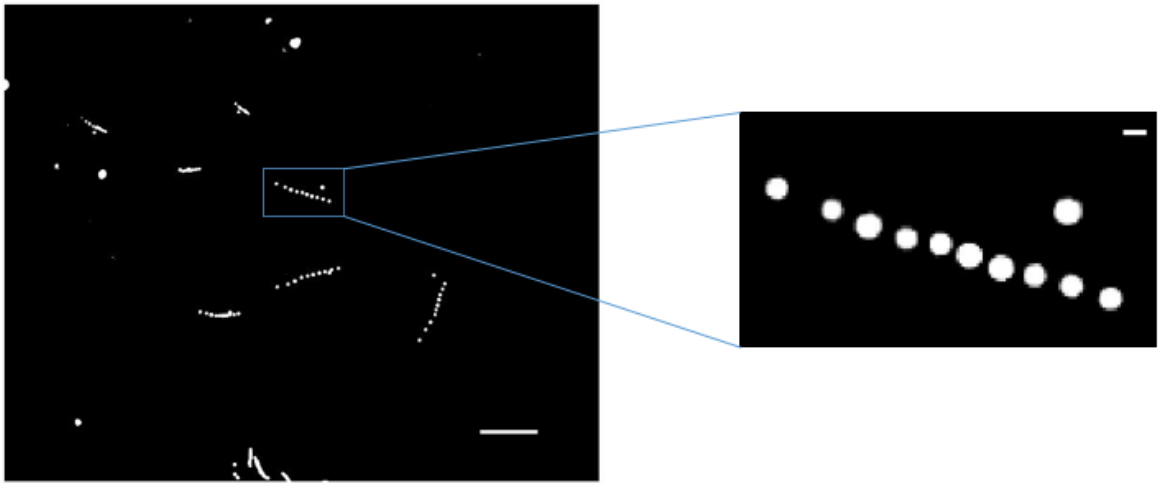

Figure 5.17: (left) accumulation sequence of 11 images with scale bar of 100 pixels (1 pixel is equal to 0.95 µm). (Right) Zoomed in view of the experiment accumulated images for manipulating one 10 µm particle. The scale bar at the upper right location is 10 pixels in length.

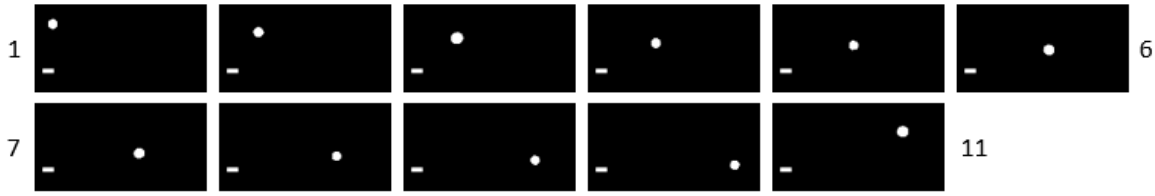

Figure 5.18: Demonstration of 11 steps for the lateral displacement of the 10 µm bead by using the automatic control system. The resultant displacement is 152.3 pixels (144.6 µm). The field of view size is 158 x 78 pixels. Each image has the scale bar at the lower left location which is 10 pixels (9.54 µm) in length.

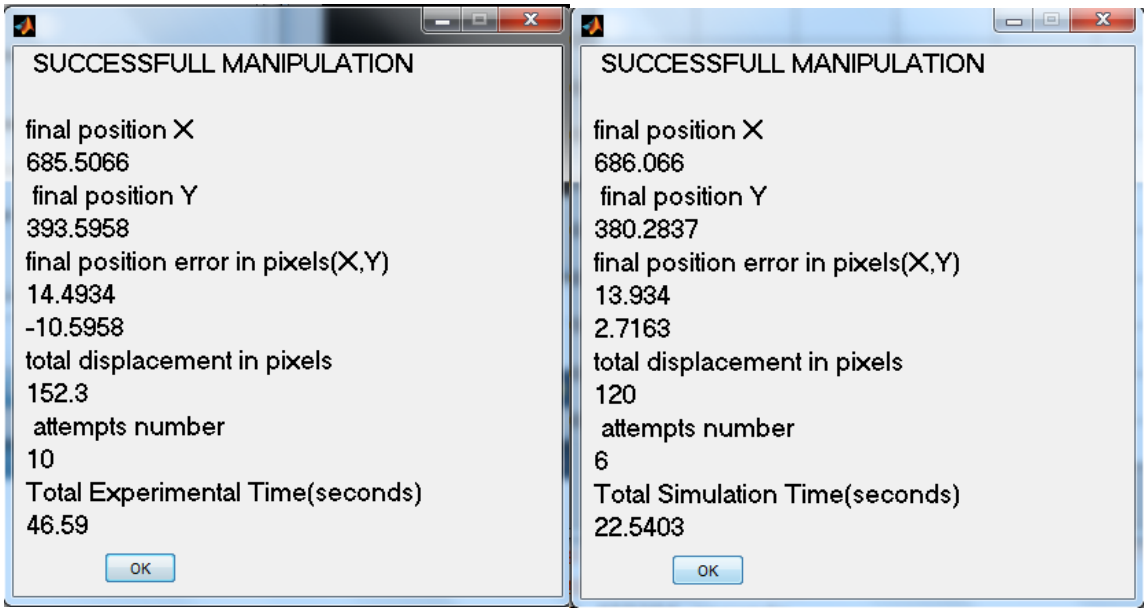

Figure 5.19: Comparison between final information for both experiment and model result. The left window is the final details for the experiment result while the right window presents the model results. The experiment final position is 17.9

pixels away from the target while the difference is 14.5 pixels for the model. The model achieved the manipulation in less time (about 24 seconds difference), with a lower displacement discrepancy (about 32 pixels difference) and less manipulation steps (about 4 steps difference).

Table 5.13: Direction decisions at every step of the experiment Example 2. Directions unit is radian.

Step	REQ_D		Interpolated Directions Matrix (*D*)					Sel_D	$Real_D$	*FM*
1	6.2563		5.4196	0.30199	0.33055	4.2932		0.30199	0.35319	2
2	6.1785		5.4091	0.31016	0.36112	4.3252		0.31016	0.43514	2
3	6.0935		5.4119	0.3119	0.38306	4.3481		0.3119	0.33159	2
4	6.0028		5.4139	0.31647	0.4095	4.3678		5.4139	0.15129	1
5	5.9234		5.4084	0.32805	0.45206	4.3807		5.4084	0.3779	1
6	5.7909		5.4013	0.37405	0.75498	4.3716		5.4013	0.38777	1
7	5.6052		5.3952	0.42082	1.074	4.3621		5.3952	0.20024	1
8	5.3863		5.3781	0.47656	1.4185	4.348		5.3781	0.27019	1
9	5.0595		5.3643	0.53421	1.7985	4.3338		5.3643	0.30636	1
10	4.7148		5.3541	0.58786	2.1728	4.3206		4.3206	4.2587	4

Table 5.14: Velocity components and manipulation time at every step of the experiment Example 2. Velocity units are in pixel/seconds, positions units are in pixels while time unit is in seconds.

Step	U_{int}	V_{int}	X_R	Y_R	X_P	Y_P	V_R	$Disp_R$	V_{mag}	T
1	8.86	2.73	586.72	386.05			9.24	19.92	9.27	2.15
2	8.06	2.53	605.41	392.94	605.83	391.94	5.83	13.80	8.44	2.36
3	7.53	2.38	617.93	398.76	624.49	398.92	5.20	13.17	7.90	2.53
4	2.36	-2.77	630.39	403.05	637	404.78	2.14	11.74	3.64	5.48
5	2.31	-2.75	642	404.82	643.34	387.81	1.92	10.70	3.59	5.56
6	2.22	-2.64	651.95	408.77	654.87	389.51	1.98	11.50	3.45	5.78
7	2.12	-2.54	662.6	413.12	664.81	393.46	1.94	11.71	3.31	6.03
8	1.99	-2.45	674.08	415.45	675.44	397.79	2.11	13.37	3.16	6.32
9	1.85	-2.35	686.97	419.02	686.7	399.94	2.03	13.56	2.99	6.67
10	-2.06	-5.03	699.9	423.11	699.37	403.33	8.93	32.83	5.44	3.67
11			685.51	393.6	692.3	404.61				

Table 5.15: Direction decisions at every step of the model Example 2. Directions unit is radian.

Step	REQ_D		Interpolated Directions Matrix (*D*)					Sel_D	*FM*
1	6.2563		5.4196	0.302	0.33056	4.2932		0.302	2
2	6.1885		5.4052	0.31299	0.36368	4.3238		0.31299	2
3	6.0863		5.4	0.32224	0.40125	4.3537		0.32224	2
4	5.9215		5.4008	0.34048	0.51158	4.3767		5.4008	1
5	6.1494		5.2952	0.4582	0.93312	4.3307		0.4582	2
6	5.7757		5.2849	0.54298	1.4946	4.3152		5.2849	1

Table 5.16: Velocity components and simulation time at every step of the model Example 2. Velocity units are in pixel/seconds, position units are in pixels while time units are in seconds.

Step	U_{int}	V_{int}	$X_{current}$	$Y_{current}$	T
1	8.8667	2.7333	586.72	386.05	2.1555
2	8.0406	2.548	605.83	391.94	2.3712
3	7.2345	2.3749	624.9	397.98	2.6266
4	2.278	-2.7445	643.9	404.22	5.6074
5	5.5239	2.4426	656.67	388.83	3.3114
6	1.7162	-2.572	674.97	396.92	6.4682
			686.07	380.28	

After 10 steps, the proposed control system has steered the particle along a path length of 152.3 pixels (144.6 µm). This located the particle close to the target within an accuracy of 18 pixels. A robust correction was made after 98.5 s of simulation time (46.5 s of the manipulation time and 52 s of the computational time for 10 steps). From Table 5.13 and Table 5.14, FM4 has significantly better performance compared to FM1. Additionally, despite the weak response of FM2 in the previous attempt, it is shown to have matched the trajectory to the predicted direction. This give confidence in the reliability of experimental approach in this dedicated manipulation area.

5.4.3 Third Successful Manipulation

The third successful manipulation has been performed for a tracked particle movement from a start position (521, 300 pixels) to a final position (700, 300 pixels). The main trend of movement is again in the right direction. This example is different from the previous experiment manipulation examples as a result of the tracked particle being close to other nearby levitated particles. The accumulated images from the experiment are shown in *Figure 5.21*. *Figure 5.22* shows the 48 sequential images of the tracked particle from the initial position to the final position which is close to the target. These images give an indication of the lack of influence from secondary forces (the lateral force is the only one applied) from the other particles in each sequence image (the distance between these nearby particles and the tracked particle is always greater than 50 pixels). *Figure 5.20* shows the experimental attempt to move the tracked particle towards the assigned target. About 62 pixels is the maximum deviation between model and experiment measured at manipulation step 39 (see the black arrow). This is before the control algorithm made the correction to shift the tracked particle nearer to the target.

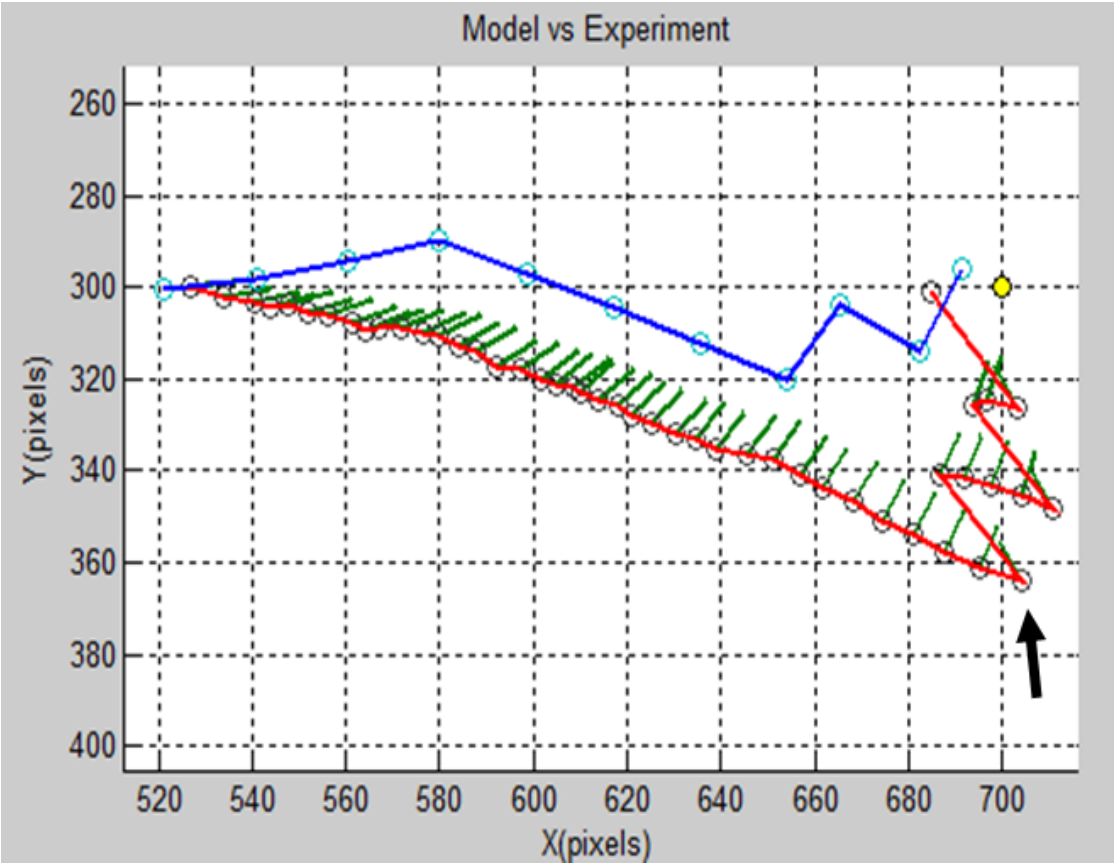

Figure 5.20: Zoomed in view of both the model and the experiment results for manipulating 10 µm particle (1 pixel is equal to 0.95 µm) in the third example. The blue path is the model result while the red path is the experimental result. The green arrows are the selected directions at each step. (The yellow circle is the target point).

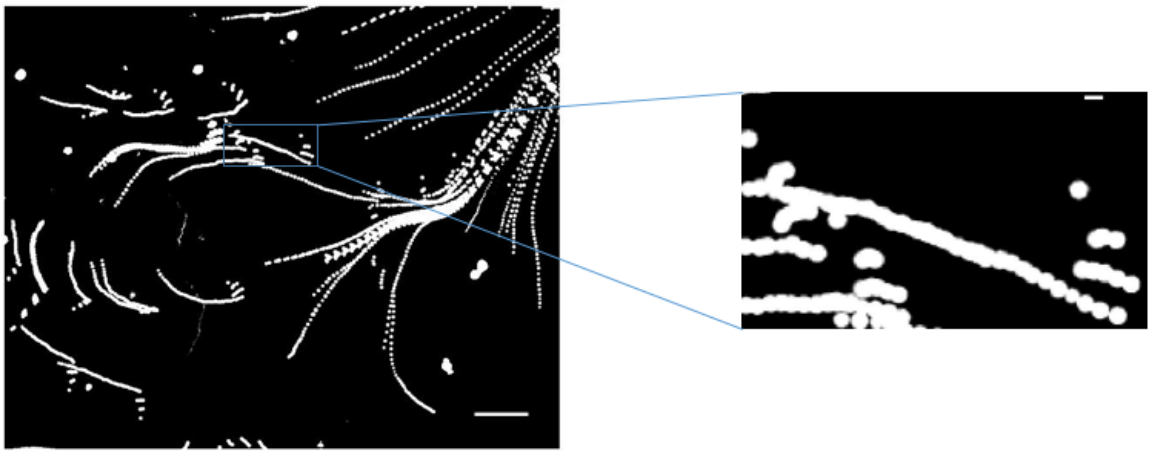

Figure 5.21: (left) Accumulation 48 sequential images with the scale bar of 100 pixels (1 pixel is equal to 0.95 µm). (Right) zoomed in view of the experimentally obtained accumulated images for manipulating one 10 µm particle. There are other interference patterns from three other moving particles in the lower left part of the image. These can be tracked in the next image sequence to verify the distances between these particles and the tracked one. The scale bar at the upper right location is 10 pixels in length.

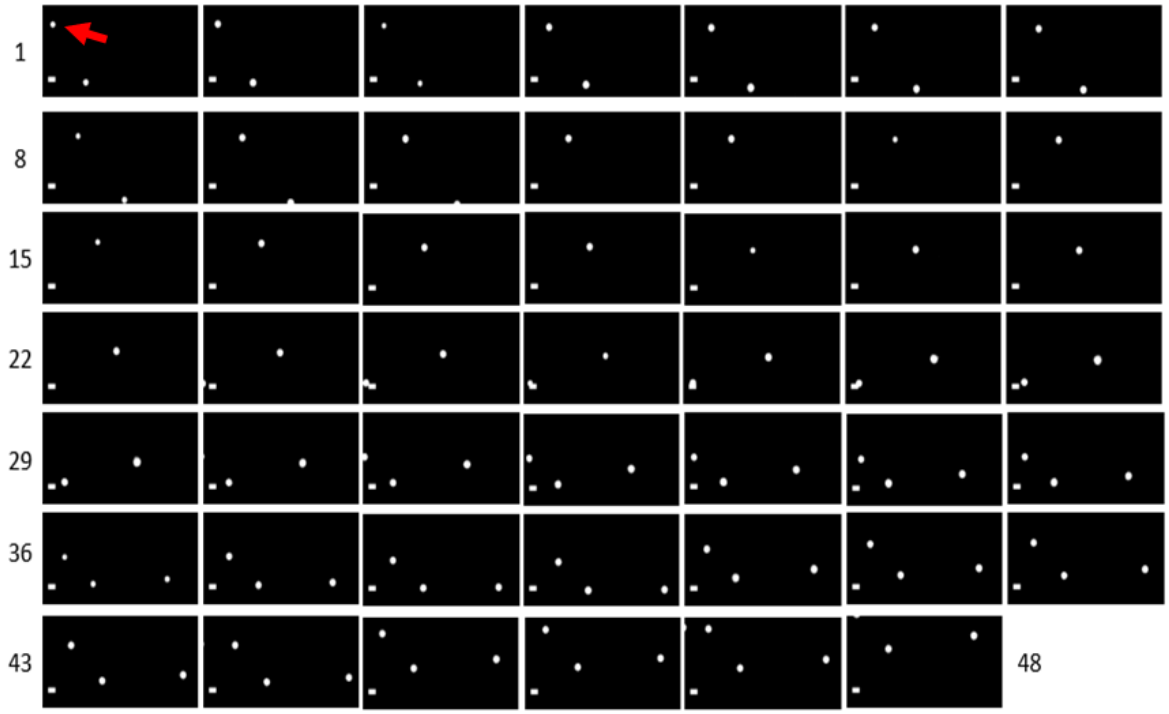

Figure 5.22: Demonstration of 48 steps for the lateral displacement of the 10 µm bead (the particle in the upper left of the images is the tracked one, highlighted with the red arrow) by using an automatic control system. The resultant displacement is 321 pixels (304.95 µm). The field of view size is 218 x 104 pixels. Each image has a scale bar at the lower left location which is 10 pixels (9.54 µm) long. There is no effect from the secondary forces from the nearby particles as the distance between them and the tracked particle is always greater than 50 pixels.

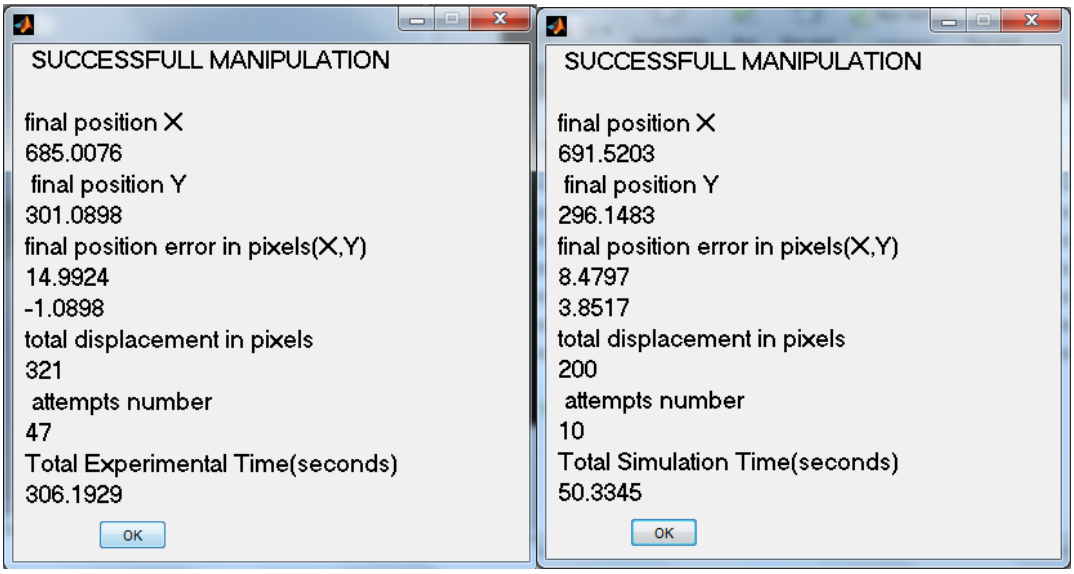

Figure 5.23: Comparison between final information for both the experiment and the model result. The left window is the final details for the experiment result while the right window represents the the model result. The experiment final position is 15 pixels away from the target while the model result is 9.3 pixels from the target. The model achieved the manipulation in less time (about 256 seconds difference), with a closer displacement (about 121 pixels difference) and fewer manipulation steps (37 steps difference).

Table 5.17: Direction decisions at every step of the experiment for Example 3. Direction unit is radians.

Step	REQ_D		Interpolated Directions Matrix (*D*)					Sel_D	$Real_D$	*FM*
1	6.28		6.15	0.44	0.41	4.08		6.15	6.19	1
2	6.28		6.13	0.44	0.40	4.10		6.13	0.28	1
3	6.27		6.08	0.43	0.40	4.11		6.08	0.21	1
4	6.26		6.04	0.43	0.40	4.13		6.04	0.22	1
5	6.26		6.02	0.43	0.39	4.14		6.02	6.14	1
6	6.26		6.01	0.43	0.39	4.15		6.01	0.37	1
7	6.25		5.97	0.42	0.39	4.16		5.97	0.14	1
8	6.24		5.95	0.42	0.39	4.17		5.95	0.33	1
9	6.23		5.91	0.42	0.39	4.18		5.91	0.41	1
10	6.22		5.89	0.42	0.38	4.19		5.89	6.22	1
11	6.22		5.88	0.41	0.38	4.20		5.88	0.04	1
12	6.21		5.86	0.41	0.38	4.21		5.86	0.15	1
13	6.20		5.83	0.41	0.38	4.22		5.83	0.16	1
14	6.20		5.81	0.41	0.38	4.23		5.81	0.54	1
15	6.17		5.77	0.41	0.38	4.23		5.77	0.32	1
16	6.16		5.73	0.42	0.38	4.23		5.73	0.60	1
17	6.13		5.68	0.42	0.39	4.23		5.68	0.20	1
18	6.11		5.65	0.42	0.39	4.24		5.65	0.42	1
19	6.08		5.61	0.43	0.39	4.24		5.61	0.32	1
20	6.06		5.58	0.43	0.40	4.24		5.58	0.26	1
21	6.05		5.55	0.43	0.40	4.25		5.55	0.46	1
22	6.04		5.54	0.43	0.40	4.25		5.54	0.43	1
23	6.01		5.52	0.43	0.40	4.25		5.52	0.30	1
24	5.98		5.49	0.44	0.41	4.26		5.49	0.59	1
25	5.94		5.47	0.44	0.41	4.27		5.47	0.39	1
26	5.91		5.45	0.44	0.41	4.27		5.45	0.43	1
27	5.85		5.42	0.44	0.42	4.28		5.42	0.23	1
28	5.82		5.40	0.44	0.42	4.29		5.40	0.45	1
29	5.76		5.38	0.44	0.43	4.30		5.38	0.15	1
30	5.70		5.34	0.47	0.52	4.29		5.34	0.23	1
31	5.63		5.31	0.50	0.64	4.29		5.31	0.54	1
32	5.52		5.28	0.53	0.78	4.28		5.28	0.56	1
33	5.43		5.25	0.55	0.89	4.28		5.25	0.41	1
34	5.31		5.22	0.59	1.07	4.27		5.22	0.61	1
35	5.18		5.19	0.62	1.25	4.27		5.19	0.43	1
36	5.05		5.16	0.66	1.44	4.26		5.16	0.56	1
37	4.92		5.14	0.69	1.64	4.25		5.14	0.43	1
38	4.79		5.12	0.73	1.88	4.24		5.12	0.31	1

39	4.65		5.09	0.78	2.16	4.23		4.23	4.06	4
40	5.03		5.11	0.70	1.44	4.24		5.11	0.07	1
41	4.91		5.09	0.73	1.56	4.23		5.09	0.26	1
42	4.76		5.06	0.76	1.72	4.22		5.06	0.35	1
43	4.62		5.03	0.80	1.89	4.22		5.03	0.41	1
44	4.49		4.99	0.94	1.75	4.20		4.20	4.06	4
45	4.96		5.04	0.76	1.42	4.21		5.04	5.91	1
46	4.85		5.02	0.78	1.46	4.21		5.02	0.23	1
47	4.59		4.98	0.81	1.61	4.20		4.20	4.08	4

Table 5.18: Velocity components and manipulation time at each step of the experiment for Example 3. Velocity units are in pixel/seconds, The positions are in pixels while the time unit is seconds.

Step	U_{int}	V_{int}	X_R	Y_R	X_P	Y_P	V_R	$Disp_R$	V_{mag}	T
1	2.7	-0.3	521.1	300.6			0.8	5.7	2.7	7.4
2	2.7	-0.4	526.7	300.1	540.9	298.1	1.0	7.5	2.8	7.2
3	2.8	-0.6	533.9	302.1	546.5	297.1	1.0	6.8	2.8	7.1
4	2.8	-0.7	540.5	303.5	553.5	298.2	0.5	3.4	2.9	6.9
5	2.8	-0.7	543.8	304.2	559.9	298.7	0.6	3.9	2.9	6.8
6	2.9	-0.8	547.6	303.7	563.1	299.1	0.7	4.7	3.0	6.7
7	2.9	-0.9	552.0	305.4	566.9	298.3	0.6	4.2	3.0	6.6
8	2.9	-1.0	556.1	306.0	571.1	299.4	0.8	5.5	3.1	6.6
9	2.9	-1.1	561.3	307.8	575.1	299.6	0.5	3.4	3.1	6.5
10	2.9	-1.2	564.4	309.1	580.0	300.7	0.5	2.9	3.1	6.4
11	2.9	-1.2	567.2	308.9	582.9	301.6	0.7	4.4	3.2	6.3
12	2.9	-1.3	571.6	309.1	585.7	301.2	0.8	4.8	3.2	6.2
13	3.0	-1.4	576.4	309.8	589.9	301.1	0.6	3.7	3.3	6.1
14	2.9	-1.4	580.0	310.4	594.5	301.4	0.7	4.5	3.3	6.1
15	2.8	-1.6	583.8	312.7	597.9	301.6	0.7	4.2	3.2	6.2
16	2.8	-1.6	587.8	314.0	601.4	303.1	0.9	5.3	3.2	6.2
17	2.6	-1.8	592.2	317.0	605.0	303.7	0.8	5.3	3.2	6.3
18	2.6	-1.9	597.4	318.0	608.8	305.8	0.7	4.7	3.2	6.3
19	2.5	-2.0	601.6	319.9	613.5	306.2	0.6	3.6	3.2	6.3
20	2.4	-2.0	605.1	321.1	617.2	307.4	0.6	3.7	3.2	6.3
21	2.4	-2.1	608.7	322.0	620.3	308.1	0.2	1.4	3.2	6.3
22	2.3	-2.1	609.9	322.6	623.5	308.7	0.7	4.5	3.2	6.3
23	2.3	-2.2	614.0	324.5	624.7	309.2	0.7	4.2	3.2	6.3
24	2.2	-2.3	618.0	325.8	628.4	310.6	0.6	3.8	3.2	6.3
25	2.2	-2.3	621.2	327.9	632.1	311.6	0.7	4.3	3.2	6.2
26	2.2	-2.4	625.2	329.6	634.9	313.4	1.0	5.9	3.2	6.2
27	2.1	-2.5	630.5	332.0	638.6	314.7	0.7	4.1	3.3	6.2
28	2.1	-2.5	634.5	332.9	643.5	316.8	0.8	5.0	3.3	6.1
29	2.0	-2.6	639.0	335.1	647.2	317.4	1.1	6.8	3.3	6.1
30	1.9	-2.6	645.8	336.1	651.3	319.3	0.9	5.7	3.2	6.2
31	1.8	-2.6	651.3	337.4	657.6	320.0	1.0	6.6	3.2	6.3
32	1.7	-2.6	657.0	340.8	662.7	321.0	0.8	5.3	3.1	6.5
33	1.6	-2.6	661.5	343.7	668.0	324.1	1.1	7.5	3.0	6.6
34	1.5	-2.6	668.5	346.6	672.2	326.7	1.1	7.4	3.0	6.8

35	1.4	-2.5	674.5	350.8	678.5	329.4	1.1	7.3	2.9	6.9
36	1.3	-2.5	681.2	353.9	684.2	333.3	1.1	7.6	2.8	7.1
37	1.2	-2.5	687.6	357.9	690.3	336.1	1.1	8.2	2.8	7.3
38	1.1	-2.4	695.1	361.3	696.3	339.9	1.3	9.4	2.7	7.5
39	-2.4	-4.6	704.1	364.1	703.2	343.0	7.5	29.0	5.2	3.9
40	1.1	-2.5	686.6	341.0	694.8	346.4	0.7	5.3	2.7	7.4
41	1.0	-2.4	691.9	341.4	694.8	322.8	0.8	6.1	2.6	7.6
42	0.9	-2.4	697.8	343.0	699.6	323.0	0.8	6.6	2.6	7.8
43	0.8	-2.4	704.0	345.2	704.8	324.2	1.0	7.6	2.5	8.0
44	-2.5	-4.5	711.0	348.3	710.4	326.3	7.3	28.4	5.2	3.9
45	0.9	-2.4	693.6	325.7	701.1	330.9	0.4	3.2	2.6	7.8
46	0.8	-2.4	696.5	324.6	700.4	306.9	0.9	6.9	2.5	7.9
47	-2.4	-4.2	703.3	326.2	702.9	305.6	7.6	31.0	4.9	4.1
48			685.0	301.1	693.5	308.7				

Table 5.19: Direction decision at each step of the model for Example 3. The directions unit is radians.

Step	REQ_D		Interpolated Directions Matrix (*D*)					Sel_D	FM
1	6.28		6.15	0.44	0.41	4.08		6.15	1
2	0.01		6.08	0.44	0.39	4.14		6.08	1
3	0.04		6.03	0.43	0.38	4.20		6.03	1
4	0.09		5.99	0.43	0.37	4.26		0.37	3
5	0.03		5.82	0.44	0.39	4.27		0.39	3
6	6.23		5.66	0.45	0.40	4.29		0.40	3
7	6.10		5.49	0.46	0.42	4.30		0.42	3
8	5.87		5.30	0.54	0.64	4.27		5.30	1
9	6.17		5.34	0.59	0.76	4.28		0.59	2
10	5.60		5.14	0.69	1.10	4.24		5.14	1

Table 5.20: Velocity components and simulation time at every step of the model for Example 3. Velocity units are in pixel/seconds, the positions are in pixels while the time units are seconds.

Step	U_{int}	V_{int}	$X_{current}$	$Y_{current}$	T
1	2.69	-0.33	521.06	300.59	7.38
2	2.89	-0.56	540.91	298.12	6.79
3	3.14	-0.74	560.54	294.33	6.20
4	7.52	2.94	580.01	289.73	2.48
5	6.64	2.67	598.63	297.01	2.80
6	5.72	2.38	617.19	304.48	3.23
7	4.75	2.08	635.65	312.18	3.86
8	1.73	-2.47	653.97	320.19	6.62
9	5.15	3.08	665.44	303.80	3.33
10	1.17	-2.34	682.61	314.05	7.65
			691.52	296.15	

From the above tables (Table 5.17 and Table 5.18) and the final manipulation information in *Figure 5.23*, it is show that after 39 manipulation steps the correction was made using another frequency mode with less to give a lower error. This demonstrates model robustness to shift the particle back to the final position nearby by the target. More confirmation of the strong response of the frequency mode FM4 is demonstrated as its performance is recorded in the previous examples. Even after 545 seconds (306 seconds for the manipulation time), FM4 is still able to show an efficient response compared to the anticipated ones (measured lateral forces). FM2 and FM3 were only selected during the model manipulation (Table 5.19 and Table 5.20), therefore, they are not evaluated in this experiment example. The minimum direction error recorded for FM4 at manipulation step 47 is 0.11 rad (6.33 degrees) with over a shoot step size (31 pixels). With regards to FM1, the first manipulation step is 0.04 rad (2.29°) with a low step size (5.7 pixels). However, FM1 has the maximum direction error in this example which is 1.6 rad (91.6°). This creates less confidence for frequency mode FM1 to be included in future studies due to its lateral force unreliability.

5.4.4 Unsuccessful Manipulation

As mentioned earlier, not all of the manipulations were successful due to reasons which are discussed at the end of this chapter. One of these unsuccessful attempts is demonstrated below. The attempt was an effort to move one particle from the starting position (523, 576 pixels) to a target position (666, 615 pixels). Figure 5.24 shows that the experiment particle deviated its trajectory from the model path. As the proposed control algorithm does not have a real assessment of unstable operation conditions (the control system repeats the same procedure for every manipulation step regardless the remaining distance to the target), the manipulation process was terminated by the user based on prior knowledge. This knowledge suggested that the following trend will be surged upwards and away from the target and never came back again to the regular mode of operation. This was especially the case when there was a chance for the tracked particle to disappear out of the field of view.

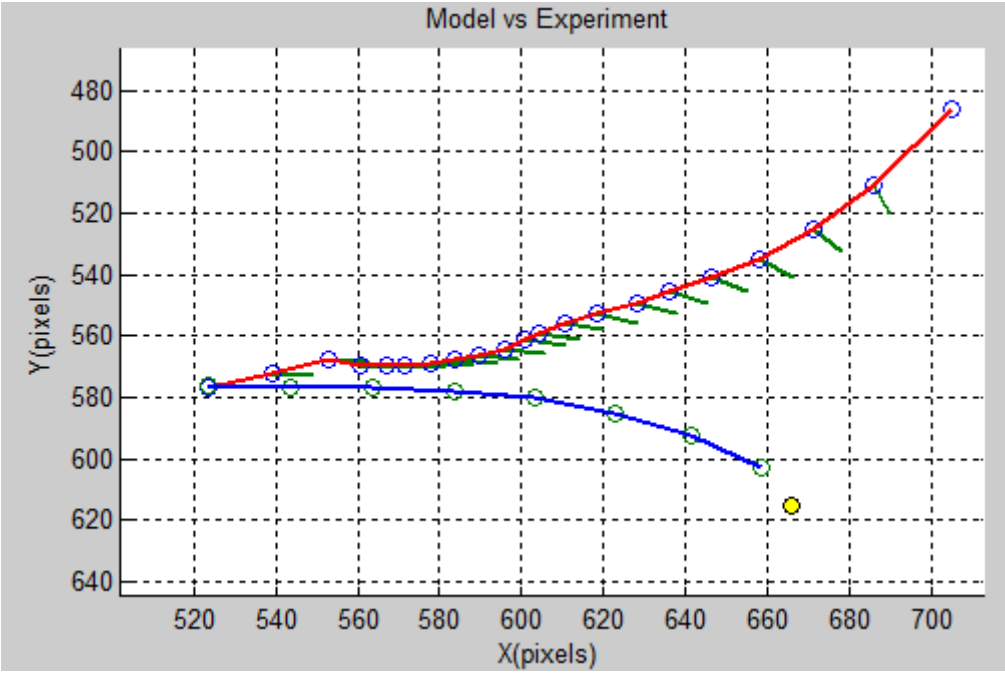

Figure 5.24: Zoomed in view of both the model and the experiment results for manipulating the 10 µm particle (1 pixel is equal to 0.95 µm) in the fourth example. The blue path is the model result while the red path is the experiment result and the green arrows are the selected directions at each step. (The yellow circle is the target point).

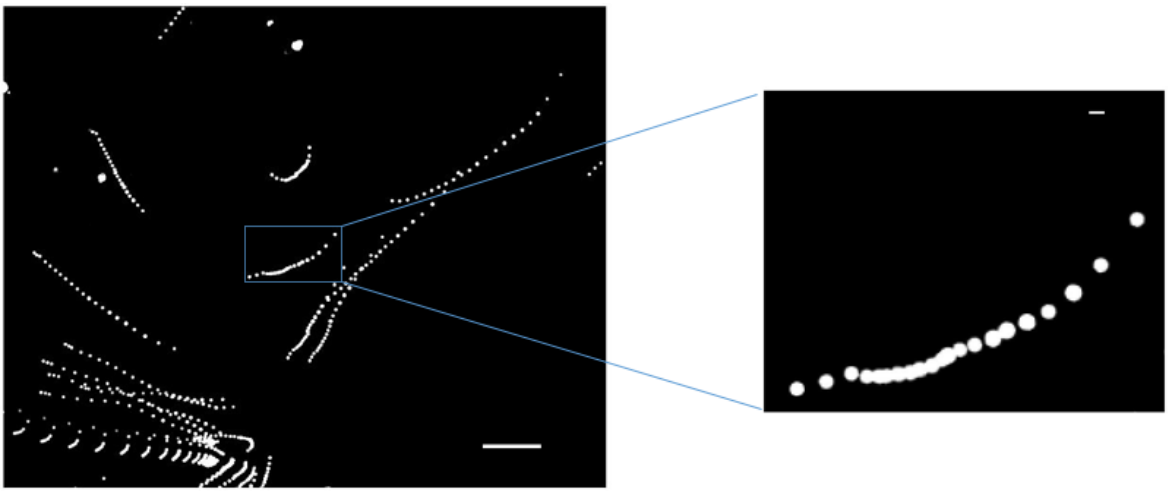

Figure 5.25: (left) Accumulation sequence of 21 images with a scale bar of 100 pixels (1 pixel is equal to 0.95 µm) in length. (Right) Zoomed in view of the experimentally accumulated images for manipulating one 10 µm particle. The scale bar at the upper right location is 10 pixels in length.

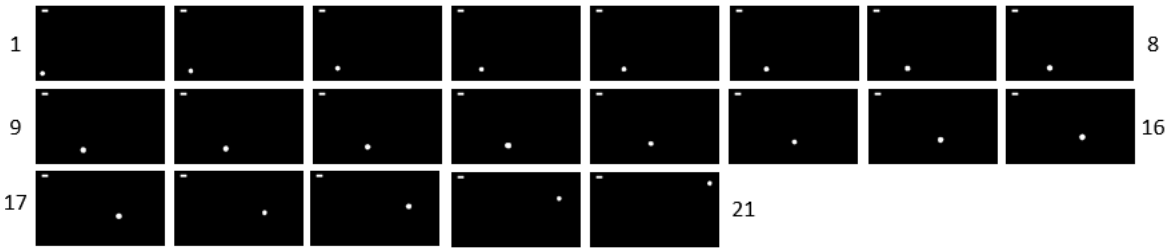

Figure 5.26: The demonstration of 21 steps of lateral displacement for the 10 µm bead by using the automatic control system. The resultant displacement is 211 pixels before the manipulation process terminated. The field of view is 218 x 104 pixels. Each image has a scale bar at the upper left location which is 10 pixels (9.54 µm) in length.

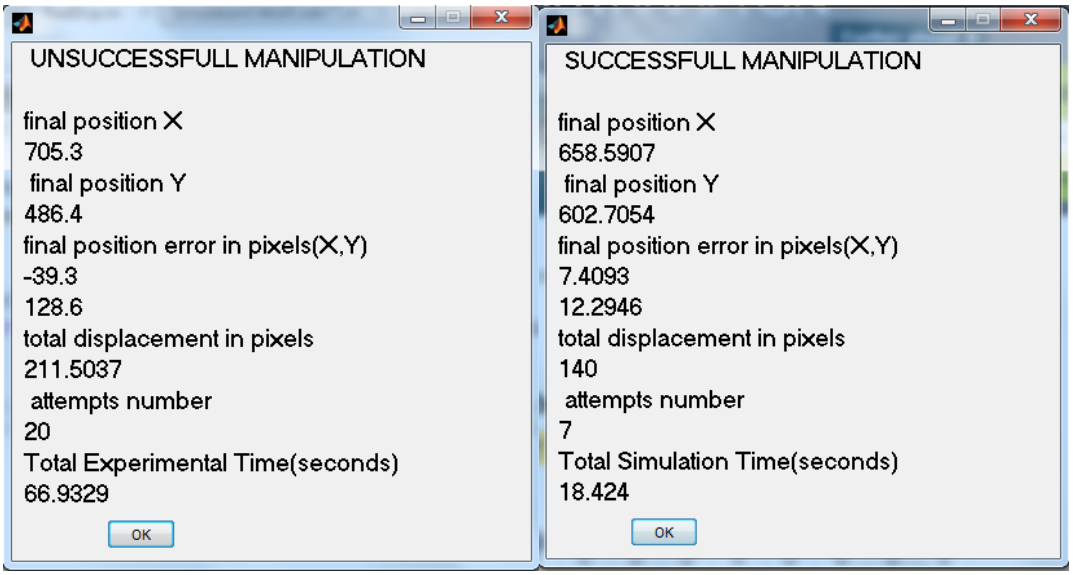

Figure 5.27: Comparison between the final information for both the experiment and model result. The left window is the final details for the experiment result while the right window shows the results for the model. The experiment final position is 134.4 pixels away from the target while the model is 14.1 pixels from the target. After 66 seconds manipulation time and 20 manipulation steps, the manipulation process was terminated by the user.

Table 5. 21: Direction decisions at each step of the experiment for Example 4. Directions unit is in radians.

Step	REQ_D		Interpolated Directions Matrix (*D*)					Sel_D	$Real_D$	*FM*
1	0.26		6.06	0.01	6.21	4.55		0.01	6.03	2
2	0.32		6.03	0.01	6.26	4.61		0.01	5.96	2
3	0.39		6.01	0.00	0.01	4.65		0.01	0.22	3
4	0.41		6.01	6.28	0.04	4.69		0.04	0.00	3
5	0.43		6.00	6.27	0.05	4.71		0.05	6.26	3
6	0.45		6.00	6.27	0.06	4.73		0.06	6.13	3
7	0.48		5.99	6.27	0.08	4.75		0.08	6.10	3
8	0.52		6.00	6.27	0.12	4.76		0.12	6.04	3
9	0.57		6.00	6.28	0.15	4.77		0.15	5.96	3
10	0.63		6.00	6.28	0.18	4.78		0.18	5.74	3

11	0.69		5.99	0.00	0.20	4.78		0.20	5.69	3
12	0.74		5.99	0.01	0.22	4.77		0.22	5.82	3
13	0.82		5.99	0.01	0.25	4.77		0.25	5.95	3
14	0.92		5.99	0.02	0.29	4.78		0.29	5.96	3
15	1.05		5.99	0.03	0.34	4.79		0.34	5.78	3
16	1.16		5.98	0.04	0.37	4.78		0.37	5.89	3
17	1.31		5.96	0.05	0.48	4.75		0.48	5.82	3
18	1.47		5.90	0.08	0.69	4.67		0.69	5.63	3
19	1.63		5.84	0.13	0.93	4.59		0.93	5.51	3
20	1.76		5.76	0.22	1.25	4.52		1.25	5.38	3

Table 5.22: Velocity components and manipulation time at each step of the experiment for Example 4. Velocity units are in pixel/seconds, the positions are in pixels while the time unit is in seconds.

Step	U_{int}	V_{int}	X_R	Y_R	X_P	Y_P	V_R	$Disp_R$	V_{mag}	T
1	8.7	0.1	523.6	576.5			6.96	15.9	8.7	2.3
2	8.8	0.1	539.0	572.6	543.6	576.8	6.37	14.5	8.8	2.3
3	6.7	0.2	552.8	568.0	559.0	572.7	2.73	8.1	6.7	3.0
4	6.9	0.3	560.7	569.8	572.8	568.5	2.28	6.6	6.9	2.9
5	7.1	0.4	567.3	569.8	580.7	570.7	1.45	4.1	7.1	2.8
6	7.2	0.5	571.4	569.7	587.2	571.0	2.45	6.8	7.2	2.8
7	7.3	0.6	578.1	568.7	591.3	571.1	2.18	6.0	7.3	2.7
8	7.2	0.8	583.9	567.6	598.0	570.4	2.02	5.6	7.2	2.8
9	7.0	1.0	589.4	566.3	603.8	569.8	2.36	6.7	7.1	2.8
10	6.8	1.2	595.7	564.2	609.2	569.1	2.02	5.8	6.9	2.9
11	6.6	1.3	600.7	561.2	615.4	567.6	1.34	4.0	6.7	3.0
12	6.5	1.4	604.0	558.9	620.4	565.0	2.36	7.1	6.6	3.0
13	6.2	1.5	610.4	555.7	623.6	563.1	2.81	8.8	6.4	3.1
14	6.0	1.7	618.7	552.8	629.8	560.5	3.20	10.3	6.2	3.2
15	5.6	2.0	628.5	549.6	637.9	558.5	2.55	8.5	6.0	3.4
16	5.3	2.1	636.0	545.5	647.3	556.3	3.24	11.3	5.7	3.5
17	4.7	2.3	646.4	541.1	654.5	552.9	3.39	13.0	5.2	3.8
18	3.7	2.5	658.0	535.4	664.3	550.0	3.73	16.7	4.5	4.5
19	2.5	2.7	671.3	525.1	674.5	546.7	3.71	20.4	3.6	5.5
20	1.2	2.7	685.9	510.9	684.8	539.8	4.66	31.2	3.0	6.7
21			705.3	486.4	693.6	529.3				

Table 5.23: Direction decisions at each step of the model. Direction unit is in radians.

Step	REQ_D		Interpolated Directions Matrix (*D*)					Sel_D	*FM*
1	0.26		6.06	0.01	6.21	4.55		0.01	2
2	0.30		6.05	0.00	6.27	4.64		0.00	2
3	0.36		6.03	6.27	0.05	4.72		0.05	3
4	0.42		6.03	6.27	0.13	4.80		0.13	3
5	0.50		6.05	6.28	0.25	4.89		0.25	3
6	0.60		6.08	0.00	0.38	5.00		0.38	3
7	0.73		6.10	0.00	0.51	5.13		0.51	3

Table 5.24: Velocity components and simulation time at each step of the model. Velocity units are in pixel/seconds, the positions are in pixels while the time unit is in seconds.

Step	U_{int}	V_{int}	$X_{current}$	$Y_{current}$	*T*
1	8.73	0.12	523.50	576.50	2.29
2	8.77	0.01	543.50	576.77	2.28
3	7.10	0.39	563.50	576.80	2.81
4	7.37	0.91	583.47	577.90	2.69
5	6.97	1.76	603.32	580.35	2.78
6	6.61	2.67	622.71	585.24	2.80
7	6.28	3.61	641.25	592.74	2.76
			658.59	602.71	

Although the above example demonstrates an unsuccessful manipulation, some useful data can be extracted from the above tables (Table 5. 21, Table 5.22, Table 5.23 and Table 5.24) and figures (Figure 5.24, Figure 5.25, Figure 5.26 and Figure 5.27). FM2 has a 0.26 rad (14.8 degree) error direction and a 15.9 pixels step size at the beginning of the manipulation, nevertheless the second step has a lower efficiency than the first step for the same selected FM2 mode. However, evaluating of the two steps belonging to the same frequency combination gives a strong indication of the repeatability. The manipulation displays an acceptable trajectory compared to the simulation study until about 10 manipulation steps with FM3 moving in a direction of 0.03 rad (1.7 degrees). At the fourth step the lowest direction error in the investigation occurs. After that the particle trajectory significantly deviated from the proposed path, thus creating the largest direction error of 2.14 rad (122 degrees) at the last manipulation step, the manipulation was terminated. With regard to the required displacement at each step, FM3 is shown to be sharply increasing in the last 4 steps which makes it difficult to evaluate the performance of this mode in this particular manipulation area.

5.5 Discussion

Figure 5.28 and Figure 5.29 summarise results from the previous runs. Both figures represent 100 manipulation data points (the total of all example manipulation steps) in two parameters, the direction error (difference between selected and real direction) and the magnitude (the real displacement resulted from each shifting).

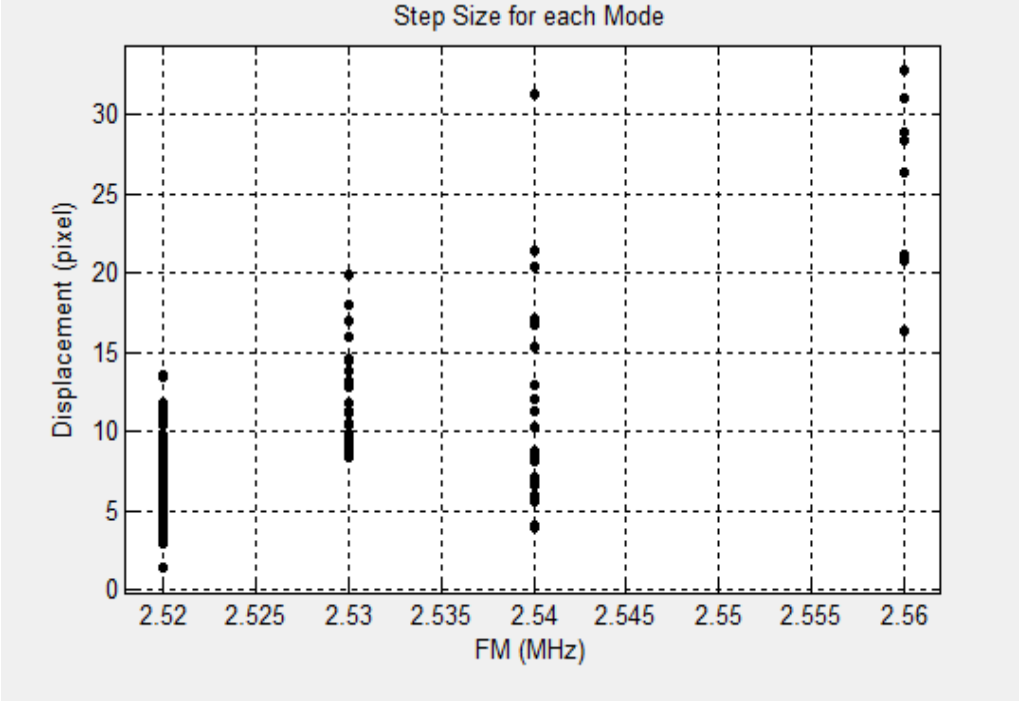

Figure 5.28: The resultant step size (real displacement of each step) for all data points (N=100) from all manipulation examples. FM= 1, 2, 3 and 4 corresponds to 2.52, 2.53, 2.54 and 2.56 MHz respectively. The required step size is 20 pixels (1 pixel is equal to 0.95 µm).

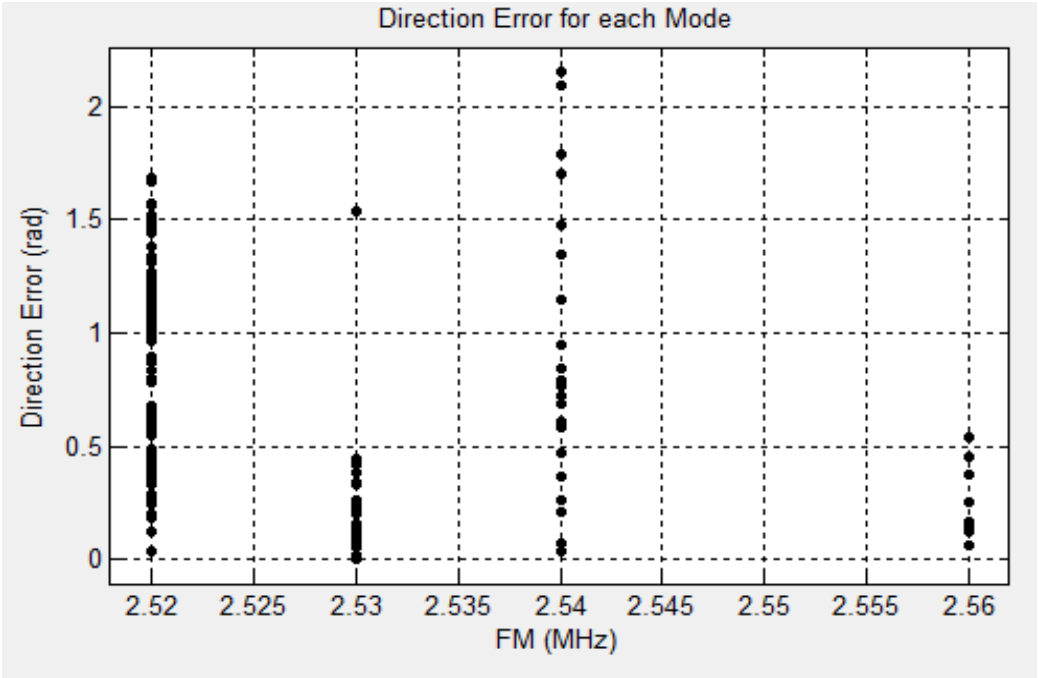

Figure 5.29: The absolute difference between the selected and the real direction (direction error) for all manipulation steps (N=100) from all experimental examples, where FM= 1, 2, 3 and 4 corresponds to 2.52, 2.53, 2.54 and 2.56 MHz respectively. The required direction error is zero radians (no absolute difference between selected and real direction).

From the above graphs, both the real displacement and the real direction are not possible to achieve accurately (20 pixels step size and zero direction error). Some FMs have higher errors and some have

lower accuracy than required. A linear interpretation can be fitted as to give a trend of higher displacement with the higher frequency modes (*Figure 5.28*). However, regarding the direction error, (*Figure 5.29*), two modes (FM 1, 3) exhibit poor behaviour with higher errors and vice versa for two other modes (FM 2, 4). The required displacement is always constant in this algorithm while different direction is selected as the dynamic particles change positions. The possible reasons for these errors are discussed next sections.

5.5.1 Fluid Layer Material

The sidewalls of the device cavity are made from a material of double sided tape which shows sufficient sealing and stability for short term usage. However, from the acoustic and mechanic properties point of view, there are disadvantages which are mentioned below:
1- Double sided tape has a lower acoustic impedance than the harder glass capillary walls, and thus creates weaker lateral resonances and hence less useful forces in this direction.
2- Air bubbles tend to form more readily at the tape walls, possibly due to its hydrophobic properties. This in turn can create unpredictable streaming patterns that interfere with manipulation.

5.5.2 Contributions from Acoustic Streaming

The control algorithms used in this thesis do not depend on (in both phases, the measurement of VVFMs and the manipulation phase) distinguishing the contributions of radiation forces from acoustic streaming.

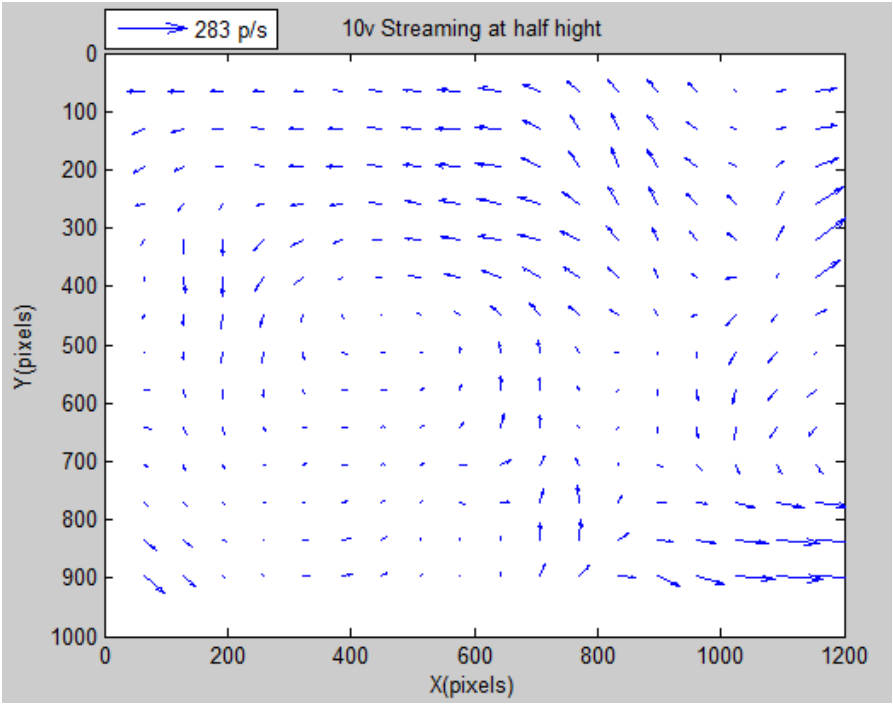

Figure 5.30: Acoustic streaming at the dedicated manipulation area within the acoustofluidic device. A 1 µm bead is used in this measurement. The vortex pattern is clearly seen at the centre of the field of view.

An investigation was performed to measure the contribution of the streaming forces. *Figure 5.30* shows a VVFM example of this acoustic streaming measured undertaken using 1 µm beads. The measured streaming velocity is much higher than the velocity belong to the radiation force (the averaged streaming velocity is 283 pixels/seconds while 11 pixel/seconds is the radiation velocity). Only one combination frequency mode was tested in the same manipulation area. A wide area can be tested to determine if either symmetric or asymmetric vortex patterns are formed in the plane parallel to the transducer plane. Finally, the determination of the type of dominating forces can be made based on the size of the micro particles [68]. Either the acoustic radiation force or acoustic streaming force can control their motion. However, special cases such as this device geometry as well as cavity material can make exceptional factors that influence both forces that are used.

5.5.3 Temperature

Temperature variation causes resonance frequencies to shift [45], which is a particular problem when there is a significant period of time between measuring the forces and navigating. It was observed that there was significant heating in the plane are resonance device.

To reduce this issue, for registering the VVFMs, the entire system temperature is reduced by flushing it with new beads every 27.5 seconds (27 seconds with 3 volts for the focus time and 0.5 seconds time lapse between consecutive images with 10 volts). This period of time yields a measured temperature rise of around 1.0^{o} C shown in *Figure 5.31*. The influence of temperature at the manipulation stage is not known as the manipulation time is not constant for every run. Thus the temperature is changing between two stages (3 volts and 10 volts).
As result of using resonances that are close to each other and close to the main levitation resonance frequency, the sensitivity to the temperature change is higher because as the influence of the temperature on the fluid and particles is known. Also, the manner in which the temperature affects the sound wave behaviour is known, and hence it creates shifts in the applied frequency [80] .

There are number of techniques listed below that can be used to minimize the temperature effect:
1- A design of the acoustofluidic device that separates the transducer from the chamber (e.g. a wedge transducer) could be built for long term stable experiments.
2- Introduce a temperature–controlled cooling system to stabilize the temperature especially for long run experiments.

As the lateral resonances used in this project are close to the main device resonance as well as being close to each other, the need for investigating the temperature influence on the sound wave by shifting the frequency, is required. A basic temperature measurement was performed to check the rate of changing of the system temperature as the driving voltage increases. *Figure 5.31* shows temperature increases of 8 ^{o}C after 30 seconds from turning on the second frequency voltage (18 volt). The ambient room temperature is 23^{o} C. The rate of heating increases as the applied voltage increases. This confirms that the temperature influence in such a system is significant. Another temperature experiment was performed to determine the thermo-effect after one minute with the same voltage applied; the selected voltage of interest was 10 volts. The measured rate of increase was 0.8^{o} C which indicates the possibility of the temperature increasing over a longer time duration. All experiments were performed with the frequency mode FM2 with a levitation voltage of 3 volts.

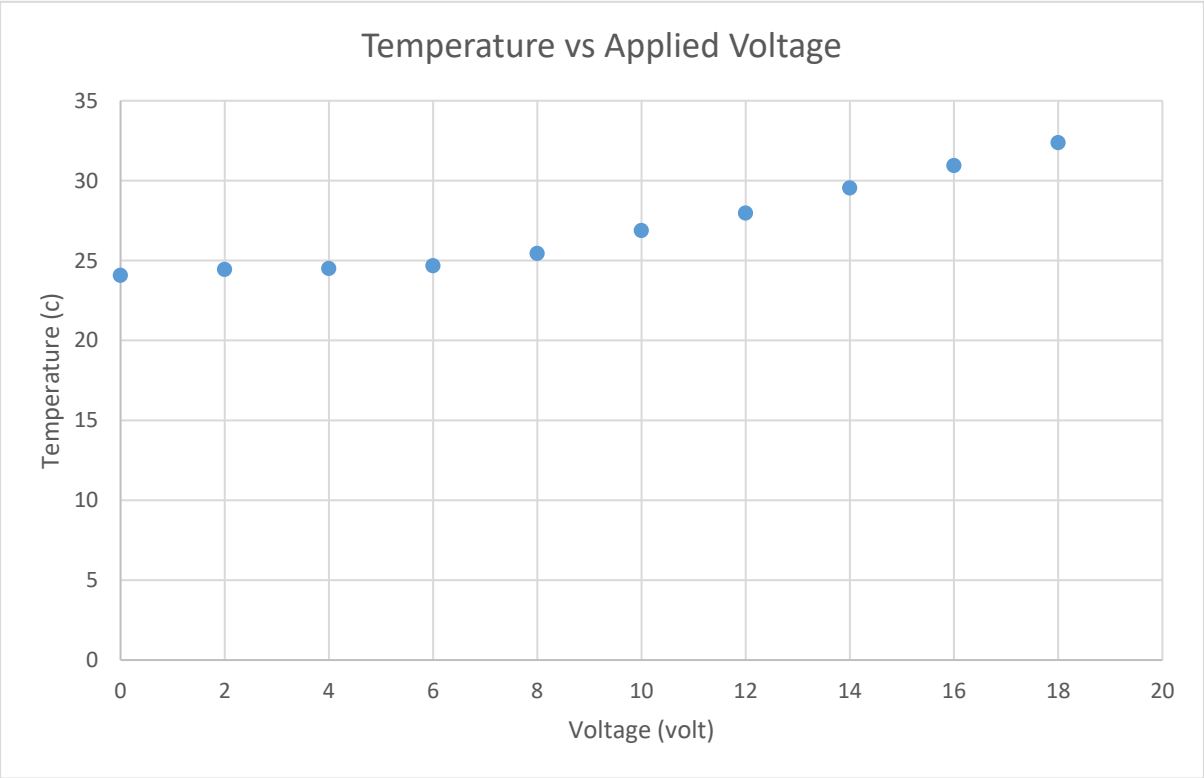

Figure 5.31: Temperature of the entire acoustofluidic device at different driving voltages. The temperature value is measured after 30 seconds of turning on the second resonance frequency.

The uncertainty of the step size was recorded with different selected frequency modes and different accumulated manipulation time. Most of the significant displacements that are shown on *Figure 5.28* happen at a late manipulation time (temperature is building up by time) and these belong to the frequency modes (FM3, 4) which are close to the main resonance frequency. The system viscosity during the later accumulated manipulation time reduces compared to the viscosity during the VVFMs generation stage. This is due to the thermo-effect. However, the FM1 frequency mode displays less velocity than the predicted frequency modes even after long manipulation times. This makes evaluation of the particular frequency modes difficulties.

5.6 Conclusion

The navigation algorithm has shown progress, but remains unsatisfactory. Only a small proportion of runs were successful, which was in part due to thermal changes causing differences in the forces between when they were initially measured versus when they were used later on. This also accounts for the significant variation between the simulated and experimental results.

Chapter 6. Steering Algorithm with Two Methods

In this chapter, a steering method is presented which does not require prior knowledge of available forces. Instead, feedback using a microscope imaging systems allows measurement of forces during manipulation. Two variations (the “Direct Method”, DM, and the “combined forces method”, CFM) are explored with examples given of each. There is analysis of the manipulation speed, noise and errors for the two methods.

6.1 Automatic Steering

The steering algorithm uses the hardware shown in *Figure 4.28* and the acoustofluidic device shown in *Figure 3.1*. Both methods that are discussed in this chapter (DM and CFM) use the flow chart shown in *Figure 6.1* which represents the initial method of this algorithm called a normal method (NM). The manipulation run starts by measuring the vibrational noise value (step 1), where a series of 20 images are taken and the positional measurement accuracy is estimated based on the variation in bead position (see Section 4.6.3). In step 2, the bead which is to be manipulated and the target position are established interactively by the user clicking first on a bead in the image and then on a target. The algorithm continues the manipulation loop by repeating steps 4 and 5 (forces measurement and shifting the bead, respectively) until the bead is driven into the target limit.

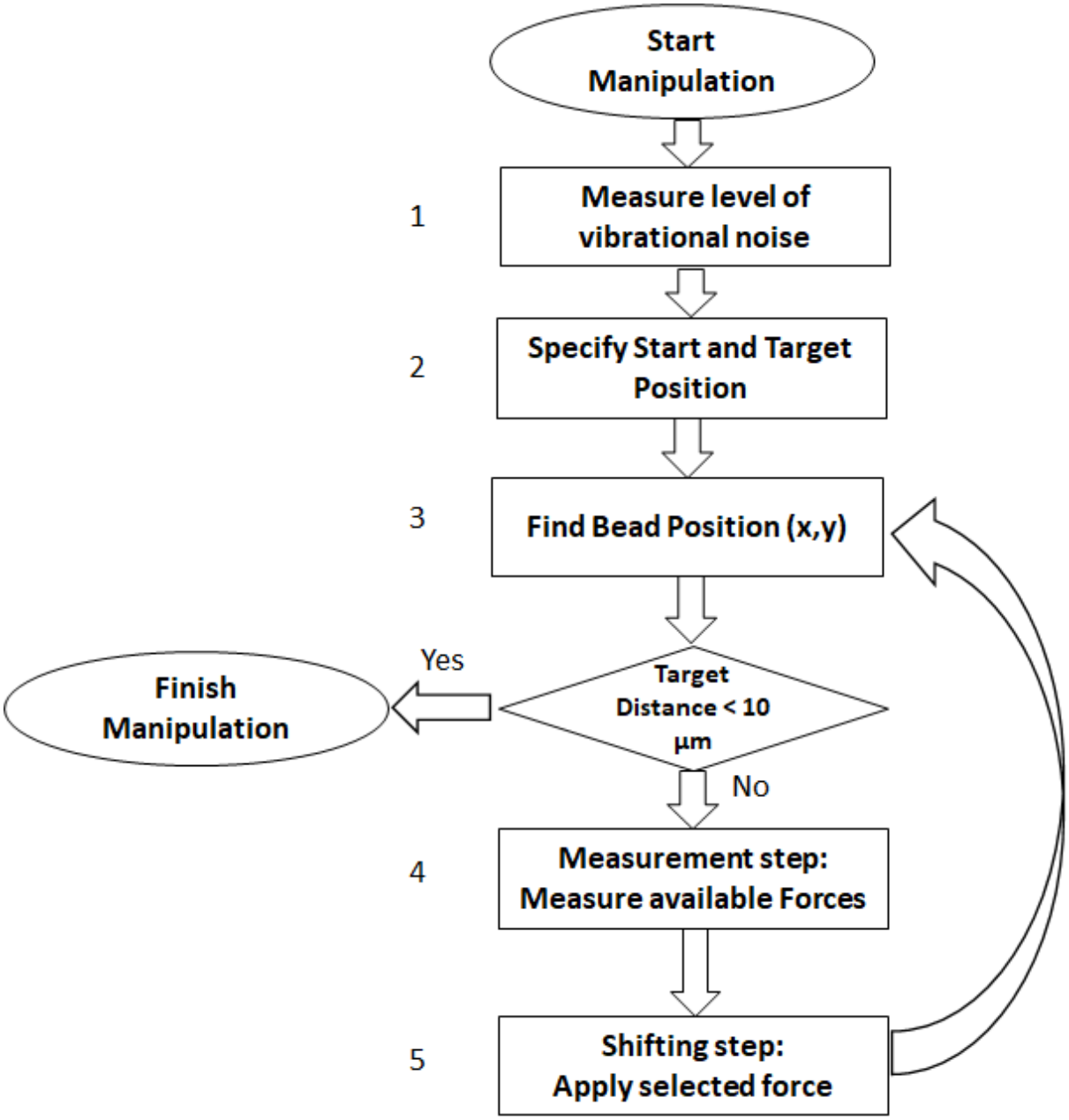

Figure 6.1: Flow chart showing elements common to both steering methods (CFM and DM). The diagram also represents the initial method which is a normal method (NM).

During the measurement stage, the manipulation modes are applied for a short time (initially for 100 ms pulse length), so that the resulting displacements do not significantly affect the track of the particle. However, the reliability of measurement of the bead displacement (during measurement stage only) is subject to error from the vibrational noise. The optimization of this error is described in Section 6.4.

Measurements of both magnitude and direction are performed for each frequency mode. Then the algorithm choses which one can best be used to shift the particle towards the target based on the

closest available direction. *Figure 6.2* illustrates steps 4 and 5 in more detail, first measuring and testing the forces available in terms of direction and magnitude, then shifting the particle by applying the selected frequency mode followed by finding the shifted particle at the predicted position. This iteration will continue until the particle reaches the target.

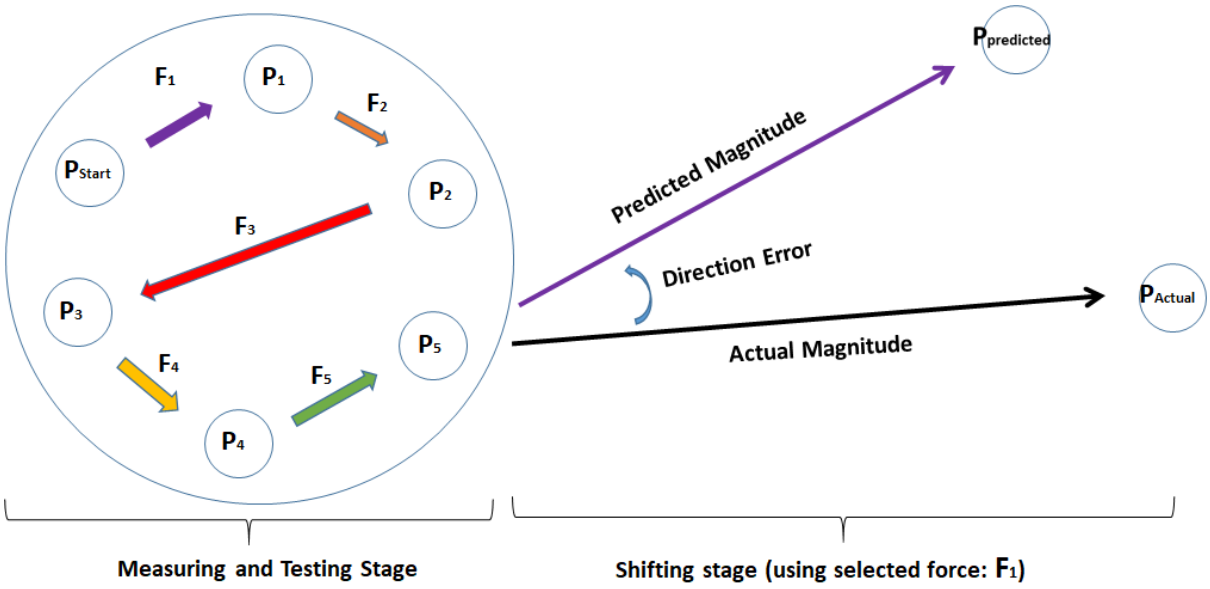

Figure 6.2: The process of testing and measuring the five manipulation resonances and selecting the one(s) most appropriate to reach the target. The system applies each resonance F_{1-5} in turn and measures the resulting displacement to deduce the force on the particle. The particle moves between five positions P_{1-5}; the system then shifts the particle along the manipulation track by applying the selected resonance (F_selected). There is an error between the predicted and actual particle position after applying the selected force due to measurement errors, timing errors, and variation in acoustic field. Figure not to scale.

The above figure is made for demonstration purposes only and not to the real scale of the testing distances between the particle positions which are presented significantly higher, and therefore not valid force measurements for the earliest FMs. A key feature of the acoustic field is that the forces created tend to vary at a scale of O (λ/4) or longer. Thus, if during a test step the particle travels too far from its initial position there will be some error between the predicted force (based on the initial position) and the actual force created when the resonance is applied starting from the perturbed position. The control algorithms make a linear approximation: that the result of a longer pulse of a resonant frequency will create a particle displacement of a correspondingly longer distance, but in the same direction. By keeping the intended step size small, the effect of the actual non-linearity is reduced.

The steering control algorithm has been designed based on the control concept that is explained previously, the early successful runs of the initial steering design have proved the ability to steer the tracked particle towards the desired target. However, the efficiency and accuracy of the manipulation at that stage was only measured by the target distance from the final particle position (where the particle can be positioned near the target by few micrometres) regardless the trajectory of the manipulation path. *Figure 6.3* shows one of these beginning successful manipulation runs where the particle has been steered automatically from a starting point to a target point based on the available forces within the dedicated manipulation area.

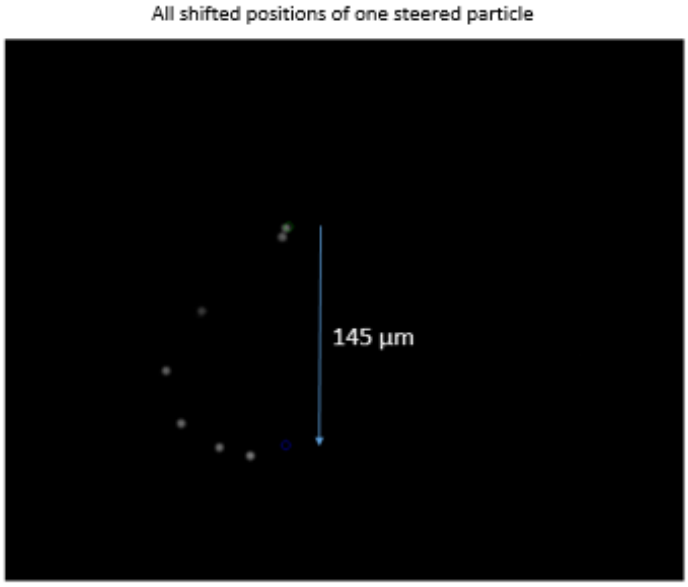

Figure 6.3: Example of early successful run to steer 10 µm particle for a specified start and target points (the green circle is the start position while the blue one is the target) with 145 µm direct distance between them. The figure demonstrates a series of accumulated consecutive images of the same controlled tracked particle (only images after each shifting stage are shown). The steering run was finished after six manipulation steps when the particle reached the target with less than 50 µm distance discrepancy.

The above figure shows an early steering example of 10 µm levitated particle with low control efficiency in term of manipulation distance and time where the deviation between the real track and the direct distance between the start and target position is significant. That early steering system had to be improved to mitigate issues caused by the initial design. These issues include; long real track distance, unnecessary extra manipulation time and steps which results in heating up the system and hence, it is not effective manipulation and control wise. The next sections describe the suggested tools and features that help in improving the steering algorithm performance.

6.2 Steering Deviation Indicator (DI)

In order to improve the shape of the manipulation track and make it as straight as possible especially when the manipulation is intended to steer the particle in shapes with multiple paths such as the squares presented below, a measure of path following precision is required. The measure called the deviation indicator (DI) is introduced which is a measure of how much the particle track deviates from a straight line trajectory where a lower DI is indicates a higher manipulation precision. The DI is defined in Equation (6.1)

$$DI = \frac{\sum_{i=0}^{n} d_i}{n} \qquad (6.1)$$

Where n is the number of manipulation steps, d is the perpendicular direct distance between the real particle position and a projected straight line between the initial and target position.

Figure 6.4 shows an example where the resulting DI value is 65 µm (130 pixels) which is considerably high.

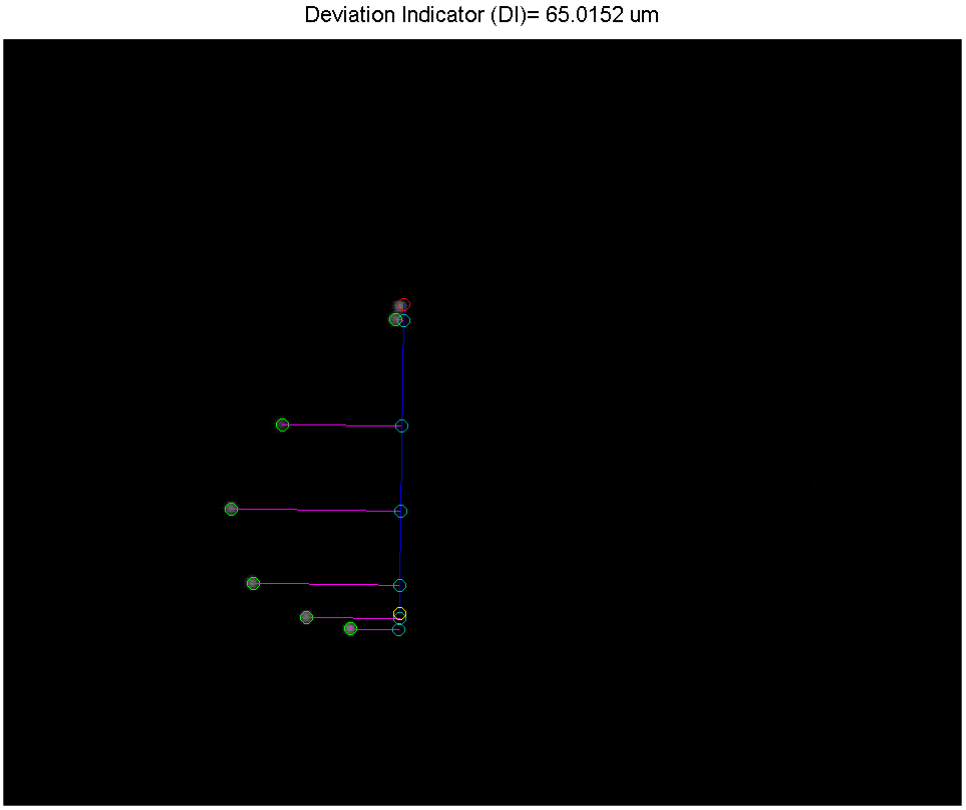

Figure 6.4: An image of the previous steering example after applying the DI method and results in 65 µm.

As result of the low efficiency of the initial steering algorithm reflected from the above example, enhancements of the steering algorithm have been established and new features will be investigated later. Assessment based on DI result will be carried out for every manipulation run.

6.3 Particle Identification and Tracking

Finding the bead's position accurately and quickly is crucial for a successful and rapid manipulation. The tracking of the particle is achieved by predicting the next position based on the known lateral force (direction and magnitude) and the current position. This proposed tracking and identifying method is designed only for a single spherical particle.

The tracking procedure in this work considers the error of the levitated particle position (< 1 μm) that can happen at any time. During forces calculations for instance, where the steering algorithm measures the error (step 1 in *Figure 6.1*) at the beginning of each run (Section 4.6.3 Vibrational Noise (Position Uncertainty)) and uses it to calibrate the particle's testing positions (Section 6.5) every time the system measures the position coordinates.

The automatic steering system relies on the user first clicking on the desired particle after the acquired image is displayed at the beginning of the manipulation process (step 2 in *Figure 6.1*). This manual first click is subject to error where the user should click exactly at the centre of the desired particle.

The system will then find the particle (step 3 in *Figure 6.1*) within a small specified area (a cropped image around the predicted position is fed to a MATLAB 'imfindcircle' function which implements a Hough transform. When the steering stage is measuring and testing the available forces which typically takes around 30 ms, the resulting displacement is expected to be small, hence the search window is set to 100 pixels² (50 μm²). The window is subject to increase if the tracked particle is not found. However, the possibility of not finding the tracked particle at the predicted position during the shifting stage is expected due to the use of linear extrapolation to predict the next particle position. Hence, the variable search window of the cropped image has one disadvantage during the shifting stage (finding particle in this stage initially takes around 200 ms for a 400 pixels² (200 μm²) cropped image and is subject to increase). The steering algorithm does not guarantee that the system is not tracking another particle especially after the long shift where the direction error can be as much as 50 degrees. Thus the current algorithm is limited to cases where only a single particle is present. Another

feature is introduced to mitigate significant direction and magnitude. This is accomplished by shifting the particle for a shorter displacement if the difference angle (between the predicted and required direction) is more than 50 degree. This feature helps in reducing the possibility of tracking a wrong particle.

6.4 Optimization of Testing Stage

The objective of the successful steering algorithm is to perform the testing stage (*Figure 6.2*) with a minimum displacement and time. However, the testing stage is subject to two issues.

- The position error uncertainty (vibrational noise) has larger effect in forces measurement with shorter displacement.
- Time error between code and actual testing time is significant for short testing time (*Figure 6.7*).

Therefore; it is necessary to include a technique to limit the effect of these issues which increases the reliability of this forces measurement. This is conducted by repeating force measurements a number of times (only two times if a very small displacement is recorded, see below) until a satisfactory displacements is established with consideration to the consequences of a large displacement (see below). *Figure 6.5* shows an example of position error thresholding resulting from one of the physical manipulation experiments where the threshold allowable bandwidth is between 10-50% and initial testing time 84 ms.

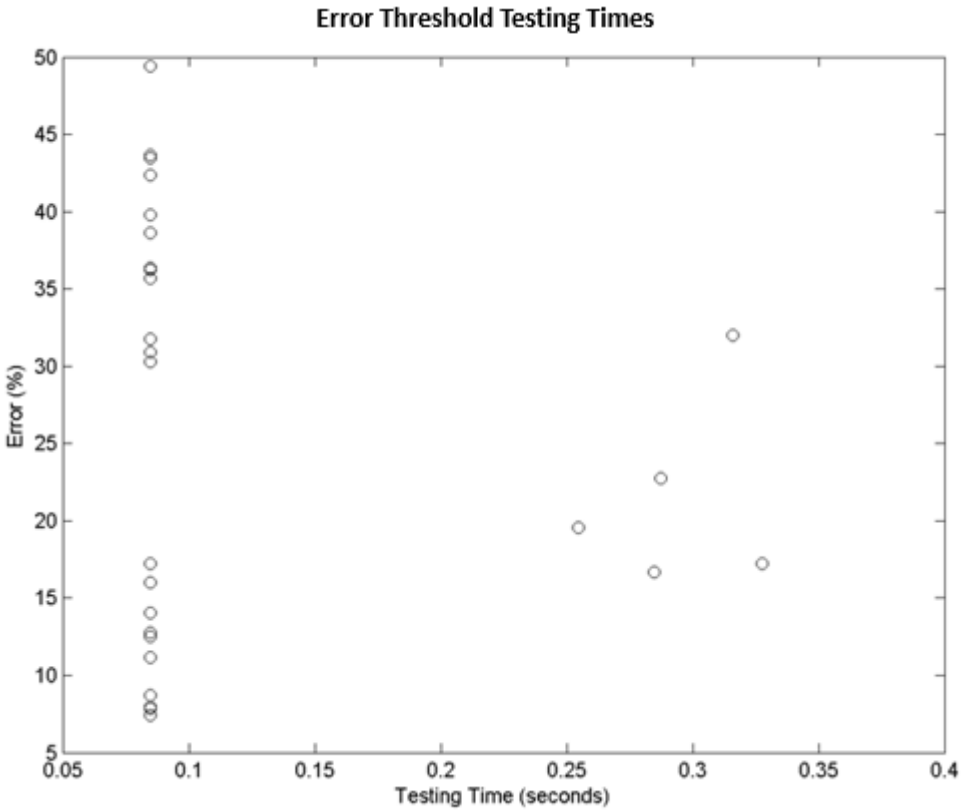

Figure 6.5: Plots of all applied testing times within the error thresholding levels 10-50%. All testing times are calculated to be applied between two allowable error limits. There are applied testing times (with 84 ms) lower than 10% (displacements are higher than the maximum allowable displacements). The steering algorithm does not repeat those frequency modes for shorter testing times for the same manipulation step and considers them as higher displacements for the subsequent manipulation steps. There are other frequency modes whose initial testing times (84 ms) are not enough to provide minimum allowable displacements, therefore, these modes are retested with higher testing times to provide optimum displacements.

The figure above shows the resulting testing times for all manipulation steps of one real steering example where every testing time has been applied based on the allowable minimum and maximum displacement during the testing stage. The allowable minimum and maximum displacement are determined with regards to the vibration magnitude (position error) and to produce the optimum displacement ($Disp_{optm}$) and the new testing time (Tm_{new}) shown in Equations 6.4 and 6.5 respectively. The next steps explain how testing time is optimised.

After performing the step for the position error measurement, the resulting value (pos_err) is used to calculate the two allowable minimum and maximum displacements ($Disp_{min}$ and $Disp_{max}$ respectively). Assuming the two minimum and maximum error thresholding percentages ($Thresh_{min}$ and $Thresh_{max}$)are 10% and 50% respectively, therefore a minimum and maximum of allowable displacement limits can be determined (Equations 6.2 and 6.3 respectively) relative to the position error value.

$$Disp_{min} = \frac{pos\_err}{Thresh_{max}} \qquad (6.2)$$

$$Disp_{max} = \frac{pos\_err}{Thresh_{min}} \qquad (6.3)$$

Then the optimum displacement $Disp_{optm}$ is calculated as,

$$Disp_{optm} = \frac{Disp_{max}+Disp_{min}}{2} \qquad (6.4)$$

The steering algorithm performs the testing stage by running a loop for the number of lateral frequency modes (5 modes in this project). The process begins by applying the initial testing time Tm_{old} (initial pulse length) for the first frequency mode and calculating the current displacement ($Disp_{cur}$). This displacement has to be within the allowable range of testing displacements (between $Disp_{max}$ and $Disp_{min}$). If the displacement is higher than $Disp_{max}$ the system will only modify this testing time for the next loop for this particular frequency mode by using Equation 6.5.

$$Tm_{new} = \frac{Disp_{optm}\ x\ Tm_{old}}{Disp_{cur}} \qquad (6.5)$$

If the displacement is lower than the $Disp_{min}$the system will then calculate Tm_{new} (using Equation 6.5) and repeat the testing for the same frequency mode. If the displacement is still lower than $Disp_{min}$, the system will avoid using this unreliable force (at the time of deciding for best direction) and flag it as a NAN value. If the displacement is not lower at this stage (reasonable displacement is observed for the current frequency mode after the second attempt), the algorithm will save this force (direction and magnitude) to be considered when deciding for best direction. This loop runs until a reasonable displacement for the all frequency modes is acquired.

6.5 Steering System Timings

The control accuracy of the proposed steering system relies on precise measurements of forces each time the system performs the testing stage. Due to the communication latencies of different system hardware components connected to the computer through USB ports, the forces measurement is subject to timing errors. In order to describe the system time latency, a 100 ms MATLAB signal is taken as an example which travels to the PZTs through hardware components. *Figure 6.16* demonstrates the effect of using different hardware components, which create 5 ms time delay and a 2 ms time reduction from the MATLAB testing time as a result of switches acting in advance of the summing amplifier output. The variations of the testing time (see *Figure 6.7*) is not considered in this demonstration.

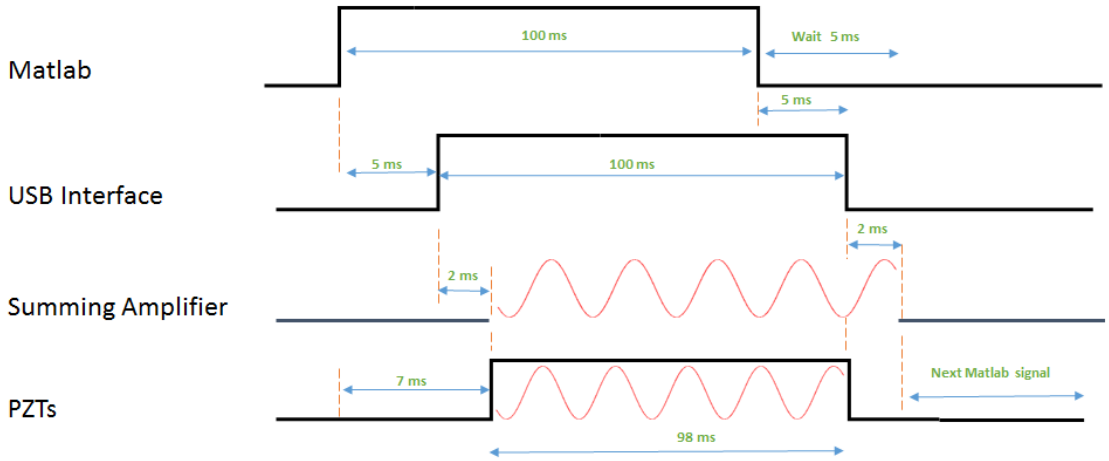

Figure 6.6: Representation of the time shifting of one MATLAB signal as it flows towards the PZTs throughout the system hardware components where the depicted MATLAB pulse length (100 ms) reaches the PZTs after 7 ms and reduced to 98 ms (this testing time example does not consider testing time variations). The 5ms waiting time after the MATLAB signal terminates is applied in real code to guarantee sufficient required testing time for PZT activation.

The above figure illustrates the testing pulse length in different hardware components from MATLAB to PZTs. However, as a result of the necessary fast testing time pulses (pulse length initially in ms), there is a need to use more sophisticated hardware components to meet the need for faster testing times and to overcome another issue that effect the reliability of these fast testing times which is uncertainty of testing time variation error. *Figure 6.7* shows the variations error of faster actual testing time for a range of MATLAB pulse lengths that gives less confidence in using pulses shorter than 50 ms.

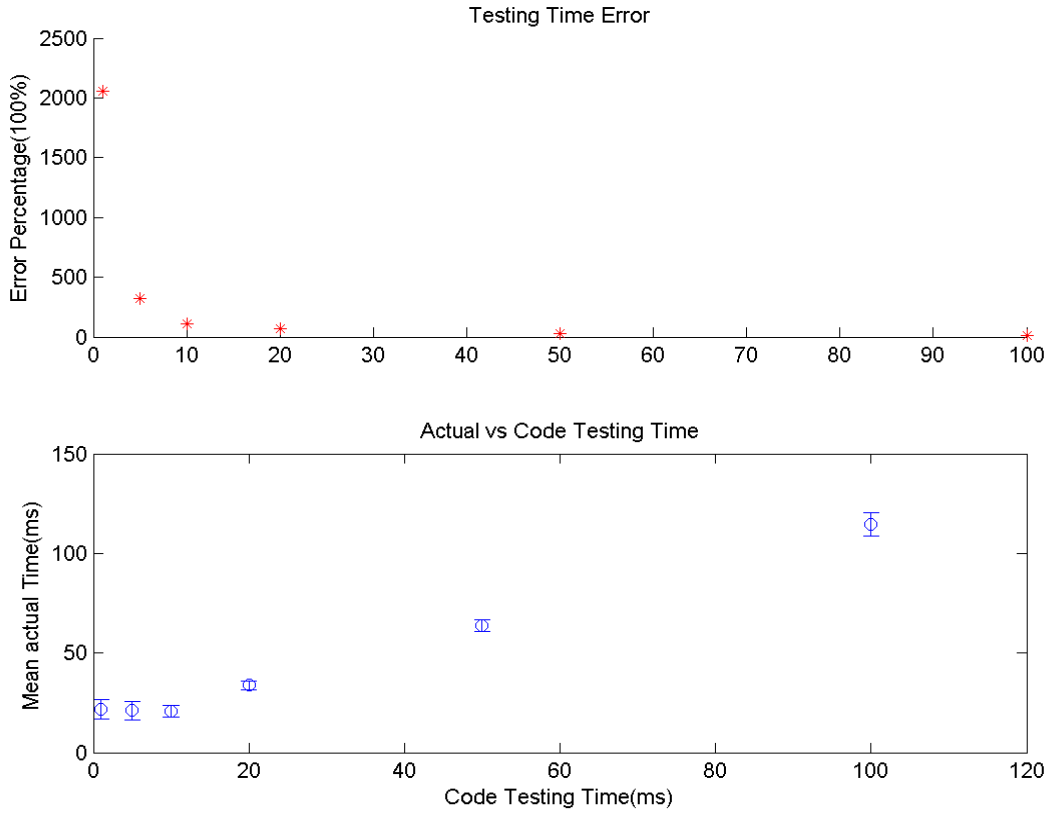

Figure 6.7: (upper) The testing time error percentage between the actual testing time and code testing time caused by the system hardware for a required fast testing time in ms. (lower) Mean of actual testing times for a range of code pulse lengths. The error bars are the standard deviations. The error is remarkably decreased after 50 ms code testing time.

From the above figure, the steering testing stage is subject to significant error percentages at low testing times of less than 50 ms. Therefore, a MATLAB function has been included to compensate for this time error using a MATLAB curve fitting tool where the system code has to calculate the real testing value before applying it to the system output.

From the above conclusion, the timing of the steering system is sketched in *Figure 6.8*. Each part of this sketch is the average of a number of a repeated time measurements. All red elements on the sketch are subject to change based on the manipulation calculations. An image cropping technique has been applied for searching the tracked particle position in both stages where the cropped image during the shifting stage is subject to wider search area.

Figure 6.8: Sketch of steering system timings for both stages (testing and shifting) where Tm is the testing time and T is the shifting time. 1670 ms is the total typical testing time of 5 frequency modes with 100 ms pulse length each. 1406 ms is the typical total shifting time with 1000 ms shifting time for one selected frequency mode.

The above figure reflects the need to reduce some periods of time that extend the steering system total manipulation time which might affect the steering quality. The Thorlab camera used in this study is making a significant delay (150 ms is the time spent to acquire one image) in both stages and the steering outcome can be enhanced by using alternative faster cameras.

6.6 Steering Methods

Two alternative implementations are explored here: 1) The combined forces method (CFM) and 2) The direct method (DM). The two alternatives trade off accuracy through more rigorous measurement (CFM) against speed through less testing (DM).

6.6.1 Combined Forces Method (CFM)

In this variation, the algorithm seeks to sequentially apply two of the available forces per step in order to achieve a movement direction directly towards the target. In order to combine two different forces to move the particle to a required projected point (If the target distance is less 25 µm, the variation will not be applied), all available forces must be measured and the algorithm will apply the following sequence of steps:

- The algorithm tries to find nearest clockwise and anticlockwise force that is less than 86 degree away from the desired direction.
- In the case where two forces are found, the system uses the combination of both to achieve the prescribed distance of 25 µm (50 pixels) if the target is located further away than this predicted displacement.
- If only one force is found (whether it is clockwise or anticlockwise), the system will use the left force only (without any combination of the other forces) to achieve the prescribed distance of 25 µm (50 pixels) if the target is further away than this prescribed displacement.
- If the result of the method condition is null, where no forces can be found, then the system will apply a single nearest force for a smaller step of 12.5 µm (25 pixels for instance). This will give a greater chance to measure more suitable forces that can be applicable to this method condition.
- The algorithm keeps applying the above conditions until the particle is located within 25 µm of the target, no more measurement steps are taken, the particle is shifted for a predicted step size of half the remaining target distance.

The combination of forces is illustrated in *Figure 6.9* where the algorithm, for example, selects two vectors R_1 and R_2 as nearest clockwise and anticlockwise forces that are not more than 86 degree away from the desired direction. Therefore, the range of angle theta θ can be written as ($0 < \theta <$ 172 °).

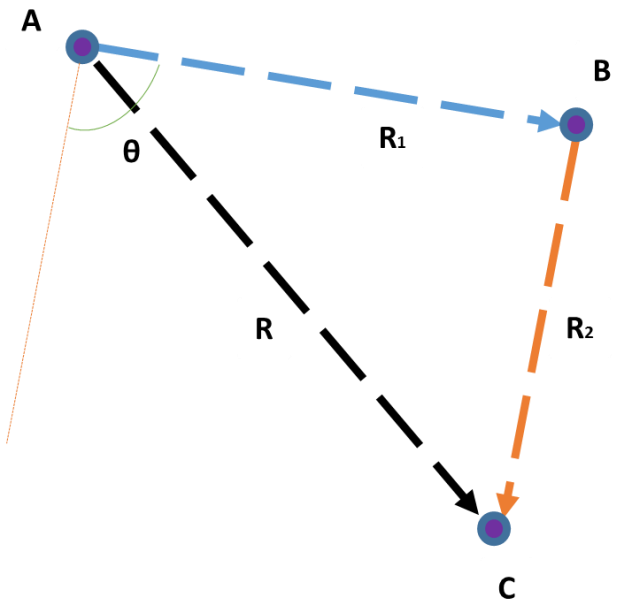

Figure 6.9: Graphical vector representation for adding two vectors (R_1 andR_2) with angle ϑ between them to mathematically obtain the vector R. The algorithm will sequentially apply the first force for a distance R_1 and then apply the second force for a distance R_2 .

The above graphical vectors sketch demonstrates a particle movement from point *A* to point *B* then to point *C* to achieve a required displacement *R* in a certain direction from point *A* to point *C*

In this combination method of acoustic forces, the two selected forces are measured in term of direction and magnitude. However, the scalars of both force step magnitudes are not known to achieve the proposed displacement of *R* and the position of point *B* is also unknown.

To derive the $R_1$and R_2 magnitudes from the fundamentals of vectors, both R_1 , R_2 can be derived using the algebraic solution of the equivalent vector *R* x and y components R_x , R_y respectively (equations (6.6) and (6.7)) and these represent the Cartesian distance between the known two points *A* and *C*.

$$R_x = R_{1x} + R_{2x} \tag{6.6}$$

$$R_y = R_{1y} + R_{2y} \tag{6.7}$$

Next step, the Equations (6.6) and (6.7) can be converted to Equations (6.8) and (6.9) to be defined in term of magnitudes R_1 , R_2 and directions θ_1 , θ_2 for the selected first and second forces respectively.

$$R_x = R_1 \cos\theta_1 + R_2 \cos\theta_2 \tag{6.8}$$

$$R_y = R_1 \sin\theta_1 + R_2 \sin\theta_2 \tag{6.9}$$

From equation (6.8), R_1 can be defined temporarily in Equation (6.13), with unknown R_2

$$R_1 = \frac{R_x - R_2 \cos\theta_2}{\cos\theta_1} \tag{6.10}$$

Next, R_2 can be solved by substituting R_1 in Equation (6.9), therefore Equation (6.12) defines R_2 and the denominator is simplified using Pythagorean Identities which is written in Equation (6.11).

$$\sin(\theta_2 - \theta_1) = \sin(\theta_2)\cos(\theta_1) - \sin(\theta_1)\cos(\theta_2) \tag{6.11}$$

$$R_2 = \frac{R_y \cos\theta_1 - R_x \sin\theta_1}{\sin(\theta_2 - \theta_1)} \tag{6.12}$$

Finally, R_1 is defined (Equation (6.13)) by substituting R_2 in Equation (6.10).

$$R_1 = \frac{R_x - \left(\frac{R_y \cos\theta_1 - R_x \sin\theta_1}{\sin(\theta_2 - \theta_1)}\right)\cos\theta_2}{\cos\theta_1} \tag{6.13}$$

The displacement ***R*** is proportional to velocity v, and from Stoke's equation, velocity is also proportional to the drag force F_d then, ***R*** is proportional to F_d .

6.6.2 Directed Method (DM)

In order to create faster manipulation times and to take advantage of the knowledge that acoustic forces only vary over distances of order λ/4 or greater, this method measures the available forces less often. After an initial measurement step, the force that is closest to the desired direction is chosen. If the selected force is within 0.5 radians (28.6 degrees) of the required direction then an actuation pulse is applied for a time that is calculated to give a 25 µm displacement. However, if the difference is more than 0.5 radians, then the system aims for only 12.5 µm displacement per step. This is in order to allow for the possibility of more suitable forces in subsequent steps. The requested distance is also reduced to half the target distance if the bead is closer than 50 µm to the target (if closer than 25 µm to the target, further measurements are not taken, relying instead on the last measurement phase).

In subsequent steps, the forces are not measured again unless the distance to the last measurement point is more than 25 µm. Instead, the algorithm stores the values previously measured in a table and uses these. After each movement step, the entry in the table registering the force that was used is updated to reflect the actual force observed acting over the step. This takes account of the higher accuracy of the measurement given the larger displacements compared to the measurement phase. It also makes allowance for the force changing with position and changing over time due to any drift associated with heating effects.

An example manipulation is shown in *Figure 6.18*, with details presented in Table 6.3. It can be seen that measurements are only made in 5 of the 10 steps.

6.7 Steering Simulation Results

In order to evaluate the proposed algorithms, and to obtain insights into whether the available forces within typical devices would be sufficient to achieve useful manipulation, a model was created that used actual force maps measured previously in Section 4.6 to test the movements of a modelled particle.

The following simulation results have included the steering Normal Method (NM) (which uses the basic steering flow chart in *Figure 6.1*) to help for more sophisticated analysis. Unlike the real steering algorithm, the next simulation results have two unrealistic issues:

- The interpolated forces at every position in the force maps (the simulator is only reading these existed forces from the known force maps).
- The zero direction/magnitude error (the prediction of the next position estimation is always correct).

The simulation model has been established for this steering algorithm based on the timings shown in *Table 6.1*, for all recorded manipulation time of the two stages of the steering which is calculated from *Figure 6.8*. The calculation time for force selections (best direction decision) is around 1.3 ms for each method. Tm is the measured/testing time (0.5 seconds) and T is the shifted time.

Table 6.1: Simulation time per stage (ms) showing the difference in timing between the steering methods for the two steering stages. The displayed time for each is the accumulated time for driving signals, acquisition and image saving and particle locating (see Figure 6.11).

Method / Stage Time	NM	CFM	DM
Measuring Time (5 modes)	Tm+1170	Tm+1170	0
Shifting Time	T1+406	T1+T2+416	T1+406

In order to evaluate the forces availability over the dedicated manipulation area based on the measured force maps, the simulation has performed 1000 runs (for each method). These were performed with a maximum number of manipulation steps set to 20 and 20 pixels (10 µm) as a target accuracy limit and a distance of 500 pixels (250 µm) towards random targets (random target positions are predetermined by a MATLAB function). *Figure 6.10* presents the evaluation in term of successful rates for each method for the random manipulation targets. The figure shows the simulation result in two ways, a colour map of the gradient of the successful rate (colour bar is provided) distributed over the manipulation area in addition to a successful and unsuccessful plot of target positions which are highlighted in two different colours. Furthermore, the manipulation time (the steering speed for each method) is considered (*Figure 6.11*). Deeper analysis of the manipulation time is divided into various target distances that helps towards investigation of the steering capability of the acoustofluidc device.

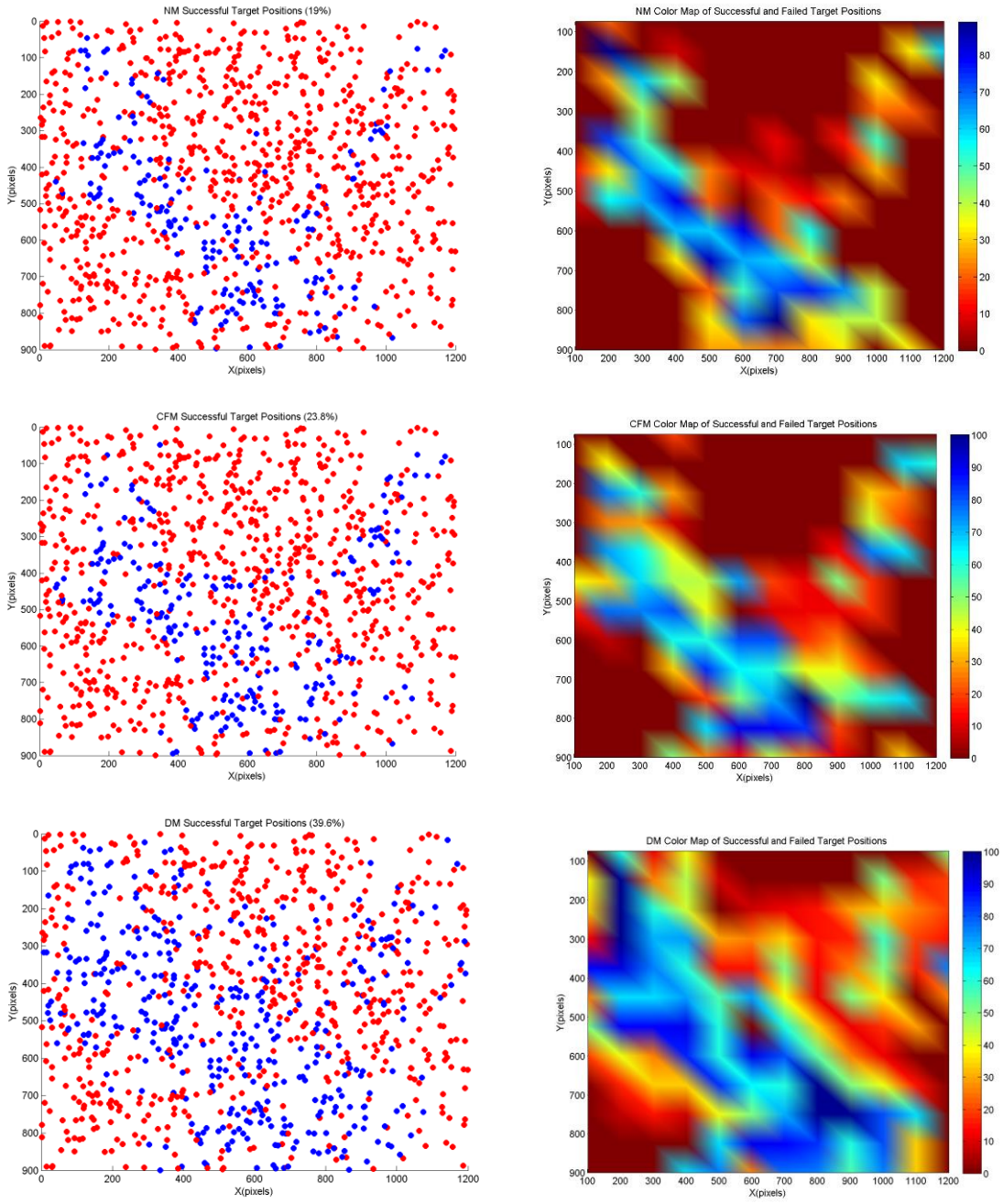

Figure 6.10: (Left column) Successful (blue) and failed (red) target positions for the three steering methods over the dedicated manipulation area. (Right column) Gradient colour plots of successful rate of the target positions for the three steering methods over the dedicated manipulation area. Remarkable improvement of the possibility to steer particles to those target positions (blue shaded areas is an indication of the improvement), where the successful percentage is increased and recorded as 19, 24 and 40% for NM, CFM and DM respectively. The limited number of steps to generate these graphs is 20 manipulation steps that can be an effect of manipulation area assessment. The highest concentration of the successful target positions is in the left diagonal manipulation area while lack of target positions was achieved on the other half.

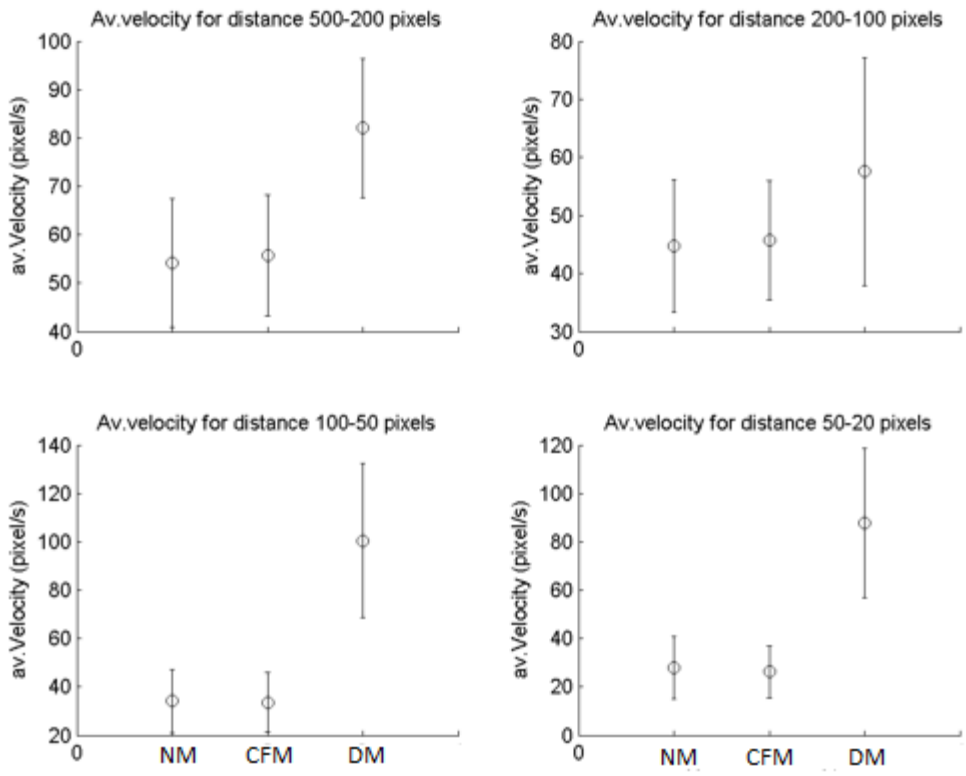

Figure 6.11: The averaged velocity for each method measured over a certain target distance for precise evaluation methods. The DM has a notably faster velocity compared with the other methods. Error bars are the standard deviations.

Figure 6.11 shows that the DM has the fastest velocity (lowest manipulation time) compared to NM and CFM, hence it reaches the target rapidly. As a result of forces measurements not being required for DM, a different velocity of around 15-60 pixels/seconds between the DM and other methods is applied as the target distance decreases. However, the CFM has a double shifting time (see *Table 6.1*) when compared to the NM; nevertheless both methods have similar velocities over the target distances.

Based on the above results, the CFM and DM methods are considered in the experimental work described in the following sections.

6.8 Steering Experimental Results

This section presents the experimental steering results for each proposed method. 125 iterations of steering runs have been performed (30 runs for CFM and 95 runs for DM) and one real successful steering example for each method is demonstrated with full details. Comparison of the efficiency of

each method is investigated, mainly in term of direction and magnitude error for every steering step and is shown in a separate histograms with discussion.

6.8.1 CFM Example

An example of a successful CFM steering run is demonstrated here. A bead is manipulated over a 200 µm distance, with the conditions at each step along the way shown in *Table 6.2*. *Figure 6.12(A-D)* demonstrates both the testing and shifting stages through the trajectory of the 10 µm bead in the real image where the bead reaches the target. The manipulation stops at a distance of 6.43 µm from the target (red circle) after a total manipulation time 9.35 seconds. This successful CFM example has a 13.7 pixels (6.85 µm) deviation indicator (DI) and is considered as one of the lowest DI among the CFM examples. The magnitude of the vibration noise measured at the beginning of the run was 1.6 pixels (0.8 µm).

Table 6.2: Details of example CFM steering run.

Manipulation Step	Required Direction (Degree)	Applied Modes	Distance caused by test phase (µm)	Magnitude error (µm) (Difference between intended and actual magnitude)	Angular error in degrees (Difference between selected and actual direction)	Activated PZT	Accumulated Total Time per Step (seconds)	Target Distance (µm)
1	0	1 & 2	11.24	-5.95	9.90	Right	0	200
2	1.71	1 & 2	14.50	-9.28	3.69	Right	1.78	173.92
3	4.41	1 & 2	15.32	-9.64	9.74	Right	3.54	145.12
4	2.29	5 & 1	20.16	-4.99	13.80	Right	4.99	114.83
5	5.68	1 & 2	21.66	-10.31	1.67	Right	7.05	75.38
6	9.48	1 & 2	22.55	-10.03	-9.88	Right	8.13	39.33
7							9.35	6.43

Table 6.2 includes a measure of the amount displacement which is created during the measurement phase (of testing each of the available forces in turn). It can be seen that this distance is significant,

however reducing it tends to increase the measurement errors (due to reduced signal to noise, the noise being the result of unwanted vibrations).

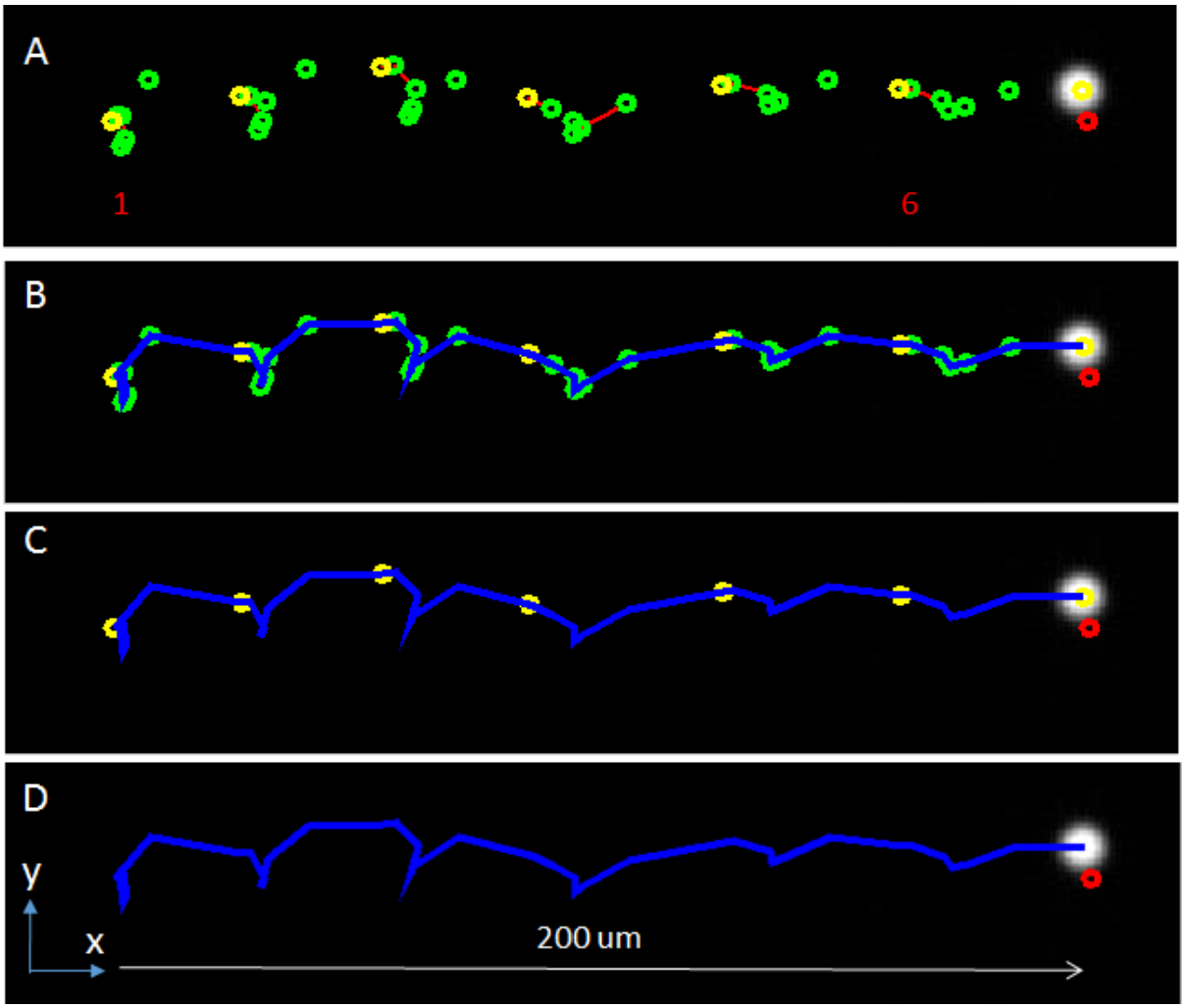

Figure 6.12: Example steering run with CFM of a levitated 10 µm bead over a 200 µm distance from left to right towards the target position (red circle). (A) The testing stage positions of all manipulation steps (green circles) with the selected combined forces (red lines, enlarged in next figure) and particle positions (yellow circles) at the beginning of each step (before measurement and after shifting). (B) The trajectory (blue line) toward the target on the right hand side, including the position at the beginning of each stage, and the positions after each measurement displacement. (C) The trajectory with only shifted positions. (D) The trajectory with no stage positions shown.

The above figures show the plot of a real manipulated particle track and the available forces for six manipulation steps. These available forces have been used to decide where to steer the particle to the desired direction at every manipulation step. As shown, each step has a type of position (tested and shifted positions) where the distance between the first and fifth tested positions is significantly increased (see *Figure 6.13* and *Figure 6.12*(A)) as the manipulation step increased because of the influence of the right PZT configuration. This right PZT configuration dominates the lateral forces

direction and contributes more direction options towards the target direction for the later steps which is an advantage in applying the combined forces method.

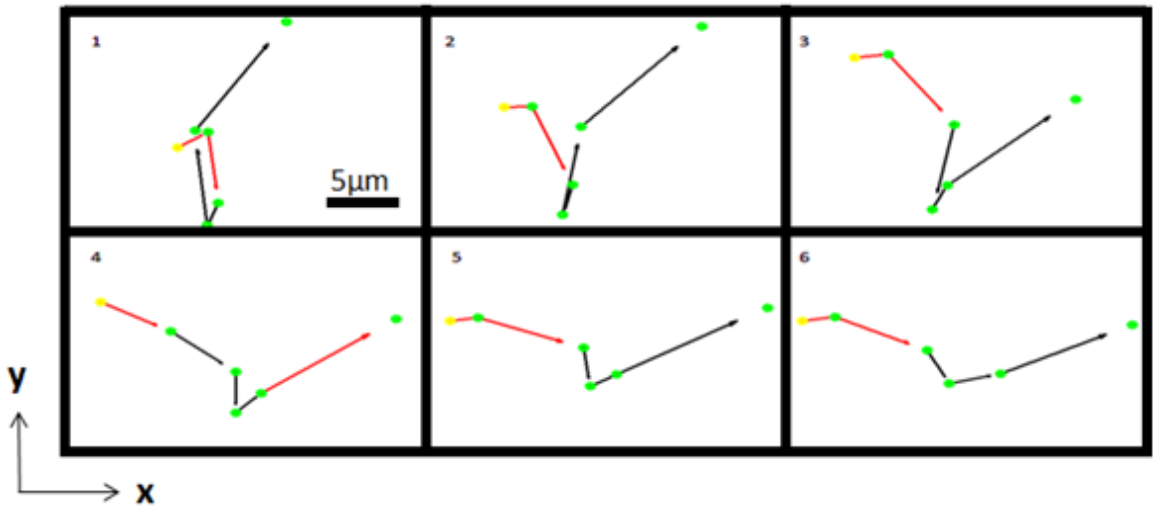

Figure 6.13: Zoomed in plot of all available forces for the six manipulation steps. The two combined chosen forces are shown with red lines. The yellow mark is the start position for each measurement step (also the bead position after each shifting stage) while the green dot marks the tested positions.

From the above figure, if describing the forces of the first step, the five available directions from first to fifth are 5.8, 1.4, 2.0, 4.6 and 5.4 rad respectively (the vectors lengths are not scaled to the distance between two green marks depicting the measuring positions). As the required direction for this step is 0 rad (in the right direction), the steering algorithm chooses two different forces within a range of a ± 1.5 rad (86 degree) from the target direction. In the figure shown, the algorithm combines the first force (the closest anti-clock wise force from required direction) and the second force (the closest clockwise force from required direction) to steer the bead exactly in the 0 rad direction. To achieve a desired step displacement of 25 µm towards the target, the steering algorithm calculates the activation time for each step which returns 947 and 213 ms for first and second lateral force respectively as well as calculating both force magnitudes. Based on the selected forces, the steering algorithm then predicts the next position. A more detailed demonstrations with images of the above example is shown in *Figure 6.14*. This demonstration shows the example of regular stages from the start position (distance to target is 200 µm and zero ms manipulation time) with levitation frequency only and both PZT configurations. This step is used for testing five frequency modes and shifting the particle by combining the two selected forces, and finally the attainment of the target position (distance to target is 6.43 µm and 9.35 seconds total manipulation time).

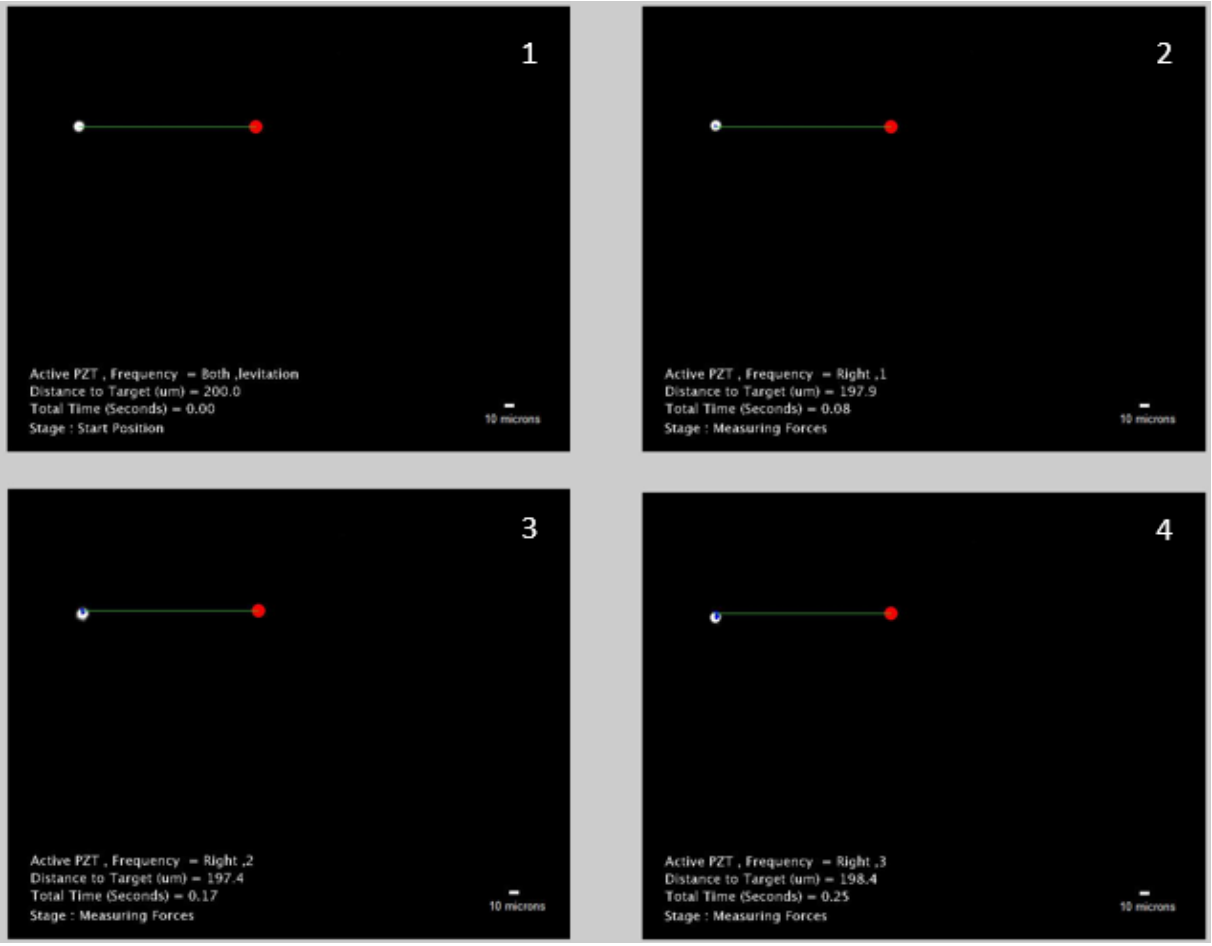
1
Active PZT , Frequency = Both ,levitation
Distance to Target (um) = 200.0
Total Time (Seconds) = 0.00
Stage : Start Position
10 microns
2
Active PZT , Frequency = Right ,1
Distance to Target (um) = 197.9
Total Time (Seconds) = 0.08
Stage : Measuring Forces
10 microns
3
Active PZT , Frequency = Right ,2
Distance to Target (um) = 197.4
Total Time (Seconds) = 0.17
Stage : Measuring Forces
10 microns
4
Active PZT , Frequency = Right ,3
Distance to Target (um) = 198.4
Total Time (Seconds) = 0.25
Stage : Measuring Forces
10 microns

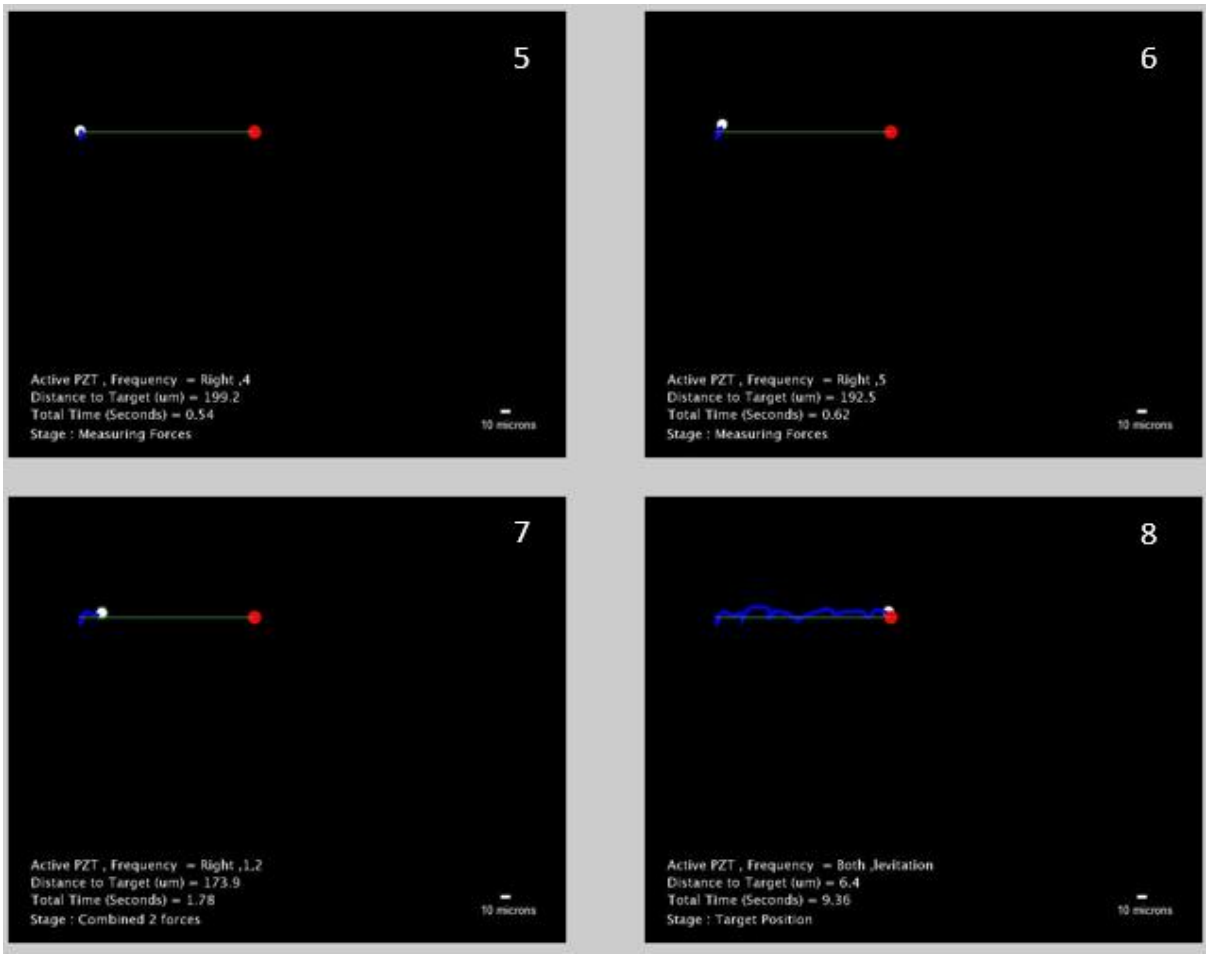

Figure 6.14: Images of steering one levitated 10 µm bead for a 200 µm distance towards the target position (red mark) in the right direction (blue trajectory line) using the combined forces method. The image sequence is only for demonstrating the steering stages: start position, measuring forces, combining the two forces for only the first manipulation step and final image of target position where the manipulation is stopped (the stage is shown in the last line of the provided information in each image).

From the above figure, the first and last images show the start and final position where the manipulation stopped at a distance of 6.43 µm from the target with total manipulation time 9.35 seconds. Both positions show that only levitation frequency and both PZT configurations are applied. Due to the required rightward direction of the target, only the right PZT is activated. The second and third images are the first and second force measurements which are obtained by applying the first and second lateral frequencies respectively for 84 ms that result in a small displacement (2.3 and 4.8 µm respectively). The steering algorithm carries on for another three lateral frequencies and measures the resulting forces (fourth, fifth and sixth images). The seventh image shows the displaced bead after combining and applying the selected first and second forces. A video of this sequence is shown with the electronic supplementary information. The statistical results for this example is demonstrated in terms of direction and magnitude error and is shown in *Figure 6.15.*

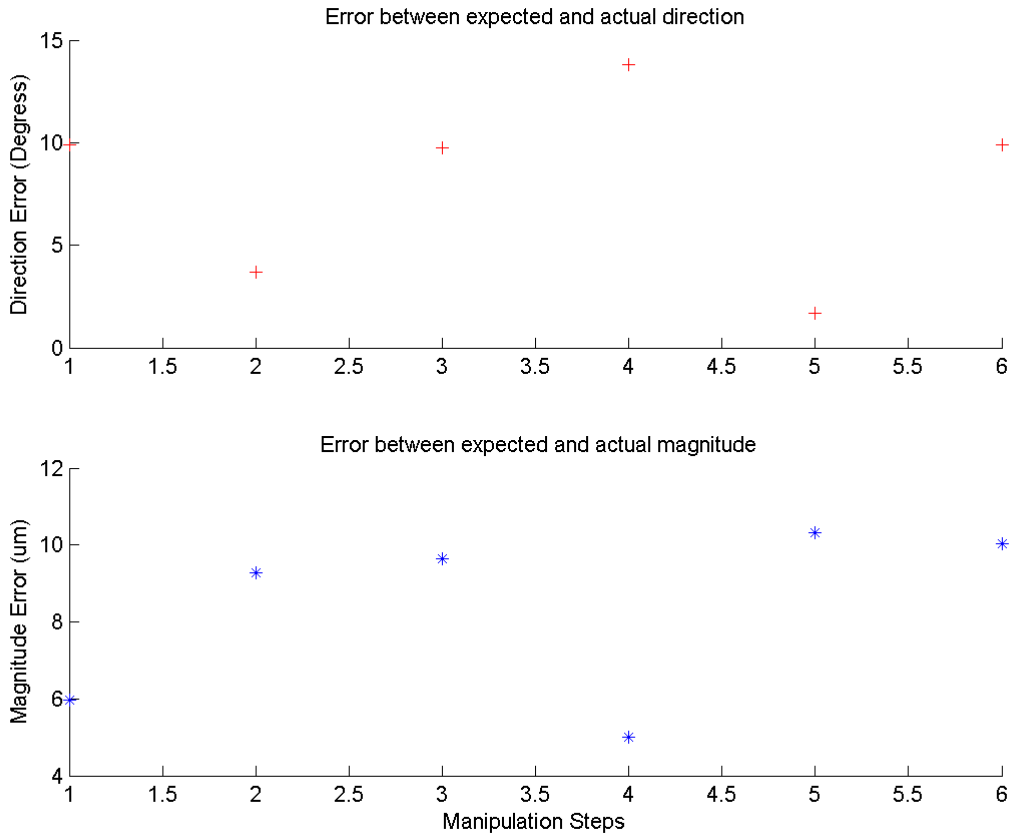

Figure 6.15: (Upper graph) Shows the resultant directional error between real and predicted direction. (Lower graph) Shows absolute difference between the expected and the real magnitude.

For every manipulation step after applying the combined forces, the steering algorithm searches for the tracked bead around the predicted position and calculates the real direction and magnitude based on the real shifted position. Both magnitude and direction errors can be either negative or positive, for instance, the errors associated with the first step are -5.95 µm and +9.9 degree from a desired magnitude of 25 µm and direction of 0 degree. A more comprehensive analysis of these two errors is explained in Section 6.9.3. *Figure 6.16* demonstrates the actual resulting displacement for both steering stages (measuring forces and combining forces).

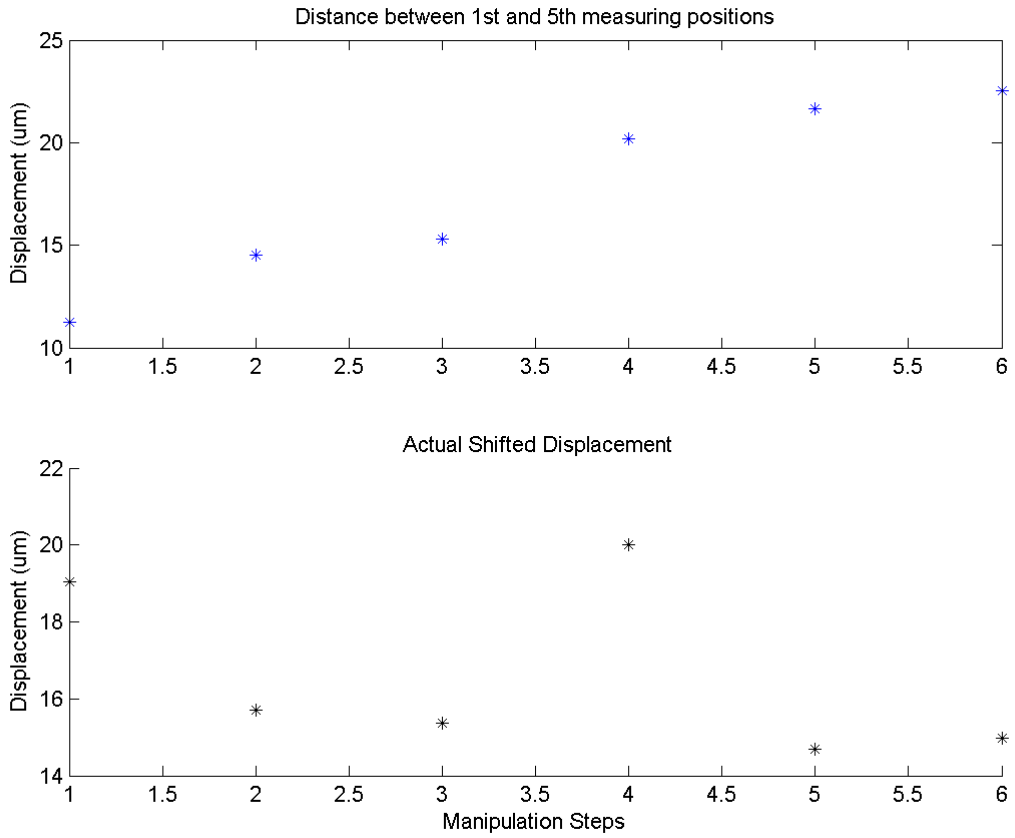

Figure 6.16: Two different displacements are recorded for each manipulation step, one is expected to be a small displacement (actual distance between first and last testing) (upper graph) when the steering system performs the forces measurements, the other displacement (actual shifted displacement) is expected to be approximately the desired step size (lower graph).

The steering algorithm aims to apply the lowest possible testing time of forces to keep the distance between the first and last testing positions as small as possible in order to maintain the validity of the early forces. The noticeable increasing in this distance is evidence of the influence of the right PZT configuration. The desired shifted displacement is often 25 µm if the distance to target is greater than 25 µm. If it is less, the steering algorithm considers that distance as a desired step displacement. In this manipulation example, all the desired steps are 25 µm, which is not achieved accurately. However, the steered particle approaches towards the target (see *Figure 6.17*) because of the contribution of both stages (indirectly for the testing stage) due to the effect of the right PZT configuration.

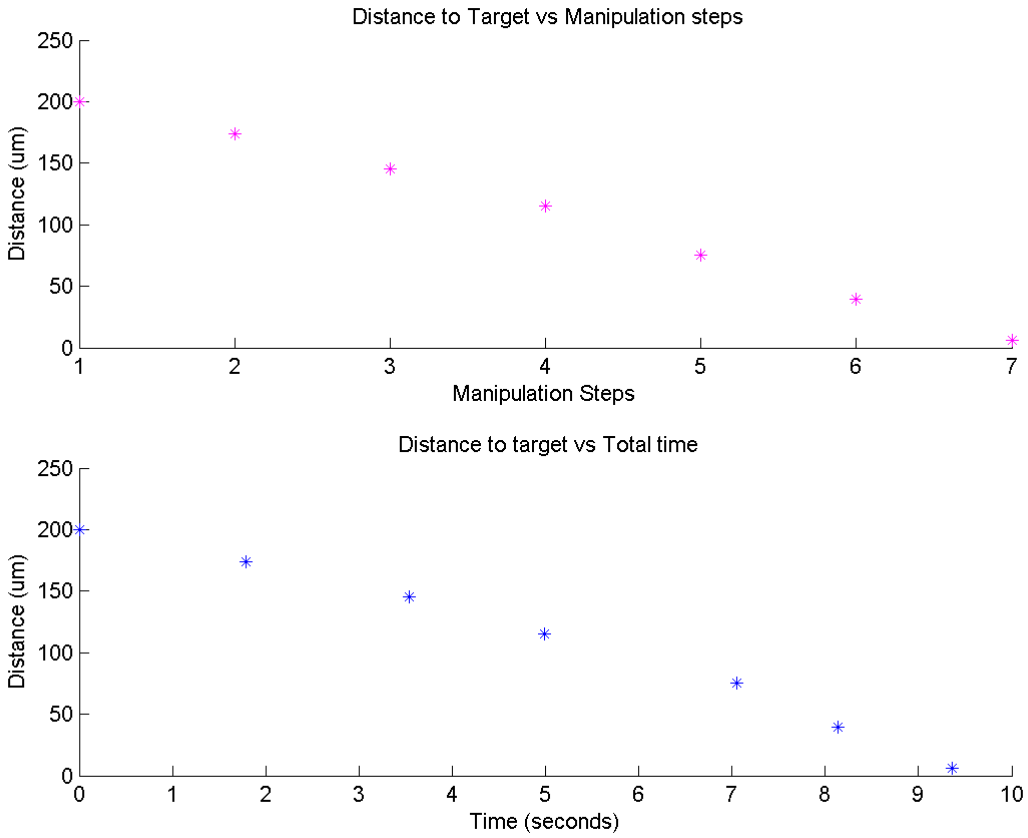

Figure 6.17: Target distance with manipulation steps (upper) and manipulation time (lower). The depicted manipulation steps and time represent both of the steering stage's (forces testing and forces combining) contribution towards achieving the target distance.

Both graphs (target distance versus steering steps and time) show a significant approach towards the target when the forces combination method was applied in every manipulation steps. Despite the nonlinear nature of the acoustic velocity fields that the steering algorithm employs to steer the levitated bead in certain directions, significant distances between the main manipulated positions (upper graph) is achieved. This is an indication of the response of the combined forces method as well as PZT configuration. The accumulated manipulation time (lower graph) is used to evaluate the efficiency of the method used to achieve the required distance to target. The plotted accumulated time is the total time of all force measurements and the shifting or combined forces activation time for each step. A more sophisticated analysis of this method is presented in Section 6.9.3 where the steering speed for each method is considered.

6.8.2 DM Example

The second suggested steering method is demonstrated with the use of one successful example. The bead is steered over a 200 µm distance, by applying the directed method conditions (see Section 6.7.2) for every step. *Table 6.3* and *Figure 6.18 (A-D)* shows a demonstration of both testing and shifting stages by showing the trajectory of the 10 µm bead. The manipulation stops at a distance of 5.2 µm from the target (red circle) after a total manipulation time 14.6 seconds. This successful DM example has a 27.8 pixels (13.9 µm) deviation indicator (DI). The vibration noise magnitude measured at the beginning of the run was 0.7 pixels (0.35 µm).

In order to understand the steering operation of the Directed Method (DM), *Figure 6.18* demonstrates steering of the 10 µm bead in the direction of y-axis for a proposed vertical distance of 200 um. Unlike Table 1 (CFM example), *Table 6.3* has extra details (intended shifting displacement and difference between selected and required direction) which show when the steering algorithm decides to reduce the intended shifting displacements. The steering algorithm uses this feature whenever the difference between the predicted (selected) and required direction is higher than 28.6 degree (see steps 2 and 3). The Algorithm also reduces the intended displacement by half of the target distance whenever the target distance is less than 25 µm (see step 10 in where the target distance is 13.149 µm).

Table 6.3: Details of example DM steering run.

Step	*Chosen Force*	*Required Direction (Degree)*	*Distance between first and last measuring positions (um)*	*Magnitude error (um)*	*Intended shifting displacement (um)*	*Angular error (degree)*	*Difference between selected and required direction (degree)*	*Activated PZT*	*Accumulated Time per Step (seconds)*	*Target Distance (µm)*
1	*1*	*270*	*4.76*	*-2.13*	*25*	*8.21*	*14.03*	*Both*	*0*	*200*
2	*1*	*274.19*	*5.11*	*-4.28*	*12.5*	*-8.78*	*33.27*	*Both*	*1.01*	*177.21*
3	*1*	*274.72*	*0*	*-5.02*	*12.5*	*-6.91*	*33.81*	*Both*	*2.06*	*174.54*
4	*1*	*275.88*	*0*	*0.05*	*25*	*-9.11*	*28.02*	*Both*	*2.31*	*167.91*
5	*1*	*279.1*	*7.12*	*-6.46*	*25*	*-0.75*	*22.13*	*Both*	*3.11*	*144.44*
6	*1*	*279.68*	*0*	*6.58*	*25*	*-0.72*	*6.65*	*Both*	*5.04*	*131.82*
7	*1*	*281.55*	*0.61*	*-7.99*	*25*	*-10.84*	*7.80*	*Both*	*6.63*	*100.45*
8	*1*	*281.23*	*0*	*8.90*	*25*	*-8.59*	*1.94*	*Both*	*9.86*	*83.91*
9	*2*	*274.23*	*14.22*	*-0.34*	*25*	*12.38*	*7.85*	*Both*	*11.76*	*50.95*
10	*1*	*293.97*	*0*	*8.60*	*6.57*	*17.33*	*2.20*	*Both*	*14.30*	*13.15*
11									*14.67*	*5.20*

Figure 6.18 demonstrates the advantage of using the Directed Method where the steering algorithm performs the measuring/testing stage only five times out of ten manipulation steps. This steering method consumes less measurement time and requires less displacement (indicated by zero displacements in steps 3,4,6,8,and 10 in *Table 6.3.* Additionally there are no position clusters of measuring/testing in *Figure 6.18(A)* (only yellow circle marks are shown)).

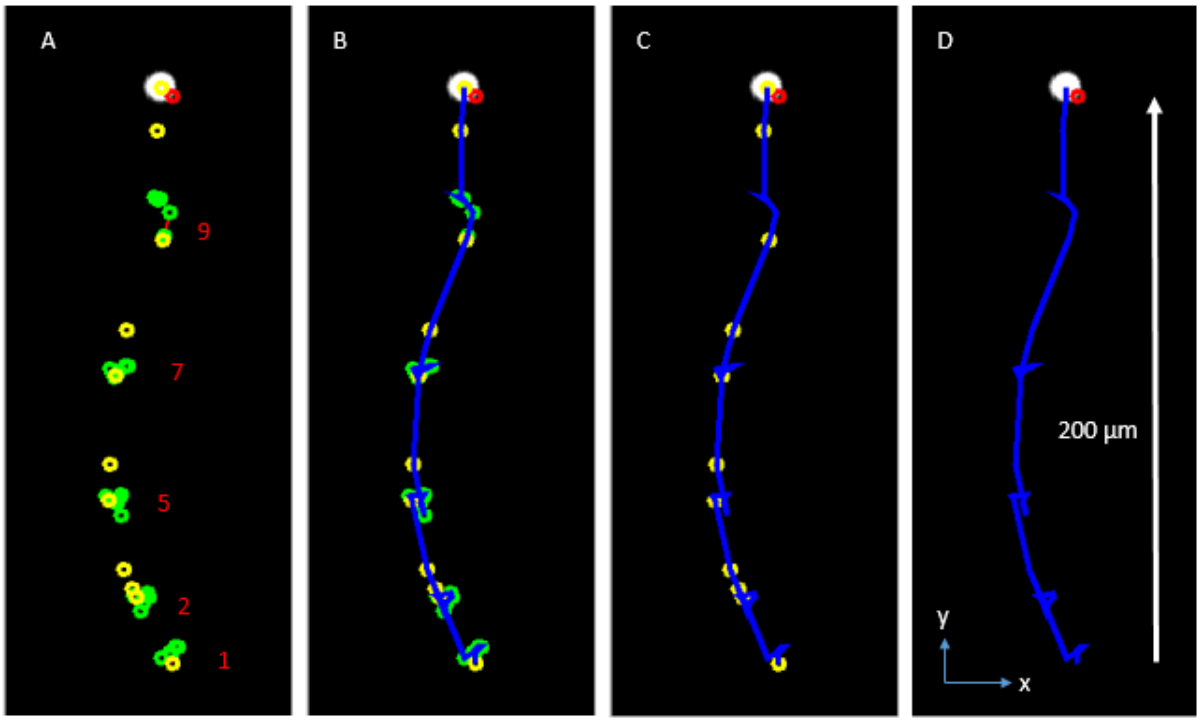

Figure 6.18: Example steering run with DM applied to a levitated 10 µm bead over a 200 µm distance for upward direction towards the target position (red circle). (A) The numbered testing stage positions of all manipulation steps (green circles) with the selected forces (red lines, zoomed in next figure) and particle positions (yellow circles) at the beginning of each step (before measurement and after shifting). (B) The trajectory (blue line) towards the target on the upwards direction, including positions of both stages. (C) The trajectory with only the shifted positions. (D) The trajectory only. The window size for all images is 100x250 µm.

The figure above shows that the manipulation steps 3, 4, 6, 8 and 10 (only the yellow circles are shown in these steps) used the latest forces when no forces measurement is required. This is because either the accumulated or the actual shifted displacement reduced to less than 25 um, while manipulation steps 1,2,5,7 and 9 (green circles) show the forces measurement stage for each step. *Figure 6.19* shows the magnified available forces and the selected ones for these five manipulation steps 1,2,5,7 and 9.

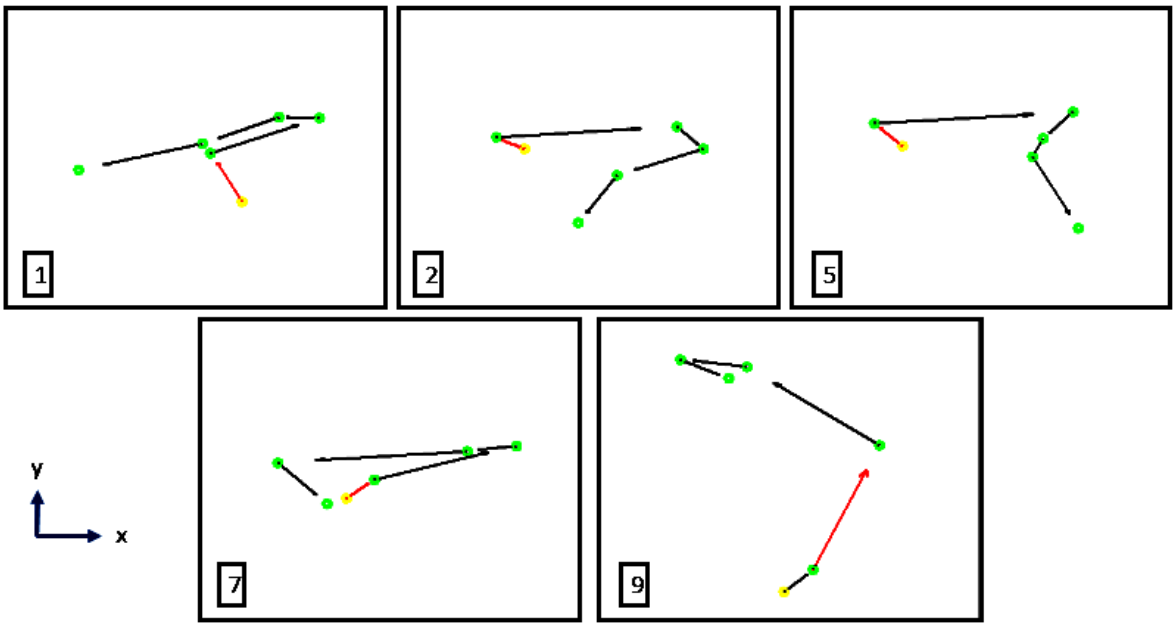

Figure 6.19: Zoomed in view of all available forces (red arrows signify the selected ones) for different manipulation steps that have a testing stage (window size is 10x20 µm).

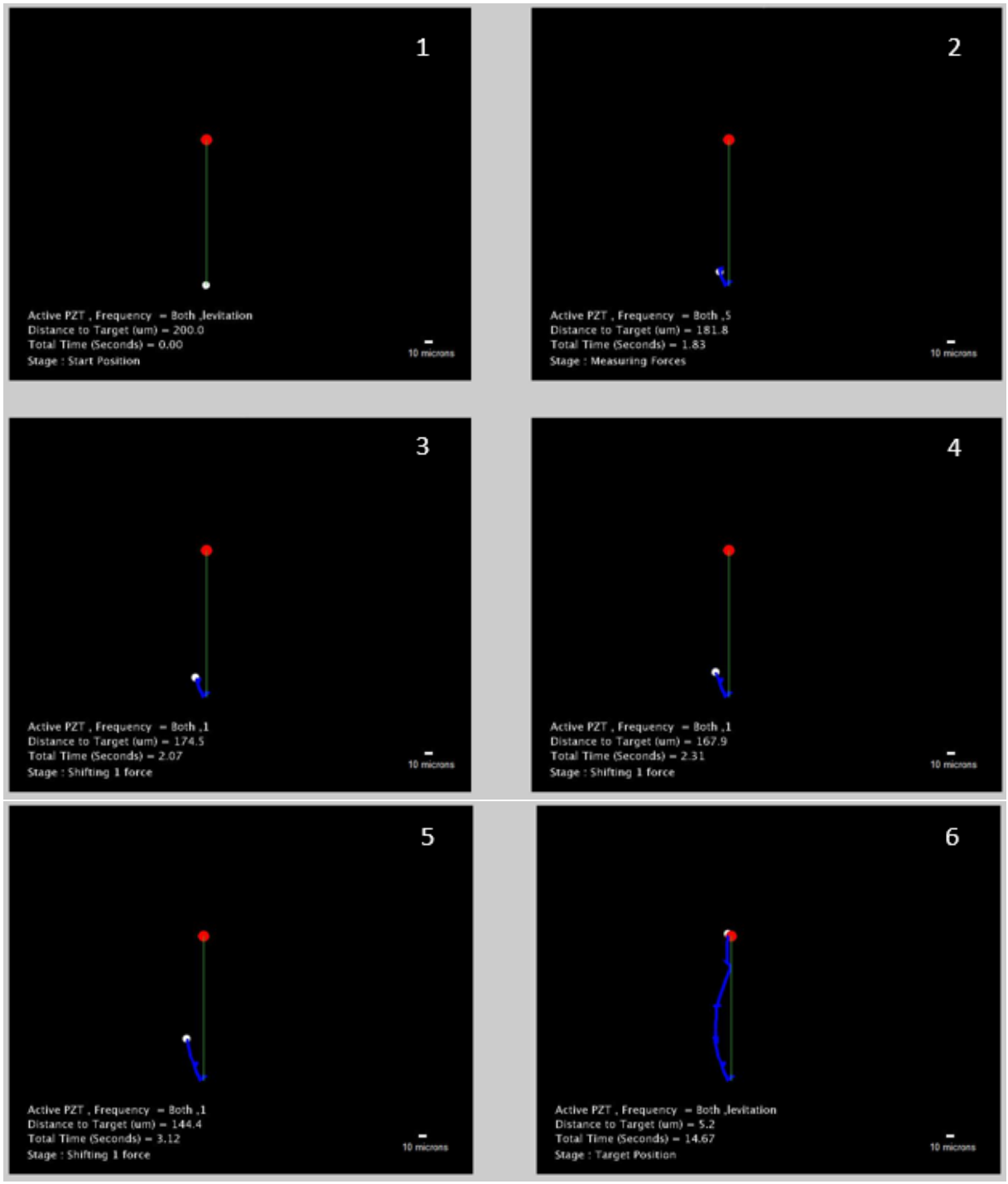

Figure 6.20: Demonstration of real manipulation run of the steering algorithm using the Directed Method to steer a levitated 10 µm bead for a 200 µm distance on the target direction (red mark) in the direction of the microfluidic device sidewalls where the used configuration is both PZTs. The shown images are only selected among the rest of manipulation images to show how the Directed Method works at some steps.

From *Figure 6.20*, the first and last image shows the bead at the start and at the target position respectively with the blue trajectory. In both these images, the bead is levitated using both the PZT configurations only. The bead arrives to the target position after 14.6 seconds of total steering time and is 5.2 µm away from the target. The second image shows the last measuring step of the second

manipulation step. In the third image, the algorithm decides to apply the first frequency for the shifting stage with a desired step size of 12.5 µm as result of the angle difference between the required and the selected direction being more than 28.5 degrees (see step 2 in *Table 6.3*). The resulting actual displacement is 8.2 µm. In this step, the steering algorithm begins to learn from the applied force (only updates the magnitude and direction of the applied force) of the previous step. Then it checks if it is the true condition to perform the measuring stage of forces for the next step. For the second step in *Table 6.3* and the third image, both the accumulated and the actual shifted displacement is 8.2 µm which is less than 25 µm. Therefore the algorithm decides to exit the measuring/testing stage and use the available forces from the previous step which include the used force.

In the fourth image and in step 3 on *Table 6.3*, the accumulated and actual shifted displacement is 15.6 and 7.4 µm respectively. These are again less than 25 µm, therefore another directed shifting displacement is required. In the fifth image and in step 4 on *Table 6.3*, the actual shifted displacement is 25.05 µm, then the algorithm performs the stage of measuring forces. The last image shows the entire bead trajectory (after reaching the target limits) including both displacements due to measuring and shifting forces. The statistical results for this example is demonstrated in terms of direction and magnitude error as shown in *Figure 6.21*.

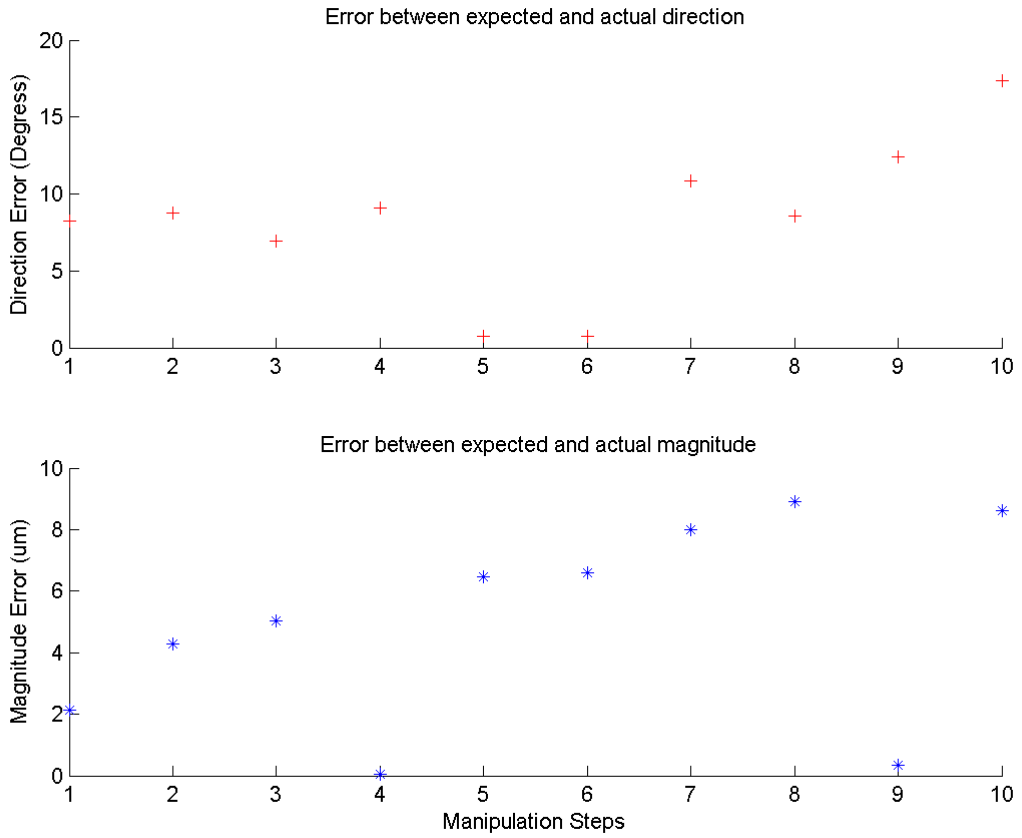

Figure 6.21: Figure 6.15: (Upper graph) Shows the resultant directional error between real and predicted direction. (Lower graph) Shows absolute difference between the expected and the real magnitude.

The difference between the predicted and real positions is demonstrated as a direction error (upper graph) and magnitude error (lower graph). Although there are direction errors associated with both steps 4 and 9 (the algorithm performs the testing stage in step 9 unlike step 4), these two steps show the lower magnitude error. The lowest direction errors are in steps 5 and 6 (the algorithm performs testing the stage in step 5 unlike step 6). The highest direction/magnitude error is recorded in the last step where the bead position is near the target and the algorithm omits the stage of force measurements at this step. However, no clear advantage of using the Directed Method with the designed conditions of shifting the bead for different required step displacement in this particular example is obvious. A more comprehensive analysis of these two errors is presented in Section 6.9.3. *Figure 6.22* demonstrates the actual resulting displacement for both steering stages (measuring forces and combining forces).

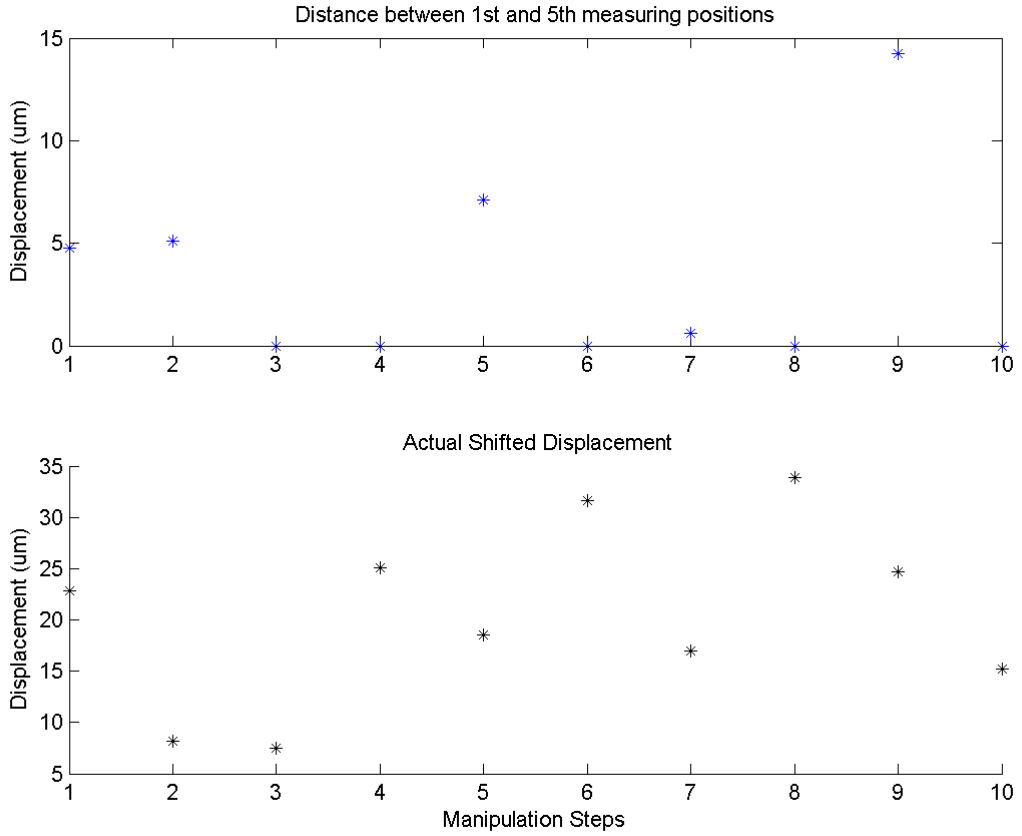

Figure 6.22: Two different displacements are recorded for each manipulation step. One is expected to be a small displacement (actual distance between first and last testing) (upper graph) when the steering system performs the forces measurements while the other displacement (actual shifted displacement) is expected to be approximately equal to the desired step (lower graph).

In the above figure, the direct distance between the first and last measuring position is shown in the upper graph where steps 3, 4, 6 and 8 indicate no measuring forces stage applied. Updated forces were used on those steps as a result of either the accumulated or actual shifted displacement being less than 25 µm. In addition, step 10 also has no measurement stage, this is because the target position is closer to the bead position by less than the desired step displacement of 25 µm. This graph indicates that no clear influence of both the PZT configurations exists. This is in contrast to the single PZT configuration. In the lower graph various actual shifted displacements were recorded for each manipulation step. These varying magnitude displacements are desired to be 25 µm except in steps 2, 3 and 10. With regards to the steps which belong to the Directed Method, steps 4, 6 and 8 show a significant displacement regardless of the magnitude error especially in step number 8. This DM example, despite the variations in displacement, shows the efficiency of the algorithm to steer the particle towards the target where the approaching target distance is shown in Figure 6.23.

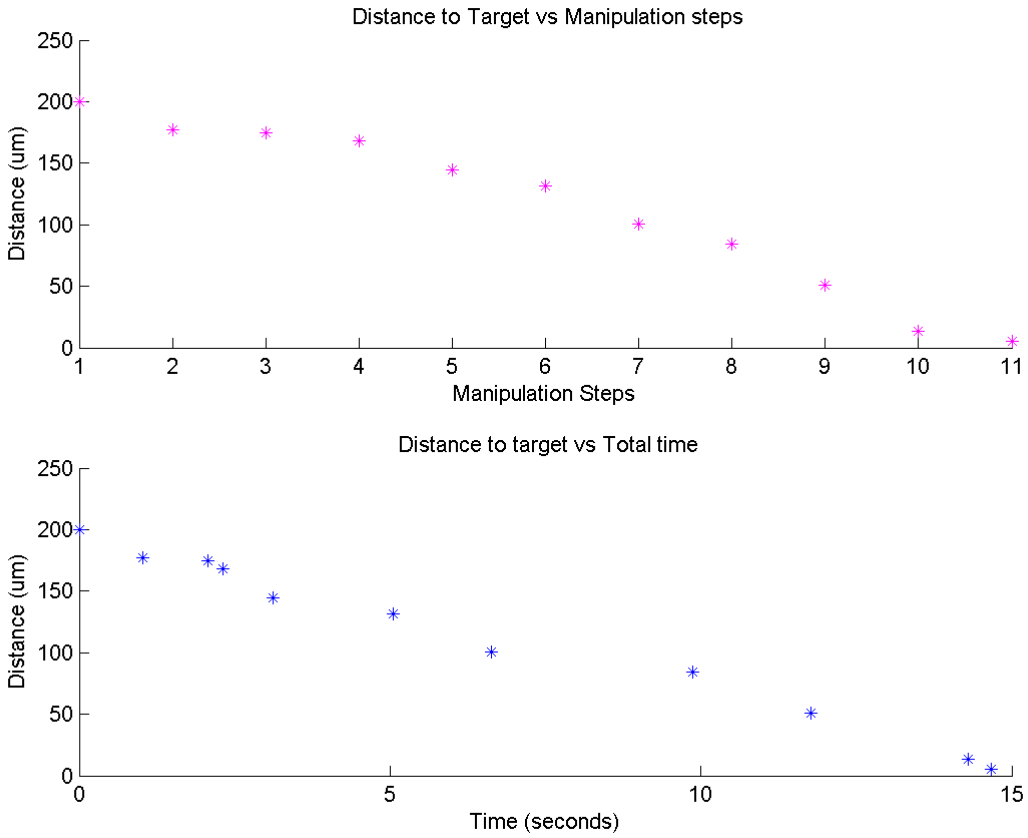

Figure 6.23: Target distance with manipulation steps (upper) and manipulation time (lower). The shown manipulation steps and time represent the both steering stages (forces testing and forces combining) contribution towards achieving the target distance.

The upper graph shows the approach distance to the target with some weakness in the accuracy especially for steps 3 and 4. This is as a result of using the combined PZT configuration which reduces the availability of the forces. Only the main positions of the shifted bead is used to generate this graph (the target distances while performing testing stage is not shown). Unlike the single PZT configuration, the steering algorithm using DM achieved the required distance to the target with the required target accuracy in the limited time. The lower graph shows unsteady improvement of the increased accumulated total time of manipulation for the decreased distance to the target. This total time includes the time of force measurements stage and shifting stage. A more sophisticated speed analysis for this method is shown in Section 6.9.3.

6.8.3 Square Shape Example

The ability of the steering algorithm to achieve certain manipulation shape is represented below to demonstrate the steering of single particle in multiple directions. DM was used to perform this square

shape. Initially the first corner is set as target, followed by subsequent corners once it has been reached. Figure 6.24 shows the steering of a single 10 µm particle through the four target positions.

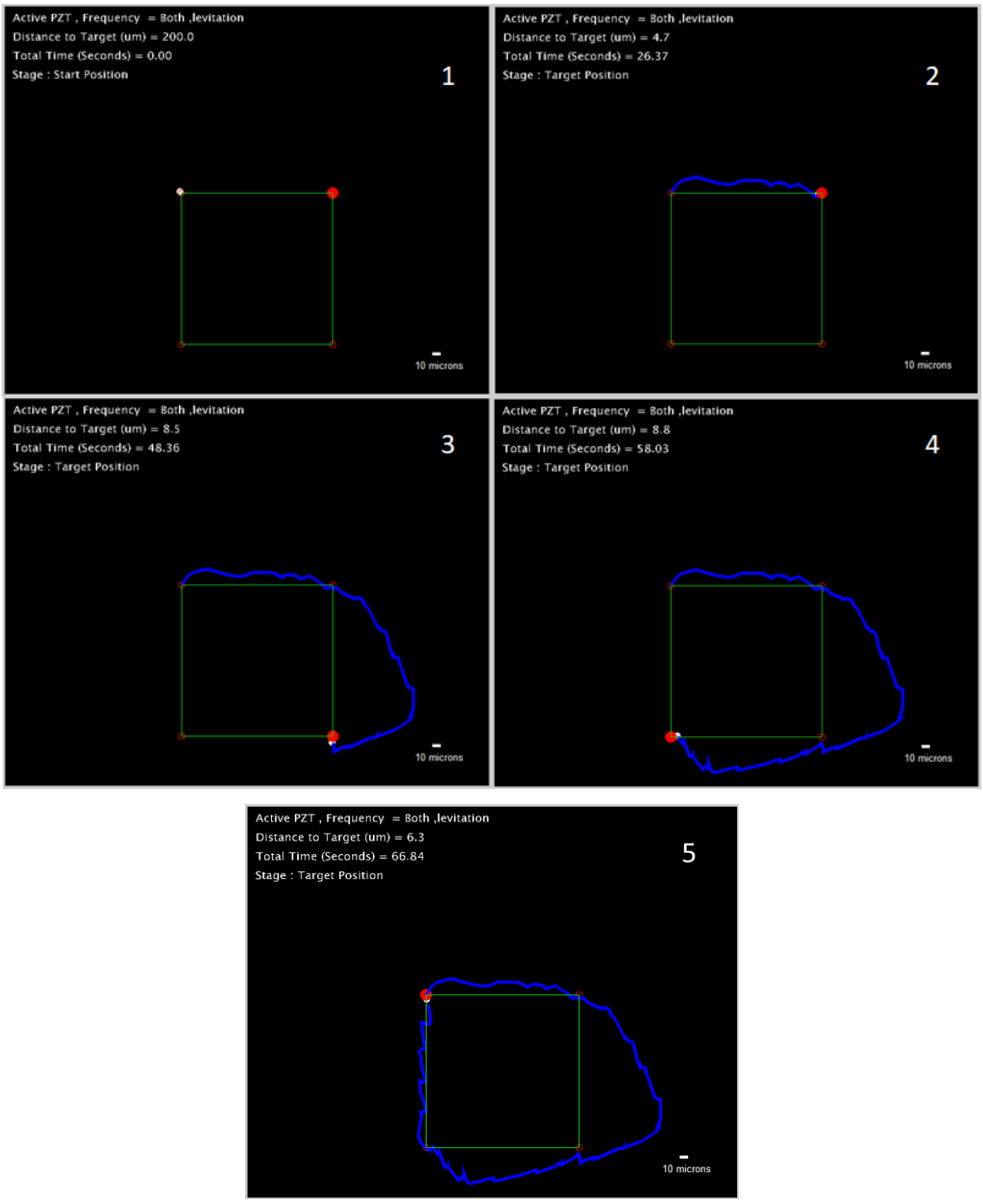

Figure 6.24: Demonstration manipulation run (blue trajectory) set to reach the corners of a square shape (green) using the DM. The levitated 10 µm bead was manipulated for a 200 µm distance four times towards the targets (bolded red circle) in a clockwise direction. Selected images from the sequence are shown to illustrate the progress. The first image shows the starting point when the next target position is 200 µm away. Images 2-5 show the accumulated time since the start of the

manipulation while the target distance is only for that manipulation stage. Finally the square shape was achieved after 66.8 seconds and 6.3 µm away from the starting position.

6.8.4 Comparison between Steering Methods

In order to evaluate the steering algorithm system with its two proposed methods and discuss its efficiency, a number of real experimental steering manipulation runs have been performed for each method. The following histograms can be used to display an analysis of different aspects (successful and failed runs, magnitude and direction errors associated with each manipulation steps and finally the steering speed to manipulate the levitated particles from the start to the end position) that create an overview of the advantages and disadvantages of the proposed steering methods.

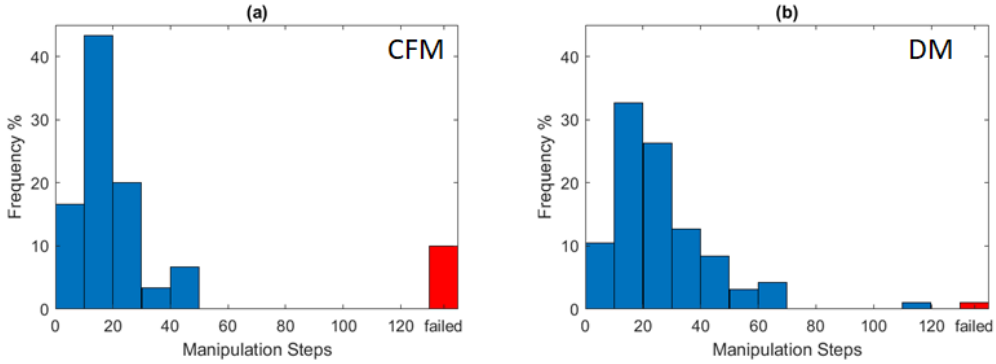

Figure 6.25: Histograms showing the number of steps for a successful manipulation for a) the Combined Forces Method (CFM) and b) the Direct Method (DM). The algorithm continued in all cases until either the bead came to within the 10 µm target distance (successful runs) or until the bead was lost by the tracking code (failed runs). It can be seen that on average the CFM is more effective at reaching the target in fewer steps than the DM. The plots represent data from 30 and 95 runs respectively.

The distribution of the number of steps required to reach the target and the proportion of successful runs is shown in *Figure 6.25*. Runs are allowed to continue until either the target is reached ("success") or until the particle is lost by the tracking algorithm ("fail" – typically due to the particle leaving the field of view). The CFM typically reaches the target in fewer steps than the DM: 80% of successful runs are completed in 0-30 steps for the CFM compared to only 69% for the DM. The difference between the number of failures in each case is not significant, as this relates mainly to runs when the bead was lost by virtue of having started close to the edge of the field of view.

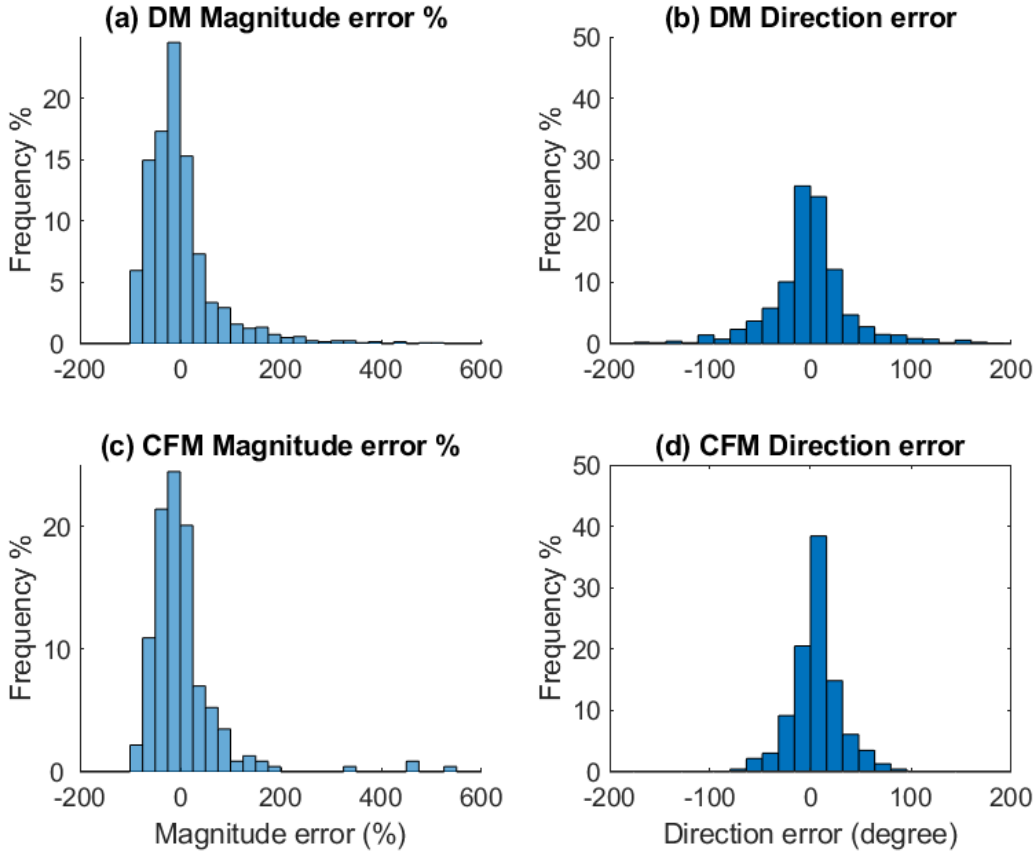

Figure 6.26: The distribution of errors calculated at each step for both of the steering methods. The error between the predicted (selected) and the actual (real) values is presented, where the positive values indicate greater magnitudes and increasing clockwise direction in the actual displacement. (b, d): CFM shows a smaller standard deviation in direction error (24 and 41 degrees for CFM and DM respectively). This is most likely due to there being a measurement step associated with each manipulation step (compared to the DM that relies on measurements from previous steps). (a, c) The magnitude errors are grouped close to the zero mean, and have similar distributions. The plots are formed from 1190 and 229 data points for the DM and CFM methods respectively.

The error between the predicted (as calculated from measurement) and the actual bead displacements during the shifting stage is shown in *Figure 6.26*, where the positive values indicate that the actual directions and magnitudes are greater than predicted values.

In *Figure 6.26(b, d),* the CFM shows less direction error than DM, which is anticipated as it makes measurements more often. Both methods are similar in terms of magnitude errors *Figure 6.26(a, c)* where the mean and standard deviation magnitude errors are 3.6% ± 71.6% and 3.4% ± 76.0% for DM and CFM respectively. These errors can be explained as being most likely to be resulting from the following causes:

A) Timing: variable latencies of ±5.3 ms in communication between the code and the USB interface caused the frequencies to be applied for periods different to those anticipated.

B) Heating effects: Changing temperatures can lead to drift in resonance frequencies that may cause forces to differ between the testing and shifting phases. The DM records less measurements of forces and hence has less computation time. This leads to a more sustained application of the manipulating resonances, and hence a higher temperature rise. a temperature rises was typically observed in the order of 1.7 and 1.0 °C for DM and CFM respectively during the course of a 1-minute manipulation, and thus slightly larger errors are expected in the DM from this source.

C) Acoustic field uniformity: The steering algorithm assumes that forces do not vary with small changes of position in order to linearly extrapolate predicted manipulation distances. However, there will be small changes (since the manipulation steps are a significant proportion of a wavelength), and this will contribute to the errors seen, particularly when the particle displacements approach the scale of force-field variation which is of the order $\lambda/4$ (75 μm at the levitation frequency used here). The force fields will vary between the actual start position of the shift phase and the position at the beginning of the test phase due to the movement caused by each measurement (see *Figure 6.2*). This can be mitigated by keeping the test steps as small as possible (subject to the constraint of also keeping the measurement errors resulting from vibrational noise small). The field also varies along the path of the shift phase; this effect is reduced by keeping the shift step size small (25 μm). However, there is a trade-off as if this becomes too small, it can become overwhelmed by the offsets in position that occurs during the testing phase.

The contributions of each cause (A,B and C) are hard to quantify, however it is observed that over a shifting distance of 25 μm the forces can often vary by as much as 50%.

Figure 6.27 compares the average manipulation velocity of the two methods. The reported value is the average velocity that would be required if the manipulation path were straight (i.e. the total straight distance between run start position and target position divided by the total manipulation time), and does not reflect the average speed over the actual, indirect path that is taken. It can be seen that the DM is typically faster than the CFM, which is likely to be a result of the DM measuring forces less frequently.

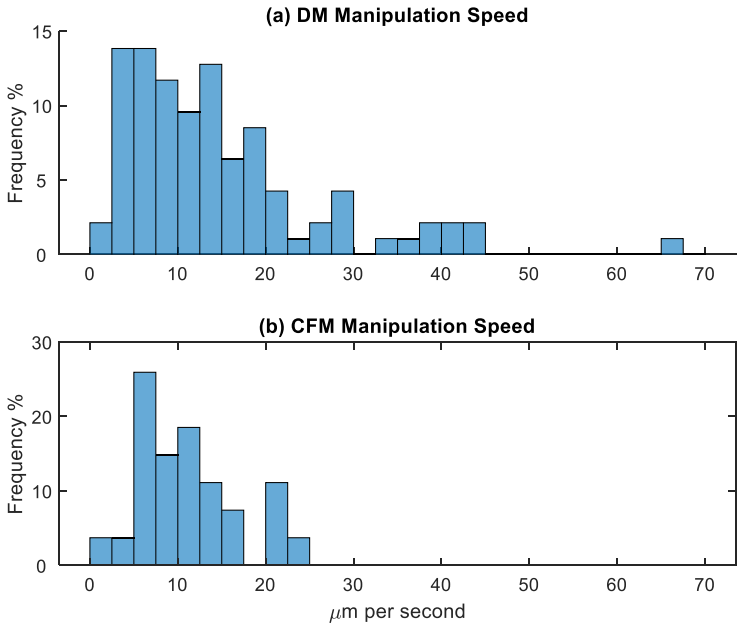

Figure 6.27: The distribution of average manipulation speeds for the two different steering methods. Only successful steering runs are included in the generation of these histograms. The average manipulation speed over the course of a run (from initial position to target position) for the two different steering methods have mean value of 15±11.5 and 11.2±5.6 μm/seconds for the DM and CFM respectively. The CFM is typically slower than the DM as a result of it measuring forces at each step. The graphs formed from 94 and 27 data points respectively.

In order to measure the forces available at each step without unduly disturbing the particle trajectory, the displacements during the test phase have a small value of μm (typically 5-10 μm), which in the presence of the vibrational noise (typically ±1 μm) leads to reasonably high errors between the predicted and actual particle displacements at each shift step. Despite this, the method is robust and is able to successfully bring back tracked particles to the direction of the intended target trajectory in around 96% of runs. The 3D printed and laser cut microscope design that was employed in this study is more sensitive to such vibrations compared to conventional microscopes. It is suspected that with lower vibrational noise, it would be possible to achieve more precise and quicker manipulation as smaller, more precise measurement steps could be taken. Another key method to enhance manipulation speed would be to reduce latencies in the system. This could be achieved by using a real-time operating system, I/O hardware with lower latencies, and a camera operating with lower exposure times and faster readout.

Also it is noted that more sophisticated, model based algorithms could be employed to significantly enhance manipulation accuracy and speed. For example the acoustic force fields derive from periodic potential landscapes; prior knowledge of the typical wavelength scales of these landscapes coupled with predictions based on stored values from prior locations would give the possibility of reduced

testing (through informed prediction), reducing both the number of forces tested and how often they are tested.

Observation of the forces associated with each mode under microscopy suggests that the lateral forces associated with each mode primarily result from radiation forces as the forces tend act towards points rather than display significant vorticity. However, it is a useful feature of the approach taken here that the source of the forces on the particles is not important from the point of view of the control algorithm, as it progresses by measuring the total force from all sources at each measurement step.

Armani et al[56], demonstrate that in a fluidic system with n degrees of freedom it is possible to manipulate (n-1) particles independently. In the current device some additional forces have been obtained through the multiple PZT areas that can be independently actuated, however the available forces are still limited, and the existing forces overlap in terms of directions they offer. It is envisaged that with more attention to device design it would be possible to create more degrees of freedom in an acoustic device, and hence manipulate more than just one particle at a time.

6.9 Conclusion

The steering algorithm has shown a promising performance which is demonstrated by the two suggested methods (CFM and DM). Both steering methods show manipulating capability to steer the selected 10 µm particles into the target positions within 10 µm accuracy. However, applying CFM or DM is limited by the range of force variations longer than λ/4. The simulation of the steering algorithm helped in troubleshooting the lack of forces availability where another identical acoustofluidic device has replaced the malfunctioning one and has shown a more optimal steering result.

Chapter 7. Conclusions and Further work

The 2D lateral positioning of micro particles is important for applications which require bringing cells to a specific position for further processes such as measurement and interaction. However, the recent techniques and methods that have been employed for positioning micro particles using ultrasonic waves, have not demonstrated a precise positioning of cells and particles.

In this thesis, a novel concept for controlling the position of micro particles within MEMS (micro-electro-mechanical systems) devices has been introduced. The lateral acoustic radiation forces are considered as the main actuating force. Two different types of control algorithms (navigation and steering) have been established with both simulation and experiments. The common concept of both control algorithms is in using an automatic feedback loop which uses a camera to dynamically track the particle positions and to modify the applied forces.

Both types of algorithm uses two resonance frequencies, the first one is the acoustic half-wave resonance frequency for particle levitation at the half-height of the device using the axial radiation force. The second resonance frequency functions to shift the levitated particles in different directions using the lateral forces that are different from one resonance to another. The algorithms choose which resonance frequency mode is applied at each step.

The main contributions that this research has achieved are listed below:

- Investigation of various acoustofluidic devices, evaluating their ability to contribute useful lateral forces for the type of manipulation explored here. In particular a novel design incorporating a cut electrode, and investigation of the resulting forces it produced. (Chapter 3).

- Investigations into ways to reduce background flow in acoustofluidics devices, resulting in a clearer picture of this effect and quantification of the advantages of closing the fluidic loop to prevent unbalanced hydrostatic pressures. (Chapter 4).

- Evaluation of the feasibility of a novel navigation type control algorithm that measures forces prior to a manipulation run. Identification of the key practical issues that make this subject to large errors. (Chapters 4&5).

- A novel control algorithm based on a feedback loop have been formulated and formed from a camera system. This includes the hardware architecture, evaluation of the level of accuracy

that can be obtained in measurement steps, evaluation of alternative strategies, and statistical comparison of a large number of manipulations in order to compare them (Chapter 6 and submitted paper, Appendix A).

Both algorithms (navigation and steering) are still considered as proof of principle. Future work to extend and improve the algorithms might include:

- Temperature control to make the system more stable. Temperature variation tends to change the resonance frequencies, making the device less effective.
- VVFMs can be considered as a tool for investigating lateral modes in any acoustofluidic devices and can be used to characterise the type of lateral forces anywhere (even away from the pressure nodes, transducer streaming forces for instance) in the acoustofluidic device (proper particle size might be required).
- It is believed that increased precision and manipulation speeds could be achieved beyond this proof of principle study. More sophisticated, predictive steering algorithms could make better use of the available data to better actuate the acoustofluidic device. Control algorithms based on machine learning concepts are more likely to achieve such requirements where the number of the measurement stages per run will be less as more steering runs are performed over the same manipulation area.
- In addition, the acoustofluidic devices presented here have a rather limited number of resonances (hence different forces) available to the algorithm and that with an alternative acoustofluidic device design this could be improved (e.g. by increasing the number of transducers or using a multi-SAW actuator).
- Manipulating multiple particles is also a possibility in a device with more available resonances. This could be important for applications that require bringing two cells together or moving separate particles to multi target areas concurrently.
- More sophisticated hardware could reduce latencies and hence improve both accuracy and manipulation speed. In particular, errors in measuring small particle displacements during the test phases significantly limits the algorithm.

APPENDIX A

Paper Submitted to the Journal of Acoustical Society of America

Acoustofluidic particle steering

Zaid Shaglwf [1], Bjorn Hammarström [3], Dina Shona Laila [2], Martyn Hill[1], Peter Glynne-Jones[1]*

[1] School of Engineering, Faculty of Engineering and Physical Sciences, University of Southampton, SO17 1BJ, UK.

[2] School of Mechanical, Aerospace and Automotive, Coventry University, CV1 5FB, UK.

[3] Department of Applied Physics, Royal Institute of Technology, AlbaNova University Center, Stockholm, Sweden

* Corresponding author: P.Glynne-Jones@soton.ac.uk

Keywords: Acoustofluidics, particle manipulation.

APPENDIX A

ABSTRACT

Steering micro objects using acoustic radiation forces is challenging for several reasons: resonators tend to create fixed force distributions that depend primarily on device geometry, and even when using switching schemes, the forces are hard to predict a-priori. In this paper an active approach is developed that measures forces from a range of acoustic resonances during manipulation using a computer controlled feedback loop based in MATLAB, with a microscope camera for particle imaging. The arrangement uses a planar resonator where the axial radiation force is used to hold particles within a levitation plane. Manipulation is achieved by summing the levitation frequency with an algorithmically chosen second resonance frequency, which creates lateral forces derived from gradients in the kinetic energy density of the acoustic field. Apart from identifying likely resonances, the system does not require a-priori knowledge of the structure of the acoustic force field created by each resonance. Manipulation of 10 µm microbeads is demonstrated over 100s µm. Manipulation times are of order 10 seconds for paths of 200 µm length. The microfluidic device used in this work is a rectangular glass capillary with a 6 mm wide and 300 µm high fluid chamber.

I. INTRODUCTION

In the recent years, manipulating micro particles and cells using an acoustic radiation forces – acoustofluidics - has found numerous applications in lab-on-chip devices[1]. Potentially useful manipulation operations include bringing cells to specific positions, bringing cells or cells and microbeads together and the control of motile organisms for observation. Early devices typically trapped or focussed particles towards locations that were fixed, and dictated by the modes dependent on device geometry [2,3]. A number of approaches have been explored to create flexible manipulation devices that are able to dynamically modulate trapping positions.

One option is to switch between resonant modes to create trapping positions that form a continuum of positions, to either translate particles through a range of positions [4-7] or to create a new fixed manipulation position [8]. An alternative, analogous to optical tweezing, is to use higher frequency

systems that form a localised focus and translate the manipulation chamber relative to the transducer [9-11].

The standing wave pattern that determines trapping locations can be considered a superposition of two counter propagating waves. By aligning transducers at an oblique angle [12,13], utilising transducers that minimise reflections [14], or relying on absorption [15], systems can be created that allow each of these components to be independently created with arbitrary phase differences. Thus by modulating the phase difference arbitrary trapping positions can be attained.

Extending this work to circular 2D arrays of transducers, more complex acoustic fields can be created, including acoustic vortices, which contain pressure minima at their centres [16,17]. This is useful since acoustic forces often (see below) direct particles towards these locations. Other more complex array based schemes have also been explored in air based resonators [18], though these go beyond the scope of the current review.

An alternative to controlling the pressure node position is to exploit the kinetic energy gradient contribution to the radiation force (see below), which tends to move particles levitated in a 2D pressure node to regions of maximum acoustic velocity. This movement can be effected by arrays of transducers [19,20], or simply by changing the resonance frequency employed as there are often a number of closely spaced resonances around the half-wave resonance of a planar resonator[21-23].

In this paper, we present a control system that uses radiation forces (and potentially acoustic streaming too) to manipulate particles levitated in a half-wave resonator. A microscope/camera arrangement images the position of particles, and applies a control algorithm based on a PC to actuate a PZT transducer that can excite a number of different acoustic modes within the resonant manipulation chamber. The frequencies of the modes are determined in advance, but the forces that result from them are assessed and used dynamically without prior knowledge of their magnitude or direction.

APPENDIX A

II. BACKGROUND

As an acoustic wave travels back and forth throughout the chamber of a planar microfluidic device, it creates a standing wave. Due to non-linear effects, there is a small non-zero time average force on particles, the acoustic radiation force [24]. These forces depend on the properties of the particle as well as the shape and amplitude of the acoustic field. The force on a small (compared to the wavelength) particle is given (in a non-viscous approximation) by the following gradient [25]:

$$F = \nabla\left(\left(\frac{3(\rho_p - \rho_f)}{(2\rho_p + \rho_f)}\langle E_{kin}\rangle - \left(1 - \frac{\beta_p}{\beta_f}\right)\langle E_{pot}\rangle\right)\right)V \qquad (1)$$

with

$$E_{pot} = \frac{\beta_f}{2}\,p^2 \qquad (2)$$

$$E_{kin} = \frac{\rho_f}{2}\,u^2 \qquad (3)$$

where *F* is the time averaged force on a particle of volume *V*, and E_{kin} and E_{pot} are the kinetic and potential energy densities respectively, which are functions of acoustic velocity magnitude u and acoustic pressure field p, and the brackets $\langle \ldots \rangle$ denote the time average. The particle and fluid densities are ρ_p and ρ_f, while β_p and β_f are the particle and fluid compressibilities.

It can be seen that there are two terms that contribute to the force, based on gradients of the kinetic and potential energy densities which (for particles less compressible and denser than the surrounding fluid) direct particles towards acoustic velocity antinodes and pressure nodes respectively. In planar resonators it is convenient to decompose the primary acoustic radiation forces into two components, the axial and lateral component. The axial force, which is aligned with the standing wave direction, has contributions from both terms of equation (1), and in a half-wave system tends to levitate particles at the pressure node (which is also coincident with the velocity antinode) at the chamber centre. In the plane of the pressure node, which may undulate[26], there are

no gradients in the potential energy term, and it is only gradients in the kinetic energy which give rise to the lateral component[23]. In this work the levitation position of particles may vary depending on the precise mode that is excited, thus forces from gradients in both terms are likely to act. Additionally, acoustic streaming could potentially be present and put to use for manipulation (though in the results presented below, we conclude that this is a weak effect).

III. MICROFLUIDIC DEVICE

We created a device based on a rectangular glass capillary (ID 0.3 x 6 x 50 mm; Vitrocom, NJ, USA). A PZT (1 x 6.6 x 25 mm, PZ26, Ferroperm) transducer was coupled to the glass capillary using epoxy adhesive (Epoxy 301 Epotek Billerica, MA, USA). The capillary has advantages of mechanical stability, and also lower losses compared to devices with more damping or thicker chamber walls, which will tend to reduce heating effects.

The glass capillary was found to create strong lateral modes (and hence forces) across the width of the device(the *y* coordinate in Figure 1), but relatively less useful forces in the *x* direction along its length. In order to create modes with forces in the *x* direction, the transducer was configured with cuts across both the top and bottom electrode surfaces as shown in Figure 1; this divided the transducer into two separate regions, creating asymmetry such that modes created by activating just one of the regions had useful forces in the length direction. It was found that in the area between the two electrode regions there was insufficient levitation forces, so the results in this paper are presented for a manipulation region above the left transducer that is 1 mm away from the cut and 2.7 mm from the capillary sidewalls. In this region there was typically a correspondence between the direction of the lateral forces and which transducer was activated, thus the control algorithm chose which transducer to activate based on the direction of the required force (as described below). However, since the algorithm measures forces dynamically this simply increased the chance of a suitable force being found without needing to test all possible combinations at each step.

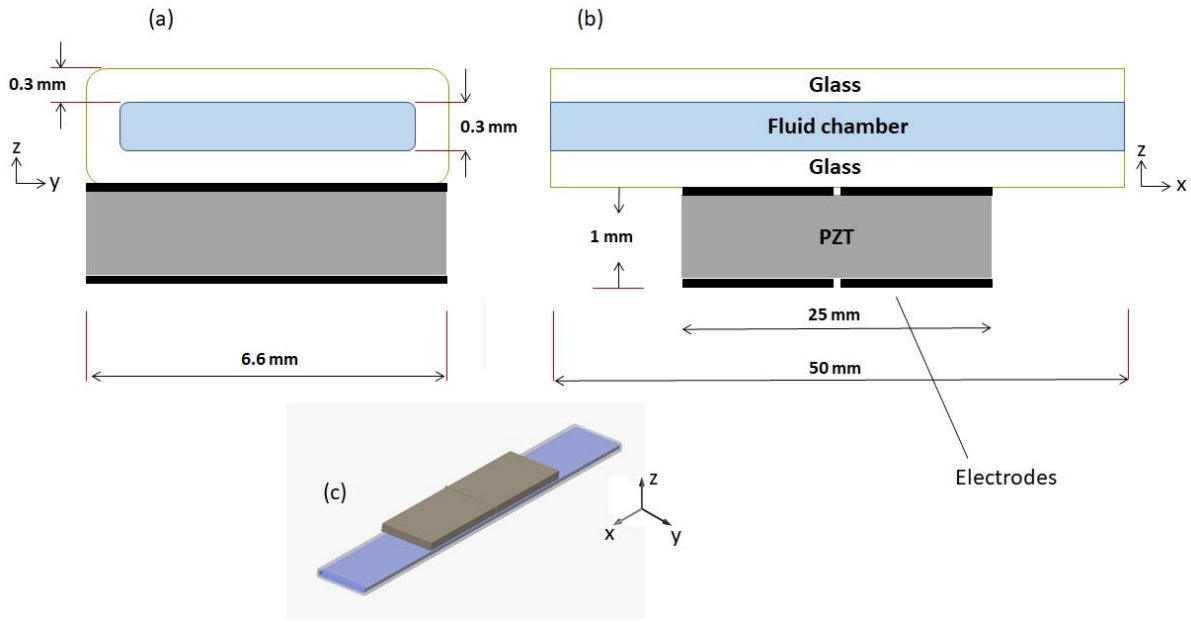

Figure 1. Device configuration. (a) Cross-section, (b) Length section and (c) 3D representation. The electrodes have been scored (as seen in the length section) to divide the transducer into two electrically independent regions. Not to scale.

Resonances were found at: 2.48, 2.536, 2.568, 2.814 and 2.382 MHz (hereafter referred to as resonances or frequencies 1-5). These modes were used for lateral manipulation. The close proximity of these modes does, however, create some sensitivity to temperature variations. The strong half-wavelength resonance found at 2.382 MHz was also used for background levitation, and was applied simultaneously (see hardware, below) with the manipulating resonances. This mode was applied at lower amplitude for the background levitation, compared to the higher amplitudes used when the lateral forces it produced were required for manipulation.

Measuring the acoustic pressure amplitude within the resonant cavity is difficult due to the confined space. The acoustic pressure amplitude inside the capillary for a given drive voltage was found by balancing the weight of a 10 µm fluorescent polystyrene bead against the acoustic radiation force in the manner described by Spengler et al.[27]. For the levitation mode at 2.382 MHz, acoustic pressure was found to be related to drive voltage applied to the PZT by a factor of 31 kPa/Vpp.

IV. SYSTEM CONFIGURATION

Figure 2 shows the layout of the system hardware. A USB microscope camera (Thorlabs DCC1645C) uses a 10× objective and FITC emission fluorescence filter (Thorlabs MF530-43) to visualise fluorescent microspheres (Fluoresbrite YG 10 µm, polysciences) that are illuminated by a royal blue 1W LED (Lumileds, Luxeon Rebel Star, 440-450 nm).

The camera is connected to a Windows PC that uses MATLAB to execute the control algorithm. Output from the program is routed via a USB digital IO board (NI, USB-6002). This board controls two devices: a) analogue switches (VO14642AT, Vishay Semiconductors) that control which of the transducer regions are activated; and (b) a microcontroller (Arduino UNO) which in turn communicates with two DDS (direct digital synthesis) modules (Analogue devices, AD9850). The Arduinos are preloaded with the required frequencies (determined in advance by examining the impedance spectrum of the transducers and selecting modes that are observed to offer a useful range of forces), and are able to rapidly change the outputs of the DDS modules depending on control signals from the IO board.

It was found that variable latencies between program commands and corresponding changes in USB controller outputs caused errors in the requested pulse length of ± 5.3 ms, contributing in part to the errors discussed in Section VII. By keeping pulse lengths to more than 100 ms, these errors were kept reasonably small. The camera exposure time was set to 25 ms, and there was a total delay of 150 ms between issuing a command to capture an image and the data being uploaded and available to the program.

One of the DDS modules is used to create a background levitation field ($\boldsymbol{F_{lev}}$) while the second is used to switch between different resonances to carry out the lateral manipulation of the levitated beads ($\boldsymbol{F_{lat}}$). The two signals are combined by a custom summing amplifier (based on Analogue devices, LT1210). The output amplitudes of the two components are kept fixed at 1.5 and 20 Vpp for the levitation and manipulation frequencies respectively.

In order to prevent small fluidic flows occurring during levitation that would interfere with the manipulation, a 6-port valve is used to connect the inlet and outlet ports of the device together after the initial introduction of the sample containing the beads. This equalises pressures and results in drift rates lower than 1 µm/s.

The camera, pentaprism mirror, fluorescence filter and objective are arranged as shown in Figure 2. Rather than using an expensive microscope, the results presented here were collected from an arrangement that held the imaging components in alignment through a custom laser cut acrylic and 3D printed holder. This arrangement is likely to be more sensitive to vibrations than a conventional microscope, however the steering algorithm was robust to these. (See the next section for how the algorithm deals with this noise in the location measurement).

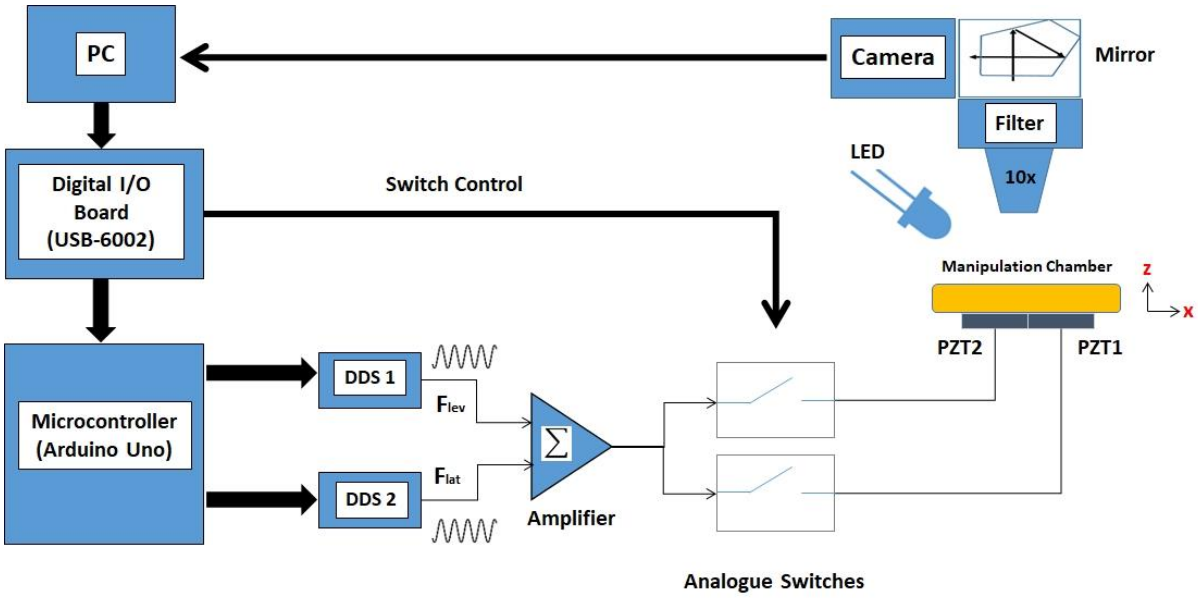

Figure 2. System hardware. A 10× objective is coupled to a camera via a fluorescence filter and pentaprism mirror cube. It images the microfluidic chamber where ultrasonic resonances are actuated by a PZT transducer with two electrode regions. The control algorithm based on the PC takes input from the camera and uses an interface board and microcontroller to communicate with

DDS boards to synthesise MHz waveforms to excite resonances. The signals are summed and amplified, then applied to the electrodes under the control of an analogue switch.

V. STEERING ALGORITHM

The control algorithm is coded in MATLAB, and follows the outline shown in Figure 3, which is common to both alternative methods discussed below. At the beginning of the manipulation run, a series of 20 images are taken, and the positional measurement accuracy is estimated based on the variation in bead position (resulting primarily from vibration in the system). Typically, this is of order ±1 μm.

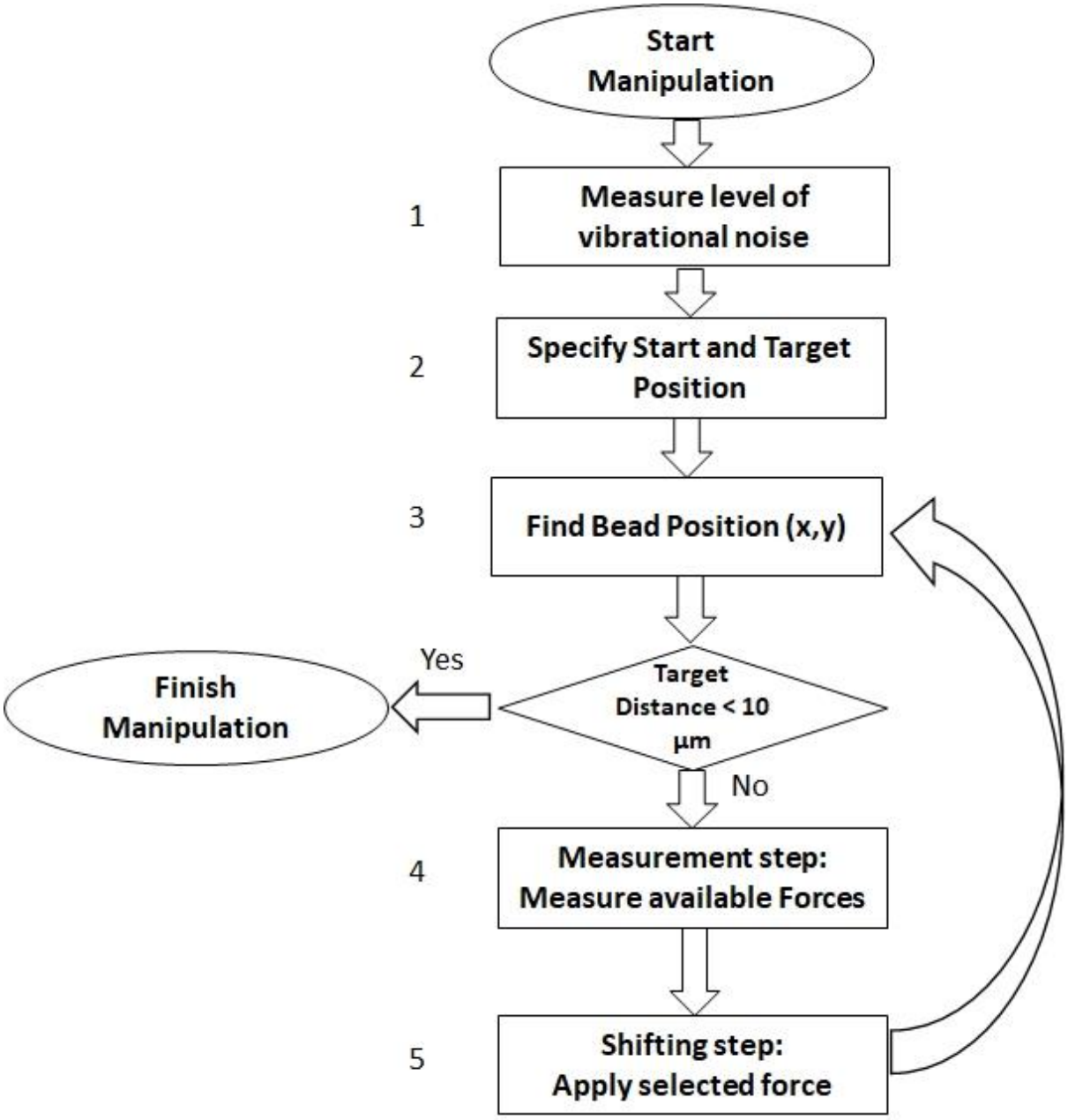

Figure 3. Flow chart showing elements common to both steering algorithms.

A key feature of the acoustic field is that the forces created tend to vary at a scale of O(λ/4) or longer. Thus, if during a test step the particle travels too far from its initial position there will be some error between the predicted force (based on the initial position) and the actual force created when the resonance is applied starting from the perturbed position. The control algorithms make a linear approximation: that the result of a longer pulse of a resonant frequency will create a particle

displacement of a correspondingly longer distance, but in the same direction. By keeping the intended step size small, the effect of the actual non-linearity is reduced. Figure 4 illustrates the measurement process, showing how during the measurement phase the bead makes small movements from its initial one (positions P_{1-5}) as the resonances are tried in turn.

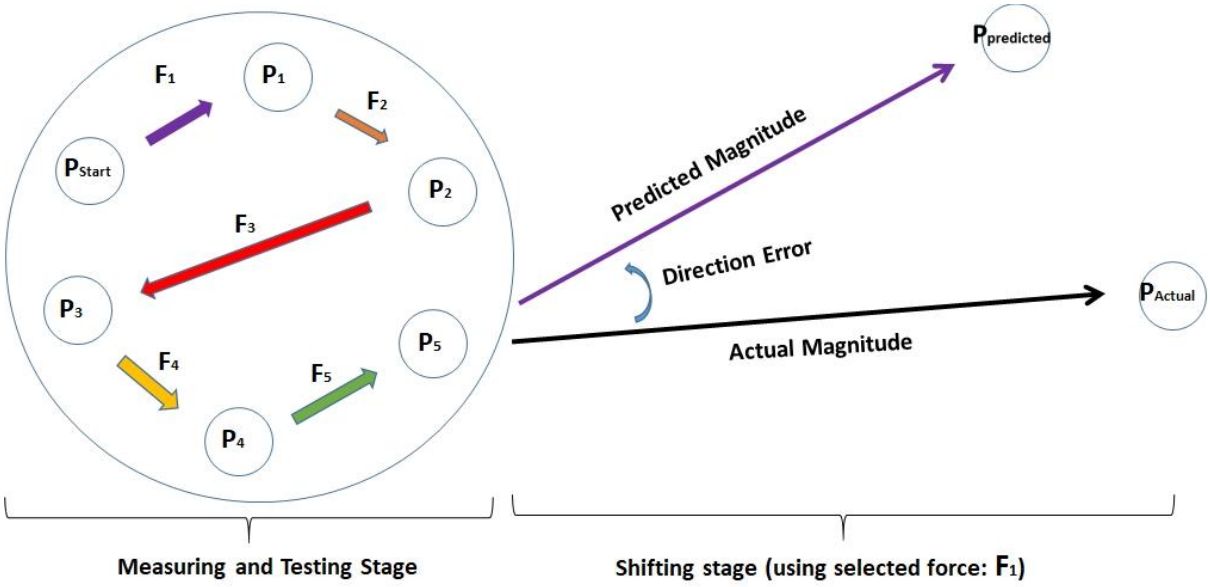

Figure 4. The process of testing and measuring the five manipulation resonances and selecting the one(s) most appropriate to reach the target. The system applies each resonance (F_{1-5}) in turn and measures the resulting displacement to deduce the force on the particle. The particle moves between five positions (P_{1-5}); the system then shifts the particle along the manipulation track by applying the selected resonance ($F_{selected}$). There is an error between the predicted and actual particle position after applying the selected force due to measurement errors, timing errors, and variation in acoustic field. Figure not to scale. (Colour online)

During measurement phases, the pre-determined set of resonance frequencies are initially tested with a pulse length of 100 ms. Based on the measurements of vibration amplitudes carried out at

the beginning of the run and the observed displacement, the predicted error from this source is calculated. If this error is greater than 50 % (i.e. only a small displacement is seen compared to the estimated vibrational noise level) then the measurement is repeated with pulse length calculated to give a 30% measurement error. If more than 2 secs is required, that resonance is ignored for the step. If this error is lower than 10 % (i.e. the resulting displacement over the measurement step is relatively large) a shorter pulse length is used in for the same frequency in the next measurement step, subject to a minimum pulse length of 100 ms. This strikes a balance between testing the available forces with larger pulses of the resonant frequencies (more accurate) versus shorter pulses (which perturb the manipulation track less).

After the measurement phase, the algorithm chooses which resonance, or combination of resonances, is most suitable and applies it to create movement along the manipulation track. The algorithm continues until either the bead is within 10 µm of the target or (as occasionally happens) the bead is lost from the field of view.

Finding the bead's position accurately and quickly is crucial for a successful and rapid manipulation. Speed is achieved by initially searching for particles close to their predicted position by feeding a cropped image to the MATLAB '*imfindcircles*()' function which implements a Hough transform. If the particle is not found, a wider region is searched. This approach also helps avoid tracking the wrong particle when more than one is present (although in the current study we typically try to work with only one particle present). Image processing typically takes around 30 ms.

VI. STEERING METHODS

Two alternative implementations are explored here: 1) The combined forces method (CFM) and 2) The Direct method (DM). The two alternatives trade off accuracy through more rigorous measurement (CFM) against speed through less testing (DM).

In both approaches, the choice of which transducer to activate (see Figure 2) is given by:

-45° < (desired direction) < 45°	*PZT1 actuated;*
135° < (desired direction) < 225°	*PZT2 actuated;*
Other cases:	*both PZT1 and PZT2.*

where the angular direction is measured from the x-axis (as defined in Figure 1). The desired direction is the target direction measured from the particle current position. In other words, if the desired direction is in the left or right quadrants, just one transducer is activated (based on the prior knowledge that this tends to produce x-directed motion of the correct direction), while if the desired direction is predominantly *y*-directed then both are used.

A. Combined Forces Method (CFM)

In this approach, the available forces are tested (Figure 3, step 4) after each larger shift step (step 5). After testing, two forces are chosen that when applied sequentially are predicted to produce a net displacement in the direction of the desired target. The algorithm chooses the appropriate forces by finding the nearest pair of clockwise and anticlockwise from the desired direction. Pulse lengths are chosen to create a predicted step of 25 µm (except under the special condition b), below). With the current setup this is achieved by applying each force in turn without imaging to find bead position between them.

The following special conditions apply:

a) If the combination of forces required includes using a force that is more than 86° from the target direction, then just a single force is used, choosing the one closest to the required direction.

b) If neither of the forces are within 86° then the closest available force is used with a smaller step size of 12.5 µm. Although the resulting step is not directly towards the target, there is a chance that a more suitable force will be found after this step.

c) If the particle is within 25 µm of the target, no more measurement steps are taken, and the pulse length is set to achieve a predicted step of half the remaining distance.

Statistical results from a large number of runs are presented below, but we first present an example run to illustrate the process. A bead is manipulated over a 200 µm distance, with the conditions at each step along the way shown in Table 1. Figure 5(a) shows the trajectory. The manipulation stops at a distance of 6.43 µm from the target (red circle) after a total manipulation time 9.35 seconds.

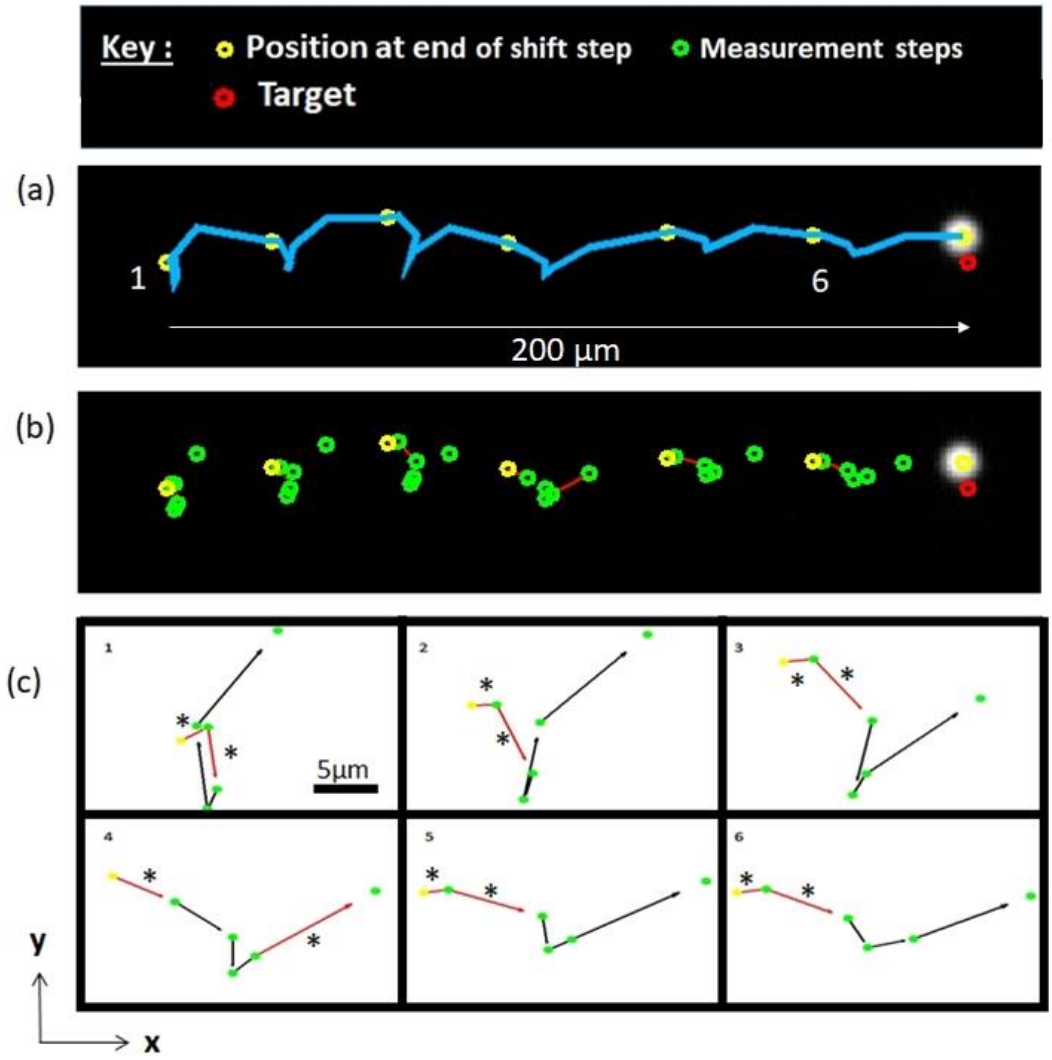

Figure 5. Example steering run with CFM of a levitated 10 µm bead over a 200 µm distance from left to right towards the target position. (a,b) The trajectory toward the target on the right hand side, including the position at the beginning of each stage, and also the positions (b) after each measurement displacement. (c) A magnified view highlights the two forces that were subsequently chosen for the next shift step with a star (*). The relationship between the zoomed views, (c), and (a)

can be determined from the starting points that they both show. A video of this sequence is shown in the supplementary information[30]. (Colour online)

Table 1 includes a measure of how much displacement is created during the measurement phase (of testing each of the available forces in turn). It can be seen that this distance is significant, however reducing it tends to increase the measurement errors (due to reduced signal to noise, the noise being the result of unwanted vibrations). See above for discussion of this.

Table 1: Details of example CFM steering run.

Step	Required Direction (deg)	Applied Modes	Distance moved during test phase (µm)	Magnitude error (µm) (Difference between predicted and actual magnitude)	Angular error in degrees (Difference between predicted and actual direction)	Activated PZT	Time (seconds)	Distance to target (µm)
1	0	1 & 2	11.24	-5.95	9.90	Right	0	200
2	1.71	1 & 2	14.50	-9.28	3.69	Right	1.78	173.9
3	4.41	1 & 2	15.32	-9.64	9.74	Right	3.54	145.1
4	2.29	5 & 1	20.16	-4.99	13.80	Right	4.99	114.8
5	5.68	1 & 2	21.66	-10.31	1.67	Right	7.05	75.4
6	9.48	1 & 2	22.55	-10.03	-9.88	Right	8.13	39.3
7							9.35	6.4

As shown in Figure 5 (b) and (c), the steering system measures the forces available at each step. For example, for the first step, the available five forces have directions: 332.3, 80.2, 114.5, 263.5 and 309.3 degrees respectively. As the required direction towards the target for this step is 0 degrees, the steering algorithm chooses forces 1 & 2, the nearest to this direction in the anticlockwise and clockwise directions and applies them sequentially, for 947 and 213 ms respectively, aiming to achieve a step of 25 μm in the required direction. Note that no image is taken by the system between these two actuations. This is repeated at each step until the bead is within 10 μm of the target. The advantage of combining forces in this method are clearer in steps (such as step 1), when the available forces only have small components in the desired direction.

B. Direct method (DM)

In order to create faster manipulation times and to take advantage of the knowledge that acoustic forces only vary over distances of order λ/4 or greater, this method measures the available forces less often. After an initial measurement step (as described above), the force that is closest to the desired direction is chosen. If the selected force is within 0.5 radians (28.6 degrees) of the required direction then an actuation pulse is applied for a time that is calculated to give a 25 μm displacement. However, if the difference is more than this then the system aims for only 12.5 μm per step. This is in order to allow for the possibility of more suitable forces in subsequent steps. The requested distance is also reduced to half the target distance if the bead is closer than 50 μm to the target (and at this range, further measurements are not taken, relying instead on the last measurement phase).

In subsequent steps, the forces are not measured again unless the distance to the last measurement point is more than 25 μm. Instead, the algorithm stores the values previously measured in a table and uses these. After each movement step, the entry in the table for the force that was used is updated to reflect the actual force observed acting over the step. This takes account of the higher accuracy of the measurement given the larger displacement compared to the measurement phase,

and also makes allowance for the force changing with position and changing over time due to any drifts associated with heating effects.

An example manipulation is shown in Figure 6, with details shown in Table 2. It can be seen that measurements are only made in 6 of the 11 steps. A further example of a bead being manipulated along a square trajectory is shown in a video provided in the supplementary information[28].

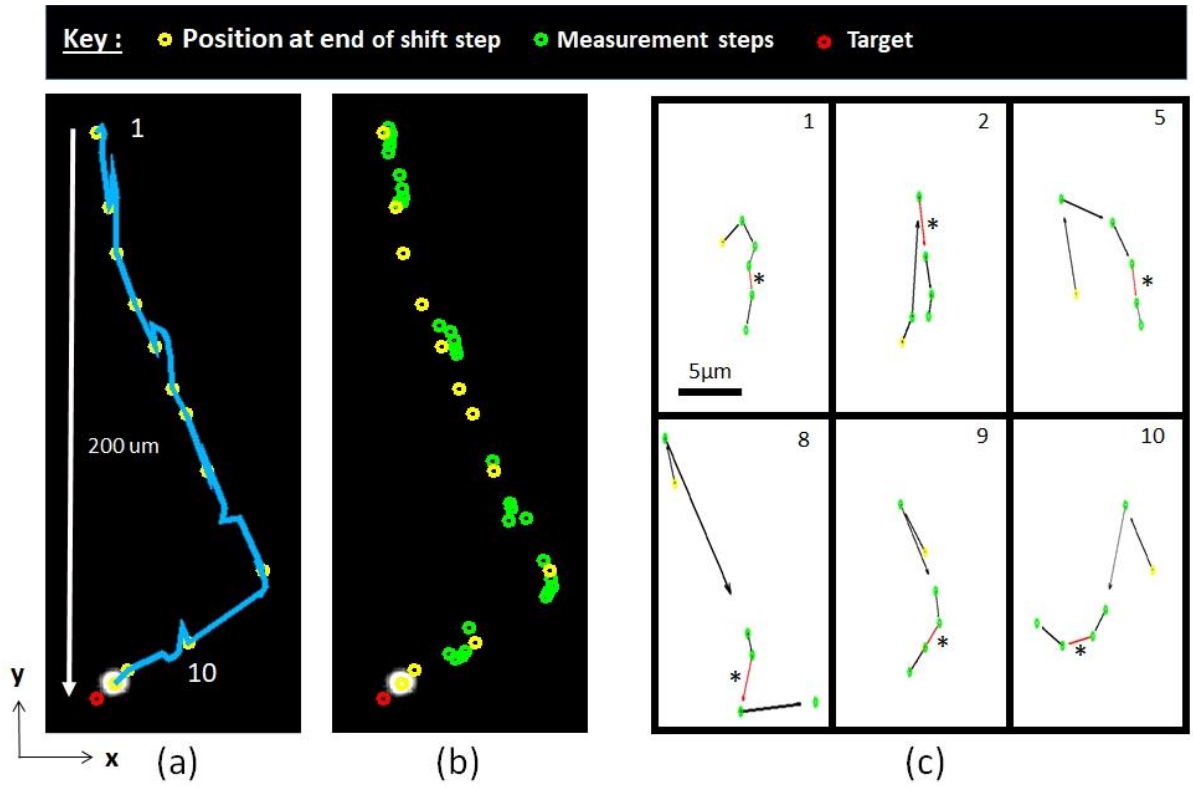

Figure 6. Example steering run for the direct method (DM) of a levitated 10 µm bead over a 200 µm distance from top to bottom towards the target position. (a,b) The trajectory toward the target, including the position at the beginning of each stage, and also the positions (b) after each measurement displacement. (c) A magnified view highlights the forces that were subsequently chosen for the next shift step with a star (*). A video of this sequence is shown in the supplementary information[31]. (Colour online)

Table 2: Details of example DM steering run.

APPENDIX A

Step	Required Direction (deg)	Applied Mode	Distance moved during test phase (μm)	Magnitude error (μm) (Difference between predicted and actual magnitude)	Intended shifting magnitude (μm)	Angular error (deg) (Difference between predicted and actual direction)	Difference between selected and required direction (deg)	Activated PZT	Time (seconds)	Distance to target (μm)
1	90.00	4	7.06	-5.28	25	-1.15	6.83	BOTH	0	200
2	91.49	3	2.88	-7.00	25	0.08	3.15	BOTH	0.63	173.7
3	92.57	5	No Test	-5.61	25	-27.24	4.81	BOTH	1.64	157.82
4	95.60	4	No Test	-8.45	25	-16.51	14.51	BOTH	2.14	140.1
5	99.48	4	5.63	-12.61	25	1.98	16.46	BOTH	2.42	126.2
6	103.80	5	No Test	-15.09	25	-17.97	24.87	BOTH	3.12	113.0
7	107.45	3	No Test	9.03	12.5	1.57	39.24	BOTH	3.60	105.9
8	115.88	4	20.28	-4.70	25	-31.25	18.84	BOTH	4.16	89.8
9	142.29	4	7.37	6.70	25	17.79	14.54	LEFT	5.65	74.1
10	148.33	4	9.89	-5.55	19.07	-5.61	13.47	LEFT	7.12	38.2
11	136.54	3	No Test	-0.97	7.63	14.32	19.97	LEFT	7.70	15.3
12									7.81	8.7

VII. COMPARISON AND DISCUSSION

The two steering algorithms were compared through conducting a large number of manipulation runs for each method.

The distribution of the number of steps required to reach the target and the proportion of successful runs is shown in Figure 7. Runs are allowed to continue until either the target is reached ("success") or the particle is lost by the tracking algorithm ("fail" – typically due to the particle leaving the field of view). The CFM typically reaches the target in fewer steps that the DM: 80% of successful runs are completed in 0-30 steps for the CFM compared to only 69% for the DM. The difference between the number of failures in each case is not significant, as this relates mainly to runs when the bead was lost by virtue of having started close to the edge of the field of view.

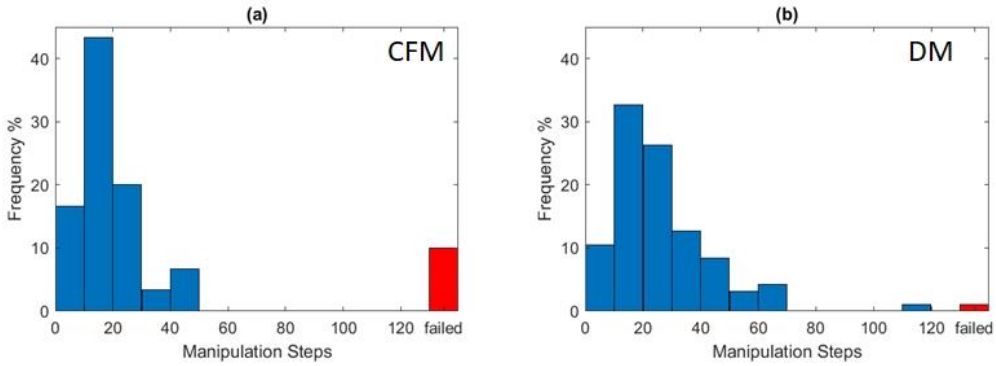

Figure 7. Histograms showing the number of steps to a successful manipulation for a) the combined forces method (CFM) and b) Direct method (DM). The algorithm continued in all cases until either the bead came within the 10 µm target distance (successful runs) or the bead was lost by the tracking code (failed runs). It can be seen that on average the CFM is more effective at reaching the target in fewer steps than the DM. The plots represent data from 30 and 95 runs respectively.

The error between the predicted (as calculated from measurement) and the actual bead displacements during the shifting stage is shown in Figure 8, where the positive values indicate the actual (direction/magnitude) are greater than predicted values.

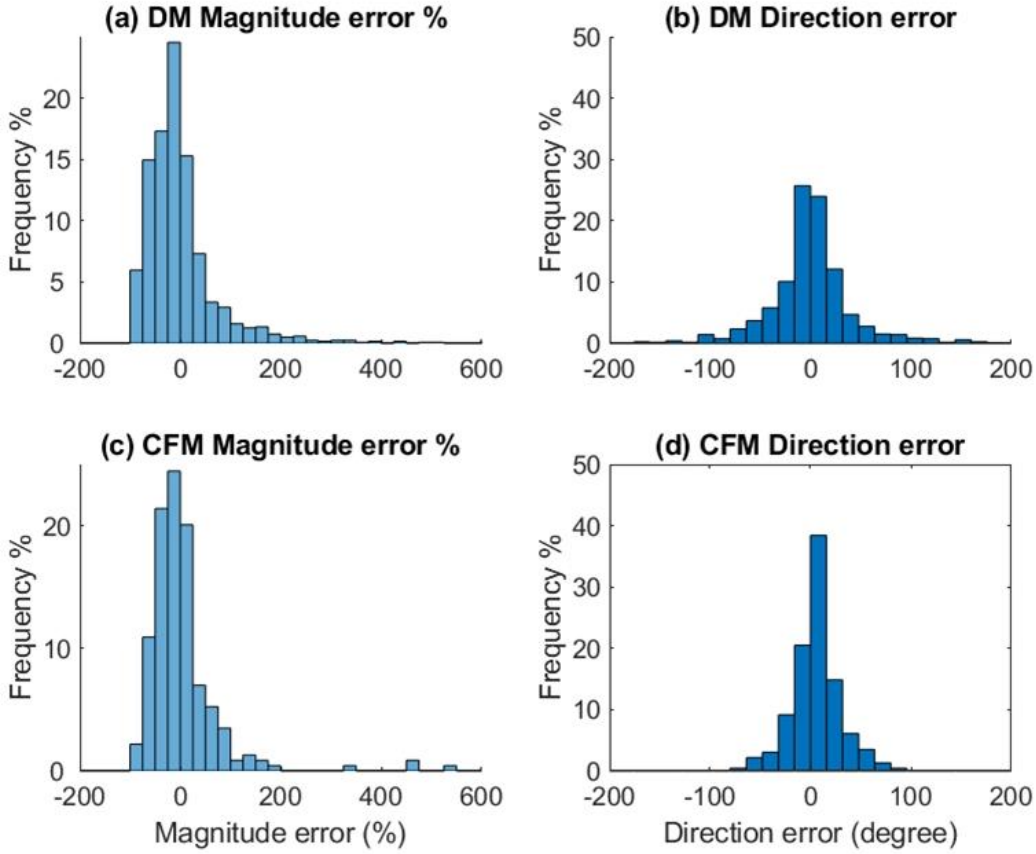

Figure 8. The distribution of errors calculated at each step for both of the steering methods. The error between the predicted (selected) and the actual (real) values is presented, where the positive values indicate greater magnitudes and more clockwise direction in the actual displacement. (b,d): CFM shows a smaller standard deviation in direction error (24 and 41 degrees for CFM and DM respectively), likely due to there being a measurement step associated with each manipulation step (compared to the DM that relies on measurements from previous steps). (a,c) The magnitude errors are grouped around close to zero mean, and have similar distributions. The plots are formed from 1190 and 229 data points for the DM and CFM methods respectively.

In Figure 8(b,d), the CFM shows less direction error than DM, which is anticipated as it makes measurements more often. Both methods are similar in terms of magnitude errors Figure 8(a,c) where the mean and standard deviation magnitude errors are 3.6 ± 71.6% and 3.4 ± 76.0% for DM

and CFM respectively. These errors can be explained as likely to be resulting from the following causes:

A) Timing: variable latencies of ±5.3 ms in communication between the code and the USB interface caused the frequencies to be applied for periods different to those anticipated.

B) Heating effects: Changing temperatures can lead to drift in resonance frequencies that may cause forces to differ between the testing and shifting phases. The DM does less measurement of forces and hence less computation time, which leads to a more sustained application of the manipulating resonances, and hence a higher temperature rise. We typically observe a temperature rises of order 1.7 and 1.0 °C for DM and CFM respectively during the course of a 1-minute manipulation, and thus expect slightly larger errors in the DM from this cause.

C) Acoustic field uniformity: The steering algorithm assumes that forces do not vary with small changes of position in order to linearly extrapolate predicted manipulation distances. However there will be small changes (since the manipulation steps are a significant proportion of a wavelength), and will contribute to the errors seen, particularly when the particle displacements approach the scale of force-field variation which is of order $\lambda/4$ (75 μm at the levitation frequency used here). The force fields will vary between the actual start position of the shift phase and the position at the beginning of the test phase due to the movement caused by each measurement (see Figure 4). This can be mitigated by keep test steps as small as possible (subject to the constraint of also keeping measurement errors resulting from vibrational noise small). The field also varies along the path of the shift phase; this effect is reduced by keeping the shift step size small (25 μm). However, there is a trade-off as if this becomes too small, it can become overwhelmed by the offsets in position that occur during the testing phase.

The contributions of each cause (A,B and C) are harder to quantify, however we observe that over a shifting distance of 25 μm forces can often vary by as much as 50%.

Figure 9 compares the average manipulation velocity of the two methods. The reported value is the average velocity that would be required if the manipulation path were straight (i.e. the total straight distance between run start and target divided by total manipulation time), and does not reflect the average speed over the actual, indirect path that is taken. It can be seen that the DM is typically faster than the CFM, which is likely to be a result of the DM measuring forces less often.

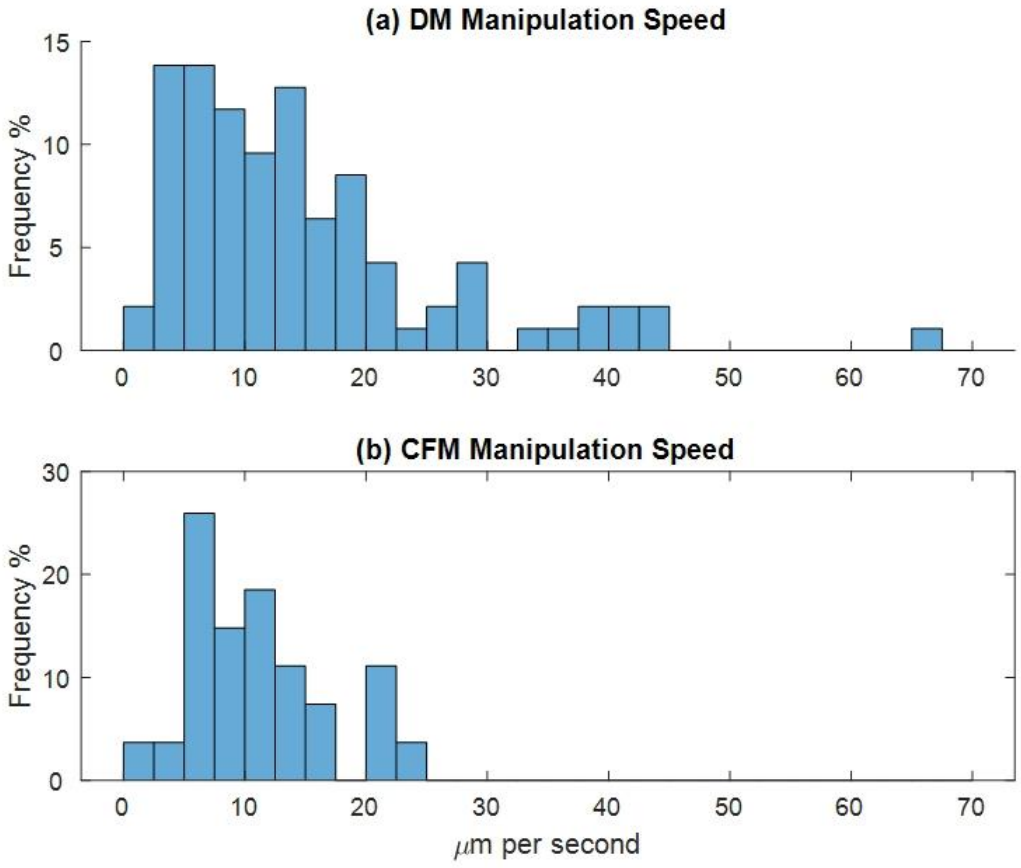

Figure 9. The distribution of average manipulation speed for the two different steering methods. Only successful steering runs are included in the generation of these histograms. The average manipulation speed over the course of a run (from initial position to target) for the two different steering methods have mean values of 15±11.5 and 11.2±5.6 µm/seconds for the DM and CFM respectively. The CFM is typically slower than the DM, as a result of it measuring forces at each step. Graphs formed from 94 and 27 data points respectively.

In order to measure the forces available at each step without unduly disturbing the particle trajectory, the displacements during the test phase are a small number of μm (typically 5-10 um), which in the presence of the vibrational noise (typically ±1 μm) leads to reasonably high errors between the predicted and actual particle displacements at each shift step. Despite this, the method is robust and able to successfully bring back tracked particles to the direction of the intended target trajectory in around 96% of runs. The 3D printed and laser cut microscope design that was employed in this study is more sensitive to such vibrations compared to conventional microscopes. We suspect that with lower vibrational noise, it would be possible to achieve more precise and quicker manipulation as smaller, more precise measurement steps could be taken. Another key way to enhance manipulation speed would be to reduce latencies in the system, which could be achieved by using a real-time operating system, I/O hardware with lower latencies, and a camera operating with lower exposure times and faster readout.

We also note that more sophisticated, model based algorithms could be employed to significantly enhance manipulation accuracy and speed. For example the acoustic force fields derive from periodic potential landscapes; prior knowledge of the typical wavelength scales of these landscapes coupled with prediction based on stored values from prior locations would give the possibility of reduced testing (through informed prediction), reducing both the number of forces tested and how often they are tested.

Observation of the forces associated with each mode under microscopy suggests that the lateral forces associated with each mode primarily result from radiation forces as the forces tend act towards points rather than display significant vorticity. However it is a useful feature of the approach taken here that the source of the forces on the particles is not important from the point of view of the control algorithm, as it progresses by measuring the total force from all sources at each measurement step.

APPENDIX A

Armani et al. [29], demonstrate that in a fluidic system with n degrees of freedom it is possible to manipulate (n-1) particles independently. In the current device some additional forces have been obtained through the multiple PZT areas that can be independently actuated, however the available forces are still limited, and the existing forces overlap in terms of directions they offer. We envisage that with more attention to device design it would be possible to create more degrees of freedom in an acoustic device, and hence manipulate more than just one particle at a time.

VIII. CONCLUSIONS

This paper has presented a steering algorithm which uses lateral acoustic radiation forces to control the position of micro particles. It uses feedback based on a microscope imaging system to achieve closed loop control/steering. The successful steering runs have delivered the tracked particles to within 10 μm of the target over tracks limited only by the field of view of the microscope. Two variations, labelled the combined forces method (CFM) and the direct method (DM), have been explored, with trade-offs for more accurate paths vs enhanced speed respectively. The methods do not rely on a prior knowledge of the distribution of acoustic forces within the device, but instead measures the forces dynamically during the manipulation run. Hence, the methods presented are applicable to a wide range of devices and acoustic field structures.

We believe that increased precision and manipulation speed could be achieved beyond this proof of principle study. More sophisticated and predictive algorithms could make better use of the available data to better actuate the device, and we also anticipate designs which limit disturbing temperature variations through wither active cooling, or alternative acoustic design. We also note the device presented here has a rather limited number of resonances (hence different forces) available to the algorithm and that with an alternative device design this could be improved. Manipulating multiple particles is also a possibility in a device with more available resonances.

ACKNOWLEDGEMENTS

APPENDIX A

Zaid Shaglwf gratefully acknowledges the support of the Ministry of Higher Education and Scientific Research, Libya, for scholarship funding. Peter Glynne-Jones thanks the EPSRC for support from fellowship EP/L025035/1.

Data used to produce the figures in this paper is openly available from the University of Southampton repository at http://dx.doi.org/xxxxx

REFERENCES

[1]H. Bruus, J. Dual, J. Hawkes, M. Hill, T. Laurell, J. Nilsson, S. Radel, S. Sadhal, and M. Wiklund, "Forthcoming Lab on a Chip tutorial series on acoustofluidics: Acoustofluidics-exploiting ultrasonic standing wave forces and acoustic streaming in microfluidic systems for cell and particle manipulation", Lab on a Chip (2011).

[2]S. Gupta, D. L. Feke, and I. Manaszloczower, "Fractionation of Mixed Particulate Solids According to Compressibility Using Ultrasonic Standing-Wave Fields", Chemical Engineering Science **50**, 3275-3284 (1995).

[3]J. J. Hawkes and W. T. Coakley, "Force field particle filter, combining ultrasound standing waves and laminar flow", Sensors and Actuators B-Chemical **75**, 213-222 (2001).

[4]S. Oberti, A. Neild, and J. Dual, "Manipulation of micrometer sized particles within a micromachined fluidic device to form two-dimensional patterns using ultrasound.", Journal of the Acoustical Society of America **121**, 778-785 (2007).

[5]M. Wiklund, O. Manneberg, B. Vanherberghen, and B. Onfelt, "Flow-free transport of cells in microchannels by frequency-modulated ultrasound", Lab on a Chip **9**, 833-837 (2009).

[6]C. D. Wood, J. E. Cunningham, R. O'Rorke, C. Walti, E. H. Linfield, A. G. Davies, and S. D. Evans, "Formation and manipulation of two-dimensional arrays of micron-scale particles in microfluidic systems by surface acoustic waves", Applied Physics Letters **94**, 054101 (2009).

[7]X. Y. Ding, S. C. S. Lin, B. Kiraly, H. J. Yue, S. X. Li, I. K. Chiang, J. J. Shi, S. J. Benkovic, and T. J. Huang, "On-chip manipulation of single microparticles, cells, and organisms using surface acoustic waves", Proceedings of the National Academy of Sciences of the United States of America **109**, 11105-11109 (2012).

[8]P. Glynne-Jones, R. J. Boltryk, N. R. Harris, A. W. J. Cranny, and M. Hill, "Mode-switching: A new technique for electronically varying the agglomeration position in an acoustic particle manipulator", Ultrasonics **50**, 68-75 (2010).

[9]J. R. Wu, "Acoustical Tweezers", Journal of the Acoustical Society of America **89**, 2140-2143 (1991).

[10]J. Lee, S. Y. Teh, A. Lee, H. H. Kim, C. Lee, and K. K. Shung, "Single beam acoustic trapping", Applied Physics Letters **95**, 073701 (2009).

[11]J. Lee, C. Lee, H. H. Kim, A. Jakob, R. Lemor, S. Y. Teh, A. Lee, and K. K. Shung, "Targeted cell immobilization by ultrasound microbeam", Biotechnol Bioeng **108**, 1643-1650 (2011).

[12]T. Kozuka, T. Tuziuti, H. Mitome, T. Fukuda, and F. Arai, "Control of position of a particle using a standing wave field generated by crossing sound beams", 1998 IEEE Ultrasonics Symposium - Proceedings, Vols 1 and 2, 657-660 (1998).

[13]A. L. Bernassau, P. Glynne-Jones, F. Gesellchen, M. Riehle, M. Hill, and D. R. S. Cumming, "Controlling acoustic streaming in an ultrasonic heptagonal tweezers with application to cell manipulation", Ultrasonics **54**, 268-274 (2014).

[14]C. Courtney, C.-K. Ong, B. Drinkwater, P. Wilcox, C. Démoré, S. Cochran, P. Glynne-Jones, and M. Hill, "Manipulation of microparticles using phase-controllable ultrasonic standing waves", Journal of the Acoustical Society of America **128**, EL195-199 (2010).

[15]L. Meng, F. Cai, J. Chen, L. Niu, Y. Li, J. Wu, and H. Zheng, "Precise and programmable manipulation of microbubbles by two-dimensional standing surface acoustic waves", Applied Physics Letters **100**, 173701-173704 (2012).

[16]C. R. P. Courtney, C. E. M. Demore, H. X. Wu, A. Grinenko, P. D. Wilcox, S. Cochran, and B. W. Drinkwater, "Independent trapping and manipulation of microparticles using dexterous acoustic tweezers", Applied Physics Letters **104**, 154103 (2014).

[17]A. Riaud, M. Baudoin, O. B. Matar, L. Becerra, and J. L. Thomas, "Selective Manipulation of Microscopic Particles with Precursor Swirling Rayleigh Waves", Physical Review Applied **7**, 154103 (2017).

[18]A. Marzo, S. A. Seah, B. W. Drinkwater, D. R. Sahoo, B. Long, and S. Subramanian, "Holographic acoustic elements for manipulation of levitated objects", Nature Communications **6**, 8661 (2015).

[19]T. Kozuka, T. Tuziuti, H. Mitome, and T. Fukuda, "Control of a standing wave field using a line-focused transducer for two-dimensional manipulation of particles", Japanese Journal Of Applied Physics Part 1-Regular Papers Short Notes & Review Papers **37**, 2974-2978 (1998).

[20]D. Foresti, M. Nabavi, M. Klingauf, A. Ferrari, and D. Poulikakos, "Acoustophoretic contactless transport and handling of matter in air", Proceedings of the National Academy of Sciences **110**, 12549-12554 (2013).

[21]U. S. Jonnalagadda, M. Hill, W. Messaoudi, R. B. Cook, R. O. C. Oreffo, P. Glynne-Jones, and R. S. Tare, "Acoustically modulated biomechanical stimulation for human cartilage tissue engineering", Lab on a Chip **18**, 473-485 (2018).

[22]P. Glynne-Jones, R. J. Boltryk, and M. Hill, "Acoustofluidics 9: Modelling and applications of planar resonant devices for acoustic particle manipulation", Lab on a Chip **12**, 1417-1426 (2012).

[23]P. Glynne-Jones, C. E. Demore, C. Ye, Y. Qiu, S. Cochran, and M. Hill, "Array-controlled ultrasonic manipulation of particles in planar acoustic resonator", IEEE Trans Ultrason Ferroelectr Freq Control **59**, 1258-1266 (2012).

[24]*Microscale acoustofluidics*. (Royal Society of Chemistry).

[25]L. Gor'Kov, On the forces acting on a small particle in an acoustical field in an ideal fluid, proc: Soviet Physics Doklady, Vol. 6 (1962) 773.

[26]P. Glynne-Jones, R. J. Boltryk, and M. Hill, "Acoustofluidics 9: Modelling and applications of planar resonant devices for acoustic particle manipulation", Lab Chip **12**, 1417-1426 (2012).

[27]J. F. Spengler, M. Jekel, K. T. Christensen, R. J. Adrian, J. J. Hawkes, and W. T. Coakley, "Observation of yeast cell movement and aggregation in a small-scale MHz-ultrasonic standing wave field", Bioseparation **9**, 329-341 (2001).

[28]See supplementary material at [URL will be inserted by AIP] for SuppPubmm3.avi, an exanple video of a square trajectory with the DM method.

[29]M. D. Armani, S. V. Chaudhary, R. Probst, and B. Shapiro, "Using feedback control of microflows to independently steer multiple particles", Journal of Microelectromechanical Systems **15**, 945-956 (2006).

[30]See supplementary material at [URL will be inserted by AIP] for SuppPubmm1.avi, an exanple video of the CFM method.

[31]See supplementary material at [URL will be inserted by AIP] for SuppPubmm2.avi, an exanple video of the DM method.

References

1. Bruus, H., et al., Forthcoming Lab on a Chip tutorial series on acoustofluidics: Acoustofluidics—exploiting ultrasonic standing wave forces and acoustic streaming in microfluidic systems for cell and particle manipulation. Lab Chip, 2011. **11**: p. 3579-3580.
2. Glynne-Jones, P., R.J. Boltryk, and M. Hill, Acoustofluidics 9: Modelling and applications of planar resonant devices for acoustic particle manipulation. Lab Chip, 2012. **12**(8): p. 1417-26.
3. Gupta, S., D.L. Feke, and I. Manas-Zloczower, Fractionation of mixed particulate solids according to compressibility using ultrasonic standing wave fields. Chemical Engineering Science, 1995. **50**(20): p. 3275-3284.
4. Hawkes, J.J. and W.T. Coakley, Force field particle filter, combining ultrasound standing waves and laminar flow. Sensors and Actuators B: Chemical, 2001. **75**(3): p. 213-222.
5. Augustsson, P., et al. Measuring the 3D motion of particles in microchannel acoustophoresis using astigmatism particle tracking velocimetry. in 16th International Conference on Miniaturized Systems for Chemistry and Life Sciences (MicroTAS 2012).
6. Gor'Kov, L. On the forces acting on a small particle in an acoustical field in an ideal fluid. in Soviet Physics Doklady. 1962.
7. Woodside, S.M., et al., Acoustic force distribution in resonators for ultrasonic particle separation. Aiche Journal, 1998. **44**(9): p. 1976-1984.
8. Hammarstrom, B., T. Laurell, and J. Nilsson, Seed particle-enabled acoustic trapping of bacteria and nanoparticles in continuous flow systems. Lab on a Chip, 2012. **12**(21): p. 4296-4304.
9. Glynne-Jones, P., et al., Array-controlled ultrasonic manipulation of particles in planar acoustic resonator. IEEE Trans Ultrason Ferroelectr Freq Control, 2012. **59**(6): p. 1258-66.
10. Crum, L.A., Bjerknes forces on bubbles in a stationary sound field. The Journal of the Acoustical Society of America, 1975. **57**(6): p. 1363-1370.
11. Gröschl, M., Ultrasonic separation of suspended particles - Part I: Fundamentals. Acustica, 1998. **84**(3): p. 432-447.
12. MANNEBERG, O., Multidimensional Ultrasonic Standing Wave Manipulation in Microfluidic Chips. 2009.
13. Wiklund, M., R. Green, and M. Ohlin, Acoustofluidics 14: Applications of acoustic streaming in microfluidic devices. Lab on a Chip, 2012. **12**(14): p. 2438-2451.

14. Lei, J., P. Glynne-Jones, and M. Hill, Acoustic streaming in the transducer plane in ultrasonic particle manipulation devices. Lab on a Chip, 2013. **13**(11): p. 2133-2143.
15. Rayleigh, L., On the circulation of air observed in Kundt's tubes, and on some allied acoustical problems. Philosophical Transactions of the Royal Society of London, 1884. **175**: p. 1-21.
16. Eckart, C., Vortices and streams caused by sound waves. Physical Review, 1948. **73**(1): p. 68.
17. Schlichting, H. and K. Gersten, Boundary-layer theory. 2003: Springer Science & Business Media.
18. Riley, N., Acoustic streaming. Theoretical and Computational Fluid Dynamics, 1998. **10**(1-4): p. 349-356.
19. Beyer, R.T., Nonlinear acoustics. Physical acoustics, 1998. **2**(Part B): p. 231-332.
20. Kozuka, T., et al., Acoustic manipulation of micro objects using an ultrasonic standing wave. 1994 5th International Symposium on Micro Machine and Human Science Proceedings, 1994: p. 83-87.
21. Kozuka, T., et al. Control of position of a particle using a standing wave field generated by crossing sound beams. in Ultrasonics Symposium, 1998. Proceedings., 1998 IEEE. 1998. IEEE.
22. Bernassau, A., et al., Controlling acoustic streaming in an ultrasonic heptagonal tweezers with application to cell manipulation. Ultrasonics, 2014. **54**(1): p. 268-274.
23. Courtney, C.R., et al., Manipulation of microparticles using phase-controllable ultrasonic standing waves. J Acoust Soc Am, 2010. **128**(4): p. EL195-9.
24. Meng, L., et al., Precise and programmable manipulation of microbubbles by two-dimensional standing surface acoustic waves. Applied Physics Letters, 2012. **100**(17): p. 173701-4.
25. Kozuka, T., et al., Control of a standing wave field using a line-focused transducer for two-dimensional manipulation of particles. Japanese journal of applied physics, 1998. **37**(5S): p. 2974.
26. Foresti, D., et al., Acoustophoretic contactless transport and handling of matter in air. Proceedings of the National Academy of Sciences, 2013. **110**(31): p. 12549-12554.
27. González, I., et al., A polymeric chip for micromanipulation and particle sorting by ultrasounds based on a multilayer configuration. Sensors and Actuators B: Chemical, 2010. **144**(1): p. 310-317.
28. Tolt, T.L. and D.L. Feke, Separation Devices Based on Forced Coincidence Response of Fluid-Filled Pipes. Journal of the Acoustical Society of America, 1992. **91**(6): p. 3152-3156.
29. Petersson, F., et al., Continuous separation of lipid particles from erythrocytes by means of laminar flow and acoustic standing wave forces. Lab Chip, 2005. **5**(1): p. 20-2.

30. Sadikova, D.G. and T.N. Pashovkin, Cell Concentration and Separation in the Field of a Standing Ultrasonic Wave for Medicine and Biotechnology. Open Journal of Biophysics, 2013. **03**(01): p. 70-75.
31. Petersson, F., et al. Particle flow switch utilizing ultrasonic particle switching in microfluidic channels. in 7th International Conf on Miniaturizing Chem and Biochem Analysis Systems. 2003.
32. Lenshof, A. and T. Laurell, Continuous separation of cells and particles in microfluidic systems. Chemical Society Reviews, 2010. **39**(3): p. 1203-1217.
33. Shi, J., et al., Continuous particle separation in a microfluidic channel via standing surface acoustic waves (SSAW). Lab on a Chip, 2009. **9**(23): p. 3354-3359.
34. Harris, N., et al., A novel binary particle fractionation technique. Physics Procedia, 2010. **3**(1): p. 277-281.
35. Liu, Y. and K.M. Lim, Particle separation in microfluidics using a switching ultrasonic field. Lab Chip, 2011. **11**(18): p. 3167-73.
36. Jeong, J.S., et al., Particle manipulation in a microfluidic channel using acoustic trap. Biomed Microdevices, 2011. **13**(4): p. 779-88.
37. Oberti, S., A. Neild, and J. Dual, Manipulation of micrometer sized particles within a micromachined fluidic device to form two-dimensional patterns using ultrasound. Journal of the Acoustical Society of America, 2007. **121**(2): p. 778-785.
38. Courtney, C.R.P., et al., Independent trapping and manipulation of microparticles using dexterous acoustic tweezers. Applied Physics Letters, 2014. **104**(15).
39. Manneberg, O., et al., Flow-free transport of cells in microchannels by frequency-modulated ultrasound. Lab Chip, 2009. **9**(6): p. 833-7.
40. Drinkwater, B.W., Dynamic-field devices for the ultrasonic manipulation of microparticles. Lab on a Chip, 2016.
41. Marx, V., Biophysics: using sound to move cells. Nat Meth, 2015. **12**(1): p. 41-44.
42. Coakley, W., et al., Analytical scale ultrasonic standing wave manipulation of cells and microparticles. Ultrasonics, 2000. **38**(1): p. 638-641.
43. Laurell, T., F. Petersson, and A. Nilsson, Chip integrated strategies for acoustic separation and manipulation of cells and particles. Chemical Society Reviews, 2007. **36**(3): p. 492-506.
44. Wiklund, M., Acoustofluidics 12: Biocompatibility and cell viability in microfluidic acoustic resonators. Lab on a Chip, 2012. **12**(11): p. 2018-2028.

45. Augustsson, P., et al., Automated and temperature-controlled micro-PIV measurements enabling long-term-stable microchannel acoustophoresis characterization. Lab on a Chip, 2011. **11**(24): p. 4152-4164.
46. Bernassau, A.L., et al., Controlling acoustic streaming in an ultrasonic heptagonal tweezers with application to cell manipulation. Ultrasonics, 2014. **54**(1): p. 268-74.
47. Haake, A. and J. Dual, Contactless micromanipulation of small particles by an ultrasound field excited by a vibrating body. The Journal of the Acoustical Society of America, 2005. **117**(5): p. 2752-2760.
48. Courtney, C.R., et al., Dexterous manipulation of microparticles using Bessel-function acoustic pressure fields. Applied Physics Letters, 2013. **102**(12): p. 123508.
49. Ding, X., et al., MANIPULATING SINGLE PARTICLES USING STANDING SURFACE ACOUSTIC WAVES.
50. Wood, C., et al., Formation and manipulation of two-dimensional arrays of micron-scale particles in microfluidic systems by surface acoustic waves. Applied Physics Letters, 2009. **94**(5): p. 054101.
51. Orloff, N.D., et al., Manipulating particle trajectories with phase-control in surface acoustic wave microfluidics. Biomicrofluidics, 2011. **5**(4): p. 044107.
52. Haake, A., et al., Positioning, displacement, and localization of cells using ultrasonic forces. Biotechnology And Bioengineering, 2005. **92**(1): p. 8-14.
53. Kayani, A.A., et al., Optofluidics incorporating actively controlled micro- and nano-particles. Biomicrofluidics, 2012. **6**(3).
54. Cohen, A.E., Control of nanoparticles with arbitrary two-dimensional force fields. Physical review letters, 2005. **94**(11): p. 118102.
55. Cohen, A.E. and W. Moerner, Method for trapping and manipulating nanoscale objects in solution. Applied physics letters, 2005. **86**(9): p. 093109.
56. Armani, M.D., et al., Using feedback control of microflows to independently steer multiple particles. Journal of Microelectromechanical Systems, 2006. **15**(4): p. 945-956.
57. Huang, Y., et al., Three-axis rapid steering of optically propelled micro/nanoparticles. Review of Scientific Instruments, 2009. **80**(6): p. 063107.
58. Khalil, I.S., et al. Magnetic-Based closed-loop control of paramagnetic microparticles using ultrasound feedback. in 2014 IEEE International Conference on Robotics and Automation (ICRA). 2014. IEEE.

59. Kim, D.H., et al., Artificial magnetotactic motion control of Tetrahymena pyriformis using ferromagnetic nanoparticles: A tool for fabrication of microbiorobots. Applied Physics Letters, 2010. **97**(17): p. 173702.

60. Martel, S., et al., Flagellated magnetotactic bacteria as controlled MRI-trackable propulsion and steering systems for medical nanorobots operating in the human microvasculature. The International journal of robotics research, 2009. **28**(4): p. 571-582.

61. Capretto, L., et al., Microfluidic reactors for controlled synthesis of polymeric micelles. Journal of Controlled Release, 2010. **148**(1): p. e25-26.

62. Guo, F., et al., Three-dimensional manipulation of single cells using surface acoustic waves. Proceedings of the National Academy of Sciences, 2016. **113**(6): p. 1522-1527.

63. Svennebring, J., O. Manneberg, and M. Wiklund, Temperature regulation during ultrasonic manipulation for long-term cell handling in a microfluidic chip. Journal of Micromechanics and Microengineering, 2007. **17**(12): p. 2469.

64. Manneberg, O., et al., Wedge transducer design for two-dimensional ultrasonic manipulation in a microfluidic chip. Journal Of Micromechanics And Microengineering, 2008. **18**(9): p. 095025.

65. Demore, C., et al., Transducer Arrays for Ultrasonic Particle Manipulation, in 2010 International Ultrasonics Symposium. 2010, Ieee. p. 412-415.

66. Qiu, Y., et al., Screen-printed ultrasonic 2-D matrix array transducers for microparticle manipulation. Ultrasonics, 2015. **62**: p. 136-146.

67. Glynne-Jones, P., et al., Mode-switching: a new technique for electronically varying the agglomeration position in an acoustic particle manipulator. Ultrasonics, 2010. **50**(1): p. 68-75.

68. Lei, J., P. Glynne-Jones, and M. Hill, Modal Rayleigh-like streaming in layered acoustofluidic devices. Physics of Fluids (1994-present), 2016. **28**(1): p. 012004.

69. Hill, M., Y. Shen, and J.J. Hawkes, Modelling of layered resonators for ultrasonic separation. Ultrasonics, 2002. **40**(1): p. 385-392.

70. Santiago, J.G., et al., A particle image velocimetry system for microfluidics. Experiments in fluids, 1998. **25**(4): p. 316-319.

71. Adrian, R.J., Twenty years of particle image velocimetry. Experiments in fluids, 2005. **39**(2): p. 159-169.

72. Lindken, R., et al., Micro-particle image velocimetry (μPIV): recent developments, applications, and guidelines. Lab on a Chip, 2009. **9**(17): p. 2551-2567.

73. Wereley, S.T. and C.D. Meinhart, Recent Advances in Micro-Particle Image Velocimetry, in Annual Review of Fluid Mechanics. 2010, Annual Reviews: Palo Alto. p. 557-576.

74. Glynne-Jones, P. and M. Hill, Acoustofluidics 23: acoustic manipulation combined with other force fields. Lab on a Chip, 2013. **13**(6): p. 1003-1010.
75. Spengler, J., W. Coakley, and K. Christensen, Microstreaming effects on particle concentration in an ultrasonic standing wave. AIChE journal, 2003. **49**(11): p. 2773-2782.
76. Jonnalagadda, U.S., et al., Acoustically modulated biomechanical stimulation for human cartilage tissue engineering. Lab on a Chip, 2018. **18**(3): p. 473-485.
77. Phillips, C.L. and J.M. Parr, Feedback control systems. 5th ed. 2011, Boston ; London: Pearson/Prentice Hall. x, 774 p.
78. Ljung, L., System identification : theory for the user. 2nd ed. Prentice Hall information and system sciences series. 1999, Upper Saddle River, NJ: Prentice Hall. xxii, 609 p.
79. Nise, N.S., Control systems engineering. 5th ed. 2008, Hoboken, N.J.: Wiley. xviii, 861 p.
80. Johansson, L., Acoustic manipulation of particles and fluids in microfluidic systems. 2009.